Magnetization Dynamics in the Lanthanide Metal Gadolinium

Dissertation
zur Erlangung des Grades eines Doktors der Naturwissenschaften

am Fachbereich Physik der Freien Universität Berlin

vorgelegt von
Kamil Nick Bobowski

Berlin 2020

Erstgutachter: Prof. Dr. Martin Weinelt
Zweitgutachter: Prof. Dr. Ralph Ernstorfer

Tag der Disputation: 31.08.2020

Abstract

In this thesis we investigate the rare-earth metal Gd aiming to gain more insight into the complex interplay of physical processes leading to optically induced ultrafast magnetization dynamics. Using X-ray magnetic circular dichroism (XMCD) we study the magnetization dynamics in Gd over a wide range of time scales and pump laser fluences, while using photoemission spectroscopy (PES) we focus on the first 100 fs of the dynamics showing an increase in exchange splitting of the $5d6s$ bulk bands. Moreover, we analyze oscillations in the kinetic energy of the photoemitted electrons for negative pump-probe delays in our PES data.

Using XMCD in reflection we find a two-step demagnetization on sub-ps and tens of ps time scales with a remagnetization on a hundred ps time scale for various pump laser fluences. An extended version of the microscopic three-temperature model (M3TM) captures the dynamics of the whole data set and suggests Elliott-Yafet-type spin-flip scattering to play a dominant role in the 100 fs to ns magnetization dynamics in Gd. On the fast time scale the demagnetization magnitude depends exponentially on the pump laser fluence implying that a complete demagnetization on that time scale in pure Gd is not physically possible. Results for varying pump photon energies indicate an influence of the initial hot electron distribution on the following dynamics, where lower pump photon energies cause a weaker demagnetization in the early sub-ps dynamics.

Our PES study reveals new results particularly in the first 100 fs, where the majority-spin bulk band reacts directly to laser excitation and is not delayed as found in literature. Shifts in the minority- and majority-spin bulk band binding energies lead to a surprising increase in exchange splitting of the $5d6s$ valence bands in Gd for a few dozen fs after laser excitation indicating an increase in magnetization. Concurrently, the majority-spin bulk and surface states shift in opposing directions despite the same spin polarization. We find optically induced spin transfer (OISTR) between the surface and bulk states in Gd likely to account for this phenomenon.

At negative pump-probe delays we observe oscillations in the kinetic energy of photoemitted electrons, a phenomenon explained in literature by ponderomotive acceleration by a transient grating formed by the interference of the incoming and reflected pump laser pulse. We observe a strong enhancement of the oscillation amplitudes on Gd in accordance with the model. We find similar oscillations on W and model parameters show the expected pump photon energy dependence. However, we see different amplitudes for electrons emitted out of different states in W with only slightly different kinetic energy, an unexpected result since photoemitted, free electrons subject to the same potential should experience the same force.

Kurzfassung

Diese Arbeit untersucht das seltene Erdmetall Gd mit dem Ziel, das komplexe Wechselspiel verschiedener physikalischer Prozesse besser zu verstehen, die nach optischer Anregung zu ultraschneller Magnetisierungsdynamik führen. Mit Röntgenzirkulardichroismus wurde die Magnetisierungsdynamik in Gd über einen weiten Zeitbereich von der ultraschnellen fs Entmagnetisierung bis hin zur thermischen Wiederherstellung der Magnetisierung nach 100 ps für unterscheidliche Anregungsfluenzen untersucht. In Photoemissionspektroskopiemessungen wurde der Schwerpunkt auf die Dynamik in den ersten 100 fs gelegt, in denen die Austauschaufspaltung der $5d6s$-Volumenbänder kurzzeitig zunimmt. Darüber hinaus wurden Oszillationen in der kinetischen Energie der photoemittierten Elektronen analysiert.
In fluenzabhängigen Röntgenzirkulardichroismusmessungen wird eine zweistufige Dynamik beobachtet, deren kurze Zeitskala im sub-ps-Bereich liegt und deren langsame Komponente mehrere 10 ps beträgt. Die erfolgreiche Modellierung der fluenzabhängigen Dynamik mit einem erweiterten mikroskopischen Drei-Temperatur-Modell legt nahe, dass Spinflipstreuung die der Magnetisierungsdynamik zugrundeliegenden physikalischen Prozesse in Gd auf Zeitskalen zwischen 100 fs und ns dominiert. Dabei ergibt sich ein exponentieller Zusammenhang zwischen der Entmagnetisierungsamplitude auf der kurzen Zeitskala und der Anregungsfluenz, was suggeriert, dass reines Gd auf dieser Zeitskala nicht optisch entmagnetisiert werden kann. Eine Anregung mit reduzierter Photonenenergie resultiert in einer geringeren Entmagnetisierung in den ersten 100 fs, was auf einen Einfluß der initialen nicht-thermischen Elektronenverteilung auf die Dynamik hindeutet.
Die Photoemissionsdaten zeigen neue Ergebnisse insbesondere in den ersten 100 fs. Die Verschiebung der spinaufgespaltenen Volumenbänder ergibt einen unerwarteten Anstieg der Austauschaufspaltung dieser Bänder in Gd für einige 10 fs, welches einer Zunahme der Magnetisierung entspricht. Damit einher geht, dass die Verschiebung des Majoritätsvolumenbandes und -oberflächenzustandes trotz gleicher Spinpolarisation in entgegengesetze Richtungen verläuft. Ein optisch induzierter Spintransfer zwischen den Oberflächen- und Volumenzuständen in Gd wird für diese Beobachtung verantwortlich gemacht.
Das Phänomen von Oszillationen der kinetischen Energie photoemittierter Elektronen wurden in der Literatur mit der ponderomotiven Beschleunigung durch ein transientes Gitter erklärt, welches durch die Selbstinterferenz des einfallenden und reflektierten Anregungspulses entsteht. Die Oszillationsamplitude auf Gd in unseren Daten ist, im Einklang mit Modellvorhersagen, stark erhöht gegenüber Daten in der Literatur. Die Auswertung ähnlicher Oszillationen auf W für verschiedene Anregungsenergien ergibt Fitparameterabhängigkeiten, die ebenfalls den Modellvorhersagen entsprechen. Im Widerspruch zur Erwartung, dass freie, photoemittierte Elektronen nahezu gleicher kinetischer Energie mit dem gleichen Potential auf die gleiche Weise wechselwirken, weisen die Zustände auf W jedoch unterschiedliche Oszillationsamplituden auf.

Contents

Acronyms **vii**

1 Introduction **1**

2 Theoretical Principles of Ultrafast Magnetization Dynamics **5**
2.1 Three-Temperature Model 5
2.2 Landau-Lifshitz-Based Approaches 7
    2.2.1 Macromagnetism Description 7
    2.2.2 Micromagnetism Description 9
    2.2.3 Atomistic Spin Dynamics 11
    2.2.4 High Temperatures in Micromagnetism 12
2.3 Microscopic Three-Temperature Model 15
2.4 Superdiffusive Spin Transport 18

3 Experiment **21**
3.1 Sample System 21
    3.1.1 Properties of Gadolinium 21
    3.1.2 Sample Preparation 22
3.2 X-Ray Magnetic Circular Dichroism in Reflection 23
    3.2.1 Principles of XMCD 24
    3.2.2 Sum Rules 26
    3.2.3 Ultrashort X-Ray Pulse Generation 30
3.3 Photoemission Spectroscopy with Higher-Order Harmonic Generation . 33
    3.3.1 Principles of Photoemission Spectroscopy 34
    3.3.2 Higher-Order Harmonic Generation 38
    3.3.3 Time-of-Flight Analyzer 40

4 Laser Fluence and Energy Dependence of Magnetization Dynamics **43**
4.1 Temperature Dependence of XMCD in Absorption and Reflection 44
    4.1.1 Evaluation Procedure 45
    4.1.2 Static Temperature Dependence of XMCD 47
4.2 Fluence Dependence of Magnetization Dynamics 50
    4.2.1 Evaluation Procedure and Magnetization Dynamics Studied with XMCD 51
    4.2.2 Time-Dependent Measurements at Varying Pump Laser Fluences 58
4.3 Dependence of Magnetization Dynamics on the Photon Energy of the Pump Pulse 67
4.4 Summary 69

5 Optically Induced Spin Transfer Between Bulk and Surface States in Gd 71
5.1 Preliminary Work - Coherent Excitation Model 72
5.2 Static Measurements and Data Evaluation Procedure 73
5.2.1 Evaluation Procedure 73
5.2.2 Gd Surface and Bulk States 77
5.3 Magnetization Dynamics Upon Near-Infrared Laser Excitation 80
5.3.1 Optically Induced Spin Transfer Applied to Gd(0001) 87
5.4 Summary 94

6 Ponderomotive Oscillations on Gd and W 97
6.1 Description of Ponderomotive Acceleration by a Transient Grating . . . 98
6.1.1 Model Extension and Phase Shift Influence on Electron Dynamics 101
6.2 Oscillations on Gd(0001) 105
6.2.1 1300 nm Pump Laser Excitation 106
6.2.2 1600 nm Pump Laser Excitation 109
6.3 Oscillations on W(110) 112
6.4 Summary 121

7 Summary and Conclusion 123

A Laser Fluence Dependence of Magnetization Dynamics in Gd 127
A.1 Thermocouple Calibration 127
A.2 Saturation Correction of Absorption Data 128
A.3 Laser Fluence Dependence of Magnetization Dynamics in Gd for Pump Photon Energies of 0.95 eV and 3.1 eV 132
A.4 Fit Parameter Dependence on Pump Laser Fluence 135

B Optically Induced Spin Transfer in Gd 137
B.1 Global Fit Results for All Pump-Probe Delays 137

Bibliography 145

Publications 163

Supervised Theses 165

Acknowledgments 167

Lebenslauf 169

Selbstständigkeitserklärung 171

Acronyms

2TM	two-temperature model
3TM	three-temperature model
APD	avalanche photodiode
ARPES	angle-resolved photoemission spectroscopy
ASD	atomistic spin dynamics
CCD	charge-coupled device
CLF	Cental Laser Facility
FMR	ferromagnetic resonance
FWHM	full width at half maximum
HHG	higher-order harmonic generation
HWHM	half width at half maximum
IR	infrared
LEED	low-energy electron diffraction
LLB	Landau-Lifshitz-Bloch
LLG	Landau-Lifshitz-Gilbert
M3TM	microscopic three-temperature model
ML	monolayer
MLD	magnetic linear dichroism
MOKE	magneto-optical Kerr effect
OISTR	optically induced spin transfer
OPA	optical parametric amplifier
PES	photoemission spectroscopy
TDC	time-to-digital converter
ToF	time-of-flight
UHV	ultra-high vacuum
UV	ultraviolet

XAS	X-ray absorption spectroscopy
XMCD	X-ray magnetic circular dichroism
XPS	X-ray photoemission spectroscopy
XUV	extreme ultraviolet

Chapter 1

Introduction

Data storage today is based on encoding information as bits in the magnetic state of a material. The continuing aim in data storage technology is to reduce the size of bits to increase data storage density and to increase the writing and reading speed of bits.

Downsizing is challenging because as the bits become smaller they become more prone to lose their magnetic orientation due to thermal fluctuations. Moreover, for smaller bits one has to find methods to switch them very precisely without affecting neighboring bits. Thus, materials need to be found which are magnetically hard at room temperature. However, intentionally switching such magnetically hard bits necessitates either high switching fields or new ways altogether.

The most straightforward, conventional way to switch the magnetization of a material is to apply a magnetic field in the opposite direction of the magnetization [1]. Relying on thermal excitations to move the magnetization out of the easy axis to have a finite torque [2], such a field forces the magnetization in a damped precessional motion whereby it transfers angular momentum to the crystal lattice. Although guaranteed to switch the magnetization, this process is comparably slow and takes nanoseconds as it depends on the slow transfer of angular momentum [2].
A less obvious way to switch the magnetization direction is to apply a magnetic field perpendicular to the magnetization [3]. In this geometry the precession takes place in the plane of the magnetization direction. To switch the magnetization direction, a well-timed field pulse needs to be tuned to half of a precession period [1]. However, this approach was found to become non-deterministic for field pulse durations of less than 2.3 ps [1, 4] limiting the use of magnetic fields for switching.

A means other than magnetic fields and free of the random switching limitation was found in ultrashort laser pulses. With the discovery that laser-induced quenching of magnetization can happen on time scales below 1 ps [5] the field of ultrafast magnetization dynamics was established. Soon, it was shown that circularly polarized laser pulses of 40 fs pulse duration can reverse the magnetization of a GdFeCo alloy without any applied magnetic field [6].

However, ultrafast magnetization dynamics are interesting not only from a technological point of view, but also, and especially, from a fundamental physics perspective. The demagnetization dynamics of ferromagnets offers the possibility to investigate the complex interplay of electrons, phonons, spins and photons after pushing them out of their equilibrium state with a short laser pulse.

Several mechanisms were proposed to explain the ultrafast magnetic phenomena. A purely light-driven mechanism was suggested by Bigot *et al.* [7]. In this concept, a coherent response of the spins is elicited by the direct interaction of the electromagnetic light field with the polarization of the ferromagnet. Choi *et al.* [8] studied $3d$ ferromagnets and discussed how contributions from an inverse Faraday-effect and optical spin-transfer torque affect the demagnetization in those materials. Battiatio *et al.* [9] explain laser-induced demagnetization by the so-called superdiffusive spin transport. The laser pulse excites electrons in the region where it impinges on the sample, but predominantly majority-spin electrons move away from this region leaving it depleted of majority-spin carriers and thus locally reducing the magnetization. A wealth of studies see scattering-based mechanisms behind ultrafast demagnetization. Studies find evidence for electron-electron [10–12], electron-phonon [12–17] and electron-magnon [14, 18–20] scattering. Still, despite evidence for all those mechanisms, a complete picture of the physics eludes the scientific community so far. The complex interactions between and the relative dominance of the proposed mechanisms in the various ferromangets, and multilayers and alloys thereof, are still under debate.

Among the many ferro- and ferrimagnetic materials composed of transition metals, lanthanides and compounds thereof, single-crystalline gadolinium (Gd) poses an exciting sample system. Gd has a complex magnetic structure comprised of large localized magnetic moments in the $4f$ system whose interaction is mediated by delocalized $5d6s$ valence electrons with much weaker moments. Its demagnetization is an example of the interplay and dominance of different effects. On the one hand, there are claims of Elliott-Yafet-type scattering solely being able to explain the demagnetization [15] and, on the other hand, transport effects are being observed [21]. In addition, there is a discrepancy in the dynamics observed for different probing techniques. An angle-resolved photoemission spectroscopy (ARPES) study [22] shows a decoupling of the $5d6s$ and $4f$ moments despite the large intraatomic exchange coupling. The $5d6s$ moments demagnetize on a sub-ps time scale while the $4f$ moments demagnetize only on a time scale of 10 ps. At the same time, X-ray magnetic circular dichroism (XMCD) studies [23, 24] find a two-step demagnetization in the $4f$ moments on time scales of below 1 ps and above 10 ps. These complex dynamics happen on time scales where the electronic system is in equilibrium, but there is indication that already on shorter time scales of 100 fs processes can influence the magnetization dynamics [24].

Our primary goal was to unravel the underlying dynamics in Gd and reconcile the partly inconsistent dynamics mentioned above. We set out to clarify if electron-phonon scattering of the Elliott-Yafet type can indeed extensively explain the dynamics in Gd. Thereto we measured laser fluence-dependent dynamics over a wide time range with XMCD. We calculated the magnetization dynamics with an extended model based on the microscopic three-temperature model (M3TM) by Koopmans *et al.* [15] which only assumes Elliott-Yafet-type scattering as a demagnetization mechanism. Our results corroborate the applicability of that model suggesting electron-phonon scattering to dominate the magnetization dynamics in Gd on time scales of 100 fs up to ns.

A further objective was to investigate dynamics in Gd in the sub-100 fs range. Surprisingly, a magneto-optical Kerr effect (MOKE) study [25] found an increase in the magnetic signal in Gd within the first 200 fs after laser excitation. We investigated this effect with ARPES and could find evidence of an increase in the magnetic response of the system revealing more details in the band dynamics of the exchange-split $5d6s$ valence states.
An unforseen but nonetheless interesting result ensued in our ARPES studies. With the time-of-flight setup at the Rutherford Appleton Laboratory we observed strong oscillations in the kinetic energy of photoemitted electrons due to interaction with the light field created by the self-interference of the incoming and reflected parts of the exciting laser pulse. A particularly noteworthy finding is that the oscillation strength varies for two different initial states in tungsten, despite that the photoemitted electron interacts with the light field a few ps after emission from the sample.

Chapter 2 will introduce the theoretical principles of ultrafast magnetization dynamics with a focus on current theoretical models. The Landau-Lifschitz-based approaches pose a large field of successful models describing magnetization dynamics and we will briefly review the development of the theory from its beginnings to its current developments. Providing microscopic mechanisms for demagnetization and being two very common models in the field, the M3TM and superdiffusive spin transport will be introduced in short.

Chapter 3 will provide the background information necessary to understand the methodological aspects used in this thesis. Gadolinium, the sample system, and its preparation will be described first. Following are fundamentals about the two major methods used for data acquisition, XMCD and photoemission spectroscopy (PES). After each method, key aspects about the two external setups, *i.e.* the FemtoSpeX beamline at BESSY II, HZB, Berlin and the Artemis laser lab of the Cental Laser Facility (CLF), STFC, Rutherford Appleton Laboratory, Didcot, UK, will be detailed.

Chapter 4 will present results from our investigations at the FemtoSpeX beamline using XMCD. We will compare static measurements in absorption and reflection to argue for the equivalence of both measurement geometries. Next, we will discuss time-resolved data for a set of pump laser fluences and the modeling thereof using an extended M3TM. This chapter closes with results for pump laser energy-dependent measurements showing the influence of the initial hot electron distribution on the following demagnetization.

Chapter 5 will present data from our investigations at the CLF using PES to study the sub-100 fs dynamics in Gd. With the excellent temporal resolution at the Artemis laser lab we find an increase in the magnetic signal, *i.e.* the exchange splitting of the spin-split valence bands, within the first 100 fs after laser excitation and observe the individual band dynamics leading to this effect. We will discuss a possible explanation that assumes an optically induced spin transfer between bulk and surface states.

Chapter 6 will deal with large oscillations of the kinetic energy of photoemitted electrons. A modulation of the kinetic energy by a standing light field created by the interference of the incoming and reflected infrared (IR) laser pulse will be discussed. Surprising results of measurements on tungsten indicate a different interaction strength between the light field and the photoemitted electron depending on the initial state of the electron.

Chapter 7 will summarize the contents of the thesis, the major points of discussion and open questions.

Chapter 2

Theoretical Principles of Ultrafast Magnetization Dynamics

Since its beginnings in the 1990s with the discovery of sub-ps demagnetization of Ni by fs laser pulses [5] laser-induced ultrafast magnetization dynamics has been a fruitful field of research [26]. However, the understanding of the underlying microscopic processes is still under investigation. In particular, the theoretical modeling is challenging because the involved phenomena happen on a wide range of time and length scales, from atomic to macroscopic dimensions. Especially, with smaller time scales the complexity of the description of the relevant processes increases vastly. Moreover, various constituents of the magnetically ordered solid like electrons, phonons and spins are out of equilibrium and interact in complex ways.

In this chapter we review some promising models describing ultrafast magnetization dynamics in ferromagnets. But let us first assess on which time scales ultrafast magnetization dynamics occur.
Interactions governing magnetization dynamics in solids like inter- and intra-atomic exchange typically are on energy scales in the order of 1–100 meV ([2]; exemplary exchange energies for Gd, FeGd see [22, 27], respectively). These energies translate to natural time scales of about 50–5000 fs using the relation $t = h/E$ [2] and so delineate the ballpark time scale of ultrafast magnetism.
A second relevant time scale comes from the spin-lattice relaxation time which describes how long a precessing spin takes to dampen its precession and align itself with the anisotropy axis. The magnetic anisotropy energy is of the order of 1–10 µeV [2, 28] and the characteristic time scale is on the order of 100–1000 ps. Thus, as a more general rule, we can state that ultrafast magnetization dynamics explores processes occurring on time scales of less than a hundred ps, the intrinsic spin-lattice relaxation time [2].

Eventually, we are looking for a theoretical description to model how a fs laser pulse excites a magnetic material which then demagnetizes on a sub-ps to ps time scale and recovers its initial magnetization on a ns time scale.

2.1 Three-Temperature Model

Irradiating a sample with an intense short laser pulse puts the system out of equilibrium. For times smaller than the electron-phonon relaxation time a separation of the electron and phonon subsystems is necessary. A typical approach to understanding the energy flows and dynamics in a magnetic material in such a non-equilibrium is to regard the system as being comprised of three subsystems [2, 5], see Fig. 2.1. This approach extends the two-temperature model (2TM) [29, 30] which was applied for the description of electron and phonon dynamics in various metals [25, 31–35].

Each subsystem is treated as an energy reservoir with a certain equilibrium temperature T_i, the subscripts e,p,s denoting the electron, phonon and spin subsystems, respectively. An external stimulus can excite any of the subsystems to trigger a dynamic response[1]. The excited subsystem will be out of equilibrium, then start to equilibrate and, at the same time, distribute the energy among the other subsystems via available interaction channels on characteristic time scales τ_{ij}. Apart from the exchange of energy, when the spin subsystem is involved angular momentum needs to be conserved. Ultimately, people are interested in the evolution of the spin subsystem after an external fast stimulus triggers the dynamic exchange of energy and angular momentum within and in between the subsystems. Additionally, the pathways and time scales of the energy and angular momentum flow are of interest.

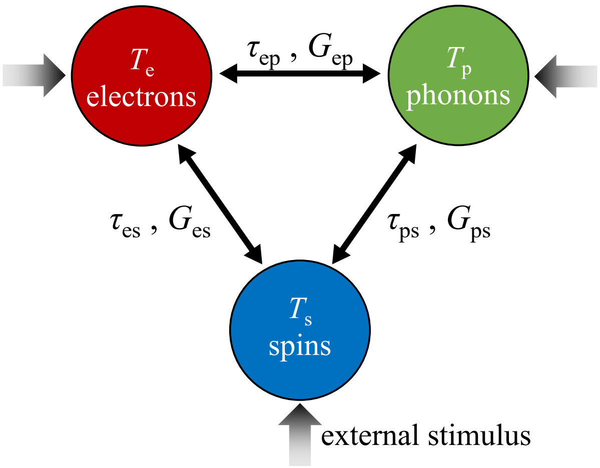
T_e
electrons
τ_ep , G_ep
T_p
phonons
τ_es , G_es
τ_ps , G_ps
T_s
spins
external stimulus

Figure 2.1: 3TM of a ferromagnetic metal. Each reservoir has a certain energy and is assigned an equilibrium temperature T_i where i denotes the subsystem. Any one subsystem can be excited by an external stimulus (outer arrows) to trigger a dynamic response. The subsystem will start to equilibrate and distribute the energy via available channels (double-arrows) to the other subsystems on characteristic time scales τ_{ij} related to the coupling rates G_{ij}.

In the basic phenomenological description, the exchange of the energy between the subsystems is described by three coupled differential equations (adapted from [5]):

$$\begin{aligned} C_\mathrm{e}(T_\mathrm{e})\partial_t T_\mathrm{e} &= G_\mathrm{ep}(T_\mathrm{p}-T_\mathrm{e}) + G_\mathrm{es}(T_\mathrm{s}-T_\mathrm{e}) + P(t) \\ C_\mathrm{p}(T_\mathrm{p})\partial_t T_\mathrm{p} &= G_\mathrm{ep}(T_\mathrm{e}-T_\mathrm{p}) + G_\mathrm{ps}(T_\mathrm{s}-T_\mathrm{p}) \\ C_\mathrm{s}(T_\mathrm{s})\partial_t T_\mathrm{s} &= G_\mathrm{es}(T_\mathrm{e}-T_\mathrm{s}) + G_\mathrm{ps}(T_\mathrm{p}-T_\mathrm{s}) \ . \end{aligned} \tag{2.1}$$

---

[1] An optical or near-infrared (IR) laser pulse can excite the electron subsystem, a pressure or IR heat pulse can excite phonons and magnetic field pulses or spin currents excite the spin system [2].

The coupling strength is given by the coupling constants G_{ij} which initially are free parameters [5]. In Eqs. 2.1, the external stimulus $P(t)$ affects only the electron subsystem. It can take any form to describe the stimulus, *e.g.* a Gaussian laser pulse. The heat capacities of the subsystems C_i can either be constants or functions of T.

In the model, the laser pulse excites the electron subsystem and the electron distribution thermalizes instantly. Thereby one neglects the initial non-equilibrium distribution of the hot electrons in the first 100 fs after excitation [34].
To consider a relaxation of the system as a whole, one needs to add a heat dissipation term which models the energy flow from the magnetic material to the environment. It can take the form of a gradient in the electron temperature as described in the 2TM by Elsayed-Ali *et al.* [30]. The model can describe the flow of energy well and reproduce experimentally measured magnetization dynamics [36, 37]. The coupling constants have a microscopic origin and so the three-temperature model (3TM) can include microscopic mechanisms for the dynamics. However, the exchange of angular momentum is not described in the model.

2.2 Landau-Lifshitz-Based Approaches

The section about Landau-Lifshitz-based approaches to magnetization dynamics modeling and the connection to the microscopic three-temperature model is based on a personal discussion with Dr. Unai Atxitia.

2.2.1 Macromagnetism Description

A different approach to model magnetization dynamics phenomenologically is based on the Landau-Lifshitz equation of motion. The Landau-Lifshitz equation describes the precessional motion of a normalized magnetic moment $\mathbf{m} = \mathbf{M}/M_\mathrm{s}$ (M is the total magnetic moment of a body, M_s is the saturation magnetization) in an effective magnetic field $\mathbf{H}_\mathrm{eff}$ [38], see Fig. 2.2 (a). The equation of motion is

$$\frac{\mathrm{d}\mathbf{m}}{\mathrm{d}t} = -\gamma(\mathbf{m} \times \mathbf{H}_\mathrm{eff}) \ , \tag{2.2}$$

where γ is the gyromagnetic ratio. The effective field $\mathbf{H}_\mathrm{eff}$ includes all interactions like the external field, magnetocrystalline and shape anisotropy, magnetic dipole interaction etc. [26]. It is given by

$$\mathbf{H}_\mathrm{eff} = -\frac{1}{M_\mathrm{s}}\frac{\partial E_\mathrm{m}}{\partial m} \ , \tag{2.3}$$

where E_m is the magnetic energy at the macroscopic level.

To enable the precessing spin to relax back to the equilibrium orientation Landau and Lifshitz introduced a dissipation term to Eq. (2.2) which, in general, is a functional

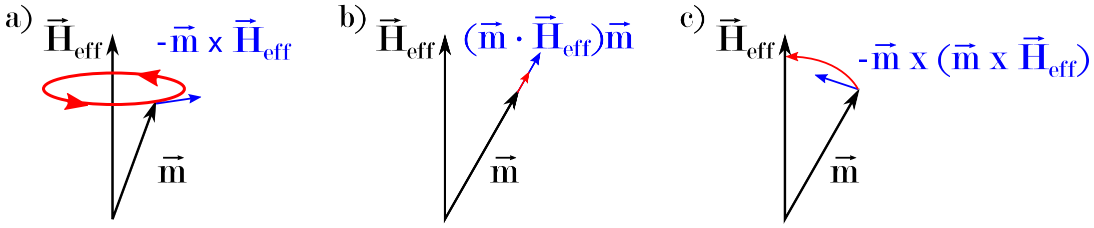
a)
$\vec{H}_{eff}$
-$\vec{m}$ x $\vec{H}_{eff}$
$\vec{m}$
b)
$\vec{H}_{eff}$
$(\vec{m} \cdot \vec{H}_{eff})\vec{m}$
$\vec{m}$
c)
$\vec{H}_{eff}$
-$\vec{m}$ x ($\vec{m}$ x $\vec{H}_{eff}$)
$\vec{m}$

Figure 2.2: Illustration of the effect on the magnetization of the terms in Eq. (2.6): a) is the precession, b) the longitudinal damping and c) the transverse damping.

$R(\mathbf{m}, \dot{\mathbf{m}})$. As the simplest ansatz they assumed $\mathbf{R}(\mathbf{m}, \dot{\mathbf{m}}) = \lambda \mathbf{H}_{\text{eff}}(\mathbf{m}, \dot{\mathbf{m}})$ neglecting higher order terms. This ansatz assumes $\mathbf{H}_{\text{eff}}$ to be small and that the dissipated power can be expressed in terms of even powers of $\mathbf{H}_{\text{eff}}$ $(\mathbf{H}^2_{\text{eff}}, \mathbf{H}^4_{\text{eff}}, \dots)$. At equilibrium, $\mathbf{H}_{\text{eff}} = 0$. Additionally assuming isotropy, the damping λ is a scalar.
Then, the effective field is separated into components parallel and perpendicular to the magnetization direction:

$$\mathbf{H}_{\text{eff}} = \frac{(\mathbf{H}_{\text{eff}} \cdot \mathbf{m})\mathbf{m}}{m^2} - \frac{[\mathbf{m} \times [\mathbf{m} \times \mathbf{H}_{\text{eff}}]]}{m^2} \ . \tag{2.4}$$

The resulting equation of motion is:

$$\begin{aligned} \frac{\mathrm{d}\mathbf{m}}{\mathrm{d}t} &= -\gamma \mathbf{m} \times \mathbf{H}_{\text{eff}} + \gamma \mathbf{R} \qquad (2.5) \\ &= -\gamma \mathbf{m} \times \mathbf{H}_{\text{eff}} + \gamma\lambda \frac{(\mathbf{H}_{\text{eff}} \cdot \mathbf{m})\mathbf{m}}{m^2} - \gamma\lambda \frac{[\mathbf{m} \times [\mathbf{m} \times \mathbf{H}_{\text{eff}}]]}{m^2} \ . \qquad (2.6) \end{aligned}$$

Equation (2.6) contains both a longitudinal and a transverse relaxation term. Their effects are shown in Fig. 2.2 (b) and (c). In general, the longitudinal relaxation is stronger and its dynamics faster than the transverse damping. On the ns time scales of spin dynamics and precessional motion, the magnitude of the magnetization is set constant, $|\mathbf{m}| = m_{\text{e}}$. In particular for small excitations, one assumes a negligible longitudinal relaxation and the term containing $(\mathbf{H}_{\text{eff}} \cdot \mathbf{m})\mathbf{m}$ vanishes in Eq. (2.6).

In the initial description by Landau and Lifshitz, the damping λ is assumed small. For strong damping Gilbert improved upon the damping term by introducing an alternative dissipation function. The Gilbert damping parameter α is equivalent to λ for small damping, but for large damping $\alpha \gg 1$ it yields physically correct results in contrast to λ. Typically, the Gilbert damping parameter $\alpha \ll 1$ [39, 40]. So far, the assumption of small damping is valid for all magnetic materials[2]. The equation of motion then reads:

$$\frac{\mathrm{d}\mathbf{m}}{\mathrm{d}t} = -\gamma \mathbf{m} \times \mathbf{H}_{\text{eff}} - \gamma\alpha \frac{[\mathbf{m} \times [\mathbf{m} \times \mathbf{H}_{\text{eff}}]]}{m^2} \ , \tag{2.7}$$

---

[2] Personal correspondence with Dr. U. Atxitia, FU Berlin, Nov. 2019.

where we have for the Gilbert damping parameter α:

$$\alpha = \frac{\lambda}{1+\lambda^2} \qquad \begin{cases} \lambda \to 0: & \alpha \simeq \lambda \\ \lambda \gg 1: & \alpha \simeq 1/\lambda \end{cases} . \tag{2.8}$$

Equation (2.7) is known as the Landau-Lifshitz-Gilbert (LLG) equation of motion. In small systems like nanoparticles thermal fluctuations gain importance. This can lead to spontaneous magnetization reversal between two stable states (superparamagnetism) on time scales of the order 10^{-9}–10^{-13} s [41–43]. To account for such fluctuations, a stochastic approach based on Langevin dynamics is implemented in Eq. (2.7). One adds a white noise term to the effective field and demands it to be uncorrelated and its time average to be zero [44].

2.2.2 Micromagnetism Description

The macromagnetism description is inherently insufficient to model inhomogeneous systems, *e.g.* systems that exhibit domain walls. Additionally, the global magnetization cannot include interactions between spins (or groups thereof) like exchange interaction or collective excitations like spin waves. To describe such phenomena, Brown [45] introduced a theory termed micromagnetism where the magnetization becomes a continuous function of space. The magnetization at different space coordinates can point at any direction due to the classical character of the micromagnetic theory. However, there exist problems in magnetism extremely difficult to solve analytically by the continuum theory. For those problems, one needs to resort to numerical schemes for the solution of the equations, which in turn are solved by computer simulations. Since computer simulations cannot handle continuous functions, the magnetization space needs to be divided into cells containing only one vector field of the magnetization, see Fig. 2.3.

In practice, small cells (of about a few nm [26, 47]) are each described with the LLG equation. The effective field at those cells, in addition to anisotropy and external fields, is comprised of the exchange field and dipolar fields. The former is described as the gradient of the magnetization and dominates short range magnetic order. The exchange coupling in the micromagnetic approach is derived from a direct exchange coupling between the magnetization at different positions in space, but assuming cubic and isotropic materials, it is reduced to the gradient form in Eq. (2.9). The energy of the interacting cells is given by[3]:

$$E = \int \underbrace{A(\boldsymbol{\nabla}\mathbf{m}(\mathbf{r}))^2}_{\text{exchange}} + \underbrace{\frac{\mu_0}{2}\mathbf{m}(\mathbf{r}) \cdot \mathbf{H}_{\text{demag}}}_{\text{demagnetization}} + \underbrace{K(\mathbf{m}_z(\mathbf{r}))^2}_{\text{anisotropy}} + \underbrace{\mu_0\mathbf{H}_z(\mathbf{r}) \cdot \mathbf{m}(\mathbf{r})}_{\text{Zeeman}} \,\mathrm{d}\mathbf{r} \ , \tag{2.9}$$

where A is the exchange stiffness parameter, μ_0 the vacuum permeability, $\mathbf{H}_{\text{demag}}$ is the demagnetization field, K the macroscopic uniaxial anisotropy constant and $\mathbf{H}_z$ the external Zeeman field.

---

[3] Personal correspondence with Dr. Unai Atxitia, Berlin (2019)

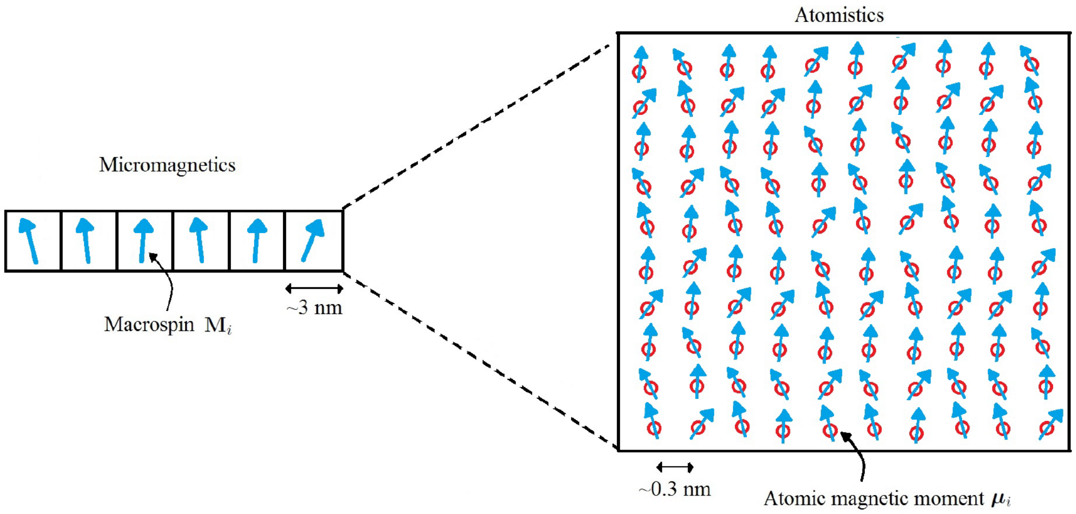

Figure 2.3: Sketch of the division of the magnetization into cells in micromagnetics and its relation to the atomistic approach. Image taken from [46].

Similarly to the stochastic macromagnetic approach, white noise is added to the effective field to account for thermal fluctuations. For each cell $\mathbf{H}_{\text{eff}}^{ijk} \to \mathbf{H}_{\text{eff}}^{ijk} + \xi^{ijk}$ where i, j, k stand for the space coordinates of each cell. The equation of motion is described by:

$$\frac{\mathrm{d}\mathbf{m}(\mathbf{r}_{ijk})}{\mathrm{d}t} = -\gamma[\mathbf{m}(\mathbf{r}_{ijk}) \times \mathbf{H}_{\text{eff}}(\mathbf{r}_{ijk})] - \gamma\alpha[\mathbf{m}(\mathbf{r}_{ijk}) \times [\mathbf{m}(\mathbf{r}_{ijk}) \times \mathbf{H}_{\text{eff}}(\mathbf{r}_{ijk})]] \ . \tag{2.10}$$

Micromagnetism enables the description of collective magnetic excitations, *i.e.* spin waves. They are described by

$$\delta\mathbf{m}(\mathbf{r}, t) = \delta\mathbf{m}(\mathbf{k}, \omega) \cdot e^{i(\omega t - \mathbf{k}\cdot\mathbf{r})} \ , \tag{2.11}$$

where $\mathbf{k} \cdot \mathbf{r}$ is the spatial modulation of the deviations around the equilibrium state, $\mathbf{k}$ is the wave vector and ω the angular frequency. The finite size of the computational cells L_{cell} limits the range of possible $\mathbf{k}$ of the spin waves: $\mathbf{k}_{\text{max}} \propto L_{\text{cell}}^{-1}$. As an example for a ferromagnet the dispersion is $\omega(k) \propto Dk^2$ [48] with the exchange stiffness D. Thus, for larger wave vectors the energy and frequency of the excitations increases and the time scale of the dynamics decreases.

For small enough cell sizes a large number of thermal excitations relevant for magnetization dynamics can be described. However, within this approach the minimum cell size is limited due to computational power[4] and higher energetic spin wave excitations for $\mathbf{k} > \mathbf{k}_{\text{max}}$ are missed because of the so-called exchange approximation. It assumes the deviations of atomic spin moments $\mathbf{s}_i$ between neighboring spins to be small, which breaks down if the spin wave wavelength becomes too small (comparable to L_{cell}). Since a large range of spin waves with high k cannot be described and therefore excited, this can lead to a significant overestimation of the Curie temperature T_{C} [49]. In addition, temperature effects cannot be captured with the micromagnetic approach (which assumes $T = 0\,\mathrm{K}$), *e.g.* dynamics of the magnetization magnitude, slowing longitudinal and quickening transverse relaxation around T_{C} [49].

---

[4] The total size of the simulated sample gives (basically) the number of spin wave modes $k_n = \frac{\pi n}{L_{\text{cell}} N}, n = 0, 1, \dots, N-1$. Then, $k_{\text{max}} = k_{N-1} \approx \pi / L_{\text{cell}}$ (N is very large).

These problems are overcome by the atomistic spin dynamics (ASD) or by the Landau-Lifshitz-Bloch (LLB) equation. In ASD the dynamics of individual spins are treated at the atomic scale. This approach is limited to small sample sizes due to computational limitations. On the other hand, the LLB equation, which is micromagnetic, extends the micromagnetic LLG equation to finite temperatures.

2.2.3 Atomistic Spin Dynamics

The next step in the evolution of the Landau-Lifshitz-based description of magnetization dynamics is the atomistic level. Differently to the micromagnetic LLG, where cells containing thousands of atomic spins are approximated by a unique magnetization $\mathbf{m}_i$, in ASD one models the individual atomistic spins $\mathbf{s}_i = \boldsymbol{\mu}_i/\mu_0$ with the atomic magnetic moment $\boldsymbol{\mu}_i$ at a site i, see Fig. 2.3. The typical Hamiltonian in ASD is [46]:

$$\mathcal{H} = \underbrace{-\sum_i \mathbf{H}\cdot\boldsymbol{\mu}_i}_{\text{Zeeman}} \underbrace{-\sum_i d_z s_{i,z}^2}_{\text{anisotropy}} \underbrace{-\frac{1}{2}\sum_{i,j} J_{ij}\mathbf{s}_i\cdot\mathbf{s}_j}_{\text{exchange}} \ , \tag{2.12}$$

with the external magnetic field $\mathbf{H}$, the uniaxial anisotropy constant d_z and the exchange constant J_{ij} between atoms at sites i and j. The equation of motion for each individual spin is described by the LLG equation [46]:

$$\frac{\mathrm{d}\mathbf{s}_i}{\mathrm{d}t} = -\frac{\gamma}{1+\lambda^2}\mathbf{s}_i \times \mathbf{H}_{\text{eff},i} - \frac{\gamma\lambda}{1+\lambda^2}[\mathbf{s}_i \times [\mathbf{s}_i \times \mathbf{H}_{\text{eff},i}]] \ , \tag{2.13}$$

where γ and λ are, as above, the gyromagnetic ratio and the damping constant and $\mathbf{H}_{\text{eff},i} = -\partial\mathcal{H}/\partial\boldsymbol{\mu}_i$ is the effective field.

In contrast to the micromagnetic approach, the exchange coupling is treated as a direct exchange between spins. The gradient form from Eq. (2.9) cannot be used in ASD as only single spins are regarded instead of a continuous magnetization.

The evolution of the total magnetization $\mathbf{m}$ in ASD can be calculated as:

$$\mathbf{m} = 1/N \sum_{i\in N} \mathbf{s}_i \ , \tag{2.14}$$

where N is the number of spins. With ASD methods based on the atomic stochastic LLG equation one is able to also describe the high-energy spin wave dynamics which are missed in the micromagnetic approach. In current developments more complex spin structures for the individual spins like antiferromagnetic coupling or $5d$-$4f$ coupling are implemented [50]. However, the computational power limits the sample volumes to, for example, cubes with edge lengths of few dozens of nm or similar volumes [46].

As for the micromagnetic approach, stochastic dynamics can be included in ASD by introducing a stochastic field to the effective field $\mathbf{H}_{\mathrm{eff},i} \rightarrow \mathbf{H}_{\mathrm{eff},i} + \boldsymbol{\xi}_i$. Without the stochastic field, energy and angular momentum only dissipate into the heat bath via the damping term. The addition of stochastic fields means that the heat bath can in turn induce fluctuations in the system. Assuming a particular shape for the distribution function of the stochastic field, in this case the Boltzmann distribution, one can relate the dissipation term, the Gilbert damping, and the fluctuation fields and thus calculate thermal equilibrium properties of the spin system.

Then, as the fields depend on temperature, one can also change the temperature of the heat bath and calculate the dynamics towards the new equilibrium. The magnetization $m(T = 0\,K) = 1$ becomes $m(T) = m_\mathrm{e}$ with the equilibrium magnetization m_e at finite temperature T. With this approach, even high temperatures can be captured.

2.2.4 High Temperatures in Micromagnetism

The ASD approach allows us to describe magnetization dynamics in all ranges of T. However, atomistic models have size restrictions from a computational point of view. Thus, it is desirable to have a micromagnetic approach which is able to describe finite temperatures and large sample sizes.

To encompass also high temperatures in micromagnetic magnetization dynamics modeling longitudinal relaxation has to be implemented. The LLG equation (Eq. (2.7)) conserves the magnitude of the magnetization. First steps towards addressing this problem were done by Baryakhtar [51, 52] who proposed an equation of motion for the total magnetization $\mathbf{m}$ implementing longitudinal dynamics:

$$\frac{\mathrm{d}\mathbf{m}}{\mathrm{d}t} = -\gamma[\mathbf{m} \times \mathbf{H}_\mathrm{eff}] - \gamma\hat{\alpha}\mathbf{H}_\mathrm{eff} \,. \tag{2.15}$$

Here, $\hat{\alpha} = \alpha_{ij}$ is a tensor. The effective field is [52]:

$$\mathbf{H}_\mathrm{eff} = a\frac{\partial^2\mathbf{m}}{\partial x_i^2} - \frac{(m^2 - m_\mathrm{e}^2)\mathbf{m}}{2\chi m_\mathrm{e}^2} \,, \tag{2.16}$$

with the constant of the non-uniform exchange interaction a (which is the same as A in Eq. (2.9) in the micromagnetic approach), the magnetic susceptibility χ and the equilibrium magnetization m_e. The last part in Eq. (2.16) is responsible for the longitudinal relaxation and its rate is determined by $\hat{\alpha}\mathbf{H}_\mathrm{eff}$. It originates from exchange interaction and is related to the deviation of the homogeneous magnetization from its equilibrium orientation. The first term originates from exchange interaction as well, but it is non-local being related to deviations of the local spin from neighboring magnetic moments. The susceptibility χ is a function of temperature and typically increases strongly around T_C resulting in a critical slowing down of the dynamics at temperatures around T_C.

For the field of rapid excitation by lasers it is important to know how parameters change with temperature, even above the Curie temperature. However, the equation of motion proposed by Baryakhtar is only valid for temperatures below T_C [53] and the temperature dependence of $\hat{\alpha}$ is unknown from a theoretical point of view. Moreover, it is a phenomenological equation which does not consider underlying microscopic spin degrees of freedom.

Landau-Lifshitz-Bloch Equation

Garanin *et al.* investigated the magnetization dynamics of single-domain magnetic particles analytically [54] and later Garanin extended the formalism to derive the LLB equation for ferromagnets [53, 55]. He derived an equation capable of modeling the magnetization dynamics at finite temperatures below and above T_C, including the temperature dependence of the damping parameters [55]. An outline of the approximations and derivation of the model is given in [53]. The final equation of motion is:

$$\frac{\mathrm{d}\mathbf{m}}{\mathrm{d}t} = -\gamma[\mathbf{m}\times\mathbf{H}_\mathrm{eff}] + \gamma\alpha_\parallel\frac{(\mathbf{m}\cdot\mathbf{H}_\mathrm{eff})\mathbf{m}}{m^2} - \gamma\alpha_\perp\frac{[\mathbf{m}\times[\mathbf{m}\times\mathbf{H}_\mathrm{eff}]]}{m^2}\ . \tag{2.17}$$

This LLB equation depends on the effective field $\mathbf{H}_\mathrm{eff}$ and the longitudinal and transverse damping parameters $\alpha_\parallel$ and $\alpha_\perp$. For ferromagnets the latter are given by [46]:

$$\alpha_\parallel = 2\lambda\frac{T}{3T_\mathrm{C}}, \qquad \alpha_\perp = \lambda\cdot\begin{cases}\left[1-\frac{T}{3T_\mathrm{C}}\right] & T\lesssim T_\mathrm{C}\\ \frac{2T}{3T_\mathrm{C}} & T\gtrsim T_\mathrm{C}\end{cases}\ , \tag{2.18}$$

with the damping λ, which describes the coupling to the heat bath at the atomic level and coincides with λ from Eq. (2.13), and the Curie temperature T_C. The effective field is [53]:

$$\mathbf{H}_\mathrm{eff} = \mathbf{H} + \mathbf{H}_\mathrm{A} + \mathbf{H}_\mathrm{ex} + \begin{cases}\frac{1}{2\tilde{\chi}_\parallel}\left(1-\frac{m^2}{m_\mathrm{e}^2}\right)\mathbf{m} & T\lesssim T_\mathrm{C}\\ \frac{1}{\tilde{\chi}_\parallel}\left(1+\frac{3}{5}\frac{T_\mathrm{C}}{T-T_\mathrm{C}}m^2\right)\mathbf{m} & T\gtrsim T_\mathrm{C}\end{cases}\ , \tag{2.19}$$

with the longitudinal susceptibility $\tilde{\chi}_\parallel$ and the normalized equilibrium magnetization $m_\mathrm{e} = M_\mathrm{e}(T)/M_\mathrm{e}(0)$. The last term in Eq. (2.19) is the longitudinal field which acts along $\mathbf{m}$ and describes the internal homogeneous exchange field inside the macrospin. It coincides with the longitudinal part of the effective field proposed by Baryakhtar (Eq. (2.16)). The other components are the applied external field $\mathbf{H}$, the anisotropy field $\mathbf{H}_\mathrm{A} = -(m_x^2+m_y^2)/\tilde{\chi}_\perp$ with the transverse susceptibility $\tilde{\chi}_\perp$ and the exchange field between macrospins $\mathbf{H}_\mathrm{ex} = A\Delta\mathbf{m}(\mathbf{r})$ with the exchange stiffness $A = J_0a_0^2/(z\mu_\mathrm{s})$ and the Laplacian operator Δ. Here again, A is the same as in Eqs. (2.9) and (2.16), where J_0 is the zero Fourier component of the exchange interaction, a_0 is the lattice constant, z the number of nearest neighbors and μ_s the atomic magnetic moment. When the system is split into cubic cells of lateral size l_cell for computer simulations Atxitia *et al.* [49] have shown the micromagnetic exchange to become [53]:

$$\mathbf{H}_\mathrm{ex} = -\frac{2A(T)}{m_\mathrm{e}^2 M_\mathrm{s}(0) l_\mathrm{cell}^2} \sum_{j \in \mathrm{neigh}(i)} (\mathbf{m}_j - \mathbf{m}_i) \ , \tag{2.20}$$

with the zero-temperature saturation magnetization $M_\mathrm{s}(0)$.

The temperature dependence in the LLB approach comes about because the input parameters $\tilde{\chi}_\parallel$, $\tilde{\chi}_\perp$, A, λ and m_e depend on temperature [53]. These temperature-dependent equilibrium properties can be obtained from several sources like fitting to experimental data, ASD simulations or the mean-field approach.

The LLB describes all three components of the dynamics shown in Fig. 2.2 and as already described by Eq. (2.6). The first term corresponds to precessional motion and the second and third terms are longitudinal and transverse relaxation. Especially the addition of the longitudinal term provides a more accurate description of the dynamics at elevated temperatures in comparison to the LLG equation (Eq. (2.7)).

A stochastic version, in which thermal fields are added to the effective field, was derived by D. Garanin and O. Chubykalo-Fesenko [56] and later corrected by Evans *et al.* [57] to recover a Boltzmann distribution around T_C at equilibrium [46].

The LLB equation can be brought into the form derived by Baryakhtar (Eq. (2.15)) for an accordingly chosen $\hat{\alpha}$. It captures the symmetry considerations of the Baryakhtar equation but additionally correctly describes the temperature dependence of the relaxation dynamics for the whole temperature range and not only below T_C [53]. Likewise, it contains the LLG equation (Eq. (2.7)) and thus can describe dynamics taking place in the range of 0.1–1 ns dominated by damped precessional motion [46].

Chubykalo-Fesenko *et al.* [58] find that the LLB correctly describes the temperature dependence of static properties and also transverse and longitudinal relaxation dynamics comparing it to ASD simulations. Moreover, they show that the LLB model outperforms the micromagnetic spin dynamics approach based on the LLG. The LLB-based model naturally captures enhanced damping around the Curie temperature and a time-varying magnetization magnitude where LLG-based calculations fail. They draw a very positive conclusion regarding the LLB model as a powerful theoretical tool to describe various aspects of magnetization dynamics.

A quantum mechanical derivation of the LLB equation also exists which incorporates the quantum nature of magnetism [59]. Classical LLB models assume an infinite quantum number S for the localized magnetic moments leading to results deviating from the Bloch $T^{3/2}$ law [53, 60]. A derivation of the quantum LLB is beyond the scope of this thesis but can be found in [53].
The classical LLB has the advantage over the quantum LLB that it can be used in

a multi-scale approach [46, 53]. In the multi-scale approach, material parameters are calculated using *ab-initio* methods which are then used in atomistic models to obtain the temperature-dependent parameters for the micromagnetic models, see Fig. 2.4. This way, magnetization dynamics of realistic sample sizes can be calculated without relying on fitting parameters. A full quantum multi-scale approach does not exist yet and remains a challenge to develop [53].

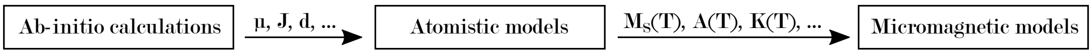

Figure 2.4: Multi-scale approach for magnetization dynamics modeling. Using *ab-initio* calculations the input parameters for atomistic models are caluclated which in turn provide the temperature-dependent parameters for micromagnetic models of large scale sample systems. Image reproduced from [46].

For further reading about Landau-Lifshitz-based magnetization dynamics modeling, the reader is referred to literature. Pablo Nieves Cordones describes the modeling of magnetization dynamics in far more detail in his PhD thesis [46]. Furthermore, references [26, 53] give an outlook and further current developments in the field of theoretical magnetization dynamics modeling.

2.3 Microscopic Three-Temperature Model

Koopmans *et al.* [15] introduced a microscopic three-temperature model (M3TM) which explains the transfer of energy and momentum during laser-induced demagnetization with a microscopic mechanism. It builds on the 2TM [29, 30] but, in contrast to the 3TM, describes the magnetization based on a simplified model Hamiltonian [61]. The dynamics are expressed in the following equations:

$$C_\mathrm{e}[T_\mathrm{e}]\frac{\mathrm{d}T_\mathrm{e}}{\mathrm{d}t} = \nabla_z(\kappa\nabla_z T_\mathrm{e}) + g_\mathrm{ep}(T_\mathrm{p} - T_\mathrm{e}) \tag{2.21}$$

$$C_\mathrm{p}\frac{\mathrm{d}T_\mathrm{p}}{\mathrm{d}t} = g_\mathrm{ep}(T_\mathrm{e} - T_\mathrm{p}) \tag{2.22}$$

$$\frac{\mathrm{d}m}{\mathrm{d}t} = Rm\frac{T_\mathrm{p}}{T_\mathrm{C}}\left(1 - m\coth\left(\frac{mT_\mathrm{C}}{T_\mathrm{e}}\right)\right) \ , \tag{2.23}$$

where $C_\mathrm{e} = \gamma T_\mathrm{e}$ is the electron heat capacity, γ is a materials-dependent parameter, C_p the phonon heat capacity, κ is the electronic thermal conductivity, g_ep is a coupling constant and T_C the Curie temperature. The magnetization M is normalized to the saturation magnetization M_s, $m = M/M_\mathrm{s}$. The thermalization of the electron gas is assumed to be instantaneous. The rate constant R is given by:

$$R = \frac{8a_\mathrm{sf}g_\mathrm{ep}k_\mathrm{B}T_\mathrm{C}^2V_\mathrm{at}}{(\mu_\mathrm{at}/\mu_B)E_D^2} \ , \tag{2.24}$$

with the Boltzmann constant k_B, the atomic volume V_at, the atomic magnetic moment μ_at, the Bohr magneton μ_B and the Debye energy E_D. The spin-flip probability a_sf is related to the microscopic mechanism. Koopmans and coworkers base the spin relaxation on Elliott-Yafet-type spin-flip scattering between electrons and phonons [15, 62, 63]. When an electron scatters with a phonon, the electron can flip a spin and transfer momentum to the phonon.

U. Atxitia and O. Chubykalo-Fesenko could trace back the M3TM to the quantum version of the LLB equation for $S = 1/2$ assuming Elliott-Yafet-type spin-flip scattering as the underlying mechanism [64]. The crucial point to see this equivalence is to realize that both equations of motion for the magnetization can be written in the form:

$$\frac{\mathrm{d}m}{\mathrm{d}t} = \lambda \frac{1}{2\mu_\mathrm{s}\chi} \frac{(m^2 - m_\mathrm{e}^2)m}{m_\mathrm{e}^2} = \lambda \mathrm{H}_\mathrm{eff} \ . \tag{2.25}$$

Here, similar to the assumption made in the micromagnetic approach, one assumes only small deviations of the magnetization m from the equilibrium magnetization m_e, *i.e.* $m - m_\mathrm{e} < m_\mathrm{e}$. The effective field H_eff can be expressed in terms of the Landau-like free energy F (only second order in m) [55]:

$$\mathrm{H}_\mathrm{eff} = -\frac{\partial F}{\mu_\mathrm{s} \partial m} \ , \tag{2.26}$$

$$F = \frac{1}{8\chi} \frac{(m^2 - m_\mathrm{e}^2)^2}{m_\mathrm{e}^2} \ . \tag{2.27}$$

Then Eq. (2.25) is of a form similar to the longitudinal part of Eq. (2.15). U. Atxitia and O. Chubykalo-Fesenko have reformulated Eq. (2.23) into the form of Eq. (2.25) and identified a relation between the proportionality factors from Eqs. (2.15) and (2.23):

$$\lambda = \frac{3R}{2\gamma} \frac{\mu_\mathrm{at}}{k_\mathrm{B} T_\mathrm{C}} \frac{T_\mathrm{p}}{T_\mathrm{e}} \ . \tag{2.28}$$

Thereby, they could show the equivalence of the two models [64]. This link between the M3TM and the LLB approach allows to identify λ as a function of R, where λ also defines the transverse relaxation dynamics (see Eqs. (2.17) and (2.18)).

One can thus model ultrafast magnetization dynamics with the M3TM using the spin-flip probability a_sf as a parameter and compare the resulting damping constant λ_M3TM (via Eqs. (2.24) and (2.28)) with the damping constant λ_FMR which can be measured in ferromagnetic resonance (FMR) experiments. Though the damping constants describe the longitudinal (M3TM) and transverse (FMR) relaxation, respectively, they do not specify the physical mechanism behind the relaxation process. Thus, similar values for the damping constants could, for instance, indicate that in both cases, ultrafast laser-induced and slow magnetization dynamics, the excitation of magnons drives the dynamics. However, in the slow case, only low-frequency magnons could be excited while in the ultrafast case, high-frequency magnons could contribute to the dynamics. In both cases, the damping constant λ would be the same proportionality factor for the

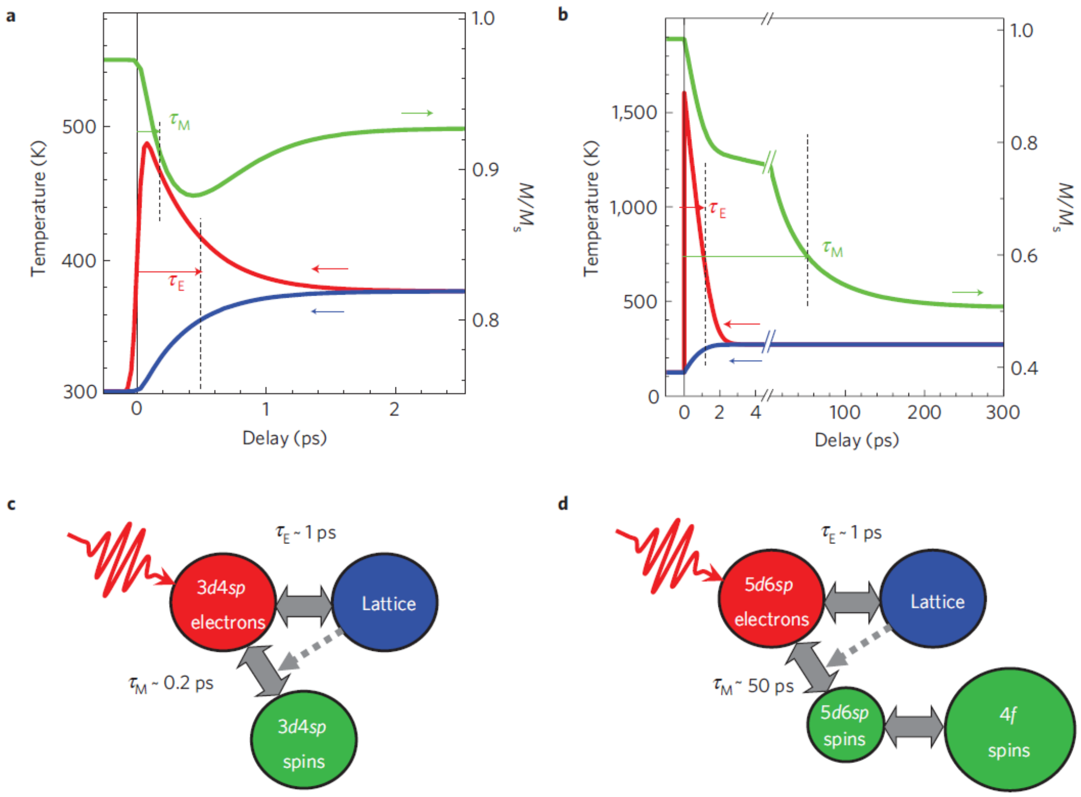

Figure 2.5: M3TM proposed by Koopmans *et al.* [15]. (a) indicates the dynamics of the three subsystems shown in (c) for Ni, a so-called type I material. (b) displays the according dynamics of the subsystems shown in (d) for Gd, a type II material. For Gd, the magnetization is nevertheless described by only a single variable m and not by two variables for the two spin subsystems. The energy equilibration between the subsystems happens on the characteristic time scales τ_i. The dashed arrow indicates the phonon contribution to angular momentum dissipation. Images (a)–(d) taken from [15].

relaxation rate $\Gamma = \lambda\omega$ but the frequency ω of the magnons would determine the time scale of the magnetization dynamics.

The M3TM successfully models magnetization dynamics for several materials [15, 65], also reproducing two different types of demagnetization behavior for transition metals and lanthanides, *cf.* Fig. 2.5 (a) and (b). However, its role in demagnetization processes is contested [66, 67]. In addition, the spin system is treated rather simplistically with a single magnetization for the whole sample which might be insufficient for more complex systems or in cases where the spins are not in equilibrium and transport effects might play a role. In Section 4.2 we will discuss an extended version of the M3TM that was used by Dr. Unai Atxitia to model our data.

2.4 Superdiffusive Spin Transport

The fundamental idea behind demagnetization in the M3TM is a transfer of angular momentum from the spin to the phonon system via spin-flip scattering events. Battiatio *et al.* [9] introduced a microscopic mechanism of magnetization dynamics which, in the broadest sense, describes a transfer of spin momentum in real space without spin flipping events.

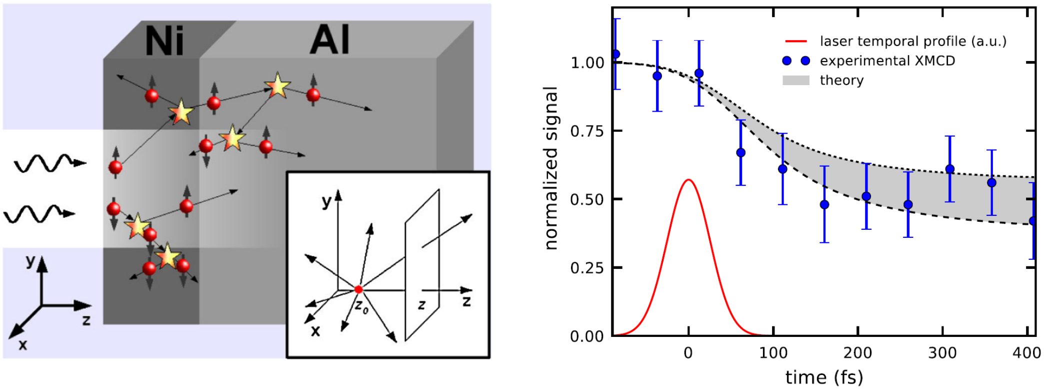

(a) Sketch of superdiffusive transport

(b) Mangetization dynamics in Ni

Figure 2.6: Sketch of the superdiffusive spin transport processes introduced by Battiato *et al.* [9] and computed magnetization dynamics in comparison to experimental data of a Ni film grown on an Al substrate. (a) A laser excites majority- and minority-spin electrons which start scattering and exciting a cascade of electrons. Majority-spin electrons have a larger inelastic mean free path and travel further away from the region of excitation than minority-spin electrons. The inset shows the geometry used for the computation. The electron flux through the plane at z is calculated. (b) Magnetization dynamics in Ni calculated with the superdiffusive transport model for two different treatments of the low-energy life time (top and bottom of the gray area). Blue data points are experimental XMCD data taken from [68]. The laser profile is given in red. Images (a) and (b) taken from [9].

The demagnetization in that model is caused by majority-spin carriers moving away from the probed region, see Fig. 2.6a. The initial laser-induced excitation is spin conserving but the following transport of electrons out of the probed region is different for minority- and majority-spin carriers because of their different life times and inelastic mean free paths [69]. Thus, the long-lived majority-spin electrons carry away more spin momentum than short-lived minority-spin electrons effectively reducing the spin polarization at the site where the excitation happened.
The authors describe the transport of electrons as superdiffusive [9] as it is neither fully ballistic nor diffusive. Instead, in the beginning the transport is ballistic but it becomes diffusive for long times.

The superdiffusive spin transport model successfully reproduced time-resolved X-ray magnetic circular dichroism (XMCD) measurements for Ni by Stamm *et al.* [68], see Fig. 2.6b and highlights the importance of transport effects in ultrafast magnetization dynamics. In contrast to the M3TM, it treats the dynamics of the excited electrons explicitly by considering the involved states in the excitation and taking into account the whole range of electron scattering events.

The concept of superdiffusive spin transport will play a role in Chapter 5 where we will discuss transport effects between bulk and surface states in Gd to explain an increase in exchange splitting on time scales of tens of femtoseconds after laser excitation.

Chapter 3

Experiment

In this chapter we will briefly introduce the experimental setups and methods that were used to measure the data and give basic information about the sample system. The data treated in this thesis was obtained at beamtimes at external facilities and we will limit ourselves to a concise description of the aspects relevant for the understanding of the measurement and evaluation of the data. The X-ray magnetic circular dichroism (XMCD) data discussed in Chapter 4 was measured at the PM3 and FemtoSpeX beamlines at BESSY II, HZB, Berlin; the photoemission data presented in Chapters 5 and 6 was obtained during beamtimes at the Cental Laser Facility (CLF) at the STFC Rutherford Appleton Laboratory. In parallel a setup for higher-order harmonic generation and photoemission spectroscopy (PES) was improved and reinstalled at FU Berlin.

First, we will introduce the sample system properties and how it is prepared. Then, we will describe the setups and methods used at the two facilities.

3.1 Sample System

In this section we will recapitulate some basic properties of Gd, the sample system under investigation. Afterwards, we describe how single-crystalline Gd thin films are grown on a tungsten substrate and why tungsten is particularly suitable for our sample system.

3.1.1 Properties of Gadolinium

Gadolinium (Gd) is a rare-earth metal (or lanthanide) with an electron configuration of [Xe] $4f^7\,5d^1\,6s^2$. Thus, its $4f$ shell is half-filled implying an orbital momentum of $L_f = 0$, a spin moment of $S_f = 7/2$, and a total angular momentum of $J_f = 7/2$. The vanishing orbital momentum leads to a small magnetocrystalline anisotropy of $E_{\mathrm{MCA}} = 0.03\,\mathrm{meV}$ [70]. The $4f$ electrons have a magnetic moment of $7\,\mu_{\mathrm{B}}$ and their wave functions are localized with negligible overlap to neighboring $4f$ electrons making Gd a model Heisenberg ferromagnet. The system attains ferromagnetic order by polarizing the itinerant $5d6s$ electrons with a magnetic moment of $0.55\,\mu_{\mathrm{B}}$ [22] which mediate the spin polarization among the $4f$ moments within the crystal. This kind of indirect coupling is known as Ruderman–Kittel–Kasuya–Yosida interaction. The bulk Curie temperature of Gd is 292.5 K [71]. Its band structure has been calculated by Kurz *et al.* [72]. A simple sketch of the spin-resolved bulk density of states is shown in Fig. 3.1. The unoccupied $4f$ states are located at about 4 eV above [73–75] and the occupied $4f$ states approximately 8 eV [74] below the Fermi level.

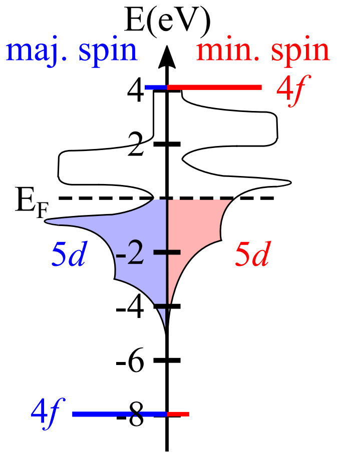

Figure 3.1: Sketch of the spin-resolved bulk electronic density of states of ferromagnetic Gd. Sketch drawn based on the calculated density of states in [72].

3.1.2 Sample Preparation

With PES we are using a surface-sensitive technique which requires the test systems to have clean surfaces. Even in ultra-high vacuum (UHV) conditions with a base pressure below 10^{-10} mbar adsorbates cover the Gd surface within several hours due to its high reactivity. Hence, we have to prepare fresh samples on a regular basis for measurements and need a method which allows for fast and clean growth of the samples.

We brought self-made evaporators[1] to the external facilities to grow samples *in situ* following a procedure well-established in our group. We are using commercially available single-crystalline tungsten (W) substrates cut at the (110) plane. A drawback of these crystals is that they are usually contaminated with carbon to some degree. A new crystal has to be tempered at around 1800 K in an oxygen atmosphere of about $5 \cdot 10^{-8}$ mbar for some hours to desorb the carbon. Then, the crystal is flashed to 2100 K within half a minute to remove the remnant oxygen [77, 79, 80]. Several cycles of this tempering routine can be necessary to clean the W(110) surface depending on its degree of contamination. The quality of the surface is assessed using low-energy electron diffraction (LEED) or PES. A short cleaning cycle might also be necessary if longer periods of time pass between measurements.

---

[1] The evaporator design has been described in other theses of our group, see *e.g.* [76–78].

Despite the drawback, tungsten is an especially suitable substrate for the epitaxial growth of Gd thin films. Due to its high melting point, it can stand the high temperatures during sample preparation and used thin films are easily desorbed by flashing the crystal. The pseudo-hexagonal surface structure of bcc W(110) has only a small mismatch of 2 % to the Gd(0001) hcp bulk lattice structure [81]. After about 3 ML the Gd thin film relaxes and the lattice constant approaches the value for bulk Gd [81]. Finally, W(110) has a high surface energy which prevents Gd alloying with and diffusing into the substrate [76].

We grow our samples with a thickness of about 100 Å which corresponds to about 35 ML [82]. With this sample thickness we are in a range where Gd thin films already exhibit electronic bulk behavior and have negligible influence from the substrate but are thin enough to have an in-plane easy axis and grow layer-by-layer on W(110) [22].

The actual growth procedure starts by heating the crucible of the evaporator filled with 99.99 % pure Gd and establishing a constant evaporation rate[2] of about 2–7 Å min^{-1}. The deposition rate is controlled with a quartz microbalance. A shield keeps the beam of evaporated particles focused on a small area around the sample holder.
Before starting to grow the thin film on the substrate, it is flashed to remove possible contamination. Once the substrate cools down to room temperature, we open a shutter or rotate the sample holder to face the evaporator and the 100 Å thin film is grown. Afterwards, we anneal the sample at 650–750 K for 1 min to let the sample reconstruct and heal lattice defects. The annealing temperature depends on the sample thickness [71, 83] and too high temperatures can cause breakup and island formation [71, 83, 84].

Despite UHV conditions, adsorbates, typically oxygen and hydrogen, bind to the Gd surface within hours and can interfere with the Gd surface magnetism [85, 86]. While the contamination appears in surface-sensitive photoemission measurements, we could not measure a deterioration of the more bulk-sensitive XMCD signal in test measurements comparing a newly made with an aged sample.

3.2 X-Ray Magnetic Circular Dichroism in Reflection

As the name suggests, in XMCD circularly polarized X-rays are used to probe a sample for magnetic information. This is done by utilizing dichroism, *i.e.* the photon absorption depends on the polarization of the X-rays. Thole, van der Laan *et al.* first predicted and measured such a dichroic effect of magnetic origin in rare-earth elements [87, 88]. The fundamentals regarding XMCD are well described in literature [2, 89] and we will only briefly touch on the main aspects to understand the method for later evaluation.

---

[2] The evaporation rate varies due to the different distances between evaporator and sample holder at BESSY II and CLF. The evaporation rate was at the lower end of the given range at BESSY II due to a larger distance and at the upper end at CLF due to a smaller distance.

X-rays spectroscopy methods have some advantages over other optical methods. They are element-specific, sensitive to the chemical state and offer a better spatial resolution than optical methods due to the smaller wavelength [2]. Moreover, the signal averages over all valence states of the Brillouin zone and thus can be referred to various physical quantities like spin and orbital quantum numbers [2].

3.2.1 Principles of XMCD

The origin of XMCD lies in the fact that the angle-averaged intensity $\langle I \rangle$ of a core to valence transition is proportional to the number of available holes N_h [2]:

$$\langle I \rangle = \mathcal{A}\mathcal{R}^2 \frac{L}{3(2L+1)} N_\mathrm{h} \ , \tag{3.1}$$

where $\mathcal{A} = 4\pi^2 \hbar\omega\alpha_\mathrm{f}$ with the photon energy $\hbar\omega$ and the fine structure constant α_f, $\mathcal{R} = \langle R_{n',l'}(r) | \, r \, | R_{n,l}(r) \rangle$ is the radial dipole matrix element with the radial parts of the wave function $R_{n,l}$ with the shell and subshell quantum numbers $\{n, l\}$ and L is the angular momentum. Importantly, N_h is the total number of valence holes in the ground state. Now, XMCD makes use of a difference in the absorption of circularly polarized X-rays due to a different number of spin-up and spin-down holes which also corresponds to the magnetic moment. The XMCD thus is the difference between the X-ray absorption spectroscopy (XAS) intensities for parallel and antiparallel orientation of photon spin and sample magnetization:

$$I_\mathrm{XMCD} = I^{\uparrow\downarrow} - I^{\uparrow\uparrow} \ . \tag{3.2}$$

Figure 3.2 shows a schematic of the XMCD process in a one-electron picture for the example of a $3d \rightarrow 4f$ transition in Gd together with an experimental absorption spectrum. We will describe the situation for maximum XMCD, *i.e.* we assume the following conditions: The X-rays are 100 % circularly polarized. The polarization of the light and the sample magnetization are aligned collinearly. The unoccupied $4f$ state is not spin-mixed due to elevated temperatures but is purely of minority-spin character. If any of those conditions are not met the XMCD signal intensity is decreased.

In the two-step model of XMCD, a circularly polarized X-ray pulse excites electrons from the spin-orbit split $3d$ state. First, via spin-orbit coupling, part of the photon angular momentum is transferred to the electrons which become spin polarized, *i.e.* there is a higher probability to excite one spin direction than the other. The spin polarization of the excited electrons is opposite for the opposing light helicities. Equivalently, instead of changing the light helicity, the sample magnetization can be switched for a fixed light helicity [2]. The sign of the spin polarization is opposite for the two spin-split $3d$ states although the magnitude of the spin polarization can vary.
Second, the final state of the transition serves as a spin detector for those spin polarized excited electrons. The unoccupied state is of one spin character and as the dipole

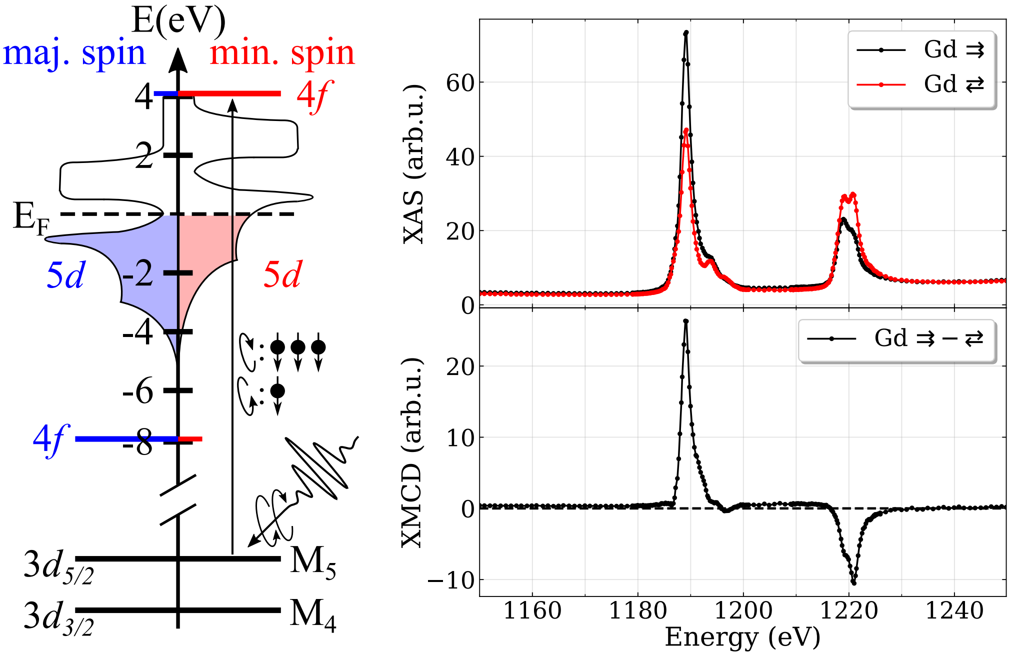

Figure 3.2: Sketch of XMCD for the example of Gd. Left: Circularly polarized X-rays excite a $3d \to 4f$ transition (M$_5$ absorption edge). The excited electrons are spin-polarized and the transition probabilities for right- and left-circularly polarized X-rays is different (indicated by the number of excited minority-spin electrons). The unoccupied $4f$ state is of minority-spin character and functions as a detector for the excited spin-polarized electrons. Disregarding spin mixing due to elevated temperatures, only minority-spin electrons can occupy the $4f$ state resulting in different absorption intensities. Right: Absorption spectra of the Gd M$_5$ (1190 eV) and M$_4$ (1220 eV) absorption edges. At the top, the normalized signals for parallel (⇉) and antiparallel (⇄) magnetization of the sample with respect to the probing light polarization are plotted. Below, the difference between these signals, the XMCD, is depicted. Note, the absorption data is corrected for saturation effects, see Appendix A.2.

transition conserves spin only electrons of the correct spin polarization can be excited. In Gd, at 0 K (no spin-mixing), only minority-spin electrons are excited from the $3d$ to the unoccupied minority-spin $4f$ state. However, if the final state does not have a different number of spin-up and spin-down holes (*e.g.* no Stoner splitting in $3d$ transition metals above T_C), the signal for both X-ray helicities will be the same and the XMCD vanishes.

Under realistic conditions the states will have both minority- and majority-spin character. Then, the total transition intensities need to be calculated quantum mechanically from all individual transition intensities (example for a $2p \rightarrow 3d$ transition in a transition metal, angular part only) [2]:

$$I^q_{n,m_s,j,m_j} = \left| \langle d_n, \chi^\pm | \frac{P^q_z}{r} | p_j, m_j \rangle \right|^2 , \tag{3.3}$$

with the index n of the d orbital and its spin state $|\chi^\pm\rangle = |m_s = \pm 1/2\rangle$, the dipole operator P^q_z, $q = 0, \pm 1$ for linearly and circularly polarized light, r the absolute value of the electron position vector and the initial p state with quantum numbers j and m_j. Figure 3.3 shows these polarization-dependent transition intensities graphically (only for one spin direction in the d state). The XMCD for a certain absorption edge (with fixed j and m_s) thus becomes:

$$I_\mathrm{XMCD} = \sum_{n,m_j} I^{q=-1}_{n,m_s,j,m_j} - I^{q=+1}_{n,m_s,j,m_j} . \tag{3.4}$$

3.2.2 Sum Rules

A very useful fact about XMCD is that one can determine the orbital and spin contributions to the magnetic moment element-specifically by applying the so-called sum rules. The sum rule for the orbital moment was originally derived by Thole *et al.* [90] and the spin sum rule by Carra *et al.* [91].

We regard a transition from a state with ground state configuration l^n to a state with configuration cl^{n+1}, where c stands for the hole in the core level and l^n for the number n of electrons in the final state l ($c = 2$ and $l = 3$ for $d \rightarrow f$ transitions, and $n = 7$ in Gd). Then, the ground-state expectation value of the orbital angular momentum per hole ρ is [91]:

$$\begin{aligned} \rho &= \int_{x+y} (\mu^+ - \mu^-) dE \Big/ \int_{x+y} (\mu^+ + \mu^- + \mu^0) dE \qquad (3.5) \\ &= \frac{1}{2} \frac{l(l+1) + 2 - c(c+1)}{l(l+1)(4l+2-n)} \langle L_z \rangle , \qquad (3.6) \end{aligned}$$

where x, y denote the absorption edges like the M_5 and M_4 absorption edges in Gd (see Fig. 3.2). The absorption coefficients $\mu^{+,-,0}$ are integrated over the whole energy

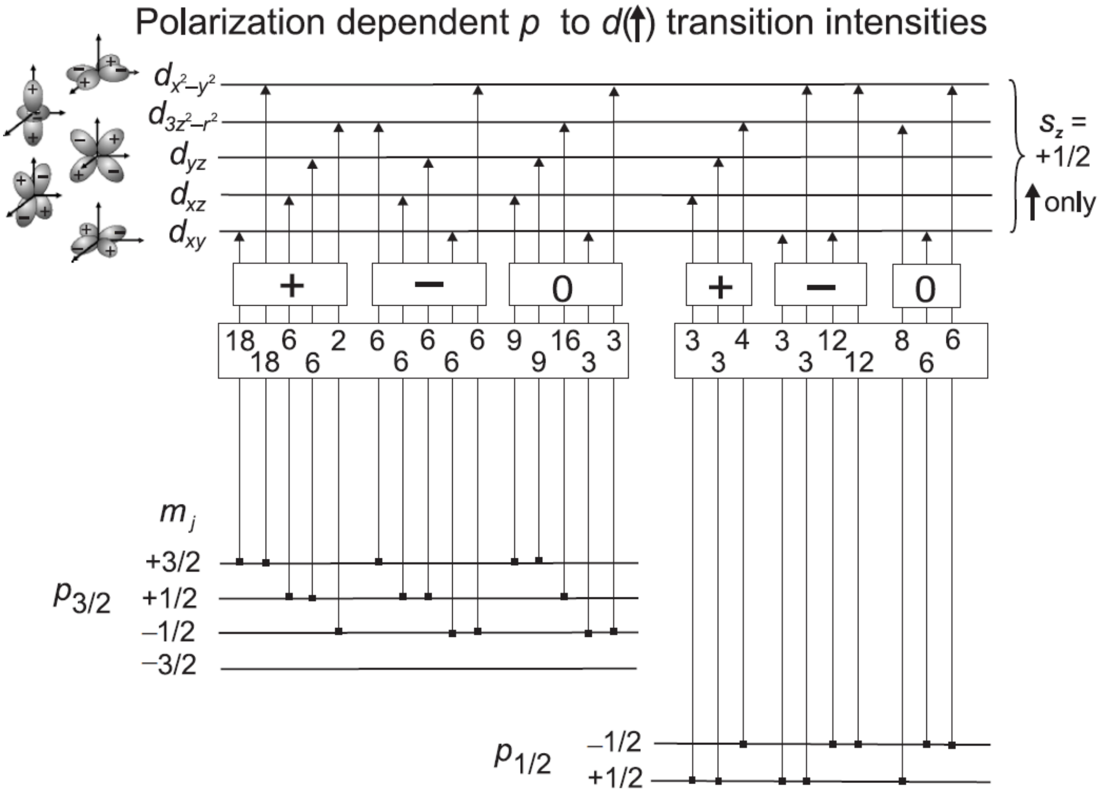
Polarization dependent p to d(↑) transition intensities
$d_{x^2-y^2}$
$d_{3z^2-r^2}$
d_{yz}
d_{xz}
d_{xy}
s_z = +1/2
↑only
+
−
0
+
−
0
18 18 6 6 2 6 6 6 6 6 9 9 16 3 3
3 3 4 3 3 12 12 8 6 6
m_j
+3/2
+1/2
−1/2
−3/2
$p_{3/2}$
$p_{1/2}$
−1/2
+1/2

Figure 3.3: One-electron model polarization-dependent transition intensities for a $p \to d$ transition. The initial p states $|j, m_j\rangle$ are assumed to be spin-orbit and exchange split lifting the m_j degeneracy. Only the spin-up $m_s = +1/2$ final valence d states are regarded. The intensities are given in units of $\mathcal{AR}^2$ if divided by 90. The spin quantization axis is along z and the light polarization is denoted $+/-$ for right-/left-handed circular polarization with $k \parallel z$ and 0 for linear polarization with $E \parallel z$. Image taken from [2].

ranges of the absorption edges x and y and the integrals added. The signs $+/-$ indicate parallel or antiparallel orientation of sample magnetization and circularly polarized light, and 0 stands for linearly polarized light.
The ground-state expectation value of the spin-dependent part of the local magnetic field per hole δ is [91]:

$$\delta = \int_x (\mu^+ - \mu^-)dE - [(c+1)/c] \int_y (\mu^+ - \mu^-)dE \bigg/ \int_{x+y} (\mu^+ + \mu^- + \mu^0)dE \tag{3.7}$$

$$= \frac{l(l+1) - 2 - c(c+1)}{3c(4l+2-n)} \langle S_z \rangle \ , \tag{3.8}$$

where we leave out the magnetic dipole term $\langle T_z \rangle$ since it is negligible in the case of the Gd $4f$ spins [75].

Before writing down the sum rules for the case of the $3d \rightarrow 4f$ transition in Gd, we introduce a shorthand notation used by M. Wietstruk in his PhD thesis [92] for the intensities of the integrals of the difference D_x and the average A_x of the absorption edges:

$$D_x = \int_x (\mu^- - \mu^+)dE \quad \text{and} \quad A_x = \int_x \mu_0 dE = \int_x \frac{\mu^- + \mu^+}{2} dE \ . \tag{3.9}$$

Note that we simplify μ_0 to be the average of the two opposite circular polarization measurements as we do not have a measurement with linear polarization. Thus, $3A_x$ corresponds to the integral over $(\mu^+ + \mu^- + \mu^0)$ for one absorption edge.
With this notation, the orbital moment sum rule for the $3d \rightarrow 4f$ transition in Gd is (with $l = 3$ and $c = 2$):

$$\langle L \rangle_{d \rightarrow f} = -\frac{D_5 + D_4}{A_5 + A_4} n_\mathrm{h} \ , \tag{3.10}$$

where $n_\mathrm{h} = 4l + 2 - n$ is the number of holes ($n_\mathrm{h} = 7$ for Gd).

The sum rule for the expectation value of the spin moment $\langle S \rangle$ is proportional to the difference of the XMCD absorption edges. The simplified version is [92]:

$$\langle S \rangle_{d \rightarrow f} = -\frac{1}{4} \frac{2D_5 - 3D_4}{A_5 + A_4} n_\mathrm{h} \ . \tag{3.11}$$

In this sum rule the small contribution from the expectation value of the magnetic dipole operator is neglected. In particular, this magnetic dipole term is zero for Gd [93, 94].

However, we cannot directly apply the sum rules to our absorption measurements since the absorption signal from total electron yield is not directly proportional to the absorption coefficient but suffers from saturation effects [95]. One has to consider how many holes are created by the X-rays and how many electrons escape from the sample surface, which is reflected in the X-ray penetration depth λ_x and electron escape depth λ_e. In simplified terms, there is complete saturation in the case $\lambda_e \gg \lambda_x$, whereas for $\lambda_x \gg \lambda_e$ no saturation occurs. In particular, for near-grazing incidence angles $\theta \lesssim 90°$

the penetration depth along the surface normal $\lambda_x \cos(\theta)$ becomes small leading to strong saturation effects and a reduction of magnetic contrast. This is the case for our measurements as we optimized the setup for the reflection signal, see Section 4.1.1.
Using data for the absorption coefficients in [96], we corrected for saturation effects in our data using the correction factor $f(\theta, \lambda_x, \lambda_e)$ described in [95] (see Appendix A.2 for details). Though this approach increases the magnetic contrast significantly, the data still yields partly erroneous results. In particular, the orbital moment $\langle L \rangle_{d \to f} = -1.7$ is non-zero. However, the spin moment $\langle S \rangle_{d \to f} = -3.4$ is similar to literature values [97][3] and close to the expectation value of $-7/2$ for Gd.
Naturally, since the orbital momentum sum rule effectively depends on the difference of the absorption edges (the edges have opposite sign) while the spin sim rule depends on the sum of the absorption edges, the calculation of the orbital momentum is more sensitive to deviations in the data. For instance, the absorption edge intensities need to be equal for $\langle L \rangle_{d \to f} = 0$, whereas a small imbalance in the intensities can cancel out in the spin sum rule.

Generally, even for transmission measurements not affected by saturation effects, before applying sum rules one has to consider that several approximations are made in the derivation, like demanding that the core level is characterized by a good quantum number [98, 99]. For practical usage, the background in measured absorption peaks from photoelectron excitation into continuum states has to be subtracted *e.g.* by using a step function [100].
The limitation of the sum rules can be observed in the case of Ni. In Ni, the radial matrix elements depend on photon energy and as such a dependence is not considered in the derivation of the sum rules they give incorrect results [98]. Moreover, sum rules are only derived for absorption measurements. To the author's knowledge, equivalent sum rules for reflectivity measurements have not been derived yet. However, first theoretical studies suggest that the sum rules do apply in the non-equilibrium conditions of laser-induced ultrafast magnetization dynamics experiments [101].

Pump-Probe Technique

A common method used in experiments investigating ultrafast dynamics on fs to ps time scales is the so-called pump-probe technique. A first laser pulse, the "pump" pulse, excites a sample and triggers some dynamic response of the system. A second laser pulse, the "probe" pulse, arrives at the sample with a certain delay after the pump pulse and takes a snapshot of the system's instantaneous state. By repeating the experiment for varying pump-probe delays one can obtain a series of instantaneous states of the system, which can be combined into a kind of stroboscopic movie of the dynamics taking place in the system. The resolution in these experiments is typically given by the pulse durations of the pump and probe pulses.

---

[3] In [97] $\delta = -1/3$, while we have $\delta = -0.32$ since $\delta = 2/21 \cdot \langle S \rangle_{d \to f}$ for Gd, *cf.* Eq. (3.8).

3.2.3 Ultrashort X-Ray Pulse Generation

We want to use XMCD for our ultrafast magnetization dynamics experiments and thus need a source producing fs X-ray pulses. Such sources vary in scale and energy range from lab-based higher-order harmonic generation (HHG) sources to free-electron lasers. FemtoSpeX is a beamline at the BESSY II facility providing short X-ray pulses in the energy range suited for investigating the Gd M absorption edges.

We will summarize the main aspects of the generation principles and output parameters of this beamline. More extensive accounts of the beamline and technical details can be found in literature [93, 102–106]. We will describe aspects relevant for data evaluation later in the according sections in Chapter 4.

Femtoslicing at the FemtoSpeX Facility

X-ray pulses at synchrotrons are generated by bunches of electrons circulating in the storage ring. Bending magnets and undulators create fields that bend the path of the electrons which causes them to emit radiation. These electron bunches have a certain extension in space which translates to a finite pulse duration of the emitted X-rays. The pulse duration at the BESSY II storage ring in normal operation mode is 50–70 ps [93] and thus too long for ultrafast magnetization dynamics experiments where sub-ps time resolution is needed.

Zholents and Zolotorev were the first to propose a method for generating fs X-ray pulses called femotslicing [107]. The idea is to use a fs laser pulse to modulate the energy of a slice of electrons in the longer bunch and separate the emitted light from the main light beam. This concept was first realized at the Advanced Light Source in Berkeley, USA [108].

Figure 3.4 shows the layout of the FemtoSpeX facility at BESSY II. The whole setup has a horizontal extension of about 50 m. A Ti:Sapphire oscillator which is synchronized with the storage ring master clock seeds two regenerative amplifiers. One beam is coupled into the storage ring for the generation of fs X-rays, the other travels over a delay stage to the experiments. Both beams have pulse energies of 1.8 mJ. An optical parametric amplifier (OPA) is available for tuning the pump laser wavelength (not depicted in Fig. 3.4) [106]. The pump pulses have a duration of about 40 fs and can be tuned between 240 nm and 6 µm [106].

Figure 3.5 depicts how the femtoslicing concept is realized at the FemtoSpeX facility. The 40 fs infrared (IR) laser pulse is coupled into the storage ring to run parallel to the 50 ps electron bunch in the wiggler. The electric field of the laser pulse accelerates and decelerates electrons within a “slice” of the long bunch. At the next bending magnet, those energy-modulated electrons take a different path due to their different kinetic energy and are laterally offset from the main bunch. Thus, in the radiator, the “sliced”

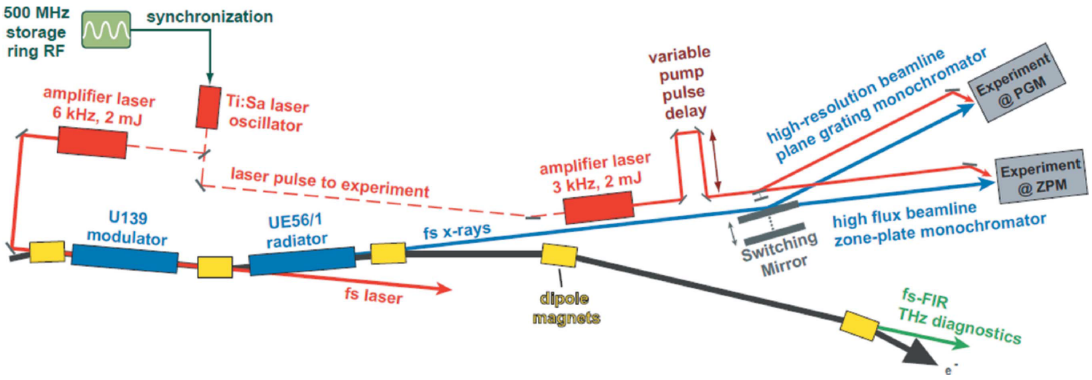
500 MHz storage ring RF
synchronization
Ti:Sa laser oscillator
amplifier laser 6 kHz, 2 mJ
laser pulse to experiment
U139 modulator
UE56/1 radiator
fs laser
fs x-rays
dipole magnets
amplifier laser 3 kHz, 2 mJ
variable pump pulse delay
high-resolution beamline plane grating monochromator
Experiment @ PGM
Experiment @ ZPM
Switching Mirror
high flux beamline zone-plate monochromator
fs-FIR THz diagnostics
e⁻

Figure 3.4: Layout of the FemtoSpeX facility at BESSY II. The Ti:Sapphire oscillator is synchronized with the master clock of the storage ring. The oscillator seeds two amplifiers. One provides the laser for the generation of the fs X-ray pulses. The other is used as a pump laser for the experiments at one of the two beamlines. The dimension of the setup is about 50 m. Image taken from [105].

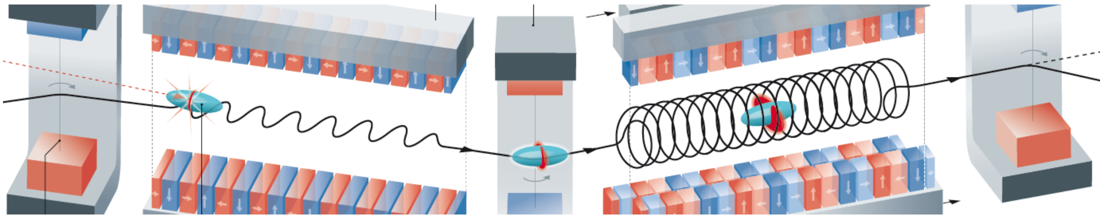

Figure 3.5: Illustration of the femtoslicing process. A fs IR laser pulse is coupled into the storage bunch and co-propagates with the electron bunch. The electric field of the laser pulse modulates the kinetic energy of a “slice” of electrons of the main bunch. At the following bending magnet, those energy-modulated electrons are deflected by a different amount compared to the regular electrons and become spatially separated. The emitted X-rays in turn are separated in space and can be detached from the main beam to be used in ultrafast experiments. Image courtesy of Helmholtz-Zentrum Berlin.

electrons emit X-rays which are also spatially separated from the much more intense main beam, see Fig. 3.6.

Due to the slicing process the electron bunch emits additional THz radiation [93, 103, 105]. The energy-modulated electrons travel as wings of the main bunch leaving behind a dip in the longitudinal profile. This dip in the electron density of about 0.1 mm leads to the emission of coherent synchrotron radiation in the THz range [103] and can be used for diagnostics of the spatial and temporal overlap of the laser and electron beam and the magnitude of the modulation of the energy of the electrons [93].

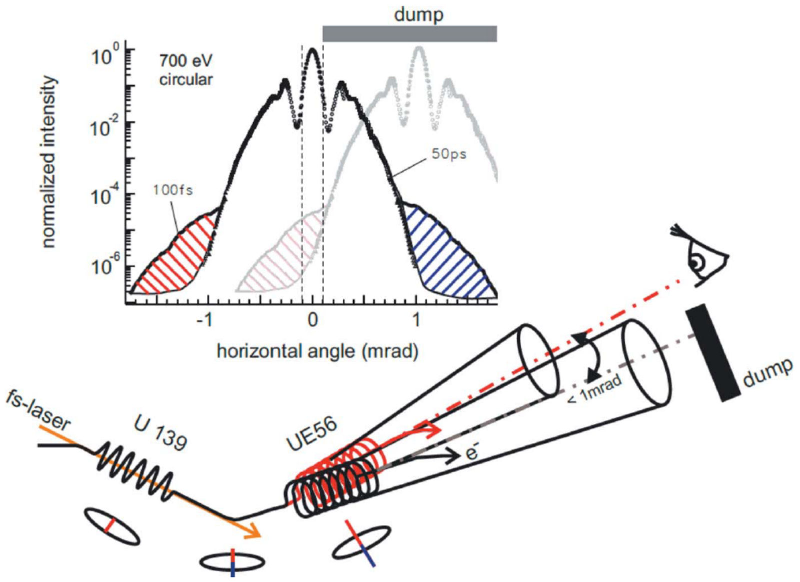

Figure 3.6: Angular distribution of the X-ray intensity emitted from the femtoslicing radiator and the principle of femtoslicing. The intensity from the “sliced” electrons is by about a factor 10^{-4} smaller than the one emitted from the main bunch. A local adjustment in the beam path of the electrons allows changing the beam direction to select either the main beam or only the sliced part (shaded intensity distribution). Image taken from [105].

Creating a local adjustment in the electron path (a local orbit “bump”) changes the direction of the emitted X-rays such that either the main beam passes the beam dump or the main beam is blocked by it and only the 100 fs “sliced” beam can pass. The “sliced” X-rays have a larger pulse duration than the IR laser pulse as electrons in the storage ring have a velocity below the speed of light. Thus, the IR pulse travels within the bunch of electrons modulating a larger slice than its own extension resulting in a larger pulse duration. As only a slice of electrons contributes to the fs X-ray beam, its intensity is much lower (about a factor 10^{-4}) than the main beam, see Fig. 3.6.
Furthermore, an elliptical polarization of 70 % is achieved in the femtoslicing operation mode [93]. The X-ray energy can be tuned between 410–1333 eV [106].

The combined temporal resolution of IR pump and X-ray probe pulses including stretching caused by optics is 140 fs [105]. The two amplifiers run at 6 kHz in the slicing and 3 kHz in the pump paths allowing to record both the pumped and unpumped signals from the sample. The pulses are nearly collinear with a small angle of 1.5°, see Fig. 3.7.

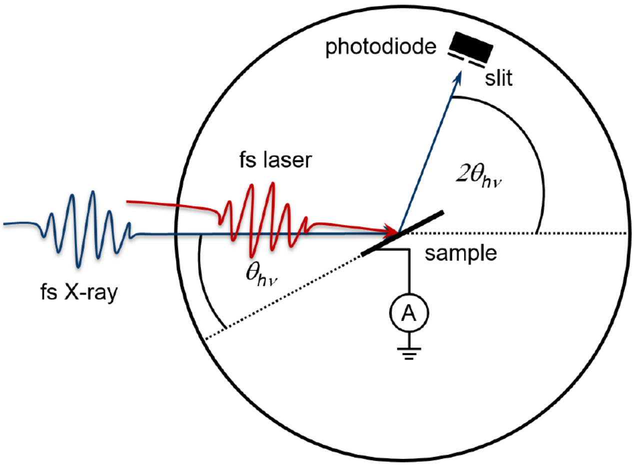

Figure 3.7: Geometry of the setup. We measured the reflected signal in a θ-2θ geometry, θ being the incidence angle of the X-ray beam onto the sample. The IR pump pulse is nearly collinear with a small deviation of 1.5°. The reflected X-rays are detected with an APD which is protected from the intense IR light by a thin aluminum foil spanned over the horizontal entrance slit. For static measurements, a Si diode was used and additionally the photocurrent at the sample was measured. Image taken from [78].

We recorded the reflected signal from our samples in a θ-2θ geometry where θ is the angle between the incident X-ray beam and the sample surface plane. In static measurements (Section 4.1), a Si diode detected the reflected signal while simultaneously the sample current caused by absorption of the light was measured. In time-resolved measurements (Sections 4.2 and 4.3), an avalanche photodiode (APD) was used. It was protected from the intense reflected IR pump beam by a thin Al foil in front of the horizontal entrance slit. The 40 µm slit [106] improves the energy resolution since the X-rays are vertically spread according to their energy by the zone plate monochromator. A horseshoe magnet was installed next to the sample providing magnetic fields up to 0.2 T [106].

3.3 Photoemission Spectroscopy with Higher-Order Harmonic Generation

In contrast to XMCD, PES does not average over the whole Brillouin zone but provides information about the dispersion relation $E(\mathbf{k})$ of electronic states in a material. It can be used for the analysis of valence band states (angle-resolved photoemission spectroscopy (ARPES)) and core-level spectroscopy (X-ray photoemission spectroscopy

(XPS)) [109]. In addition, time-resolved PES is the only technique to directly measure population dynamics in the time domain [110].

Similar to the above section, we will only concisely describe the fundamentals of PES relevant to understand the later data analysis. With a history of more than 100 years, photoemission has been described extensively in literature, see for instance [109, 111] and references therein.

3.3.1 Principles of Photoemission Spectroscopy

PES is based on the famous photoelectric effect, the emission of an electron from a solid upon absorption of light. The experimental groundwork was laid by Hertz and Hallwachs in the late 1880s [112, 113] who studied the interaction of light with solids. Einstein's revolutionary explanation of the effect with light quanta [114] earned him the Nobel prize. Einstein deduced the fundamental photoelectric equation:

$$E_{\text{kin}}^{\text{max}} = h\nu - \Phi_0 \ , \tag{3.12}$$

which relates the maximum kinetic energy of the photoexcited electron $E_{\text{kin}}^{\text{max}}$ to the incident photon energy $h\nu$ and the work function of the solid Φ_0.

A schematic of the photoemission process is shown in Fig. 3.8. It illustrates the density of states of core-levels and the valence band in the sample and the resulting photoemission spectrum with experimentally broadened features. After absorbing photons with energy $h\nu$ electrons from core-levels and the occupied valence states are excited above the vacuum level E_{vac}. Their kinetic energy E_{kin} is then detected in a spectrometer as an intensity distribution $I(E)$.

The actual theoretical description of photoemission has to consider the photoemission process in a many-body picture. The removal of an electron from the system leaves it in a state with one less electron (or a positive hole) compared to the initial state. The remaining (many) electrons can interact in complex ways and the final state can differ from the initial state substantially necessitating a complicated many-body theory to describe PES [111].

We will follow the example of Björn Frietsch in his PhD thesis [77] and only sketch a few important key concepts. A useful way of regarding photoemission is the three-step model which divides the photoemission process into three separate steps: First, the absorption of the photon and the excitation of the electron from an initial into a final state. Second, transport of the excited electron to the surface and crossing into vacuum. Third, the detection of the electron.

First Step: Absorption
Fermi's Golden rule provides the transition probability $\mathcal{W}_{if}$ for an electron from an

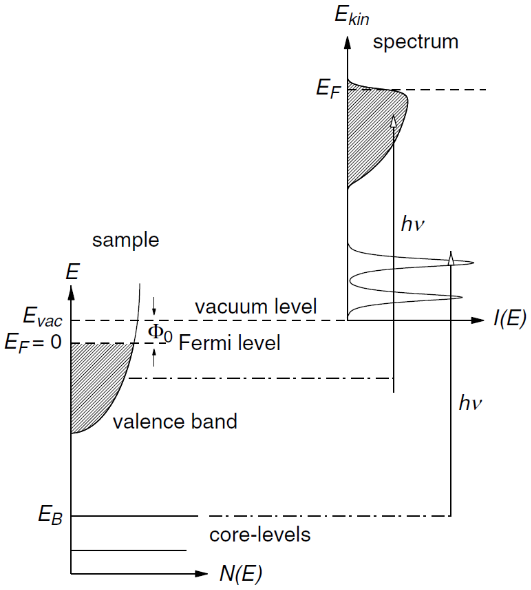

Figure 3.8: Energy scheme of the photoemission process in a single-particle picture. Photons with energy $h\nu$ excite electrons with binding energy E_B into unoccupied states above the vacuum level E_vac. The measured intensity distribution $I(E)$ reflects the occupied density of states $N(E)$ in first order approximation. Image taken from [109].

initial state $|i\rangle$ with energy E_i to a final state $|f\rangle$ with energy E_f upon absorption of a photon with energy $h\nu$:

$$\mathcal{W}_{if} = \frac{1}{h} |\langle f| \mathcal{H}_{h\nu} |i\rangle|^2 \delta(E_f - E_i - h\nu) \ . \tag{3.13}$$

The delta function δ guarantees energy conservation. The excitation happens within a solid and thus the initial and final states are Bloch states $\Psi(\mathbf{r}) = \exp(i\mathbf{kr})u(\mathbf{r})$, with a function $u(\mathbf{r})$ that reflects the lattice periodicity $u(\mathbf{r}) = u(\mathbf{r} + \mathbf{R})$, $\mathbf{R}$ being a lattice vector. The perturbation operator $\mathcal{H}_{h\nu}$ for the interaction of a spinless electron with an electromagnetic field $\mathbf{A}$ is given by [109]:

$$\mathcal{H}_{h\nu} = \frac{e}{2m_e c}(\mathbf{A} \cdot \mathbf{p} + \mathbf{p} \cdot \mathbf{A}) + \frac{e^2}{2m_e c^2} A^2 \approx \frac{e}{m_e c} \mathbf{A} \cdot \mathbf{p} \ , \tag{3.14}$$

with the electron charge e, the electron mass m_e, the speed of light c and the momentum operator $\mathbf{p}$. The approximation neglects surface effects [109] and, assuming $\mathbf{A}$ to be constant, describes a simple dipole transition. To obtain the final state density of states I_f, we need to sum over all possible initial and final states as well as the reciprocal lattice vectors G [77]:

$$I_f(E_f, h\nu) \sum_{i,f,G} |\mathcal{M}_{fi}|^2 \cdot n(E_i) \delta(E_f - E_i - h\nu) \delta(\mathbf{k}_f - \mathbf{k}_i - a\mathbf{G}) \ , \tag{3.15}$$

with the transition matrix $\mathcal{M}_{fi} = \langle f|\,\mathcal{H}\,|i\rangle$ and the Fermi Dirac distribution $n(E_i)$ of the initial state. The momentum conservation $\delta(\mathbf{k}_f - \mathbf{k}_i - a\mathbf{G}), a \in \mathbb{Z}$ neglects the small momentum of the absorbed photon, *i.e.* in the reduced zone scheme we allow only vertical transitions. Electrons with $k_\perp > 0$ travel to the sample surface, which is described in the second step.

Second Step: Transport
The photoexcited electrons propagate to the sample surface. Since electrons interact strongly with their surroundings *e.g.* via electron-electron, electron-phonon and electron-plasmon scattering, they can only travel for a limited distance before scattering and losing the energy and momentum information from the first step of the photoexcitation. Those scattered electrons appear as a background signal increasing towards low energies. Typically, the escape depth of photoelectrons is in the range of a few to a few dozen Å. This is visualized by the "universal" inelastic mean free path λ as a function of the electron kinetic energy, see Fig. 3.9.

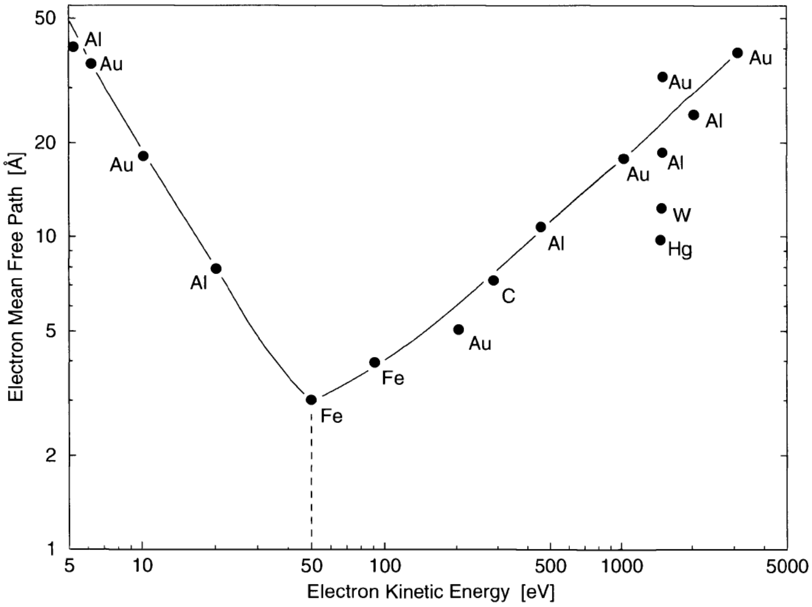

Figure 3.9: Dependence of the electron inelastic mean free path on the electron kinetic energy. This "universal" curve applies for metals and shows that typical escape depths for photoemitted electrons are in the range 3–50 Å with a minimum at about 50 eV. Image taken from [111].

The universal curve applies to all metals [115, 116], with exceptions at low kinetic energies, *e.g.*, for *d* metals. Using photon energies of about 35 eV we will probe the first 2–3 ML and gain information on surface and bulk states.

Once reaching the surface, the electrons need to transfer to the vacuum. Thereto, they have to cross the surface-vacuum interface and overcome the crystal potential Φ. The difference in potential changes the kinetic energy of the electron. Since the symmetry is broken only along the surface normal, $\mathbf{k}_{||}$ remains constant and $k_\perp$ is reduced. This leads to a refraction at the surface, see Fig. 3.10.

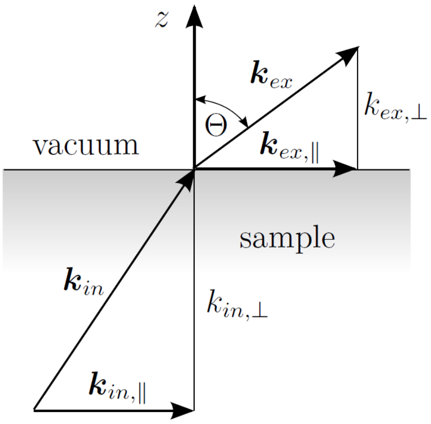

Figure 3.10: Wave-vector components of a photoemitted electron in the transition from the sample $\mathbf{k}_{\text{in}}$ to the vacuum $\mathbf{k}_{\text{ex}}$. The potential step at the surface Φ leads to a decrease of $k_\perp$ while $\mathbf{k}_{||}$ stays constant. Image taken from [77].

In vacuum, the electron is considered free and its dispersion relation is given by:

$$E_{\text{kin}} = \frac{\hbar^2 k_{\text{ex}}^2}{2m_e} \ , \tag{3.16}$$

with the kinetic energy E_{kin} and the momentum outside of the solid $\mathbf{k}_{\text{ex}}$. We obtain the parallel momentum $\mathbf{k}_{||}$ from the measured kinetic energy and the emission angle Θ:

$$k_{||} = \frac{\sqrt{2m_e E_{\text{kin}}}}{\hbar} \sin(\Theta) \ . \tag{3.17}$$

Third Step: Emission and Detection

Within the sample, the kinetic energy of the photoemitted electron is given by:

$$E_{\text{kin}} = h\nu - \Phi_{\text{S}} - E_{\text{B}} \ , \tag{3.18}$$

with the sample work function Φ_{S} and the binding energy E_{B}. However, the detection takes place inside of the detector which typically has a different work function. As sample and detector usually are grounded on the same potential their Fermi levels are equal. Then, the kinetic energy of the electron changes when entering the detector. Thus, to determine the binding energy one needs to know the detector work function in addition to the photon energy. Figure 3.11 illustrates the involved energy levels.

As mentioned above, the three-step model is a useful approximation for discussions and helps understanding the photoemission process. For a more rigid description, the overlap of the initial Bloch state with the true final state has to be calculated [111]. A

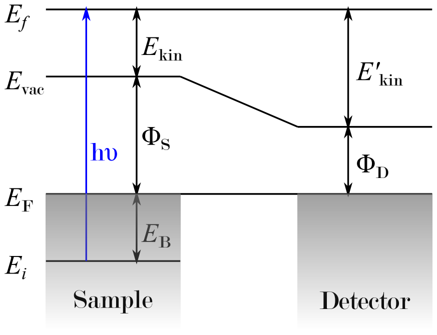

Figure 3.11: Energy diagram for the detection step in PES. A photon with energy $h\nu$ excites an electron from an initial state E_i to a final state E_f. The difference between the Fermi level E_{F} and the vacuum level E_{vac} is the work function which differs between the sample Φ_{S} and detector Φ_{D}. Thus, the measured kinetic energy $E^{'}_{\text{kin}} \neq E_{\text{kin}}$.

very successful approach is to use a so-called inverse LEED state as the final state. In LEED, a monochromatic electron beam impinges on a sample and the electrons scatter at the ions in the crystal. Thus, the reverse is just a monochromatic wave of electrons originating from ions in the crystal which resembles the electron wave generated by photoemission [111]. Such an approach is the one-step model of photoemission. We started a collaboration with Jürgen Braun to find an explanation for oscillations in our data (see Chapter 6) who uses the one-step model in his calculations. A detailed description of the one-step model can be found in [117] and references therein.

3.3.2 Higher-Order Harmonic Generation

The data presented in Chapters 5 and 6 was measured at the Artemis facility of the CLF at the STFC Rutherford Appleton Laboratory. This facility features a tunable pump laser in addition to a HHG source and provides the opportunity for pump laser wavelength-dependent PES measurements. The high energy of the probe laser allows us to measure energetically deeper lying states and high parallel momenta covering large parts or even the whole Brillouin zone for a more complete picture of the band structure compared to optical probe pulses. In the following, we will introduce the experimental setup and highlight the main features of the laser system at the Artemis facility. An extensive account of the Artemis facility is given by Turcu *et al.* [118].

For a description of the HHG process itself the reader is referred to literature. The generation of higher-order harmonics can be understood in a semi-classical model [119], see also [77] and references therein. A full quantum mechanical theory was developed by Lewenstein *et al.* [120].

The Artemis laser is based on a commercial Ti:Sapphire chirped-pulse amplification system (RedDragon from KMLabs) which provides pulses of 14 mJ, 30 fs at 1 kHz repetition rate with a central wavelength of 785 nm, see Fig. 3.12. The laser is carrier-envelope phase stabilized so that the optical electric fields of the pulses can be precisely shaped. After multiple amplification stages (not shown in Fig. 3.12) the beam is split into two branches.

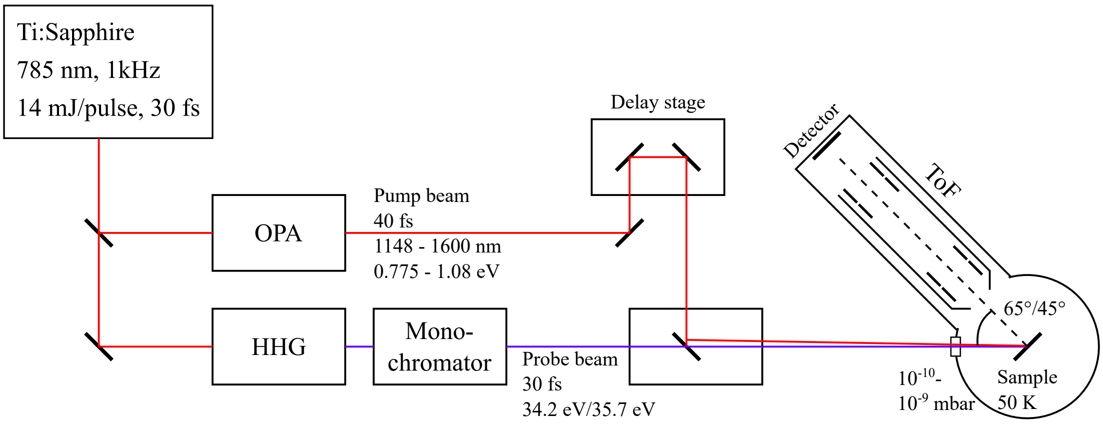

Figure 3.12: Sketch of the setup at the Artemis facility. A Ti:Sapphire oscillator produces the IR beam which is split into two branches. The pump beam is fed into an OPA to tune the wavelength to the needs of the experiment. The second part is used to generate high harmonics. After monochromatizing, the two beams are directed into the UHV chamber and impinge onto the sample nearly collinearly. In our measurements, we detected the photoemitted electrons with a ToF analyzer. The numbers in the figure relate to settings used during our beamtimes and not the full possibilities of the setup. Two different probe photon energies and incidence angles were used at two separate beamtimes.

The pump branch features a large wavelength tuneability covering a range from 230 nm to 20 µm. The OPA is a HE-Topas from Light Conversion and can be pumped with up to 8 mJ from the preceding laser system. The output at 1300 nm is up to 1 mJ with a pulse duration of 40 fs [118]. A hollow gas-filled fibre is installed for further compression of a part of the beam for high temporal resolution experiments [118]. For our experiments we used pump photon wavelengths of 1148–1600 nm or 0.775–1.08 eV.

Extreme ultraviolet (XUV) radiation is generated in the second branch of the setup. The driving IR laser pulse is focused into a gas cell where high harmonics are generated in the range of 10–100 nm (10–100 eV) [118]. With conversion rates of up to 10^{-6} at 30 eV a photon flux of up to 10^{11} photons per second and per harmonic is achieved. The XUV is synchronized with the IR driving laser with sub-fs resolution and has a similar pulse duration.

There exist two HHG setups for narrow bandwidth and broadband XUV pulses. We will focus solely on the monochromatized, narrow bandwidth setup.
The narrow bandwidth XUV beamline has a modern XUV monochromator for selecting the photon energy and bandwidth of the XUV pulses for the experiment. The monochromator comprises two toroidal mirrors, a diffraction grating and an exit slit. The first

toroidal mirror collimates the XUV light and reflects it onto one of four plane diffraction gratings. The different gratings are optimized for two spectral ranges and either high energy resolution or short pulse duration. The second toroidal mirror refocuses the diffracted beam onto the exit slit. This setup effectively images a 20 µm XUV source onto the exit slit. The throughput of this design is 30 % of the peak XUV intensity.

The spectrum of the monochromator output was measured using a XUV channeltron. We are using the 23rd harmonic and, closing the exit slit, achieve a bandwidth of around 120 meV from the natural bandwidth of about 700 meV. We measured slightly varying photon energies corresponding to the 23rd harmonic in the two beamtimes with photon energies of about 35.7 eV and 34.2 eV.

A final toroidal mirror focuses the XUV beam coming from the monochromator onto the sample with a reflectivity of 80 % and retaining the small initial XUV spot size of 20 µm [118]. The IR pump laser is coupled into the XUV beamline by a mirror with a central hole to allow the XUV to pass. A delay stage in the pump branch allows to change the time delay between the pump and probe pulses for time-resolved measurements.

To maintain a good vacuum of below 10^{-9} mbar in the UHV chamber, several differential pumping stages are installed. A $2200\,\mathrm{l\,s^{-1}}$ turbo pump is attached to the HHG chamber keeping a pressure of 10^{-3} mbar against the constant inflow of gas. A 2 mm pinhole separates the HHG from the monochromator chamber which reaches 10^{-6} mbar. Further differential pumping is provided by the exit slit and two additional pinholes at a small cube chamber.

3.3.3 Time-of-Flight Analyzer

For our experiments we were provided with a time-of-flight (ToF) analyzer which is described in more detail by Cacho *et al.* [121]. In contrast to hemispherical analyzers, which separate electrons according to their kinetic energy by different deflection paths within a static field, the ToF distinguishes kinetic energies by the time electrons need to fly through a drift tube.

We measured in normal emission, but due to the rather large acceptance angle of the analyzer of 3–10° the signal is integrated over a large $k_{\|}$ range[4]. Photoemitted electrons are decelerated by electron optics before entering the drift tube. After traveling through the 25 cm long drift tube another set of electron optics refocuses the electrons and accelerates them towards a channel plate detector with a diameter of 25 mm.

The ToF settings are optimized for a certain kinetic energy of the photoemitted electrons. In our case, electrons with about 30 eV kinetic energy were decelerated by electron optics before the drift tube to about 6 eV for optimal resolution. At this kinetic energy inside the drift tube, the best compromise is found between a large separation of the electrons and external influences like magnetic stray fields.

---

[4] The energy resolution of our spectra rather suggests an actual acceptance angle at the lower boundary, *cf.* Section 5.2.2.

The arrival times are detected with a time digitization of 120 ps and then converted to a kinetic energy. To calibrate the relation between time and energy for given settings, a series of bias voltages is applied between sample and detector. This results in a shift of the Fermi level by known amounts of energy which can be used to fit calibration parameters for the conversion. In a rough approximation that neglects all parts except for the drift tube, the kinetic energy is described by:

$$E_{\mathrm{kin}} = E_{\mathrm{F}} + \frac{1}{2} m_e \frac{L^2}{(t - t_0)^2} \ . \tag{3.19}$$

The kinetic energy E_{kin} is given with respect to the Fermi level E_{F}. The time t is the measured arrival time of electrons from the Fermi edge. The length L and time t_0 are fitting parameters, where L is the drift tube length and should be slightly larger than the real drift tube length due to the negligence of the paths outside the drift tube. The arrival time t_0 of the XUV pulse at the sample is obtained from the detection of the reflected XUV pulse. It produces a small signal in the data some 100 ns before arrival of the first electrons. We will discuss the data analysis in detail in Section 5.2.1.

Chapter 4

Laser Fluence and Energy Dependence of Magnetization Dynamics

Parts of this chapter are published [24] or are going to be published after submission of the thesis and several text passages and figures in the thesis are reused or strongly resembling the text or figures in the publications.

In addition, the data shown in this chapter was measured, evaluated and discussed together with Markus Gleich who has written about large parts thereof in his Master's thesis. Similarities in the outline and contents of both theses can occur.

In 1996, Beaurepaire *et al.* [5] published data showing how nickel demagnetizes on a sub-ps time scale upon laser excitation, thus establishing the field of ultrafast magnetization dynamics. Since then the community works to unravel the underlying physical processes governing the laser-induced magnetization dynamics in ferromagnetic transition and lanthanide metals. This field offers the possibility to study various complex interactions between electrons, phonons, spins and photons when these subsystems are out of equilibrium.

Some mechanisms were proposed to explain the magnetization dynamics in ferromagnets. First, Bigot and coworkers [7] proposed that the laser pulses directly interact with the spins. The electromagnetic light field induces a polarization in the material which in turn couples coherently to the spins. Choi *et al.* [8] discuss a different light-driven demagnetization mechanism. In their study, they investigate contributions from an inverse Faraday-effect and optical spin-transfer torque leading to a demagnetization in 3*d* ferromagnets and come to the conclusion that the former dominates over the latter inside the ferromagnet while the latter mostly is due to a platinum capping layer. Battiato *et al.* [9] propose a mechanism based on superdiffusive spin transport that depletes the majority spins at the region of the sample that is excited with the laser, *cf.* Section 2.4 for a detailed description. Many studies find evidence for scattering-based mechanisms of demagnetization, like electron-electron [10–12], electron-phonon [12–17], and electron-magnon scattering [14, 18–20]. But, despite indications for all those mechanisms, there is no coherent picture of the interplay and relative dominance of the different processes in the various ferromagnets and multilayers or alloys thereof.

We performed a broad study on the lanthanide metal Gd and can complement an extensive investigation on Ni by Roth *et al.* [65]. Koopmans *et al.* introduced their microscopic three-temperature model (M3TM) (see Section 2.3 for a description of the model) testing it on Ni, Co and Gd as examples for the two types of materials exhibiting different demagnetization dynamics [15]. While Roth and coworkers investigated the fluence and temperature dependence of magnetization dynamics for the type I metal Ni, a similar study for the type II material Gd was missing so far. A successful description of the dynamics in Gd using the M3TM would corroborate electron-phonon mediated spin-flip scattering as a dominant demagnetization mechanism in Gd.

This chapter starts with a section about static measurements on Gd which we performed to establish X-ray magnetic circular dichroism in reflection geometry as a valid probe for the sample magnetization. Simultaneous recording of the reflection and absorption signals for varying sample temperatures shows that both signals equivalently follow the trend of a Brillouin function as one would expect for a rare-earth ferromagnet. Thereafter follows a section about the pump laser fluence-dependent measurements on Gd showing the two-step demagnetization behavior that is expected for a type II material and we discuss the theoretical description of the dynamics using an extended M3TM. In more detail, we will look at the fluence dependence of the remaining magnetization at 4 ps and 96 ps after laser excitation representing the two specific time scales of the dynamics. The demagnetization within the first time scale shows an exponential dependence thus surprisingly implying a complete reduction of magnetic order via this process to not be possible in Gd. The magnetization on the second time scale decreases linearly with the fluence, but there is a kink and change of slope at high fluences. This might be related to the divergence in the $4f$ magnetic heat capacity in Gd. In Section 4.3, we investigate the dependence of the magnetization dynamics on the pump laser energy and find a slight reduction of the demagnetization amplitude in the early sub-ps dynamics for low pump energies.

4.1 Temperature Dependence of XMCD in Absorption and Reflection

To employ the samples that were grown epitaxially under ultra-high vacuum conditions on a W(110) substrate, *cf.* Section 3.1.2, we chose to measure in reflection geometry as no detectable light penetrates through the solid sample to measure in transmission geometry. In order to verify this approach and to show the equivalency of both signals as probe for magnetization we performed temperature-dependent measurements of the Gd magnetization recording both signals, reflection and absorption, simultaneously. In this section, we will introduce how the raw data is processed and compare the reflection and absorption signals with the behavior of a typical ferromagnet.

4.1.1 Evaluation Procedure

The evaluation procedure described here applies to data obtained at the PM3 beamline at BESSY II. We recorded the X-ray absorption signal via the sample current created by the absorbed X-ray radiation in the sample. We used a Si photodiode to measure the reflection signal, *i.e.* the reflected X-ray intensity from the sample. Both signals were measured for opposite directions of the external in-plane magnetic field, *i.e.* for opposite orientations of the circularly polarized light and the sample magnetization. In the data processing, these signals are normalized to the instantaneous current in the synchrotron, as during operation this current, and concurrently the X-ray intensity, periodically vary by a small amount. With these intensity-corrected signals we calculate the X-ray magnetic circular dichroism (XMCD) as the difference between the signals for opposite magnetization of the sample with respect to the polarization of the probing X-ray light. By dividing the XMCD by the sum of the signals for opposite magnetization we obtain the asymmetry which decouples non-magnetic contributions from the XMCD. We can express the signal processing with the following equations for the case of absorbed X-ray signals:

$$\mathrm{XMCD} = \mathrm{XAS}_{\mathrm{parallel}} - \mathrm{XAS}_{\mathrm{antiparallel}} \tag{4.1}$$

$$\mathrm{asymmetry} = \frac{\mathrm{XAS}_{\mathrm{parallel}} - \mathrm{XAS}_{\mathrm{antiparallel}}}{\mathrm{XAS}_{\mathrm{parallel}} + \mathrm{XAS}_{\mathrm{antiparallel}}} \,. \tag{4.2}$$

XAS stands for the X-ray absorption spectra or X-ray reflection spectra, depending on the measurement method. The subscripts refer to either a parallel or antiparallel orientation of the sample magnetic field and the polarization of the probing X-rays. Figure 4.1 shows the Gd M_5 (1190 keV) and M_4 (1220 keV) absorption edges in X-ray reflection (a) and absorption (b) spectra and the resulting XMCD signal and magnetic asymmetry.

Comparing the reflection and absorption data we find clear differences in the shape of the signals. While only the imaginary part of the scattering amplitude enters into the absorption signal, the reflectivity is determined by the absolute magnitude, *i.e.* the imaginary and real parts of the scattering amplitude. Although sum rules (*cf.* Section 3.2.2) cannot be applied to the reflection signal, for small incident angles the dichroic signal is a good approximation for the XMCD as obtained from the absorption coefficient and the total magnetization of the sample [122] (see also next section).

Furthermore, in our measurements, the overall intensity and the magnetic contrast are by one order of magnitude larger in the reflected signal than in the absorption signal. The main reason for the much higher signal in reflectivity is its higher sensitivity compared to the absorption measurement. We have chosen a geometry (with an incidence angle of $\theta = 4.5°$) for in-plane magnetization where θ is the angle between the incoming X-ray beam and the sample plane (*cf.* Fig. 3.7 in Section 3.2.3). The small angle strongly enhances the reflection signal ($R \approx 0.05$ compared to about $R \approx 10^{-6}$ for normal incidence for Gd [123, 124]). In reflection, we find the best compromise for the total

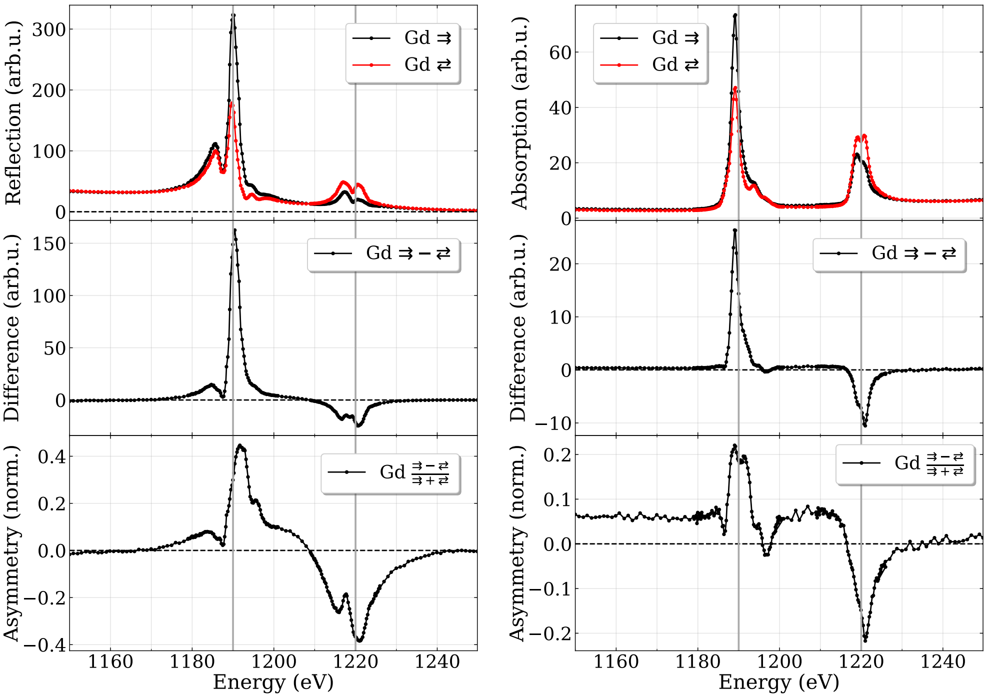

(a) Reflection data

(b) Absorption data

Figure 4.1: Spectra of the Gd M_5 and M_4 absorption edges measured in reflection geometry (a) and in absorption (b) on a 10 nm single-crystalline Gd sample. At the top, the normalized signals for parallel (⇉) and antiparallel (⇄) magnetization of the sample with respect to the probing light polarization are plotted. Below, the difference of these signals, the XMCD, is depicted. At the bottom, the asymmetry is shown. The reflection data was measured using a Si photodiode. The absorption signal was obtained from the sample current induced by the absorbed light. The incidence angle between the X-ray beam and the sample surface plane is $\theta = 4.5^\circ$ (*cf.* Fig. 3.7). The vertical lines indicate the central energies of the absorption edges at which the data in Figs. 4.2 and 4.3 was measured. Note, the absorption data is corrected for saturation effects, see Appendix A.2.

intensity and dichroic signal at $\theta = 4.5°$, which is essential for good statistics in a time-resolved experiment. The near-grazing incidence angle has the downside of strong saturation effects in the absorption measurement, see discussion in Section 3.2.2. We applied a correction factor to the absorption data according to [95], see Appendix A.2 for details.

Compared to data in [96], our data generally shows less magnetic contrast. This might be due to some contamination and therefore incomplete magnetization of the sample since during that beamtime we had rather high pressures of $p > 1 \cdot 10^{-9}$ mbar during sample preparation instead of $p < 2 \cdot 10^{-10}$ mbar, a value we typically achieve in our own labs. However, the good agreement of the spin moment expectation value calculated in Section 3.2.2 rather indicates a good quality of the samples.

The small incidence angle affects the pump laser as well. The spot size is stretched along one axis reducing the peak intensity and necessitating high pump laser fluences. Fortunately, the better thermal conductivity due to the thicker substrate makes the sample more robust against overheating at these high pump laser fluences.

4.1.2 Static Temperature Dependence of XMCD

We want to validate the dichroic signal measured in reflection as an equivalent probe for the sample magnetization as the XMCD measured in absorption via drain current or in transmission. Hence, we chose to measure the temperature-dependent magnetization of Gd and record the reflection and absorption signals simultaneously. The data for the Gd M_5 and M_4 edges is shown in Figs. 4.2 and 4.3, respectively.

We do not possess full energy-, polarization- and temperature-dependent data of the absorption coefficient for Gd and so cannot perform a saturation correction (see Appendix A.2) for the temperature-dependent absorption data. We will use the raw absorption data for the following evaluation and assume that saturation effects discussed in Section 3.2.2 should not affect the qualitative conclusions from the temperature-dependent magnetization as we regard relative intensity changes only.

We followed two different procedures to run the temperature-dependent experiment. We could either turn on liquid nitrogen cooling, which cooled down the sample from room temperature to about 120 K within about one hour. Or, we could stop the flow of liquid nitrogen and simply let the manipulator warm up which took more than ten hours. We could not use the sample filament to control the temperature as the hot filament would produce a significant sample current exceeding the small X-ray-induced photocurrent of only a few pA. The data shown in Figs. 4.2 and 4.3 was taken during the cooling phase at fixed energies of the Gd absorption edges, $E_{\mathrm{M}_5} = 1190.0\,\mathrm{eV}$ and $E_{\mathrm{M}_4} = 1221.4\,\mathrm{eV}$, respectively, and while switching the magnetic field every 4 s to obtain the XMCD and the asymmetry. Due to the decreasing temperature gradient when cooling down the sample with a constant liquid nitrogen flow into the manipulator the data point density varies with temperature. Close to room temperature, the temperature

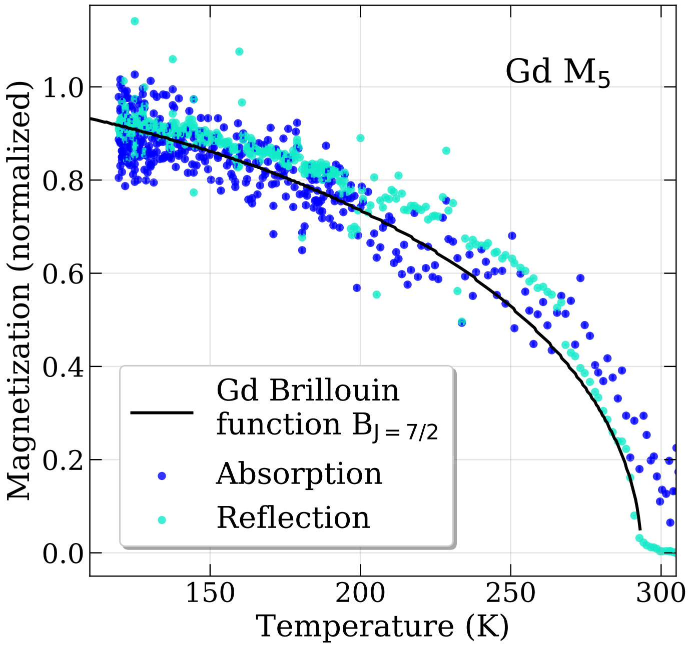

Figure 4.2: Magnetization (asymmetry) measured at the Gd M5 absorption edge ($E_{\mathrm{M}_5} = 1190.0\,\mathrm{eV}$) in absorption (dark blue) and reflection (light blue) versus the sample temperature. The black line is the Gd Brillouin function and represents the temperature-dependent magnetization of a ferromagnet according to the Weiss mean-field theory. The data agrees well with the theoretical curve. The scattering of the data points indicates the statistical uncertainty. The offset in the absorption data might arise due to the overall slight difference in intensities in the absorption signal between the two magnetization directions, *cf.* Fig. 4.1b or from possible saturation effects. Deviations in the reflection data (around 250 K) are attributed to instabilities in the setup. See the end of this subsection for more details regarding the deviations.

gradient between the sample and the liquid nitrogen is high and the point density is lower than at low temperatures when the temperature gradient becomes small.

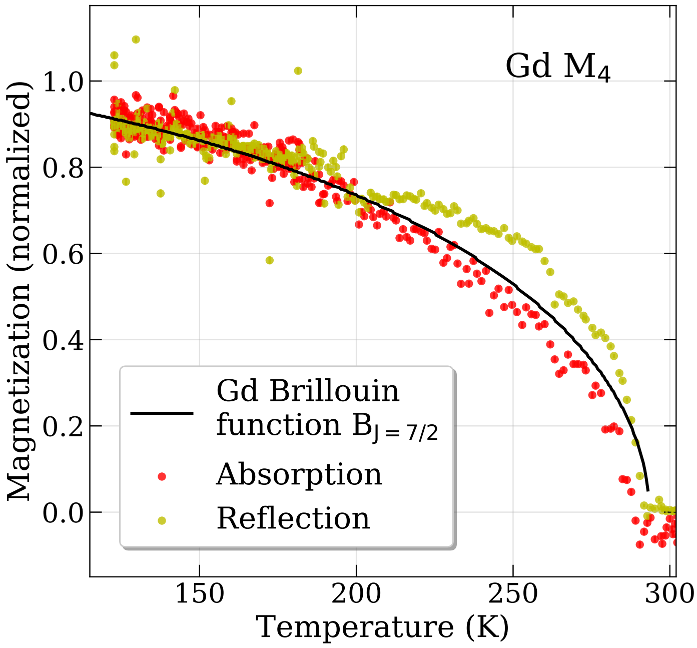

Figure 4.3: Magnetization (asymmetry) measured at the Gd M$_4$ absorption edge (E_{M_4} = 1221.4 eV) in absorption (red) and reflection (dark yellow) versus the sample temperature. The black line is the Gd Brillouin function and represents the temperature-dependent magnetization of a ferromagnet according to the Weiss mean-field theory. The data agrees well with the theoretical curve. The scattering of the data points indicates the statistical uncertainty. Deviations in the reflection data (around 250 K) are attributed to instabilities in the setup. See the end of this subsection for more details regarding the deviations.

We measured the sample temperature with the installed type-C thermocouple which has a specified operation range for temperatures between 0–2320 °C [125]. However, its utilization is necessary because of the high temperatures during sample preparation, see Section 3.1.2. In a separate setup, we calibrated the type-C thermocouple for temperatures down to −180 °C by recording the voltages of the type-C thermocouple simultaneously with the temperatures measured by an additionally installed type-K thermocouple at the sample, see Fig. A.1 in Appendix A.1. Using this calibration, we converted the type-C voltages acquired during the cool down measurements into the temperatures depicted in Figs. 4.2 and 4.3.

We normalized the data by dividing the asymmetry by the mean of the ten data points at the lowest temperatures times the value of the Gd Brillouin function (black lines in Figs. 4.2 and 4.3) at the lowest recorded sample temperature (about 120 K). The Brillouin function $B_J(x)$ indicates the expected temperature dependence of a ferromagnet according to the Weiss mean-field theory and it is given by:

$$B_J(x) = \frac{2J+1}{2J} \coth\left(\frac{2J+1}{2J} x\right) - \frac{1}{2J} \coth\left(\frac{x}{2J}\right) , \tag{4.3}$$

$$x = \frac{g_J \mu_B J B}{k_B T} , \tag{4.4}$$

where J is the total angular momentum, g_J the Landé factor, μ_B the Bohr magneton, k_B the Boltzmann constant, T the temperature and $B = B_{ext} + \mu_0 M$ is the total magnetic field where μ_0 is the vacuum permeability. Then, the magnetization M is given by implicitly solving:

$$M = N g_J \mu_B J \cdot B_J(x) , \tag{4.5}$$

where N is the number of atoms per unit volume. Hereby, one neglects the external field B_{ext}, since $B_{ext} \ll \mu_0 M$.

Despite the above challenges the measured asymmetry in reflection and absorption follow the trend given by the Brillouin function for Gd, see Figs. 4.2 and 4.3. This validates the XMCD reflection signal as an equivalent probe of the sample magnetization to the XMCD absorption signal. However, we tested the equivalence only in static measurements where the sample is in thermal equilibrium. For studies of ps dynamics, an uncertainty remains for the equivalence of both probes that is generally true for many observables between equilibrium and non-equilibrium conditions.

We attribute the deviations in the signals from the ideal curve to the stability of the setup (*e.g.* reflection data around 250 K in Fig. 4.2). First, the X-ray beam position is controlled by a position sensitive detector (PSD) [126] and a feedback loop corrects for deviations. The feedback loop in our experiment was deficient and tended to overshoot. This causes the beam position to vary making a significant change in signal intensity especially in the reflection signal. Second, the manipulator contracts and bends due to the temperature change which causes similar variations in the signal like the beam position variation.

With the knowledge that the XMCD reflection signal is a good probe for the sample magnetization we investigate the fluence dependence of the laser-induced magnetization dynamics in Gd in reflection geometry.

4.2 Fluence Dependence of Magnetization Dynamics

Koopmans *et al.* [15] could successfully model the magnetization dynamics in Ni and Gd using their M3TM. Surprisingly among the many proposed mechanisms causing demagnetization, the model only assumes Elliott-Yafet-type spin-flip scattering between electrons and phonons as a fundamental demagnetization mechanism. Despite the simple idea of the model, it reproduces two classes of dynamics showing either a single (type I) or a two-step decay of magnetization (type II). For the $3d$ metal Ni, a type I material, Roth *et al.* [65] comprehensively tested the magnetization dynamics for a series of different pump laser fluences and sample temperatures. But a likewise comprehensive test for $4f$ or type II materials is missing so far.

In spite of the success of the M3TM [15, 65] the underlying microscopic processes governing the physics are still debated (see also Section 2.3). One of the major points in [15] is the description of the two types of magnetization dynamics on the same theoretical footing. However, the description is still not complete in the sense that several physical quantities like the spin-flip probability are fit parameters and not derived from the model. Unai Atxitia extended the M3TM and we applied this model to describe the fluence dependence in Gd quantitatively using a similar spin-flip probability for all processes and time scales thus complementing the study by Roth *et al.* [65].

4.2.1 Evaluation Procedure and Magnetization Dynamics Studied with XMCD

We collected the data presented in this section at the FemtoSpeX slicing beamline at the synchrotron radiation source BESSY II. The evaluation of the data obtained at this beamline is more complex than in the case of static measurements described in Section 4.1.1 due to the beamline design. A detailed account of the beamline is given by Andrea Eschenlohr in her PhD thesis [93] and in publications by the beamline scientists [102–105]. We will briefly discuss technical details relevant for the understanding of the data evaluation.

In the slicing process essentially excited wings of electrons beside the main electron bunch are created by co-propagation of a fs-laser pulse within a modulator. Here the kinetic energy of a small part of the electrons in the bunch is modulated. The length of this slice is about 100 fs. The bending magnets divert those wing electrons more or less than the unmodulated electrons causing a horizontal displacement. In the radiator the electrons emit elliptically polarized X-rays and only the radiation emitted by one wing is kicked in the beamline and used for the experiment. The radiation emitted by the main bunch and the other wing are blocked by a thick lead block. See Section 3.2.3 for more details of the slicing process.

The slicing process cuts out only a small fraction of electrons from the bunch and the X-ray intensity is strongly reduced, with a loss factor of about 10^{-4} [104, 105]. Therefore, background radiation has to be avoided especially. One source of background radiation are the bending magnets which produce residual radiation from the electrons of the main bunch. The FemtoSpeX beamline precludes this background source by positioning the magnets in such a way that the residual radiation is not directed into the beamline.

A second source of background comes from the excitation of the electrons by the laser itself and is referred to as halo [105]. The excited electrons in the wing have a relaxation time of about 1 ms [104, 105] which is similar to the repetition rate of the slicing laser of 6 kHz [105]. This remnant from a previous slicing process produces "a stationary oscillating X-ray 'halo' background of picosecond pulse length" [105] which is superimposed on top of the new fs X-ray pulse. Thus, the halo background adds ps dynamics on top of any dynamics triggered in the actual experiment. There are two approaches implemented at BESSY II to alleviate this problem.

With a base operation frequency of 6 kHz [105] the slicing laser system would slice the same electron bunch before the halo electrons can relax. To keep the high operation frequency of the laser system, three electron bunches are singled out in the multibunch operation mode which are used alternately for slicing. In this way, the electrons can further relax between two subsequent slicing processes and the intensity of the halo background is reduced. Nevertheless, to eliminate also the remaining traces, the halo is measured separately in addition to the laser-pumped and -unpumped signals.

In the data analysis, we thus begin with the halo correction:

$$I_{\mathrm{hc}} = \frac{I_{\mathrm{sample}} - I_{\mathrm{halo}}}{I_0}, \tag{4.6}$$

with the signals of the sample dynamics (including the halo dynamics) I_{sample} and the pure halo dynamics I_{halo}. We divide by I_0, the momentary average current of the three slicing bunches in the storage ring, which is related to the emitted X-ray intensity. We calculate the halo-corrected signal I_{hc} for all combinations of laser-pumped and -unpumped data and parallel and antiparallel orientation of sample magnetization with respect to the circular[1] polarization of the X-rays.

Then, we obtain the XMCD as the difference between the signals for opposite magnetization directions and normalize the pumped data to the unpumped case:

$$\mathrm{XMCD}_{\mathrm{pumped}} = I_{\mathrm{pumped,parallel}} - I_{\mathrm{pumped,antiparallel}} \tag{4.7}$$

$$\mathrm{XMCD}_{\mathrm{unpumped}} = I_{\mathrm{unpumped,parallel}} - I_{\mathrm{unpumped,antiparallel}} \tag{4.8}$$

$$\mathrm{XMCD}_{\mathrm{normalized}} = \frac{\mathrm{XMCD}_{\mathrm{pumped}}}{\mathrm{XMCD}_{\mathrm{unpumped}}}\,. \tag{4.9}$$

In Fig. 4.4 the signals from Eqs. (4.6) to (4.9) are plotted exemplarily showing the dynamics of Gd for an absorbed[2] pump laser fluence of 8.0 mJ/cm^2 measured at the M$_5$ absorption edge (1186.3 eV). In the top part, we see the four traces for laser-pumped and -unpumped and parallel and antiparallel orientation of the sample magnetization and light polarization after halo correction. Remarkably, the two laser-pumped signals

---

[1] Actually, the X-rays are elliptically polarized with a circular polarization degree of about 70 % [127], see also Section 3.2.3.

[2] The pump laser intensity not reflected off the sample, *i.e.* absorbed within the whole sample.

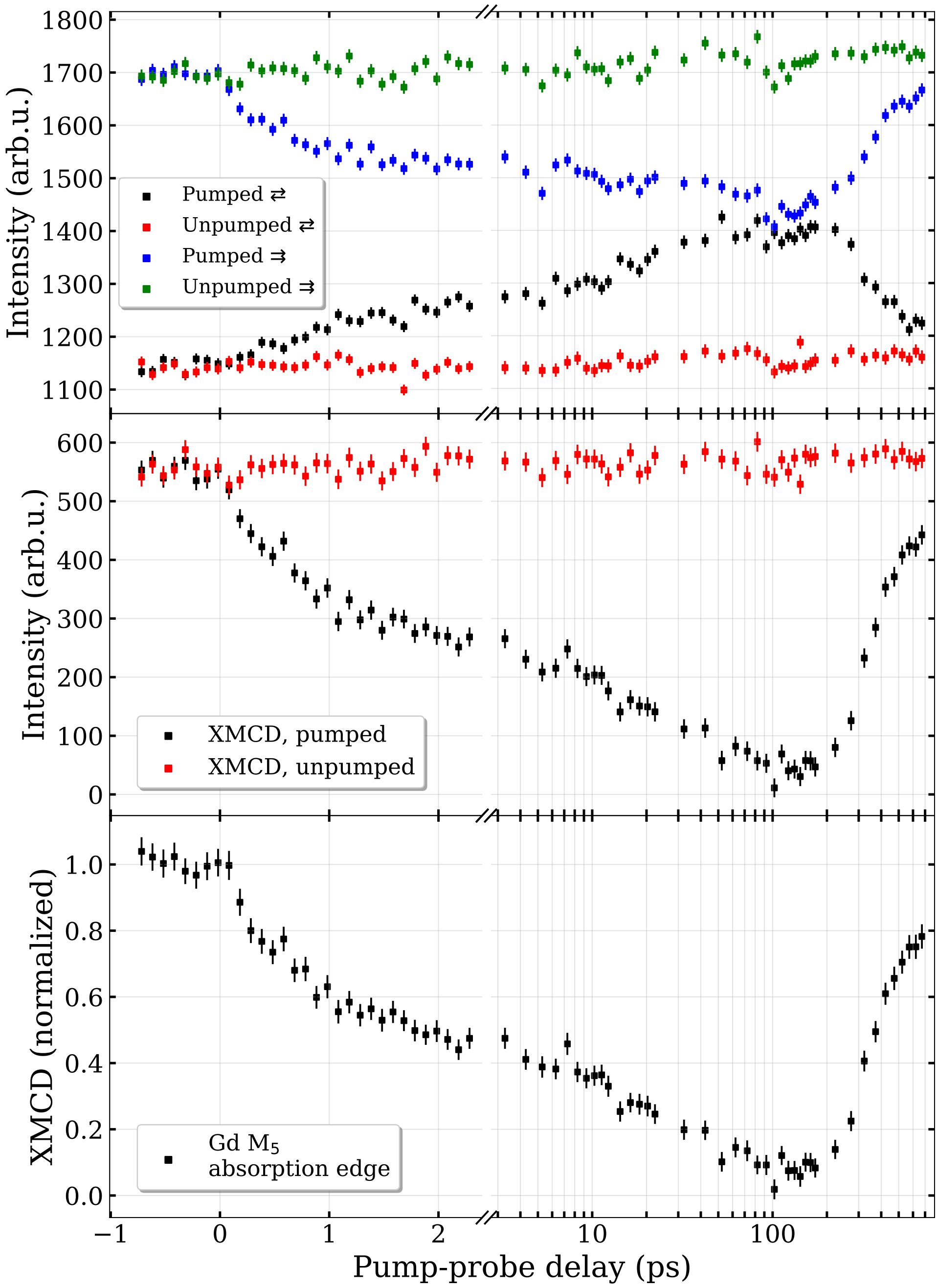

Figure 4.4: Laser-induced magnetization dynamics of Gd measured at the M_5 absorption edge (1186.3 eV), evaluated according to Eqs. (4.6) to (4.9). In the top graph, the halo-corrected signals for both magnetization directions of the sample with respect to the circular polarization of the probing X-rays are plotted, with and without pump laser excitation. The middle frame shows the corresponding laser-pumped and -unpumped XMCD signals. At the bottom, the normalized XMCD signal is displayed. The absorbed pump laser fluence for this example data set is $8.0\,\mathrm{mJ/cm^2}$, the sample temperature is $(125 \pm 10)\,\mathrm{K}$.

show different dynamics especially in the first few hundred fs. The signal for parallel magnetization drops faster than the antiparallel component.
In the middle, the corresponding XMCD signals with and without pump laser are depicted. At the bottom, the final normalized XMCD trace is plotted. The dynamics follow a double-exponential decay with an initial time scale in the sub-ps regime and a slower time scale of tens of ps. The recovery sets in at about 100 ps and proceeds within several 100 ps. This behavior is similar to previously observed dynamics on polycrystalline Gd samples in an XMCD study [23] and on single-crystalline samples in a magneto-optical Kerr effect (MOKE) experiment [128].

In the following we will discuss a discrepancy that is found between the magnetization dynamics in Gd measured using angle-resolved photoemission spectroscopy (ARPES) [22, 129] and XMCD [23]. The discrepancy is about the Gd $4f$ dynamics which feature either a single-step demagnetization on 14 ps [22] or a two-step demagnetization with sub-ps and tens of ps time scales [23]. Markus Gleich brought forward an idea regarding a hybridization of the unoccupied $4f$ state with the valence bands to explain the differences observed in both methods and discussed this idea in his Master's thesis [78]. We will pick up on this idea in the following and discuss it in a similar way to [78] for the sake of completeness.

$$\begin{aligned} M(t) = M_0 - \frac{1}{2}\Bigg[&\exp\left(\frac{\sigma^2}{2\tau_{\text{rec}}^2} - \frac{t}{\tau_{\text{rec}}} + \frac{t_0}{\tau_{\text{rec}}}\right)(A_1 + A_2)\,\text{erfc}\left(\frac{-t + t_0 + \frac{\sigma^2}{\tau_{\text{rec}}}}{\sqrt{2}\sigma}\right) \\ &+ A_1 \exp\left(\frac{-2t\tau_1 + 2t_0\tau_1 + \sigma^2}{2\tau_1^2}\right)\text{erfc}\left(\frac{-t + t_0 + \frac{\sigma^2}{\tau_1}}{\sqrt{2}\sigma}\right) \\ &+ A_2 \exp\left(\frac{-2t\tau_2 + 2t_0\tau_2 + \sigma^2}{2\tau_2^2}\right)\text{erfc}\left(\frac{-t + t_0 + \frac{\sigma^2}{\tau_2}}{\sqrt{2}\sigma}\right)\Bigg] \end{aligned} \tag{4.10}$$

Measuring magnetization dynamics in Gd seems to yield different results depending on the method employed. In [23] the authors measured the Gd $4f$ magnetization dynamics on a polycrystalline sample using XMCD obtaining a two-step decay with time scales of 750 fs and 40 ps. Though measured in transmission, it resembles the dynamics in our data recorded in reflection on a single-crystalline sample, see Fig. 4.5. We observe time scales of (0.68 ± 0.15) ps and (17 ± 6) ps that we extract from the fit with the function given in Eq. (4.10).

In contrast, Frietsch *et al.* [22] found only a single-step demagnetization of the Gd $4f$ spins on a time scale of 14 ps in a single-crystalline sample. They deduced the magnetization dynamics from magnetic linear dichroism (MLD) in an APRES study. Additionally, they observed the $5d6s$ spin dynamics on a time scale of 0.8 ps, which they derived from the exchange splitting of the valence bands. Both time constants are strikingly similar to those in the above XMCD data.
Other studies on magnetization dynamics in Gd have observed similar time scales. Carley *et al.* [129] and Teichmann *et al.* [130] have seen a decrease of the $5d6s$ exchange

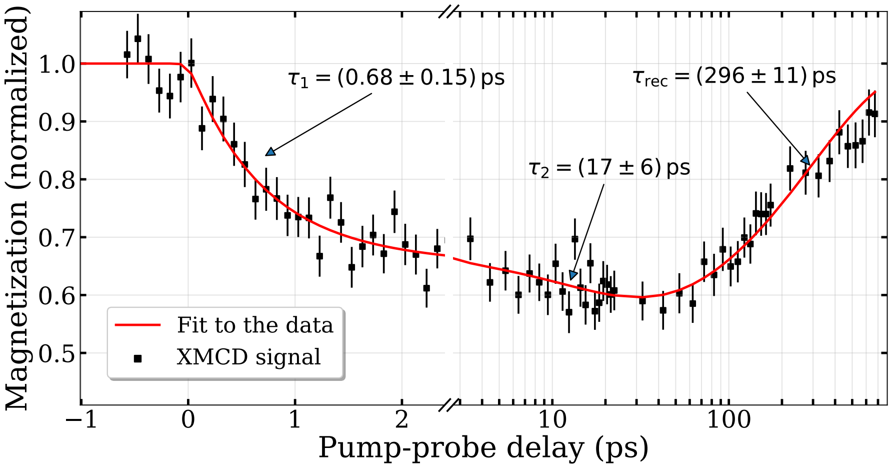

Figure 4.5: Pump-induced demagnetization in Gd measured via XMCD at the M_5 absorption edge (1186.3 eV). The fit function from Eq. (4.10) (line) contains two time constants for the demagnetization and one for the recovery. The error bars correspond to the statistical uncertainty in the data. The absorbed pump laser fluence is 3.2 mJ/cm^2, the sample temperature is (125 ± 10) K.

splitting on time scales of (0.86 ± 0.10) ps and (1.1 ± 0.2) ps, respectively. Andres *et al.* [131] studied the Gd surface state and found a Stoner-like shift of the occupied majority-spin surface state. They relate this shift to a demagnetization of the surface state and observe a time constant of (0.6 ± 0.1) ps. Interestingly, the spin polarization of the surface state changes with (15 ± 8) ps [131], similar to the $4f$ dynamics observed by Frietsch *et al.* [22]. Finally, a MOKE study by Sultan *et al.* [25] finds a demagnetization time[3] of about 0.9 ps.

All the sub-ps time constants from these ARPES and the MOKE studies emerge from probing the valence band dynamics. The similarity of the time scale in the first demagnetization step in the above XMCD studies to the time scale of the valence-band dynamics suggests the possibility of an imprint of the $5d6s$ dynamics in the $4f$ dynamics as seen in XMCD. One idea, which might explain the coincidence of time scales, is that the core-hole resulting from the XMCD transition energetically pulls downs the unoccupied $4f$ state which then hybridizes with the valence bands inheriting the valence band dynamics. Then, three questions arise: Do the energies of the involved states match the X-ray energies, can the states hybridize and can the dynamics of the $5d6s$ electrons be imprinted onto the $4f$ electrons within time scales shorter than the probing process?

---

[3] The time constant varies for different sample temperatures. The value given here refers to a sample temperature of about 100 K which is similar to the temperatures in the other studies.

In our XMCD studies at the Gd M_5 edge we are probing the $3d_{5/2} \rightarrow 4f$ transition. The energy necessary for the transition should be the sum of the binding energies of the $3d$ level and the unoccupied $4f$ state. A high-resolution X-ray photoemission spectroscopy (XPS) study [132] found a binding energy of about 1187 eV for the $3d_{5/2}$ state, the X-ray data booklet specifies the binding energy at 1189.6 eV [133]. In inverse photoemission measurements [73] the unoccupied $4f$ state is found at 4.1 eV. Another XPS and bremsstrahlung isochromat spectroscopy study observes the unoccupied $4f$ state at around 4 eV [74, 75].

Surprisingly, the X-ray energies measured in X-ray absorption spectroscopy (XAS) are smaller by a few eV compared to the sum of the $3d$ binding energy and the energy of the unoccupied $4f$ state, *e.g.* 1185 eV [96], 1188 eV [134], 1189 eV [135]. In our own measurements, we find the transition at 1190 eV, *c.f.* Fig. 4.1. The transition energies for XAS indicate that the $4f$ state shifts close to the Fermi level, presumably due to the presence of the core-hole in the $3d_{5/2}$ state.
Alouani [136] has calculated the effect of the presence of a core-hole on an X-ray absorption spectrum. He investigated the L_3 transition in ferromagnetic Fe with and without a core-hole in the $2p_{3/2}$ state and finds a shift of the transition energy of about 1 eV. The effect in Fe is thus of similar magnitude as the shift of about 4 eV in our Gd $3d_{5/2} \rightarrow 4f$ transition substantiating the hypothesis of the lowered $4f$ state.

Assuming the shift of the unoccupied $4f$ state towards the Fermi level due to the $3d$ core-hole to be true, a hybridization between the $4f$ and the $5d6s$ valence states becomes possible. For substantial hybridization the energy levels of the involved states should be similar [137] (p. 438). That a hybridization between the $4f$ and $5d6s$ states can be realized is known for cerium (Ce) [138]. Oliver Berg discusses in his PhD thesis [138] that the hybridization of the occupied $4f$ and $5d6s$ states in Ce is significantly larger than in *e.g.* Gd or dysprosium because the $4f$ states have a binding energy of only 0.2 eV in contrast to *e.g.* 8 eV in Gd.
Regarding atomic orbitals, d and f orbitals cannot hybridize due to different parity as long as inversion symmetry is given. However, in a solid inversion symmetry is broken at the surface. Moreover, hybridization is still possible between an f orbital of one atom and a d orbital of a neighboring atom, thus enabling hybridization in a solid where a hybridization in an atom is forbidden.

O. Berg discusses furthermore that a phase transition from γ-Ce to α-Ce might involve a shift of the $4f$ level towards the Fermi level and a decreased localization of the $4f$ electron [138]. The reduced localization entails a larger overlap of the $4f$ wave function with the $5d6s$ orbitals [138]. The last point is corroborated by increased fluctuations in the valence of α-Ce compared to γ-Ce which could be caused by hopping of the $5d6s$ electron between the $4f$ level and the conduction band [138].
The shift of the $4f$ level in Ce due to the phase transition with the accompanying increased hybridization with $5d6s$ electrons bears a certain resemblance to the case in Gd. In Gd, the transition is the excitation of a $3d$ electron which creates a core-hole

that shifts the unoccupied $4f$ state towards the Fermi level. Then, a hybridization of the $4f$ state with the $5d6s$ valence state seems at least plausible.

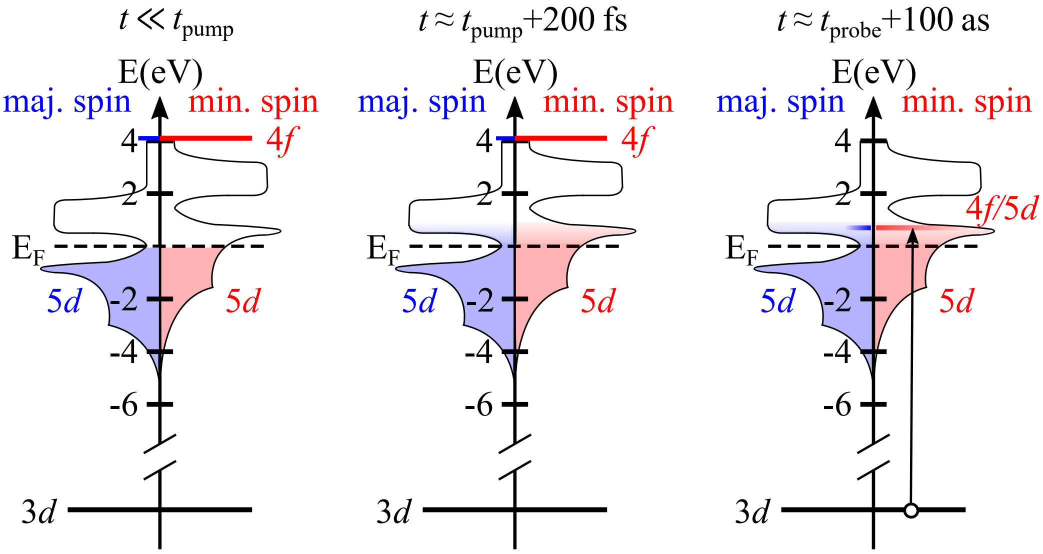
$t \ll t_{\mathrm{pump}}$
$t \approx t_{\mathrm{pump}}$+200 fs
$t \approx t_{\mathrm{probe}}$+100 as
E(eV)
maj. spin
min. spin
4f
4
2
E_F
5d
-2
-4
-6
3d
4f/5d

Figure 4.6: Schematic of the proposed hybridization of the $4f$ and $5d6s$ states in Gd for XMCD measurements. Left: Density of states in Gd in equilibrium. For brevity, the $5d6s$ valence states are abbreviated as $5d$ states. Middle: An IR pump pulse excites the system at t_{pump} and within about 200 fs the electrons thermalize. Right: The X-ray probe pulse excites a transition from the $3d$ to the unoccupied $4f$ state at t_{probe}, *e.g.* a few ps after t_{pump}. On the time scale of screening, *i.e.* within about 100 as, the unoccupied $4f$ state shifts towards the Fermi level due to the core hole in the $3d$ state and hybridizes with the $5d$ valence bands.

We have seen indications substantiating both a shift of the $4f$ state towards the Fermi level and the principle feasibility of a hybridization of the $4f$ state with the valence states. Assuming both circumstances to apply we have to convince ourselves of the imprinting of the $5d6s$ magnetization dynamics onto the $4f$ dynamics within the time scale of the probe duration. At a few ps pump-probe delay in the dynamics in the ARPES data [22] the $5d6s$ states are already significantly demagnetized while the $4f$ spins are still mostly magnetized. Thus, when probing at a few ps pump-probe delay, the XMCD signal from the $4f$ states has to be immediately affected by the $5d6s$ dynamics. To see the effect of the valence band dynamics onto the $4f$ dynamics, we regard the system after pumping with a short laser pulse. The pump laser pulse excites electrons from the valence bands and a hot electron distribution forms after a few hundred fs (*e.g.* 200 fs in Gd [34]). Once the core-hole shifts the $4f$ state towards the Fermi level, these hot electrons can populate the shifted $4f$ state. The rearrangement of the electronic states and their population will take place on time scales of electron dynamics of few hundred attoseconds[4] or charge transfer times of <1 fs [140]. Figure 4.6 shows a

---

[4] The period of the electron orbiting around the hydrogen nucleus is ≈ 150 as [139]; at Fermi velocity, an electron travels the distance of a lattice constant in Cu in ≈ 230 as [139].

schematic of the hybridization of the states with the relevant time scales.
Thus, the state hybridizes and its spin polarization is influenced by the $4f$ and $5d6s$ spin dynamics within the probe pulse duration. In XMCD the contrast arises due to different transition probabilities for different sample magnetizations with respect to the circular polarization of the light. As Johannes Grabis discusses in his PhD thesis [100] XMCD can be regarded as a two step process. First, the absorption cross section for spin-up and spin-down electrons in the initial state is different for a certain photon helicity resulting in a preferential excitation of one spin polarization of the electrons.
Second, the density of states of the final state determines the transition probabilities according to Fermi's golden rule. Only if the density of states for spin-up and spin-down electrons is different, *e.g.* due to exchange splitting, the dichroism can be detected. If the density of states is purely of one spin character the preferential excitation from step one will be detected to its full extend. If the density of states is equal for both spin directions a change of helicity and the preferential spin direction of the excited electrons will make no difference in the absorption.
If the fast hybridization affects the transition probabilities for the opposite magnetization directions, because the reduction of exchange splitting of the valence states changes the available density of states, the fast magnetization dynamics in the valence states could be imprinted on the XMCD signal.

In this picture, the similar time scales in ARPES and XMCD measurements could be explained despite disparate dynamics. In XMCD, the signal would not measure the isolated $4f$ dynamics in contrast to the MLD of the $4f$ states in ARPES [22] but a combined dynamics from a hybridized $4f$ state which shows both time scales from ARPES measurements. Nevertheless, it is desirable to obtain a better theoretical understanding regarding the hybridization and its influence on the probing process in XMCD to substantiate the speculative ideas presented here.
As an afterthought, if the hybridization picture holds, one could try to find a connection between the disparate minority- and majority-spin valence band dynamics discussed in [129] and the individual XMCD traces for parallel and antiparallel sample magnetization with respect to light polarization (blue and black traces in Fig. 4.4). But this in particular requires a better understanding both of the details of the hybridization of the $4f$ and $5d6s$ states in Gd and the details of how the transition probabilities in XMCD are affected by hybridization of the final states.

4.2.2 Time-Dependent Measurements at Varying Pump Laser Fluences

In the following, the results on demagnetization in Gd probed via XMCD in reflection for a pump laser energy of 1.55 eV are discussed. We recorded fluence-dependent data also for pump energies of 0.95 eV and 3.1 eV, see Appendix A.3. The most remarkable difference in the pump photon energy-dependent magnetization dynamics will be discussed in Section 4.3.

We performed time-dependent measurements on Gd/W(110) at the M_5 absorption edge (1186 eV) for a variety of absorbed pump laser fluences ranging from 1.6 to 9.6 mJ/cm^2. The results are displayed in Fig. 4.7. The assessment of the pump laser fluence uncertainty is difficult. The spot size used in the evaluation is 300 µm × 300 µm which was read off of a camera repeatedly. We found it to be quite stable but quick checks scanning the pump laser horizontally and vertically over the sample and measuring the XMCD showed a larger variation in spot size. However, these quick checks are intricate to evaluate and prone to other influences. From the variation of the spot size we would estimate the uncertainty to be in the range of 10–20 %, however there might be a larger systematic offset.

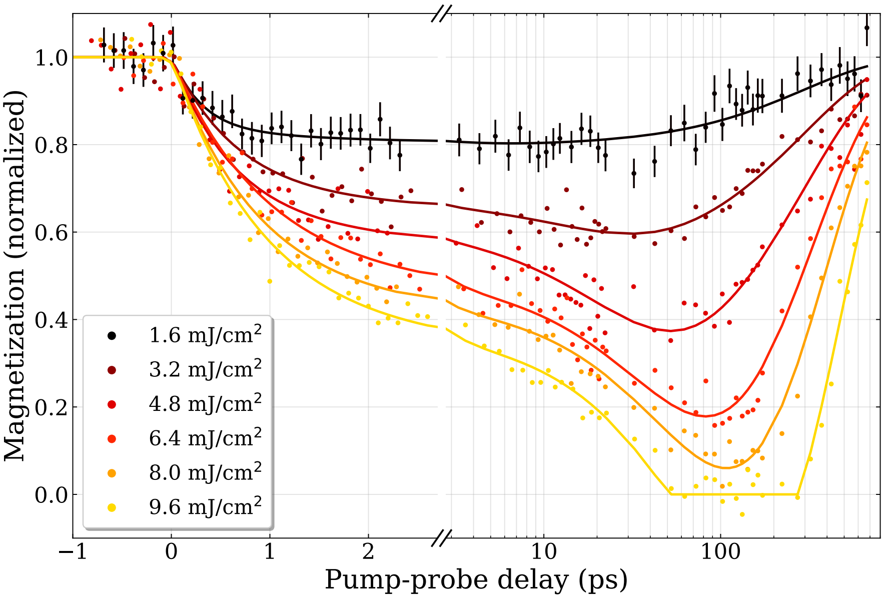

Figure 4.7: Pump laser-induced demagnetization in Gd measured via XMCD in reflection at the Gd M_5 absorption edge (1186.3 eV) (markers) including the fit function from Eq. (4.10) (lines) for a variety of absorbed pump laser fluences (absorbed in Gd and W, measured as the non-reflected part). The error bars in the top data set are derived from statistical uncertainty of the count rates and representative for all data sets. The sample temperature is (125 ± 10) K.

The general trend discussed for Fig. 4.5 is seen for all fluences. There are two steps in the demagnetization on time scales of about 1 ps and some tens of ps, *cf.* Table 4.1. The recovery was a global parameter for all fluences during the fit. The underlying assumption is that the recovery is governed by the heat transport out of the sample and should be the same for a given sample system and setup. Differences are to be expected for other sample materials or if the sample has a different (thermal) connection to the sample holder.

abs. fluence* [mJ/cm^2]	A_1 [arb. units]	τ_1 [ps]	A_2 [arb. units]	τ_2 [ps]	τ_{rec} [ps]
1.6 ± 0.3	0.17 ± 0.10	0.31 ± 0.30	0.04 ± 0.10	2 ± 6	296 ± 11
3.3 ± 0.5	0.32 ± 0.02	0.68 ± 0.15	0.15 ± 0.03	17 ± 6	296 ± 11
4.8 ± 0.8	0.39 ± 0.02	0.64 ± 0.11	0.43 ± 0.03	27 ± 4	296 ± 11
6.4 ± 1.0	0.50 ± 0.02	0.95 ± 0.11	0.83 ± 0.06	55 ± 6	296 ± 11
8.0 ± 1.2	0.56 ± 0.02	0.86 ± 0.08	1.34 ± 0.12	85 ± 7	296 ± 11
9.6 ± 1.5	0.63 ± 0.02	0.93 ± 0.09	2.64 ± 0.31	123 ± 11	296 ± 11

Table 4.1: Fit parameters for the fit curves displayed in Fig. 4.7 using the fit function Eq. (4.10). The recovery time τ_{rec} is fitted globally for all fluences. The first demagnetization step occurs on a sub-ps time scale, the second step lies between a few to a hundred ps depending on the pump laser fluence. For the lowest fluence, the demagnetization is very weak and the uncertainties in the parameters become large. The uncertainties are one standard deviation of the fit parameters. The "*" indicates that there might be a large systematic offset for all pump laser fluences. A graphical representation can be found in Fig. A.7 in Appendix A.4.

We can observe a few general features. At the lowest pump laser fluence, the demagnetization is weak. The second step nearly vanishes and the fitted time scales become uncertain. The point of minimal magnetization, *i.e.* the turning point between de- and remagnetization, shifts towards later pump-probe delays with increasing pump laser fluence. The sample remagnetizes on a time scale of 296 ps, even despite complete demagnetization at the highest fluence. The recovery time scale is shorter than measured by Wietstruk *et al.* [23], but we can presumably ascribe this observation to an increased heat flow out of the sample in our system. The sample system in [23] was a freestanding transmission sample on a 0.5 µm Al substrate. In contrast, in our setup a Gd thin film is grown on a roughly 3 mm thick W(110) crystal which is mounted on a plate directly connected with the manipulator providing a good thermal conductivity.

We set out to compare how well the M3TM can describe the fluence dependence in Gd shown in Fig. 4.7 as an example of a type II ferromagnet. In this context, we started a cooperation with Unai Atxitia who extended the M3TM and included some additional features[5]. First, instead of the Brillouin function for $S = 1/2$, $B_{1/2}(x) = \tanh(x)$, the extended model uses $B_{7/2}(x)$ for the Gd $4f$ spins. The equation of motion (Eq. (2.23)) then becomes:

$$\frac{\mathrm{d}m}{\mathrm{d}t} = Rm\frac{T_{\mathrm{p}}}{T_{\mathrm{C}}}\left(1 - \frac{m}{B_{7/2}(\frac{mT_{\mathrm{C}}}{T_{\mathrm{e}}})}\right) . \tag{4.11}$$

Second, in Eq. (2.21) a term P_{se} accounting for the heat absorbed by the spin system from the electron system is added and the excitation by a laser pulse is modeled by a term $S(z,t)$. Equation (2.21) becomes:

---

[5] Private communication with Unai Atxitia, Berlin 2020.

$$C_\mathrm{e}[T_\mathrm{e}]\frac{\mathrm{d}T_\mathrm{e}}{\mathrm{d}t} = \nabla_z(\kappa\nabla_z T_\mathrm{e}) + g_\mathrm{ep}(T_\mathrm{p} - T_\mathrm{e}) + P_\mathrm{se} + S(z,t) \ , \tag{4.12}$$

$$P_\mathrm{se} = \dot{M}_\mathrm{s} H_\mathrm{eff} \ , \tag{4.13}$$

$$S(z,t) = P_0 \exp\left(-\left(\frac{t-t_0}{\tau}\right)^2\right) \exp\left(-\frac{z}{\delta}\right) \ , \tag{4.14}$$

where P_se comes from $\mathrm{d}\mathcal{H}/\mathrm{d}t = \mathrm{d}\mathcal{H}/\mathrm{d}M_\mathrm{s}(\mathrm{d}M_\mathrm{s}/\mathrm{d}t)$ where $\mathrm{d}\mathcal{H}/\mathrm{d}M_\mathrm{s} = H_\mathrm{eff}$, M_s is the total magnetic moment of the spin system and H_eff is the effective field. The pump laser fluence prefactor P_0, the pump laser temporal offset t_0 and width τ and the laser penetration depth δ determine the pump laser pulse.

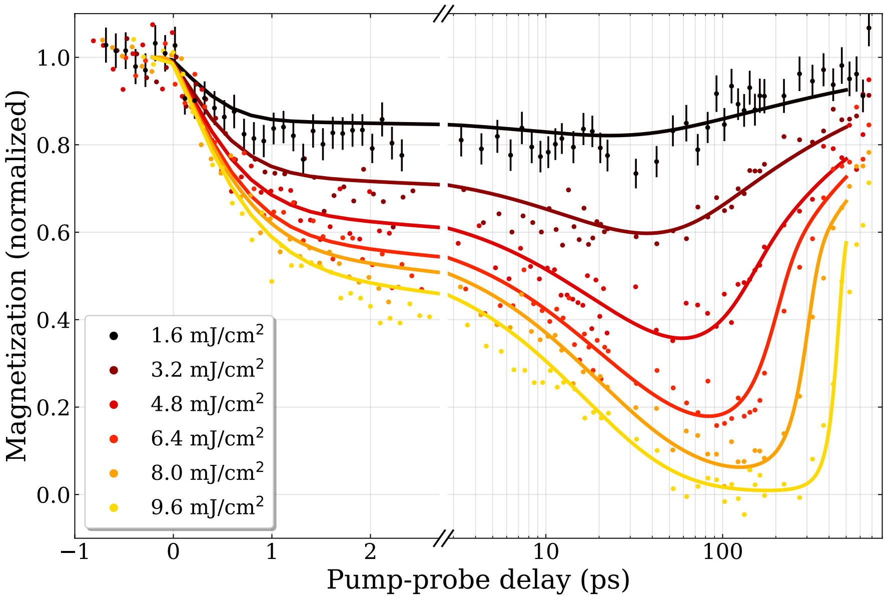

Figure 4.8: Pump laser-induced demagnetization in Gd measured via XMCD in reflection at the Gd M_5 absorption edge (1186.3 eV) for a variety of absorbed pump laser fluences, identical to the data in Fig. 4.7. The lines are calculated dynamics using the extended M3TM by Unai Atxitia and agree well with the experimental data.

Using the extended M3TM, we can model the fluence dependence of the demagnetization on all time scales capturing both equilibrium and non-equilibrium dynamics, see Fig. 4.8. In the model, the spin-flip probability a_sf only needs to vary by about 10 % and with 0.135 it is more similar to spin-flip probabilities found in other metals [15]. This is an improvement towards the original M3TM which assumed a significantly smaller value ($a_\mathrm{sf} = 0.08$) [15] to model the magnetization dynamics of Gd. As a first general conclusion, we can confirm with this data set for Gd that the M3TM captures the dominant magnetization dynamics of a type II system.

But despite the good agreement between the extended M3TM and the experimental data, one has to consider that Gd is a special case among the lanthanides, or type II systems, in that its orbital momentum $L = 0$. This is fortunate for simulating the experimental data with the M3TM as a coupling between $4f$ spins and the lattice is not implemented in the model. Such a coupling will have significantly more influence on the magnetization dynamics in *e.g.* Tb which has a large orbital momentum. The influence of a strong coupling between $4f$ spins and the lattice and whether the M3TM is capable to model such a system is still under investigation.

In the following we will examine in more detail the fluence dependence of the magnetization dynamics on the two time scales. We first consider the sub-ps dynamics.

Fluence-Dependent Dynamics on the Fast Time Scale

We will first discuss the pump laser fluence-dependent magnetization dynamics in Gd evaluated at a pump-probe delay of 4 ps. At this time, the fast sub-ps dynamics are mostly completed. In the first few ps, the dynamics are governed by the laser excitation of the valence electron subsystem, its thermalization via electron-electron scattering and the equilibration of the valence-electron and phonon heat baths via electron-phonon scattering [34]. Additionally, excitations of magnons and transport effects play a role in the early dynamics [34].

Figure 4.9 shows data extracted from Figs. 4.7 and 4.8. The gray circles are the values of the magnetization of the fit curves in Fig. 4.7 at 4 ps for the different fluences. The blue triangles are the corresponding magnetization values taken from the extended M3TM model calculation in Fig. 4.8. In a separate measurement, we additionally recorded the XMCD at the Gd M_5 absorption edge at the fixed pump-probe delay of 4 ps and incrementally increased the pump laser fluence (black squares in Fig. 4.9).

All data sets show an exponential dependence on the absorbed pump laser fluence (*cf.* red line in Fig. 4.9). At 4 ps pump-probe delay, the magnetization drops by nearly 10 % at 0.6 mJ/cm^2 absorbed pump laser fluence and reaches a residual magnetization of about 30 % at 11.5 mJ/cm^2. At these highest fluences, the average sample temperature rises by about 10 K, but the effect of thermal reduction of the magnetization is negligibly small compared to the demagnetization caused by the pump laser (compare the small decrease in magnetization between a temperature span of 10 K below 150 K in the $M(T)$ curves in Fig. 4.2).

The exponential dependence on the pump laser fluence has the striking implication that a complete demagnetization of pure Gd is not possible (or would need infinite fluence) on a time scale of about 1 ps. This result is particularly remarkable since Stanciu *et al.* [6]

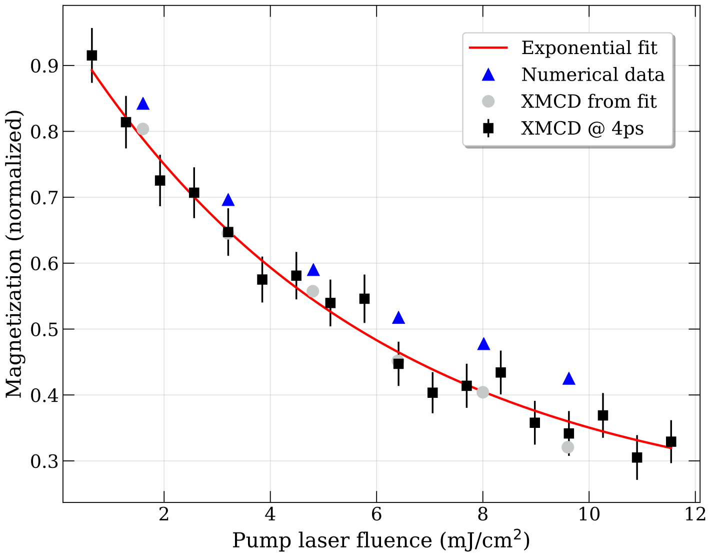

Figure 4.9: XMCD of Gd measured at the M_5 absorption edge (1186.3 eV) at 4 ps pump-probe delay (black squares) versus absorbed pump laser fluence. Gray dots are the magnetization extracted from the fit curves in Fig. 4.7 at the according pump-probe delay. The XMCD depends exponentially on the fluence, see red line (fitted to the black squares data). The numerical data (blue triangles) from the extended M3TM model (Fig. 4.8) follows the same trend.

observed all-optical switching in GdFeCo alloys where the Gd subsystem is completely demagnetized and even reverts its magnetization direction on a ps time scale [141].

In the following we analyze the fluence dependence of the magnetization on a tens to a hundred ps time scale.

Fluence-Dependent Dynamics on the Slow Time Scale

On a tens of ps time scale the electron and phonon heat baths are equilibrated and at the elevated temperatures phonon-magnon interactions drive the demagnetization [23]. In a similar fashion as for the fast time scale, we recorded the XMCD at the Gd M_5 absorption edge in a separate measurement at a fixed pump-probe delay of 96 ps while incrementally increasing the pump laser fluence, see black squares in Fig. 4.10. Again, gray dots are the values of the magnetization of the fit curves in Fig. 4.7 evaluated at a pump-probe delay of 96 ps and the numerical data (blue triangles) is the magnetization extracted from the extended M3TM in Fig. 4.8 at the same pump-probe delay.

The red lines in Fig. 4.10 indicate the double-linear trend in the data. They are fits to the black squares data for fluences up to about 8 mJ/cm^2 and above 7 mJ/cm^2,

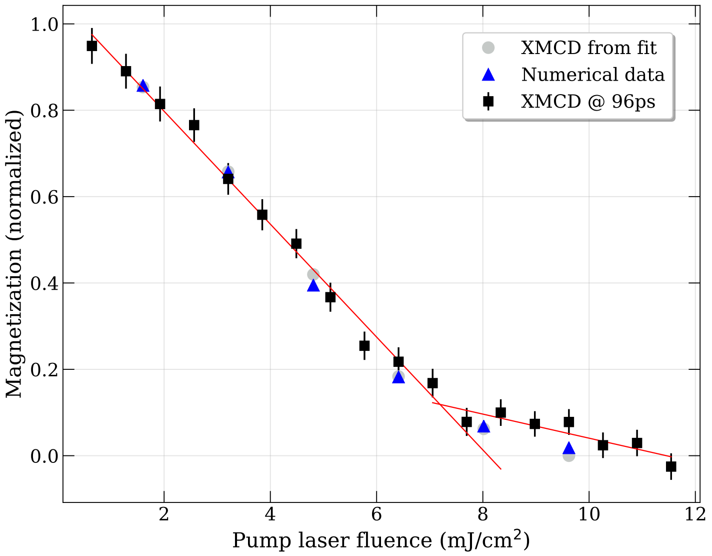

Figure 4.10: XMCD of Gd measured at the M_5 absorption edge (1186.3 eV) at 96 ps pump-probe delay (black squares) versus absorbed pump laser fluence. Gray dots are the magnetization extracted from the fit curves in Fig. 4.7 at the according pump-probe delay. The XMCD follows a double-linear trend, see red lines (two independent linear functions fitted to the black squares data). The numerical data (blue triangles) from the extended M3TM model (Fig. 4.8) follows the same trend.

respectively. We find 95 % magnetization at 0.6 mJ/cm^2 which decreases linearly to about 15 % at around 8 mJ/cm^2. At this point, the further demagnetization slows down for higher fluences and the sample demagnetizes completely at about 11 mJ/cm^2 absorbed pump laser fluence.

On this time scale, the linear dependence of the magnetization on the pump laser fluence cannot be explained simply by assuming an energy input from the pump laser which leads to a temperature increase of all subsystems. Assuming all subsystems (electrons, phonons and magnons) to be in equilibrium at tens of ps pump-probe delay, the initial energy input of the pump laser would lead to a global temperature increase determined by the total heat capacity of Gd. Despite the temperature dependence of the heat capacity [142, 143], its cumulative function describing the temperature increase for a given energy input is nearly linear. Thus, for increasing pump laser fluences, the magnetization should roughly follow the Brillouin function (Fig. 4.2) instead of being linear.

The physics behind the double-linear dependence are not clear yet. One idea is that the slowing down could be rooted in the highly disturbed state of the system at the high

pump laser fluences. At high enough fluences, the spin system will be demagnetized deeply and the spins will fluctuate strongly rendering further loss of magnetization by spin-flip scattering less efficient. The lower efficiency would manifest itself as the slowing down in the fluence dependence of the magnetization dynamics.
In this picture of reduced spin-flip scattering efficiency, the change of slopes in Fig. 4.10 should be rather continuous as it does not describe a threshold behavior. The question why we see a rather abrupt kink in the slopes in our data still needs to be clarified. More numerical data would be a valuable addition to ascertain if the kink does appear in the theoretical calculations as well.

Magnetization Dynamics at the Gd M_4 and M_5 Absorption Edges

We measured the laser-induced magnetization dynamics in Gd at the M_4 and M_5 absorption edges for a fixed fluence of about $6.5\,\mathrm{mJ/cm^2}$ to investigate if the contributions of spin and angular orbital momentum to the total spin moment change during the dynamics.

From XMCD measurements one can estimate the contributions of the spin and orbital momentum to the total magnetic moment of an element by applying sum rules for X-ray absorption spectroscopy [90, 91]. The applicability has certain limitations as discussed by J. Grabis in his PhD thesis [100]. For instance, parameters in the spin-orbit coupling Hamiltonian and the radial matrix elements of the states involved in the transition should not be dependent on the photon energy [98]. A second condition, according to which the initial states must not mix and l is a good quantum number [98] seems to be fulfilled for trivalent Gd ions [144]. Still, effects from surfaces and interfaces might play a role in the applicability of sum rules [98].
In addition to those restraints, our measurements are performed in a reflection geometry. Sum rules for this case could in principle be derived from the sum rules for absorption using the Kramers-Kronig relation, but such sum rules are not available to the author's knowledge. Moreover, it is not clear if the sum rules are applicable in non-equilibrium conditions (after laser excitation).

Fig. 4.11 shows the dynamics at the Gd M_4 and M_5 absorption edges. For the normalization of the data sets data points at pump-probe delays $\Delta t < -1.3\,\mathrm{ps}$ (not shown in the figure) were used. Unfortunately, the data points for the M_4 edge just before time zero are slightly above the average of the data points at $\Delta t < -1.3\,\mathrm{ps}$ leading to an apparent offset between the two data sets. A different normalization does not change the results qualitatively.

The dynamics at both absorption edges is nearly identical except for a small deviation in the recovery phase. For a change of spin and angular orbital momentum contributions to the total spin moment one would expect a difference in the dynamics of the two edges. Under this assumption there seems to be no significant transfer of momentum between the spin and orbital momenta on the fast time scale and up to the recovery.

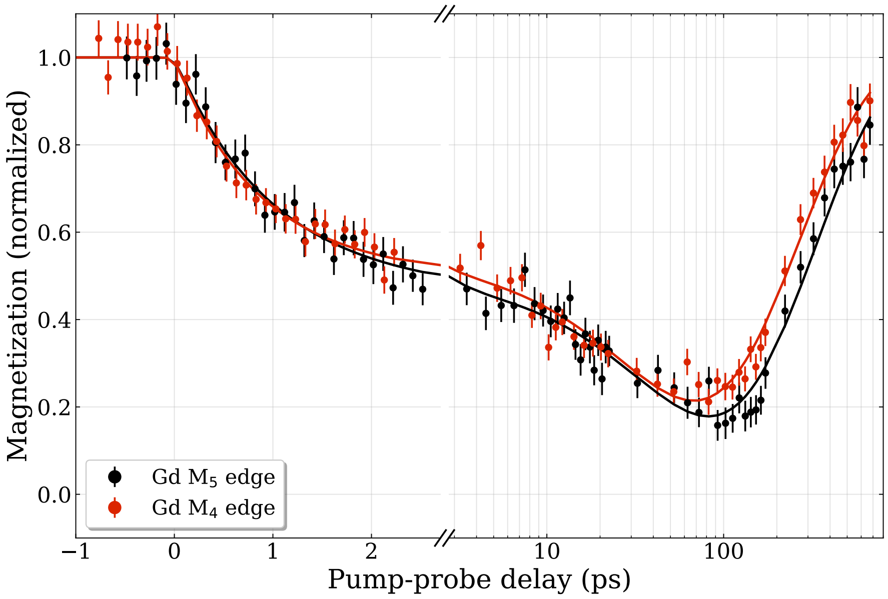

Figure 4.11: Magnetization dynamics in Gd measured at the M$_4$ (1216 eV) and M$_5$ (1186.3 eV) absorption edges. The pump laser fluence is about 6.5 mJ/cm^2. Except for a small offset in the recovery phase the dynamics at both absorption edges are nearly identical.

During recovery spin and orbital momentum contributions might vary. This result is intuitive in so far as the orbital momentum in Gd is vanishing and spin-orbit coupling is weak. However, this interpretation requires revision by applying sum rules for XMCD in reflection and validation of their applicability for a Gd thin film.

Moreover, for a quantitative analysis, different penetration depths of the X-rays could play a role. The absorption lengths for both absorption edges and polarization directions varies between 8–36 nm [96], the values for the M$_4$ edge (27 nm and 36 nm for parallel and anti-parallel orientation of spin and magnetization) being even similar to the pump laser penetration depth for 1.55 eV photon energies in Gd at 100 K ($1/\mu_{\text{abs}} = \lambda/(4\pi k) \approx 25$ nm, k taken from [145]). From the similarity of the dynamics, either different effects arising from bulk and surface contributions or effects due to the similar penetration depths of pump and probe pulses cancel out or they are too small to be resolved here.

4.3 Dependence of Magnetization Dynamics on the Photon Energy of the Pump Pulse

The contents of this section are published in [24].

As mentioned in the beginning of Section 4.2.2, we studied the magnetization dynamics of Gd thin films for pump photon energies of 0.95 eV, 1.55 eV and 3.1 eV. Typically, the excitation of a system in laser-induced magnetization dynamics experiments is used as a source of energy input triggering demagnetization processes. Using different pump photon energies should affect the initial non-thermal distribution, either because of the higher energy of excited electrons and/or because different states can be excited, both in energy and in k. Thus, effects from different pump photon energies on the initial magnetization dynamics are plausible and one would expect them to appear while the hot electrons are not yet thermalized, *i.e.* within 200 fs in Gd [34].

Figure 4.12 shows the magnetization dynamics of Gd/W(110) for the three different pump photon energies for comparable fluences. The pump laser fluences for 0.95 eV and 3.1 eV pump photon energy are unfortunately rather uncertain. The usage of an optical parametric amplifier and second-harmonic generation, respectively, caused unexpectedly high fluctuations in the laser spot size. As this side-effect was not anticipated, data for determining the spot sizes are partly not available or the determined spot sizes deviate significantly from expected values. The fluences given in Fig. 4.12 are calculated from the best available data but need to be regarded with caution.
The fact that the demagnetization at large delays of about 100 ps is similar (about 90 % demagnetization) suggests that the fluences are more similar than the numbers determined from the spot size measurements indicate. On these long time scales the dynamics should be governed by the net amount of input energy which manifests itself in an elevated temperature of the subsystems of electrons, phonons and magnons and not by the initial distribution of hot electrons before thermalization.

Additionally, the penetration depths for the three pump photon energies are different which in principle affects the distribution of hot electrons within the sample. However, the attenuation lengths for all pump photon energies are similar up to a factor of two with values of about 36 nm (0.95 eV), 25 nm (1.55 eV) and 16 nm (3.1 eV) (extinction coefficients taken from [145]). Thus, these differences should not decisively influence the dynamics.

We find the most striking difference between the three pump photon energies directly after excitation. At 0.95 eV pump photon energy the initial demagnetization is weaker than for the other two pump photon energies, see Fig. 4.12. After about 20 ps, the signals merge again within statistical uncertainty.
The reduced demagnetization for 0.95 eV indicates that the different initial hot electron distribution affects either spin-dependent transport, in the picture of superdiffusive transport [9], or the spin-flip probability, in the M3TM [15]. In both descriptions and for similar pump laser fluences the initial hot electron distribution cannot have an impact

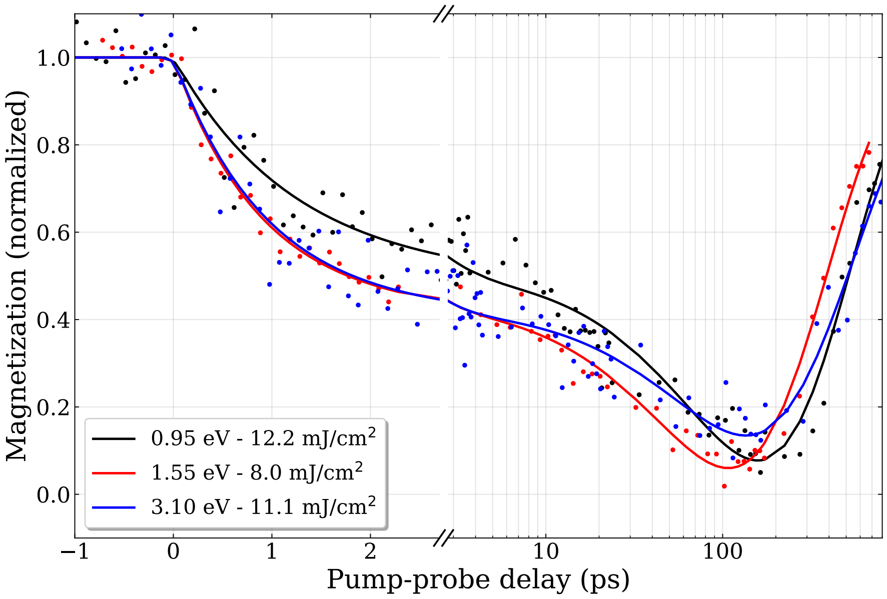

Figure 4.12: Magnetization dynamics in Gd measured at the M_5 (1186.3 eV) absorption edge via XMCD in reflection for varying pump photon energies. The lines are fits of the data using Eq. (4.10). The pump laser fluence is uncertain for 0.95 eV and 3.1 eV. The similar maximum demagnetization suggests that the fluences are similar for all pump photon energies in contrast to the fluences determined from experimental parameters. The initial demagnetization for 0.95 eV pump photon energy is lower than for higher pump photon energies. The uncertainties in the 0.95 eV data set are comparable to the 1.55 eV data shown above (*e.g.* Fig. 4.7) while they are about double the size for the 3.1 eV data set. The error bars have been left out for clarity.

on the dynamics once the electrons thermalize via electron-electron scattering. Thus, the pump photon energy dependence of either spin transport or spin-flip probability must be related to non-thermalized excited electrons.

We could reproduce the reduced fast demagnetization for 0.95 eV by using a slightly extended M3TM which M. Gleich implemented in his master thesis [78]. To account for the higher initial demagnetization in 1.55 eV and 3.1 eV, we assumed a five times higher spin-flip probability for the first 100 fs [24].

Recently, investigations found that the two-temperature model (2TM) is insufficient to describe the electron-phonon coupling and the energy flow in a metallic system [146, 147]. The studies report that a separation of phonon branches with individual electron-phonon coupling constants is needed [146] and that the initial phonon distribution is non-thermal [147]. These aspects add to the notion that the initial excess energy of the photoelectrons can affect the magnetization dynamics on the sub-ps time scale.

In the previous section we discussed the hybridization of the $4f$ and $5d6s$ states in XMCD and their imprint on the XMCD dynamics. Under this assumption, different dynamics for different pump photon energies in XMCD would imply some variance in the valence band dynamics in photoemission spectroscopy (PES) measurements for different pump photon energies. We have measured PES data on the magnetization dynamics in Gd/W(110) using 0.95 eV and earlier measurements using 1.55 eV exist [77, 129]. Unfortunately, the experimental uncertainties are too large and different parameters were used in those data sets, like the absorbed pump laser fluence which also affects the dynamics (see Section 5.3), to draw conclusions about the subtle pump photon dependence of the 100 fs dynamics.

4.4 Summary

In summary, we have investigated the applicability of XMCD in reflection as a probe for the magnetization of a single-crystalline Gd/W(110) thin film. In comparison to absorption measurements, the reflection signal provides higher magnetic contrast and overall intensity at the small incidence angle of 4.5°. Both signals, the reflection at 4.5° and the absorption measured via the drain current, follow the Gd Brillouin function in temperature-dependent measurements. Thus, we conclude that XMCD in reflection is an equivalent probe of the sample magnetization in static measurements in thermal equilibrium.

In time-resolved measurements we observe a two-step demagnetization with time scales of about 1 ps and a few tens of ps, varying with incident pump laser fluence. The two-step demagnetization confirms earlier XMCD measurements on polycrystalline samples [23] and MOKE data on single-crystalline sample [128]. However, the two time scales in the $4f$ dynamics measured in XMCD contradicts the single-step demagnetization on a time scale of 14 ps observed in ARPES measurements [22]. Interestingly, the exchange splitting of the $5d6s$ valence bands occurs on a sub-ps time scale [22, 129, 130].
We developed an idea to reconcile the observations which assumes a hybridization of the unoccupied $4f$ state with the $5d6s$ states. We find a shift of the minority-spin $4f$ state towards the Fermi level upon creation of the $3d$ core-hole during the X-ray absorption enabling such a hybridization. By hybridizing the density of states available for the $3d$-$4f$ transition would be altered due to the $5d6s$ contribution and the dynamics of the valence bands could be imprinted upon the measured $4f$ magnetization dynamics in XMCD. Clearly, this picture requires a better theoretical understanding of the hybridization and its influence on the XMCD probing process.

For varying pump laser fluences we see a fast, similar demagnetization time scale of less than 1 ps and a slow, increasing time scale from a few to about a hundred ps. Additionally, the point of minimum magnetization shifts towards later pump-probe delays with increasing pump laser fluence. Using an extended M3TM by Unai Atxitia we are able to model these fluence-dependent dynamics in Gd and supplement an extensive test for the M3TM for a type II ferromagnet. The applicability of the extended M3TM for systems with non-vanishing orbital momentum is still under investigation.

The fluence dependence on the two time scales shows interesting results. On the fast time scale, we find an exponential dependence of the magnetization on the pump laser fluence implying the impossibility to demagnetize pure Gd on that time scale. Surprisingly, in alloys Gd was found to demagnetize and even revert its magnetization within picoseconds [6, 141].
On the slow time scale, the magnetization follows a double-linear trend with a slowing down of demagnetization at high fluences above about $7.5\,\mathrm{mJ/cm^2}$. The spin-flip efficiency seems to lessen at high fluences and the related high disorder in the spin system, but we are still lacking a complete picture for the double-linear trend.

Demagnetization measured at the Gd M_5 and M_4 absorption edges shows similar dynamics except for the recovery phase. Without availability of sum rules for reflection an interpretation of changes in L and S to the total momentum is only preliminary, but the similarity in the dynamics suggests no significant changes during demagnetization in Gd.

Finally, pump photon energy-dependent measurements show a slower and reduced demagnetization on the fast time scale at low pump photon energy suggesting an influence of the initial hot electron distribution before thermalization to play a role either for spin transport or spin-flip scattering probabilities.

Chapter 5

Optically Induced Spin Transfer Between Bulk and Surface States in Gd

In a recent study Andres *et al.* [131] found a clear distinction in the demagnetization of Gd when heated thermally or laser-induced. In the former case the spin polarization drops to zero with increasing temperature, while in the latter case the spin polarization does not fall below 90 % of the initial value. In particular, the changes of spin polarization and exchange splitting occur simultaneously in the thermal case, while the change of spin polarization is slower by one order of magnitude than the reduction of exchange splitting in the laser-induced case. This result indicates that the nearly sudden non-equilibrium caused by the ultrashort pump laser pulse can produce states that do not occur when the whole system, comprised of the electron, phonon and magnon subsystems, stays in thermal equilibrium.
Thus, we wanted to observe if or to what extent the dynamics can be influenced already on very short time scales of below 100 fs, where even the electron subsystem is not yet equilibrated [34], or if an excitation of a coherent state occurs which affects the magnetization.

This chapter begins with some preliminary work from an earlier project in which Dr. C. Gahl and Prof. M. Weinelt of our group have been involved. The theory group of the collaboration developed a model of a coherent state right after excitation which provides a channel for angular momentum transfer between the localized and itinerant electrons in Gd. It predicts that the coherence time of the state increases for low excitation energies motivating an investigation of the dynamics using low pump photon energies and high time resolution. Following is a section introducing static measurements of Gd/W(110) thin films and technical details of the data evaluation. In the next section, we will discuss and evaluate the laser-induced dynamics of Gd/W(110) which show an unexpected increase of the exchange splitting during the first 100 fs. In Section 5.3.1 we will cover a theoretical work by Dewhurst *et al.* from S. Sharma's group [148], which explains magnetization dynamics in an antiferromagnet by spin-selective charge flow between magnetic sublattices. Afterwards, we will adapt this idea for our system and discuss the temperature dependence of the effect looking at the spin polarization of the involved states and how this affects possible charge transfer channels.

5.1 Preliminary Work - Coherent Excitation Model

In this section we will pick up on a model developed within an earlier collaboration in which Dr. C. Gahl and Prof. M. Weinelt of our group have been involved. This model provides a further motivation for investigating Gd on very short time scales below 50 fs using low pump photon energies. The experimental results of the collaboration are published in [23]. The theoretical model provided by A. I. Lichtenstein, T. O. Wehling and M. I. Katsnelson has not been published independently but has been put on record in the PhD thesis of M. Wietstruk [92].

The model describes the final state right after laser excitation of a Gd ion. It is assumed, that a valence electron absorbs the laser pulse and undergoes a spin flip, supposedly via spin-flip scattering with phonons. Thus, the initial excitation would lead from state $|{+1/2},{+7/2}\rangle$ to state $|{-1/2},{+7/2}\rangle$. However, $|{-1/2},{+7/2}\rangle$ is not an eigenstate of the system with total spin $M_S = 3$ and therefore a coherent superposition of the two states $\alpha\,|{-1/2},{+7/2}\rangle + \beta\,|{+1/2},{+5/2}\rangle$ evolves, with transition probabilities $|\alpha|^2$ and $|\beta|^2$, see Fig. 5.1a.

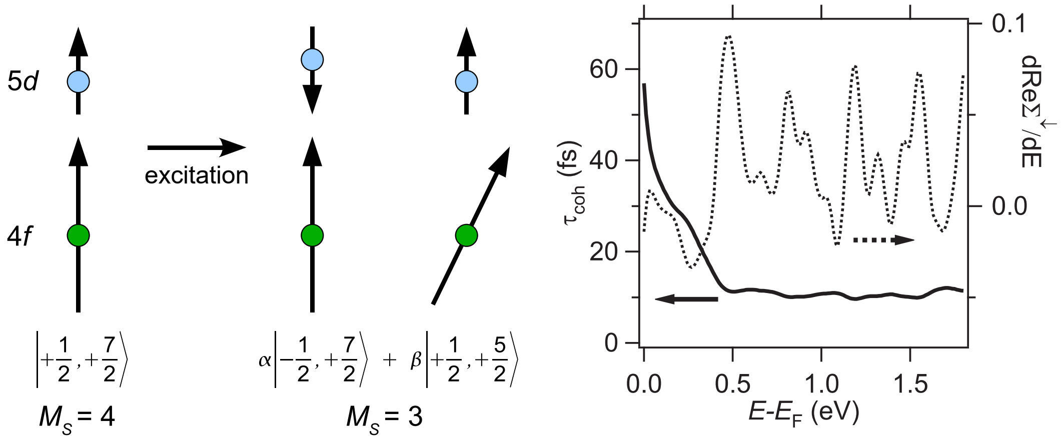

(a) Coherent excitation state **(b)** Coherence time and self energy

Figure 5.1: Coherent excitation model for laser-induced dynamics in Gd. (a) Initial state before and final state after laser excitation in Gd. The state $|{-1/2},{+7/2}\rangle$ is not an eigenstate of the system, thus the final state is a superposition of $|{-1/2},{+7/2}\rangle$ and $|{+1/2},{+5/2}\rangle$ (b) Coherence time τ_{coh} of the excited state in (a) and self energy $\mathrm{dRe}\Sigma^{\downarrow}/\mathrm{dE} \propto \beta$, dependent on electron excitation energy. The coherence time significantly increases for electron energies below 0.5 eV. Images (a) and (b) taken from [92].

This coherent state has a coherence time τ_{coh}, after which it collapses into a magnon, which depends on the energy of the excited electron, *c.f.* solid line in Fig. 5.1b. We see, that for electrons of energies below 0.5 eV above the Fermi energy the coherence time significantly increases above 10 fs.

The process describes a direct transfer of angular momentum from the excited valence electrons to the local $4f$ moments, which are not directly affected by the laser pulse. This transfer of momentum opens a very fast channel of demagnetization for the $4f$ states. The probability for this case scales with $|\beta|^2$ which is proportional to the term $\mathrm{dRe}\Sigma^{\downarrow}/\mathrm{dE}$, that reflects the contribution of spin-flip scattering processes to the self-energy of the valence electrons Σ. For low-energy electrons, the probability to collapse into a magnon is small, see dotted line in Fig. 5.1b, which is unfortunate in terms of experimental detectability.
Evidence for the coherence excitation model could manifest *e.g.* in the form of a little reduction of magnetization of the $4f$ moments on the time scale τ_{coh}. We hence performed experiments at the Artemis lab of the Cental Laser Facility (CLF) of the Rutherford Appleton Laboratory in the UK which provides low pump photon energies and very good time resolution in order to look for such effects.

5.2 Static Measurements and Data Evaluation Procedure

We recorded time-resolved photoemission data on single-crystalline Gd/W(110) thin films at the Artemis lab, see Section 3.3.2 for more details regarding the experimental setup. We used infrared (IR) pump and extreme ultraviolet (XUV) probe laser pulses from a high-harmonic generation setup to trigger and probe the dynamics and a time-of-flight (ToF) analyzer to detect the photoemitted electrons. Because of the latter, the data has to be converted from time to energy units before further evaluation and fitting. In this section, we will go into the details of how we process the data to obtain the results presented in Section 5.3 and what difficulties arise in the evaluation.

5.2.1 Evaluation Procedure

The raw data was evaluated using a self-written Python script. The first step in data evaluation is to calibrate the relation between the detected arrival time of the electrons and their kinetic energy. For this, we simplistically approximate the flight time as only a drift through the drift tube of the ToF analyzer. This is justified in so far, as the electrons are decelerated before entering the drift tube and accelerated again towards the detector behind the drift tube. Thus, the drift in the drift tube constitutes the by far biggest part of the total flight time. The other contributions are effectively taken into consideration by a larger drift tube length parameter in the fit (typically of the order of 10 %) than the real length of the tube.

The calibration itself is performed by measuring the arrival times of electrons from the Fermi level for a set of bias voltages U_{bias} between sample and analyzer on top of the retarding potential. In that way, we obtain a series of flight times for a range of kinetic energies and can fit the data with the classical relation:

$$t_{\mathrm{ToF}}(U_{\mathrm{bias}}) = l_{\mathrm{ToF}} \cdot \sqrt{\frac{m_e}{2e(U_{\mathrm{bias}} - e_0)}} + t_{\mathrm{tdc0}} \tag{5.1}$$

with the electron mass m_e and the electron charge e. The fit parameters are the ToF length l_{ToF}, the time-to-digital converter (TDC) offset t_{tdc0}[1] and e_0, the electron kinetic energy minus the retarding potential. With these parameters we convert the recorded time axis of each measurement into a corresponding energy axis.

To minimize uncertainties in the calibration several combinations of parameters were tested. For example, the TDC offset can vary for the different bias voltages or time steps in the time-resolved data by a few ns which already makes a visible change in the converted spectra. Especially, the conversion was chosen such, that the Fermi level of the spectrum was located in the flank of the surface state peak at about 200 meV which is the surface state binding energy given in literature [131], *cf.* Fig. 5.2.

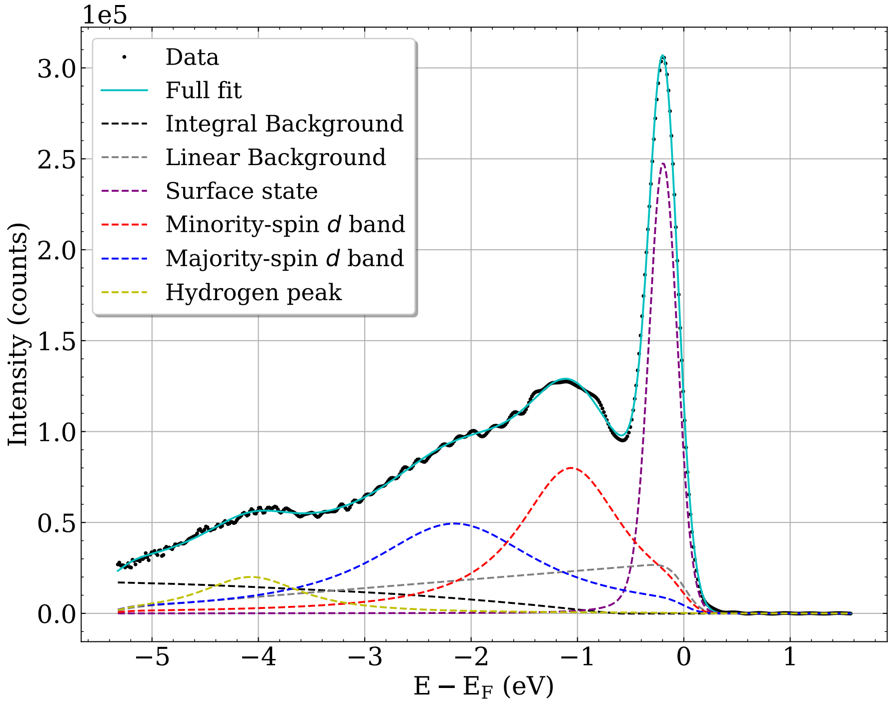

Figure 5.2: Static photoemission spectrum of a Gd/W(110) thin film. The fit consists of a sum of four Lorentz peaks multiplied with a Fermi edge and convolved with a Gaussian distribution. Added are a linear background accounting for electron-phonon scattering contributions and an integral over the spectrum as a Shirley-like background.

---

[1] The TDC offset is the time between the triggering of the TDC timer and the detection of scattered light from the sample, which can be approximately taken as the time when the electrons are photoemitted and their flight towards the detector begins.

The recorded spectra were Fourier-transformed and, if high-frequency noise *e.g.* from the TDC was present, a low-pass filter applied. The data sets were plotted and analyzed only in the energy range containing the relevant features. The mean signal intensity of the spectra between 1 eV and 1.5 eV above E_F was subtracted as a constant background, as at these energies only counts from the background are expected (see Fig. 5.2).

To determine time zero t_0, the temporal overlap of the pump and probe pulses, we looked at the hot electron dynamics between 0.25 eV and 0.5 eV, see Fig. 5.3a. The sharp increase and following decay of the electron population was fitted with an error function times an exponential decay, see Eq. (5.2) and Fig. 5.3b, and the error function position parameter was taken as time zero.

$$I(t) = \frac{1}{2}\,\mathrm{erf}\left(\frac{-(t_0 - t)}{w} + \frac{1}{2}\right) \cdot a \cdot \exp(-b \cdot t) + c \tag{5.2}$$

The pump-probe overlap t_0 is the time when pump and probe pulses arrive at the sample at the same time. The parameter w is proportional to the width of the error function, a is the amplitude, b the exponential decay constant and c the offset.

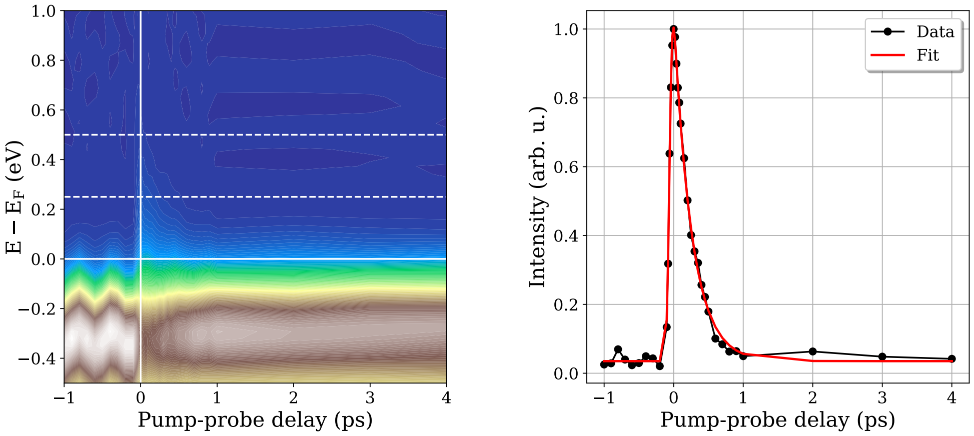

(a) Raw data of Gd/W(110) **(b)** Hot electron dynamics

Figure 5.3: (a) Raw-data image plot of Gd/W(110) pumped with 1300 nm. The region between the dashed lines is integrated over energy and used for the determination of the pump-probe overlap. (b) Dynamics of the hot electrons in the energy range in (a). The fit function Eq. (5.2) yields the pump-probe overlap t_0. The pump-probe delay and energy axes used here are a first approximation and need to be corrected for t_0 and E_F respectively for the following evaluation.

Due to the transformation of the equidistant time axis into an energy axis, the spectra have a non-uniform point density. But to avoid artifacts in the following fitting procedure (in the integration and convolution steps), a uniform point density is desirable. Thus the data was interpolated in the reduced energy range.

The fitting function can be regarded as consisting of three components, *cf.* Fig. 5.2. First, for the background, in approximation of a Shirley background, a cumulative integration from highest to lowest kinetic energies is performed using the composite trapezoidal rule. The resulting integral is normalized to 1 and its magnitude fitted as a global parameter for all time steps in the time-resolved measurements. For the integration, a uniform point density is necessary. Additionally, reflecting the rising density of states towards the Fermi level in Gd, a linear background is added to account for contributions from other k-points arising from electron-phonon scattering [77, 149]. Second, the features of the spectrum are fitted with a sum of four Lorentz peaks multiplied with a Fermi edge function to map the Gd surface, minority- and majority-spin bulk states and a peak arising due to very small hydrogen contamination.
Lastly, the second component is convolved with a normalized Gaussian distribution to account for the experimental resolution.

Unfortunately, we have only an estimate of the lower limit of about 120 meV[2] for the experimental resolution due to the high-harmonic bandwidth and the chosen opening of the exit slit. For instance, contributions from the large acceptance angle of the ToF analyzer need to be considered. From Fig. 5.2 we see that the resolution is lower, thus we need to obtain a more accurate estimate by other means. With a linewidth of less than 70 meV [35, 150, 151], the surface state is suitable to assess our total experimental resolution. Thus, we fitted the surface state peak with a simple Gaussian and obtained a standard deviation of $\sigma \approx 150\,\text{meV}$, which relates to the resolution by full width at half maximum $\text{FWHM} = \sigma \cdot 2\sqrt{2 \log 2} \approx 350\,\text{meV}$. Although large, the value seems realistic considering the example spectrum in Fig. 5.2. The contribution of the Lorentzian width to the total peak width is negligible compared to the Gaussian and justifies the use of a simple Gaussian for the assessment of the experimental resolution. However, in the global fit in Section 5.3 we obtain physically more sensible results by fitting this parameter globally (instead of fixing the value to $\sigma = 150\,\text{meV}$) which results in $\sigma = (111 \pm 1)\,\text{meV}$.

Some parameters are identical for all time steps and require a global fit. As the optimization can take a long time under bad conditions, some preparatory simple fits have been performed. In the course of the preparatory fitting, various parameters for the time-energy calibration, several optimization algorithms provided by Python's lmfit library as well as several combinations of boundary conditions for fit parameters were tested before setting up the initial conditions for the global fit.

Three particular boundary conditions were implemented. First, the amplitudes respectively the areas of the Lorentz peaks were linked for all time steps before $t_0 - 10\,\text{fs}$ as before excitation the spectral features should be the same. (At $t_0 - 10\,\text{fs}$ the pump laser starts having an impact on the states.) Due to the oscillations of the peak positions caused by the ponderomotive acceleration by the self-interfering field of the IR pulse (see Chapter 6 for details) the peak areas would change periodically if unbound. Additionally, the areas of the minority- and majority-spin bulk states were kept identical for each time step, as the peaks arise from the same exchange split state and should have the same population. Lastly, all parameters of the peak attributed to hydrogen contamination were fitted globally.

---

[2] The number was given to us by the local experimental team.

Second, the temperature parameter of the Fermi edge was fixed to 50 K before $t_0 - 10\,\mathrm{fs}$. 50 K is set, as this is the sample temperature in equilibrium.
If not fixed for small delays, the temperature parameter hits the lower boundary (tested down to 5 K) being unrealistic and preventing the determination of statistical errors within the fit. The difficulty of the temperature fit lies in the experimental resolution, as the Gaussian broadening of 350 meV is significantly larger than the temperature broadening of the Fermi edge (25 meV at 300 K). Only high temperatures can be extracted reasonably well from the fit.

Lastly, the position of the Fermi level was fixed to the peak position of the surface state by $E_\mathrm{F} = x_\mathrm{surf} + 200\,\mathrm{meV}$ for negative delays, where we use the surface state binding energy of 200 meV determined in [131]. For positive delays, E_F was set to the center energy of the oscillations before time zero. This limitation was necessary, as the correlation between the Fermi level and the surface state peak parameters is very strong and the Fermi level could not be reliably determined without the relation to the surface state.

After a global fit, the oscillations in the spectra necessitate to determine a constant Fermi level before t_0 as a suitable reference for the binding energies of the Gd states. A sinusoidal fit of the Fermi level up to t_0 using Eq. (6.5) was performed and its offset provided the constant Fermi level.

All individual fits for all pump-probe delays are shown in Appendix B.1.

5.2.2 Gd Surface and Bulk States

Figure 5.2 shows an exemplary spectrum of a 10 nm Gd/W(110) thin film probed with 34.2 eV laser pulses (23. harmonic) at a temperature of about 50 K. We used a ToF analyzer in angle-integrated mode and focused the detection around the Γ point. With an acceptance angle of about 3° and photon energies of 34.2 eV, we have a large integration range in k-space of $0.15\,\mathrm{\AA}^{-1}$, which is in accordance with the peak widths of the states we measure. The acceptance angle affects the peak width of states in the photoemission spectra due to band dispersion, in addition to the experimental resolution. The four defining features in the spectrum are, with decreasing energy, the surface state, the minority- and majority-spin valence bulk band and a peak arising from hydrogen adsorbates. Figure 5.4 shows an overview of the Gd states with a comparison to literature values. We extract binding energies for the Gd states close to the literature values [152, 153], but find deviations. It is striking, that the deviations are not equal for all states as one might expect from many experimental causes like wrong detector settings or simple calibration offsets. Possibly, an elaborate interplay of several causes could give rise to the observed small deviations, like the involved time-to-energy calibration described in the previous Section 5.2.1 together with faulty detector settings.

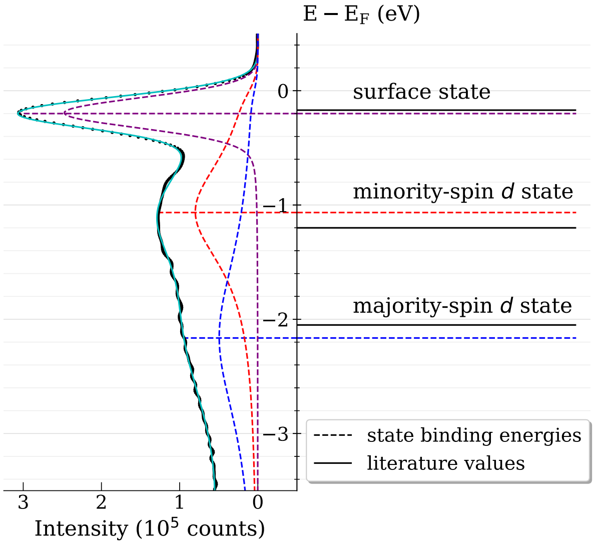

Figure 5.4: Left: Static photoemission spectrum of a Gd/W(110) thin film. It is a part of the spectrum depicted in Fig. 5.2 with a focus on the peak positions. Right: Energy diagram showing the fitted Gd state binding energies in comparison to literature values (surface state binding energy extracted from [152], *d* states from [153]).

The Gd surface state has its origin in the bulk $5d_{z^2}$ non-bonding state due to a reduction of kinetic energy in the vacuum region in front of the surface [154]. It has $5d_{z^2}$ character and is strongly localized at the surface in all space directions with the „dumbbell“ oriented along the surface normal [154], 70 % of the charge density being within the surface layer and the vacuum region [72]. The surface state lies in the band gap around Γ [155] and is split due to exchange interaction with the localized $4f$ moments, the majority-spin part being energetically located about 180 meV below and the minority-spin part about 470 meV above E_F [151]. The experimental exchange splitting at about 100 K varies in the range 580–700 meV [151, 156–158]. The state's spin polarization was found to be about 65 % at 100 K [159].

Both, in thermal equilibrium and non-equilibrium the surface state shows interesting magnetic behavior. In thermal equilibrium, the surface state was observed to behave Stoner-like [152] but also a spin-mixing behavior was reported [160]. In following studies, it was found that the surface state spin polarization breaks down at T_C, but a finite and significant exchange splitting persists [131, 152, 158, 161]. In laser-induced experiments effects acting on three major time scales were identified [162]. Within the first 70 fs, the laser pulse depopulates the surface state which leads to a local demagnetization of the surface as the electrons leaving the state are spin-polarized. On a time scale of 0.6 ps, electron-phonon interaction dissipates energy out of the surface state causing a shift of the binding energy according to a global demagnetization in the Stoner picture. Finally, on a time scale of 15 ps, the state's spin polarization declines entailing a further demagnetization.

The Gd bulk bands show several similarities in the magnetic properties to the surface state. The hybridized $5d6s$ valence bands become exchange split into minority- and majority-spin bands via intra-atomic coupling to the local $4f$ moments. In literature, the exchange splitting of the bulk bands in Gd is between 850–1000 meV [130, 159, 163], but varies with temperature [153]. At 100 K, the spin polarization of the bulk states resembles that of the surface state with about 65 % [159]. Likewise, the aforementioned persistence of residual exchange splitting above T_C exists in the bulk states as well [77, 159, 161]. Frietsch and co-workers observed the peak width of the bulk state at 35 K above T_C and found a decrease of the width upon laser pumping indicating a non-collapsed exchange splitting before excitation. They remark that the fast reduction of peak width indicates a spin transport effect rather than spin-flip excitations.

The valence states reflect bulk magnetic properties insofar as the exchange splitting is related to the magnetic order on the coherence length of the corresponding electrons [77]. The coherence length in metals in turn is bounded by the mean free path of the valence electrons, which is up to a few tens of nanometers [9]. For Gd we find coherence lengths of the bulk bands of about 30–40 Å [22], *i.e.* about 10 layers into the bulk. So, even with an escape depth of only 2–3 layers in photoemission, the electrons embody bulk properties. As an additional consequence, the exchange splitting should persist so long as there is magnetic order on the length scale of the coherence length even if long-range magnetic order, *e.g.* because of domain formation, is broken. Conversely, if the exchange splitting decreases, it indicates that some interactions like spin mixing, spin-flip scattering or spin transport disturb the short-range magnetic order. One has to be careful with interpreting the exchange splitting, though.

As B. Frietsch discussed in his PhD thesis [77], in general, the exchange splitting is not a direct measure of the magnetization. An example thereof are the theoretical curves in [22] for the $5d$ magnetization and the $5d$ exchange splitting. The two curves deviate a few ps after laser excitation. Still, the exchange splitting can be computed *ab initio* from $4f$ and $5d$ magnetic moments obtained from spin dynamics simulations. Thus, there is a relation between the two quantities and the information content can be mutually extracted.

In addition, a comparison between the measured equilibrium and non-equilibrium signal is difficult, as in the latter case other transient phononic, optical or electronic effects can add to magnetic changes. For instance, in [131] the authors found a different spin polarization for the same exchange splitting under thermal equilibrium and non-equilibrium conditions. Moreover, as mentioned above, exchange splitting is only a probe of local magnetic order. The depopulation of states, spin currents, transient lattice strains combined with magnetostriction and transitions resonant to the laser excitations do not change the global magnetization but do affect the exchange splitting [77].

The last peak stems from adsorbed hydrogen on the Gd surface [22]. Lanthanides, being excellent getter materials, easily adsorb residual gas on the surface. Hydrogen is difficult to pump and thus a common impurity. In addition to decreasing the surface state intensity, there is indication that the surface magnetism in Gd is affected by this contamination [85].

In the following section we will take a look at our measured laser-induced dynamics in Gd/W(110), first bringing it into context with previous measurements and then focusing on the dynamics happening within the first 100 fs after excitation.

5.3 Magnetization Dynamics Upon Near-Infrared Laser Excitation

To measure the data set presented in this section, we used 1300 nm s-polarized pump pulses to induce the magnetization dynamics in the Gd/W(110) sample. The IR pump pulses were incident under 65° to the sample normal with a duration of 40 fs. We probed under normal emission with 34.2 eV XUV pulses of 30 fs duration, yielding a cross-correlation of 50 fs. The incident pump fluence could not be well reproduced, but we estimate it to be about $7.6\,\mathrm{mJ/cm^2}$. The difficulty in determining a pump fluence will be addressed in Section 6.2.1, where the pump fluence plays a more decisive role for the physics discussed than in this section.

Using the procedure described in Section 5.2.1 we extract the surface state and valence band dynamics from the raw data, see Fig. 5.5. The very prominent oscillations before time zero arise due to a ponderomotive acceleration of the emitted electrons in the transient standing wave field created by the interference of the reflected and incoming pump laser pulse and will be discussed separately in Section 6.2. In this section, the focus lies on the dynamics after time zero.

Surface-State Dynamics

We begin with the surface state dynamics. In Fig. 5.6, the surface state binding energy shifts towards E_F before reaching a near steady state around -0.14–-0.15 eV a few ps after laser excitation. This behavior is mostly in line with former measurements.

Carley *et al.* [129] published data showing the surface state shifting by about 50 meV on a time scale of their experimental resolution of about 300 fs after pumping with[3]

---

[3] The pump fluence has later been corrected to about $5.5\,\mathrm{mJ/cm^2}$, *cf.* data in [130].

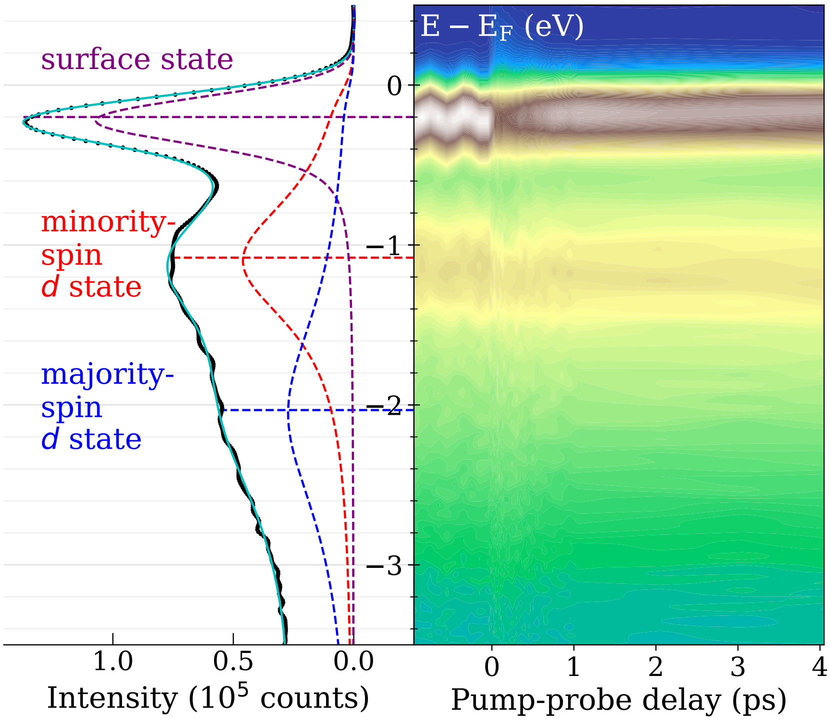

Figure 5.5: Spectrum of Gd/W(110) at $\Delta t = -1\,\mathrm{ps}$ extracted from the raw-data image plot on the right. The pump laser wavelength is 1300 nm. After time zero, a depopulation of the surface state is clearly visible.

$1.2\,\mathrm{mJ/cm^2}$. With a pump fluence of $1.0\,\mathrm{mJ/cm^2}$ and a peak position shift of about 40 meV, Loukakos *et al.* [35] fitted a continuous shift over about 2 ps. Finally, in data published by Andres *et al.* [131] the surface state peak position reaches a near steady state after about 2 ps (time constant of the exponential fit is 0.6 ps), like Loukakos *et al.*, but the applied pump fluence of $3.9\,\mathrm{mJ/cm^2}$ and the magnitude of the shift of 90 meV are much larger.

To compare our data quantitatively, we need to find a suitable fit function. We compare fit results for the two following single- and double-exponential functions with decay constants τ_i, amplitudes a_i, offsets b_i and the heavyside function $H(t)$:

$$E_{\text{single}}(t) = H(t) \cdot a_0 \exp\left(-\frac{t}{\tau_0}\right) + b_0 \tag{5.3}$$

$$E_{\text{double}}(t) = H(t) \cdot a_1 \exp\left(-\frac{t}{\tau_1}\right) \cdot a_2 \exp\left(-\frac{t}{\tau_2}\right) + b \tag{5.4}$$

With the naive choice of a single exponential function (Eq. (5.3)) and in line with the functions used in the literature [131], we find a time constant of (300 ± 160) fs and a shift of (49 ± 10) meV. However, the trend of the surface state is not well captured, *c.f.* cyan curve in Fig. 5.6. It starts off too shallowly in the first 150 fs before overshooting around 650 fs and reaching a too low steady state.

For a better result, a double exponential function (Eq. (5.4)) is necessary. A second, fast time constant is justifiable as we assume a transport effect between the majority-spin bulk band, which shows a rapid drop right after excitation, and the majority-spin surface state. This effect will be discussed in more detail in Section 5.3.1. Using the double exponential function and setting the fast time constant equal to the fast time constant of the majority-spin bulk band we obtain values of (34 ± 12) fs and (0.92 ± 0.76) ps with a total shift of (60 ± 16) meV, *c.f.* black curve in Fig. 5.6.

Leaving the fast time constant parameter free yields time constants of (7 ± 16) fs and (0.75 ± 0.43) ps with a total shift of (60 ± 12) meV, *c.f.* orange curve in Fig. 5.6. This even better fit comes at the price of being less justifiable physically as the connection to the majority-spin bulk band dynamics is reduced. In addition, the uncertainty of the first time scale is tremendous, possibly related to the strong correlation of the two time scales.

All in all, our results corroborate the shift of the peak position on time scales of around a ps, although the exact value depends on the fit function chosen. The sensitivity of the time constants upon one another prevents pinpointing exact numbers for both time scales.

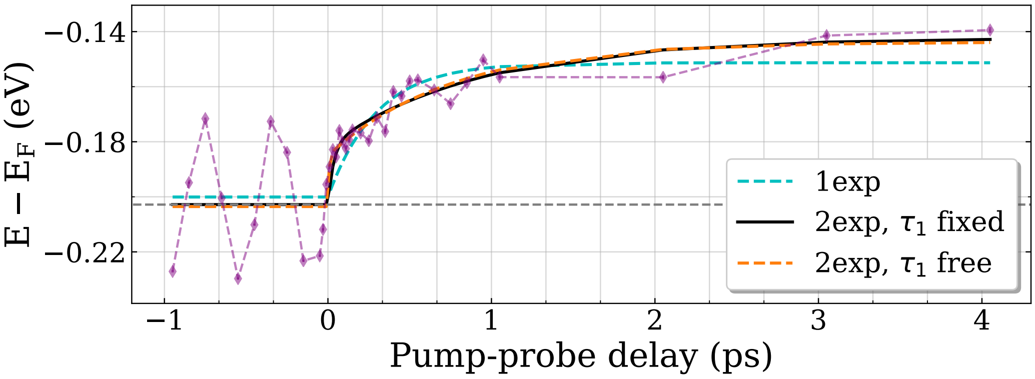

Figure 5.6: Dynamics of the Gd/W(110) surface state after pumping with 1300 nm. A single-exponential fit does not reproduce the dynamics well (cyan). The double-exponential fits reveal a fast component in the dynamics. As discussed in Section 5.3.1, we can associate this fast component with the corresponding dynamics in the majority-spin *d* state. Setting the fast time scale equal to the majority-spin *d* state time constant (black) yields a fit which is mapping the experimental data similarly well as a fit with a free first time constant (orange).

Unfortunately, we could not adequately determine our absorbed pump fluence, but we can deduce it reasonably well from the oscillations before time zero to be about

1.3 mJ/cm^2, see Chapter 6. The so determined pump fluence also agrees with respect to the amount of decrease of the 5*d* exchange splitting, since we observe only a reduction down to 90 % (see Fig. 5.9) while Frietsch *et al.* [22] report a reduction down to 75 % with a higher absorbed pump fluence of 3.5 mJ/cm^2.

Nevertheless, the step from a single to a double exponential is significant and we can clearly identify that an additional process is happening on this fast time scale. The shift of the peak position supports results found by Andres *et al.* [131]. In the publication the authors observe a time scale of 70 fs for the rising edge of the hot electron population. They deduce from the high spin polarization of the state and its fast depopulation that a demagnetization of the surface state occurs at this sub-100 fs time scale.

The demagnetization process occurs already on time scales of electron thermalization [162]. The hot electrons thermalize by exchange scattering which equalizes the hot electron population in terms of spin polarization. However, the laser pulse initially excites carriers from the majority-spin surface state, thus the first generation of hot electrons, before undergoing scattering, is spin polarized. Those carriers could efficiently demagnetize the surface by superdiffusive spin transport as proposed by Battiato *et al.* [9]. A related depopulation of the majority-spin surface state was observed in [129, 131], which is similar to the decrease of intensity of the surface state peak in our measurements, *cf.* raw-data plot in Fig. 5.5 and the gray shaded area in Fig. 5.7.

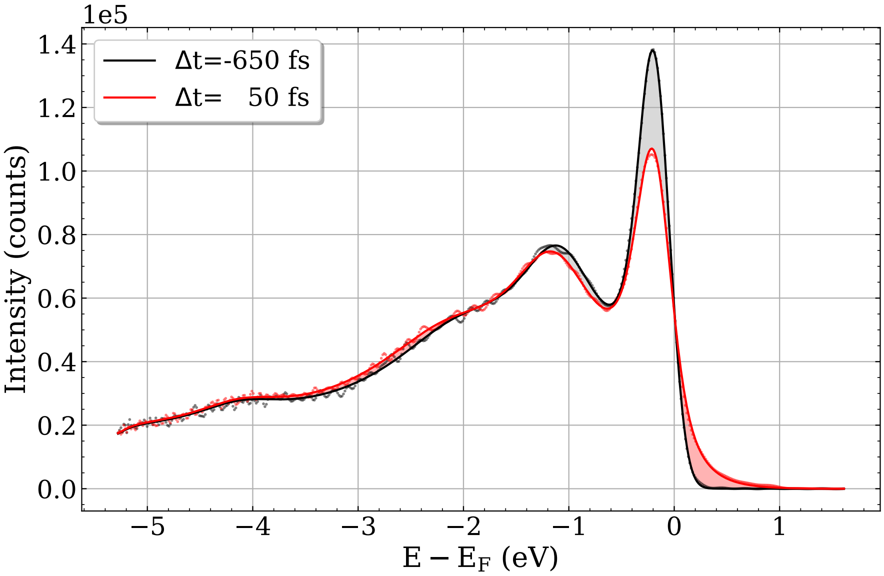

Figure 5.7: Spectra of Gd/W(110) recorded at $\Delta t = -650$ fs (black) and $\Delta t = 50$ fs (red). Upon laser excitation the surface state intensity is reduced (gray shaded area) and a hot electron distribution forms above E_F (red shaded area).

Bulk-State Dynamics

In contrast to the surface state, the minority- and majority-spin bulk states show a dip towards higher binding energies before shifting back towards the Fermi level, see Fig. 5.8. For both states, the dip minimum is reached within 100–200 fs after laser excitation. However, the majority-spin band initially drops more abruptly than the minority-spin band (the time constants are (34 ± 13) fs vs. (83 ± 45) fs) leading to an effective increase in exchange splitting, see Fig. 5.9. On time scales of (430 ± 90) fs (majority-spin) and (290 ± 160) fs (minority-spin), both bands start shifting to lower binding energies ending in a quasi-static binding energy lower than (majority-spin) or similar to (minority-spin) before excitation. While doing so, the majority-spin band shifts to a larger extent resulting in a net reduction of exchange splitting, *i.e.* a demagnetization, see Fig. 5.9.

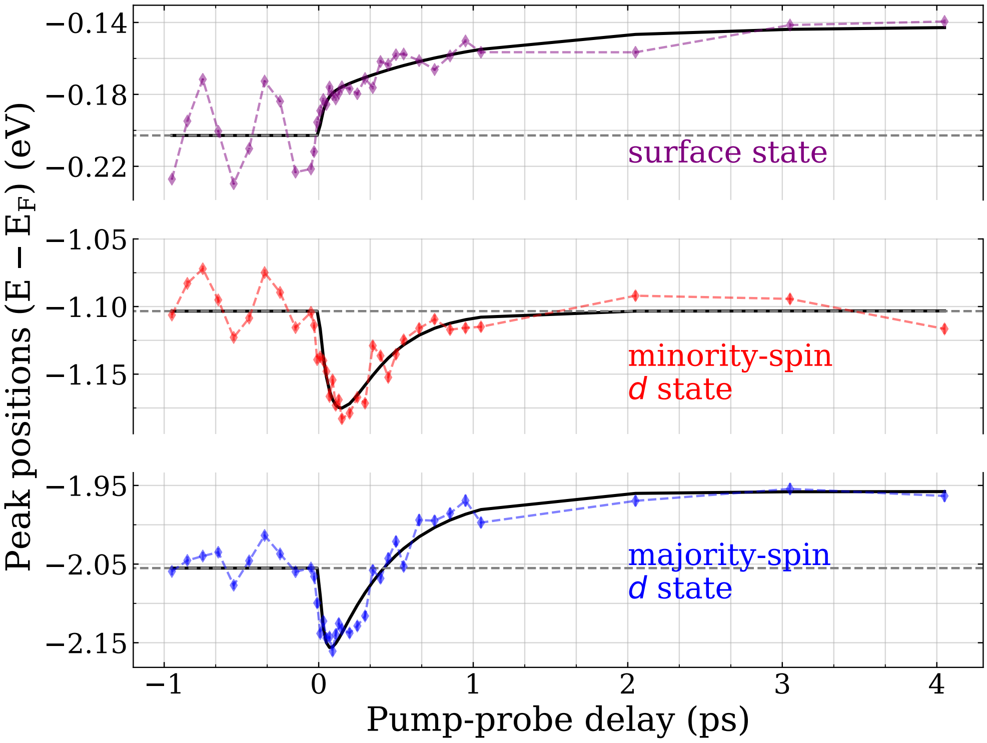

Figure 5.8: Dynamics of the Gd majority-spin surface and minority- and majority-spin bulk states. The oscillations before time zero are discussed in Section 6.2. A remarkable feature is the dip in the binding energies of the bulk states right after time zero.

The demagnetization time scale of about (400 ± 80) fs is smaller than the time constant of 0.8 ps observed in [22], but presumably the absorbed pump fluences differ significantly in both experiments (3.5 mJ/cm^2 in [22] versus estimated 1.3 mJ/cm^2 in our measurements). As B. Frietsch analyzes in his PhD thesis [77], the time constant decreases with decreasing pump laser fluence, which could account for the different demagnetization times. In addition, the sample temperature impacts the demagnetization time [25], thus the different temperatures in [22] and our recent measurement (100 K versus 50 K) could contribute to the different observed time constants.

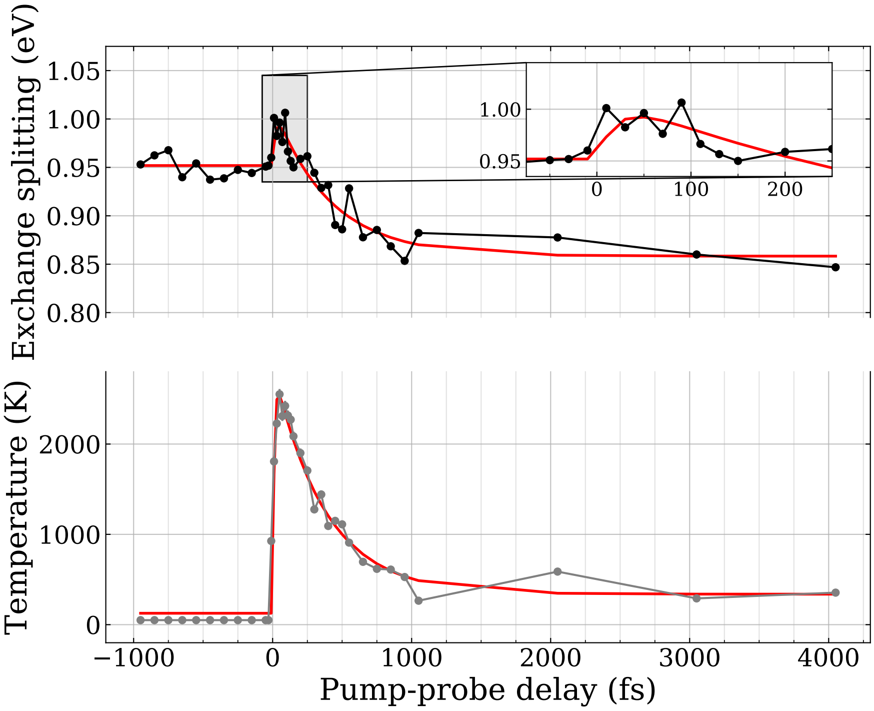

Figure 5.9: Exchange splitting (top) and electron temperature (bottom) over pump-probe delay. The 5d6s valence band exchange splitting in Gd/W(110) increases right after laser excitation for a few 10 fs before decreasing with a time constant of 400 fs. The inset is a zoom of the region where the exchange splitting increases. The fit does not fully capture the trend in the data, but allows to estimate a time constant for the rise. The electron temperature was fixed to 50 K 10 fs before laser excitation.

For several aspects of the magnetization dynamics in Gd a certain understanding of the physics exists, especially regarding time scales above 100 fs.[4] The 5d6s electrons need around 2 ps before equilibrating with the phonon system [129]. This is reflected in different minority- and majority-spin binding energies for the same exchange splitting during demagnetization and the later remagnetization, which happens in thermal equilibrium. Moreover, despite the strong intra-atomic coupling to the 4f moments, the

---

[4] A thorough study on the Gd 5d6s dynamics is described by B. Frietsch in his PhD thesis [77].

$5d6s$ spin system decouples from the $4f$ moments upon laser excitation on a ps time scale [22] implying that the $5d6s$ spins do not instantly align with the strongly localized $4f$ moments.

Apart from the dynamics of the $5d6s$ exchange splitting, the individual minority- and majority-spin bands show interesting asymmetric dynamics [129]. In a simple Stoner picture one would expect a symmetric energy shift of the two bands, which is not the case for Gd, where the majority-spin band shifts by a larger amount. Apparently, as reported by Sandratskii [155], at large k values the minority- and majority-spin bulk states become energetically close and hybridize which leads to spin mixing in the bands. Then the Stoner model becomes inapplicable and the bands can shift by unequal amounts. For Sandratskii's slab calculations [155], which better model experimental thin films than a bulk structure, the surface projection of the bands along the surface normal direction makes the spin mixing contribution already relevant at Γ, which was experimentally observed by Carley *et al.* [129].

In addition to unequal energy shifts, the dynamics of the majority-spin band upon laser excitation start with a delay and are slower compared to the minority-spin band [77, 129, 130]. Several explanations were proposed by different groups.
Sandratskii [155] speculates, that the laser-induced non-equilibrium distribution of electrons between surface and bulk might affect the $5d6s$ contribution to the spin-polarized potential, and thereby the energetic position of the bands. This distribution counters the effect from noncollinearity of the $4f$ moments, a main factor for the energetic position of the states.
In contrast, Carley *et al.* [129] explain the delay by an asymmetric magnon emission probability for the minority- and majority-spin state when they transfer a spin flip to the $4f$ system via exchange interaction. A spin flip in the minority-spin band is of majority-spin character and can be hardly transferred to the $4f$ system, as the latter is already nearly saturated with electrons of majority-spin character.

Finally, B. Frietsch [77] discusses different physical mechanisms for the shift of the minority- and majority-spin bands. Since different mechanisms underlie the dynamics of each band, this naturally leads to different time scales.
The time scales of the surface and minority-spin bulk band shifts in the measurements described in [77] are both less than 300 fs, which is below the temporal resolution of the experiment. B. Frietsch suggests, that the hot majority-spin electrons from the surface state populate the (spin-mixed) minority-spin bulk band under emission of a magnon, thereby reducing its polarization and causing a shift of the energetic position to higher binding energies. Whereas, the majority-spin bulk band shifts on a time scale of about 0.7 ps, which resembles the lattice heating time scale. This band shift can be adequately described by Elliott-Yafet-type electron-phonon scattering [15, 77].
Moreover, the two mechanisms have a different impact on the global sample magnetization. The majority-spin bulk shift entails an overall demagnetization by transferring angular momentum to the phonons in contrast to the spin-conserving redistribution of spin moments between surface and minority-spin bulk states.

Our recent measurements have several aspects in common with the above described dynamics. For instance, on the ps time scale, in our measurements the majority-spin bulk band shifts by a larger amount than the minority-spin band. But the better time resolution and lower sample temperature reveal more details, especially in the first 100 fs, that partially differ from published data.

In contrast to previous results, both bulk bands in our data exhibit similar time scales of (430 ± 90) fs (majority-spin) and (290 ± 160) fs (minority-spin), respectively. The exchange splitting decreases as one would expect due to the larger majority-spin bulk band shift. Likewise, it is remarkable, that the majority-spin state shifts so fast. This could be related to a lower pump laser fluence and sample temperature as discussed above, assuming Elliott-Yafet-type scattering to be the mechanism behind the majority-spin band shift but not the minority-spin band as discussed by B. Frietsch.

In this context, due to the faster dynamics of the majority-spin bulk band, the clear separation of time scales for the minority- and majority-spin bulk band dynamics is not apparent in our data in contrast to the data in [77]. However, our results corroborate the relation between the drop of the electron temperature ((370 ± 50) fs) and majority-spin band dynamics, despite the faster cooling of the electron temperature compared to *e.g.* [129, 131].

Apart from these irregularities, the major feature is the dip in the bulk band binding energies. Mind that the bulk band moves energetically in the opposite direction to the surface state despite equal spin polarization.

Due to the more abrupt shift in the majority-spin bulk band, the exchange splitting displays an increase during the first 100 fs, see Fig. 5.9. Simply put, this feature would correspond to a transient (at least local) increase in magnetic order, which is highly counterintuitive.
Such a transient increase in the magnetic signal was already observed in magneto-optical Kerr effect (MOKE) measurements [25], but also in the band dynamics in [77], where such a dip in the majority-spin bulk band was found to cause the increase in exchange splitting, see Fig. 5.10. In both measurements, only for low temperatures of about 50 K the transient increase in MOKE ellipticity and rotation or exchange splitting, respectively, was observed. A potential physical mechanism needs to describe this temperature dependence.

A possible mechanism explaining the increase in magnetic signal at these sub-100 fs dynamics might be the optically induced spin transfer (OISTR) that Dewhurst *et al.* [148] introduced theoretically for a Mn/Co multilayer.

5.3.1 Optically Induced Spin Transfer Applied to Gd(0001)

OISTR describes a spin transfer between different sites in a material leading to an exchange of spin moments between those sites. To explain the increase in exchange

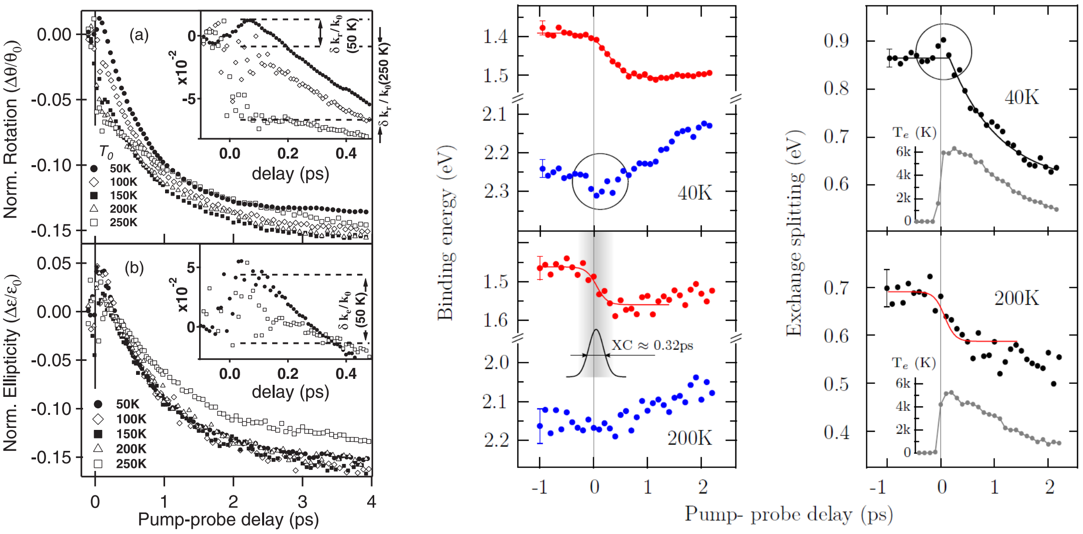

(a) MOKE signal from Gd(0001)

(b) ARPES data of Gd(0001) bulk states

Figure 5.10: Temperature-dependent time-resolved measurements of Gd(0001) showing an increase of magnetic signal at low temperatures. (a) MOKE rotation and ellipticity versus pump-probe delay. The insets highlight the transient increase in both signals for about 200 fs at 50 K. Image taken from [25]. (b) Dynamics of the Gd minority- and majority-spin bulk states at 40 K and 200 K. At 40 K, the majority-spin bulk band drops right after time zero leading to an increase in exchange splitting. This effect does not happen at 200 K. Image taken from [77].

splitting in Gd upon laser excitation, we adapt the idea of OISTR presented by Dewhurst *et al.* [148] to our system.

In their paper, Dewhurst *et al.* investigate a sample of 2 ML Mn on top of a Co substrate comprised of 4 ML, see Fig. 5.11. In the ground state, the majority spins in Co and the top Mn layer (Mn1) are oriented parallel, but the second Mn ML (Mn2) couples antiferromagnetically to the system. They show that, upon laser excitation, the spin orientation in the Mn2 layer switches within 25 fs, which is about the laser pulse duration. Dewhurst *et al.* propose that majority spins from Mn1 flow to minority-spin states in Mn2 and vice versa. This spin-selective charge flow between sublattices causes the change of spin orientation, ultimately switching the spin order in the Mn2 layer from antiferromagnetic to ferromagnetic on a very fast time scale of tens of fs.

To transfer this concept to the case of Gd, we regard the minority- and majority-spin states of the surface and the bulk. The surface state is spatially localized at the sample surface, see Section 5.2.2 and references [72, 154]. The bulk states, with a coherence length of about 30 Å (about 10 ML), extend into the sample. Thus, we can regard the surface and bulk states spatially separated equivalent to the Mn layers in the work of Dewhurst *et al.* [148]. In analogy to the spin flow between the Mn layers, the laser-induced spin flow in Gd occurs from the occupied majority-spin surface state to the (partially unoccupied) majority-spin bulk state. Concurrently, minority bulk spins

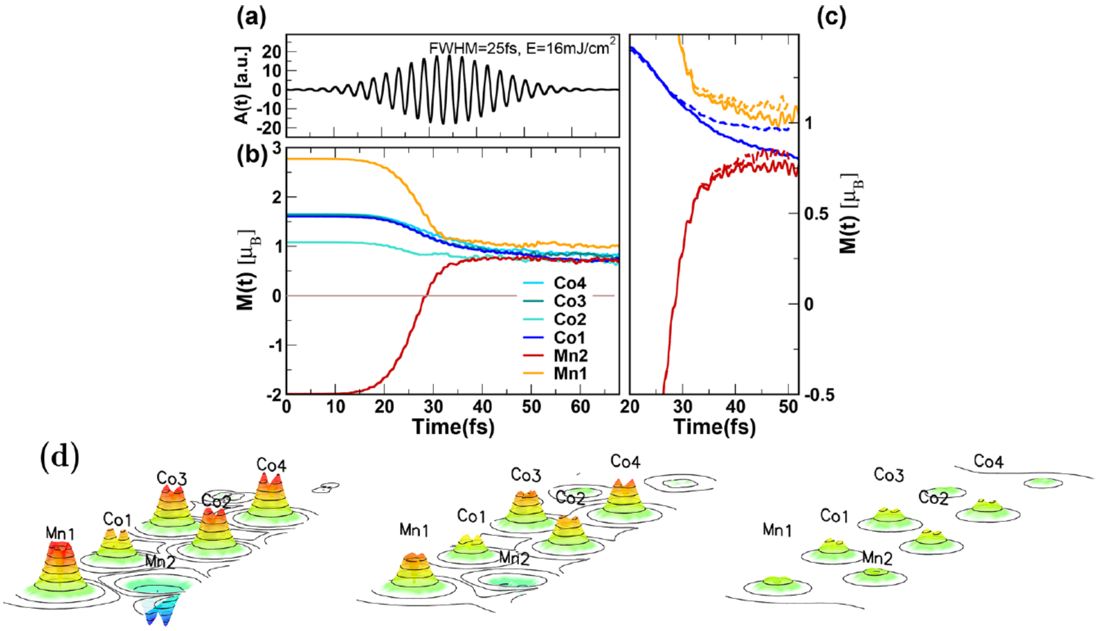

$t = 0\,\mathrm{fs}$ $t = 29\mathrm{fs}$ $t = 60\mathrm{fs}$

Figure 5.11: Calculation of optically induced spin transfer in a Mn/Co multilayer. The laser pulse (a) excites carriers which move between lattice sites transferring their spin. Spin momentum from the antiparallel Mn2 site reduces the magnetization in the Mn1 and Co layers and vice versa (b). The spin orientation in Mn2 is even reversed. The reorientation in Mn2 happens before spin-orbit coupling effects set in, compare dynamics without (dashed blue lines) and with (full blue lines) spin-orbit coupling term (c). Mind that time zero is the beginning of the simulation and not the pump-probe overlap. (d) shows the sample magnetization density at three time steps of the simulation. Images (a)–(d) taken from [148].

are excited into the unoccupied minority-spin surface state. This flow of carriers causes a rearrangement of the charge carriers between the subsystems.

The band structure calculation of Gd in Fig. 5.12 illustrates possible excitation regions around the $\overline{\Gamma}$ point for a pump laser energy of 1 eV. Obviously, for the minority-spin component no states exist around $\overline{\Gamma}$ from which the unoccupied minority-spin surface state could be directly populated. Only either indirect transitions or transitions between the (mixed) minority- and majority-spin states at finite temperatures can populate the minority-spin surface state.

In contrast, there are plenty majority-spin bulk bands which can be directly populated from the occupied majority-spin surface state.

Thus, upon laser excitation, the majority-spin surface state is depleted of majority-spin electrons and its binding energy shifts towards the Fermi level, which corresponds to a reduction of exchange splitting as well as magnetization. The majority-spin bulk band is occupied with majority-spin carriers and shifts to higher binding energies, so the exchange splitting and magnetization of the bulk band increases.

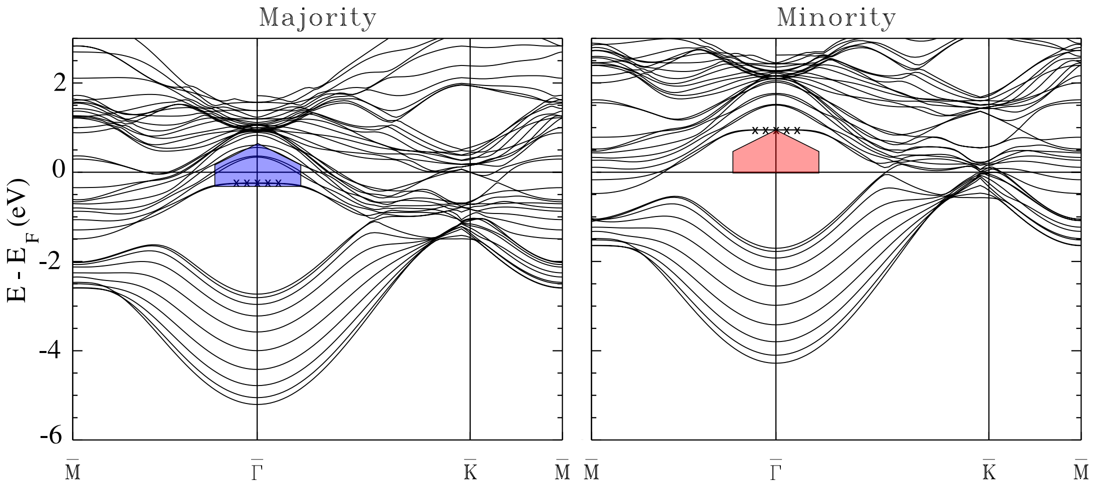

Figure 5.12: Calculated band structure of Gd. The crosses mark the surface state. The arrow boxes mark possible excitation regions around the $\overline{\Gamma}$ point, their height corresponding to the laser photon energy of 0.95 eV. In the minority-spin band structure, there are no states around $\overline{\Gamma}$ from which electrons could be directly excited into the surface state. Image taken from [72] and modified.

Conversely, the minority-spin bulk band, being depleted of minority-spin electrons as carriers are excited into the minority-spin surface state (at larger k), should shift to higher binding energies. However, pumping from the bulk into the surface state could be less efficient and therefore be weaker or slower. As remarked upon above, around the $\overline{\Gamma}$ point there are no bulk states from which electrons could be excited directly into the surface state for the minority-spin part. However, there could be a less efficient, indirect excitation. For instance, Lisowski *et al.* [157] observe a low excitation intensity in the unoccupied surface state upon excitation with 1.5 eV laser pulses.
At larger k, the surface state becomes a surface resonance. Thus, electrons could be excited from the bulk bands into the surface resonance and then transfer into the surface state. Such an indirect pathway would possibly only amount to a small OISTR effect. The population in the surface resonance has a low life time and at any time there is an equilibrium in the population between the bulk and surface states and the surface resonance. Thus, to populate the surface state, a high population of the surface resonance is necessary, which is only given during the excitation process, *i.e.* about the pump pulse duration. Hence, with the given experimental resolution, we can barely distinguish between a direct OISTR excitation and an excitation from an occupied to an unoccupied bulk state (or surface resonance) with a following charge transfer to a surface state.

Additionally, ballistic transport of electrons might further reduce the indirect OISTR effect. Electrons in a metal moving with Fermi velocity can travel distances at about 10 Å fs^{-1} and thus leave the surface region before a charge transfer from the bulk state to the surface state can happen.

In contrast, for the majority-spin states, there are available states for all k along $\overline{\mathrm{M}} - \overline{\Gamma} - \overline{\mathrm{K}}$. Thus, the majority-spin band should show a more pronounced effect and in addition could drop more abruptly.
On the other hand, due to finite temperatures, the states are spin-mixed, so that electrons from the majority-spin surface state can be excited into the minority-spin bulk state, enhancing the shift to higher binding energies. However, this channel seems to be slightly slower than for the majority-spin part.

The role of spin mixing of the states becomes clear when one observes that the effect of an increase of exchange splitting was only observed for cold samples at around 50 K, as shown above in the MOKE [25] and previous angle-resolved photoemission spectroscopy (ARPES) measurements [77], see also Fig. 5.10.
For low temperatures, the states are only weakly spin-mixed. Thus the excited carriers from the majority-spin surface state will predominantly occupy the majority-spin bulk band. Only to a minor degree will the excited carriers populate the minority-spin bulk band. At the same time, the high spin polarization of the excited majority-spin electrons will shift the spin polarization in the bulk bands more significantly to majority-spin character than if the spin polarization of the excited carriers was low. This shift of spin polarization to majority-spin character in the bulk bands entails a shift of the band positions to higher binding energies, which causes the dip in the dynamics seen in Fig. 5.8. In other words, both bands will shift to higher binding energies by a large amount because the excited carriers are highly spin polarized. Additionally, due to the large imbalance of occupation will the majority-spin bulk band be affected more strongly by this effect at low temperatures.
In contrast, if the sample has a higher temperature, the states are more spin-mixed and the imbalance of occupation is reduced. Additionally, the exited carriers will be less spin polarized and they will shift the spin polarization of the bulk bands only by a small amount to majority-spin character. Thus, the bulk band positions will shift much less. All in all, the effects from the unbalanced occupation and the high spin polarization will be less pronounced or even not observable at elevated temperatures.

However, magnetization dynamics due to scattering processes might counteract the OISTR effect as well. As was seen by Carley *et al.* [129], the minority-spin bulk band binding energy starts to react upon laser excitation directly, while the majority-spin bulk band shows a delayed reaction. The authors explain their results with different scattering probabilities for minority- and majority-spin electrons. Possibly, too many scattering events might negate the OISTR effect and thus, there is no dip in the majority-spin bulk band dynamics in the published data.
Alternatively, one could argue, that the OISTR effect is responsible for the delayed reaction of the band dynamics, as it cancels the shifting of the band to lower binding energies due to demagnetization. Lastly, the long pump laser pulses used by Carley *et al.* might reduce the effect of OISTR, as the temporal excitation density might be too low compared to the short pulses employed in our recent work.

From a quantitative point of view, the dynamics in our measurements happen on a time scale one would expect from the theoretical study of the OISTR effect by Dewhurst *et al.* [148]. In their study, the magnetic order in the Fe/Mn and Co/Mn multilayers switches on time scales of about the full width at half maximum (FWHM) of the pump laser pulses.
In our case, we employed pump and probe laser pulses with a cross-correlation of 50 fs and the peak position of the majority-spin bulk band shifts with a time constant of (34 ± 13) fs. If not set equal to the majority-spin bulk band time constant, the fast shift of the majority-spin surface state occurs with (7 ± 16) fs, which is faster than one would expect from the theoretical study of the OISTR effect.

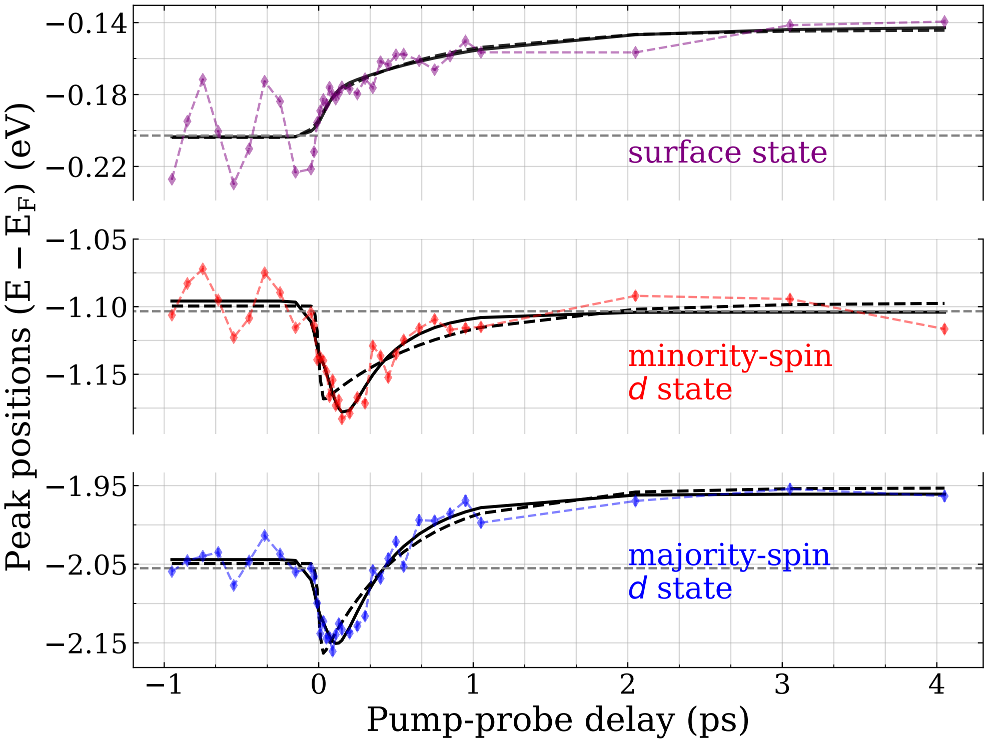

Figure 5.13: Dynamics of the Gd majority-spin surface and minority- and majority-spin bulk states. The fit functions here employ an error function for the first time scale in contrast to the exponential rise or decay in Fig. 5.8. Using the pump laser pulse parameters (dashed lines) does not capture the dynamics well. Without boundary conditions (solid lines), the trends can be reproduced, but the results are less physically meaningful.

The application of a double-exponential function for fitting the data captures the dynamics well, *c.f.* Fig. 5.8. However, the magnetization dynamics in multilayer systems

studied by Dewhurst *et al.* [148] rather follow the trend of an error function.
They explain, that the laser purely optically induces a charge flow causing the observed switching. Thus, one could argue that the charge flow should be directly proportional to the optically excited hot electron population. The hot electron population itself builds up with the presence of the laser pulse, so the error function, as an integral over the Gaussian pulse, should reflect this build-up.
In contrast, an exponential function describes, for instance, how an initial population of particles decays via a process at a certain rate. This would correspond to a population of hot electrons excited by a laser pulse, including electron scattering between surface and bulk states, which then causes the OISTR effect. The relation, in this case, is less direct. Or, to put it in different terms, in the former case, the process behind OISTR is near-instantaneous (with respect to the experimental resolution and laser pulse duration) while in the latter case the process takes a small but finite amount of time. We can see this by testing how well a fit model consisting of an error function and an exponential decay models the dynamics.

Employing a combination of an error function with an exponential decay does not capture the Gd state dynamics in our data as well as a double-exponential function if the laser pulse parameters are used, see dashed lines in Fig. 5.13. Setting the time constant of the fast increase of the surface state peak position to the time constant of the dip in the majority-spin bulk band, the fit fails to capture the trends significantly. If no restraints are set (only the first time constant for the surface state is set equal to the time constant of the majority-spin bulk state), we obtain a good fit with pulse durations of 70–80 fs with additional offsets to time zero of about 30–60 fs, depending on the state. These results, the necessity of an offset, the too large pulse duration as well as the differences between the states, are not physically justifiable in terms of the OISTR effect.

Generally, the results obtained from using a double-exponential function are more convincing than the combination of an error function and an exponential decay. When comparing our results with the calculations we need to be aware that we measure the energy shifts of particular states while Dewhurst *et al.* [148] calculate the overall electron population at different sites. Since the relation between the electron (and spin) population at certain sites and the shift of particular states caused by population changes is not clear, we do not expect an identical response between the band position shifts and the theoretical calculations, which is further confirmed by the experiment and the application of the two different fit models.

However, if we look directly at the population dynamics of the surface state, the application of an error function yields reasonable results. Figure 5.14 shows the maximum intensity of the majority-spin surface state as an approximation to its population. The fit function consists of an error function for the initial decrease with an exponential function for the following increase. With a width of $\sigma_{\text{erf}} = (38 \pm 6)$ fs the error function captures the experimental resolution, *i.e.* the duration of the employed laser pulses.

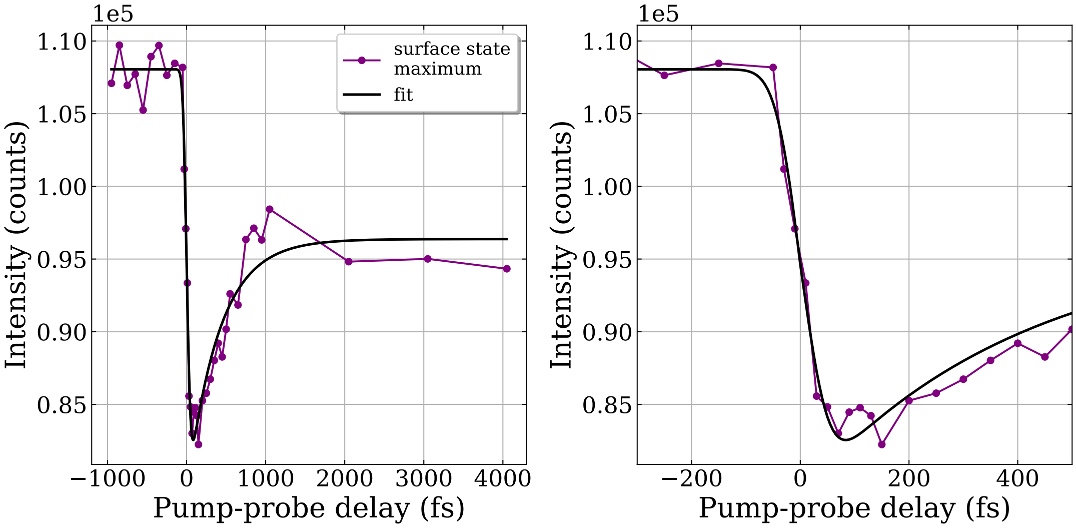

Figure 5.14: Dynamics of the Gd majority-spin surface state peak maximum. The fit function consists of an error function for the first time scale and an exponential function for the partial recovery. The peak maximum is used as an approximation for the surface state population.

All in all, the time constants of the double-exponential fit, the population dynamics in the surface state and the general trends in the dynamics of the states in Gd generally agree well with the expectations from the OISTR model and we can infer that the OISTR effect likely explains the dynamics in our data.

5.4 Summary

To conclude, we find dynamics of the Gd states and the exchange splitting similar to literature in the range above 100 fs, although some aspects deviate. Especially, the majority-spin bulk band dynamics are significantly faster than reported [129, 130] and resemble the minority-spin bulk band dynamics in that they show an immediate response to the pump laser pulse and have similar time scales. Concomitantly, the relation found in literature [77, 129] between the electron temperature and majority-spin bulk band dynamics is less distinct from the minority-spin band dynamics in our data.

However, the major findings are found in the first 100 fs after laser excitation. Our data reveals an unexpected increase of the exchange splitting and corresponding dynamics of the individual Gd states. Remarkably, despite the same spin polarization, the majority-spin surface and bulk states shift in opposing directions in terms of binding energy for a few 10 fs upon laser excitation. The majority-spin bulk band shows a dip towards higher binding energies while the majority-spin surface state decreases in binding energy.
This behavior might be caused by the OISTR effect [148], which describes the optically

induced spin transfer between different sites in a material. Adopted to Gd, OISTR describes the excitation of majority-spin electrons from the surface state to the majority-spin bulk state, thereby transferring spin momentum between the two majority-spin states and causing the opposing shift in binding energy. In the minority-spin states, the effect seems to be present as well, although the dynamics are more complex.
Inherently, OISTR should have a stronger effect at low temperatures, as the spin transfer is larger if the excited carriers are more highly spin polarized. This agrees with observations of the effect being only made at low temperatures [25, 77].

Finally, as a speculative idea, a footprint of the OISTR effect in Gd might have been hidden in literature data in the delayed response of the majority-spin bulk band [77, 129, 130]. A competition between the OISTR effect, which drives the state to higher binding energies, and the laser-induced demagnetization might contribute the observed delayed dynamics.

Chapter 6

Ponderomotive Oscillations on Gd and W

The pump-probe scheme in experimental physics is a well-established method to observe electron dynamics on very fast time scales [164–167]. Typically, a low energy pump photon pulse is employed to trigger some form of excitation and start a dynamic process in a material. Here, the role of the pump pulses is studied with respect to the dynamics it triggers in the sample, as, for instance, discussed in Chapter 5. Effects like space charge due to strong pump pulses, which do affect the probed electrons, can be experimentally avoided [129].

We observed how the pump pulse can impact the probed electrons causing oscillatory modulations of the kinetic energy of the probed electrons. We found very strong oscillations of the kinetic energy of the electrons before time zero when measuring magnetization dynamics of Gd(0001), *i.e.* when the infrared (IR) pump pulse arrives before the ultraviolet (UV) probe pulse.

In 2009, Bovensiepen *et al.* [168] published measurements of such oscillations on Gd(0001), where they also describe a model to explain the data. However, the magnitude of those oscillations was small with about 1 meV [168]. In the following, we will describe their model and extend it to times where the pump and probe pulses overlap. With the extension we can assess the impact of the kinetic energy modulation of the probed electrons on dynamics at small positive delays.

In [168] they propose that the photoexcited electrons interact with a transient grating formed in front of the sample surface by the interference of an incoming and reflected light pulse. The grating causes a ponderomotive de- or acceleration of the electrons depending on the position of the electrons inside the grating. The treatment of the interaction simplifies by assuming the transient grating to form clearly after photoexcitation of the electrons. We drop this assumption and extend the model to see if there is to be expected an influence from the oscillations during temporal overlap between the pump and probe pulses, specifically at small positive delays. Under certain conditions, this might affect ultrafast dynamics like described in Section 5.3. In our case, the simplified treatment is justified. Nevertheless, the large magnitude of the oscillations in our measurements made us perform a more extensive study and investigate the appearance of ponderomotive oscillations on a different material, our substrate W(110). We discovered different oscillation amplitudes for photoelectrons excited out of different initial states in W(110), which is unexpected in the framework of the transient grating model.

In the following, we are looking at the phenomenon of ponderomotive oscillations of photoelectrons due to a transient grating created by a reflected light pulse. Part of the data, *i.e.* the data shown in Section 6.2.1, is the same as in Section 5.3, but this time we will focus on the dynamics before time zero where an oscillatory shift of the spectrum was observed.

In this chapter, the model of ponderomotive acceleration by Bovensiepen *et al.* for describing the observed phenomenon is introduced first. Following up is an extension of this model by dropping the simplifying assumption in the original model to assess the influence of the oscillations at temporal overlap of the two laser pulses. Then we will evaluate and discuss the oscillations observed on Gd(0001) by pumping with 1300 nm and 1600 nm laser pulses, respectively. The chapter closes with a discussion of the pump wavelength dependence of the oscillation parameters in W(110) and a discussion of the different oscillation amplitudes observed for the two W(110) states.

6.1 Description of Ponderomotive Acceleration by a Transient Grating

Bovensiepen *et al.* [168] performed a pump-probe experiment on a single-crystalline Gd(0001)/W(110) sample to measure the change of kinetic energy of photoexcited electrons upon interaction with a transient optical grating. The formation of the grating is illustrated in Fig. 6.1. An IR laser pulse is reflected off a metal surface and interferes with itself generating a standing wave field in front of the surface along the surface normal. An electron in this field can be accelerated or decelerated depending on its position within the field.

To generate the optical grating, they used an s-polarized pump pulse with a pulse duration of 50 fs and central wavelength of 830 nm. The laser, with an energy of 3 µJ and at 300 kHz repetition rate, produced the grating with a peak intensity of 50 GW/cm^2. The pump beam impinged on the sample at an angle of 45°, as is illustrated by the wavy pattern in Fig. 6.1.

To photoemit electrons from the surface, they used p-polarized 6 eV laser pulses with 90 fs duration. Electrons emitted normally, with an acceptance angle of 3°, were detected with a time-of-flight analyzer with an energy resolution of 20 meV. To study the effect of the optical grating on the electrons, they chose to monitor the peak position of the Gd(0001) majority-spin surface state which was evaluated using a simple Gaussian fit, see Fig. 6.2, top. Their data shows that the kinetic energy of the surface state electrons is modulated by a few meV with a frequency of $\Omega/2\pi = 1.53\,\mathrm{THz}$ or equivalently

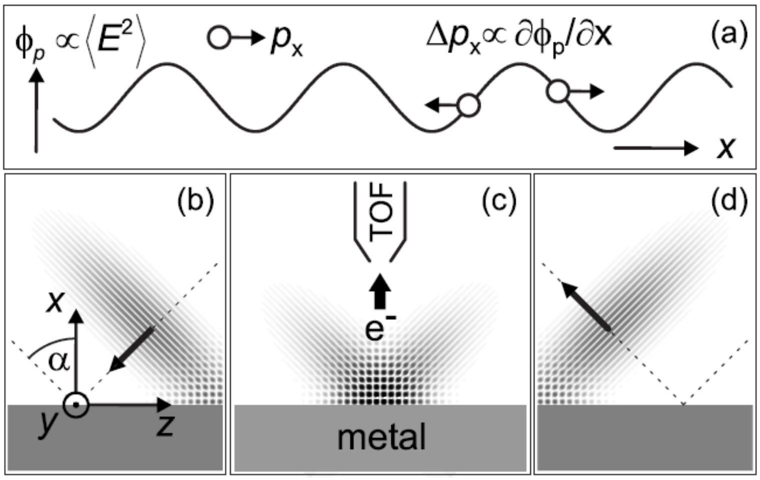

Figure 6.1: Illustration of the ponderomotive acceleration and the formation of the transient optical grating. (a) Change of momentum of electrons in the potential of the grating depending on their position within the grating. (b)-(d) An incoming near-IR laser pulse is reflected at the surface of a metal. During the time when only a part of the pulse is reflected, it interferes with the still incoming part thereby forming a two-dimensional wave pattern. Along the surface normal the wave is standing, while it is propagating along the z direction. The intensity of the electrical field, indicated by the gray scale, is maximum when the pulse's center is at the metal surface. (c) additionally shows the measurement geometry. Electrons emitted normally to the surface are detected in a time-of-flight analyzer. Images (a)–(d) taken from [168].

0.62 µm, see Fig. 6.2, bottom[1]. This is in good agreement with what one expects from the experimental parameters within the model.

To describe the effect of the transient grating on the electrons, Bovensiepen *et al.* calculated the acceleration of a free electron in the presence of an oscillating electric field with frequency ω, which is assumed to be high compared to the cyclotron frequency.[2] The motion of the electron is described by splitting it into two components: $\mathbf{r} = \mathbf{r_0} + \mathbf{r_1}$. Here, $\mathbf{r_0}$ is the motion of the center of the oscillating electron and $\mathbf{r_1}$ is the quiver motion following the electric field at ω. As the IR pump pulse duration is significantly larger than the duration of an optical cycle ($1/\nu = 2.8\,\mathrm{fs}$ for $\lambda = 830\,\mathrm{nm}$), the quiver motion $\mathbf{r_1}$ is integrated out in time yielding a potential $\Phi_\mathrm{p} \propto \langle E^2 \rangle$. Expanding the electric field up to first order leads to the following equation of motion:

$$\frac{\partial^2 \mathbf{r_0}}{\partial t^2} = -\nabla \Phi_\mathrm{p} \ , \tag{6.1}$$

with the ponderomotive potential:

$$\Phi_\mathrm{p} = \frac{e^2}{m_e^2 \omega^2} \left\langle \frac{E^2}{2} \right\rangle = \frac{e^2}{4 m_e^2 \omega^2} I \ , \tag{6.2}$$

---

[1] The sign of the pump-probe delay Δt in this figure is reversed compared to the definition used in this thesis.

[2] A more detailed derivation is given in [169], p. 47ff.

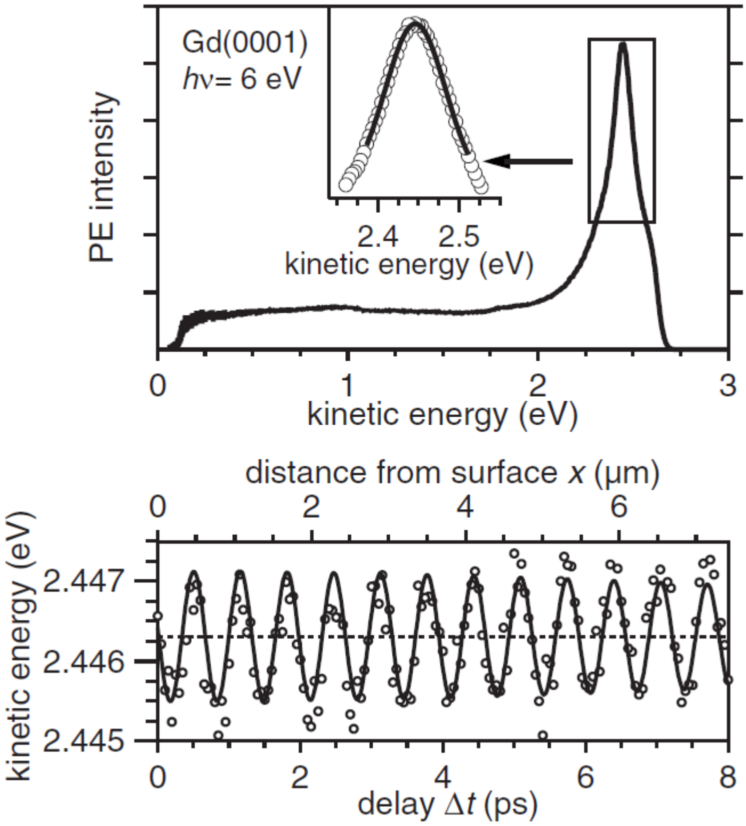

Figure 6.2: Top: Photoemission (PE) spectrum of the Gd(0001) sample at 30 K with an inset showing the Gaussian fit of the majority-spin surface state. Bottom: Oscillations of the kinetic energy of the photoemitted electrons. The cirlces depict the fitted peak positions over pump-probe delay, which is also translated into distance from the sample surface (top axis). The solid line is calculated using Eq. (6.5). Images taken from [168].

where e is the elementary charge, m_e the electron mass and I the intensity of the electric field $\mathbf{E}$. In the limit of a high frequency field, the oscillation center is subject to the ponderomotive potential. When the electric field is nonuniform in space, $\mathbf{r_0}$ drifts along a spatial field gradient in the direction of decreasing potential, as is depicted in Fig. 6.1(a).

For the derivation of the equation of motion, Eq. (6.1), some approximations are made based on assumptions in addition to expanding the field only to first order, as described in [169]. First, the oscillation center is assumed to not move significantly during an oscillation period, or:

$$\frac{(\dot{\mathbf{r}}_\mathbf{0} \cdot \nabla)\mathbf{E}}{\omega} \ll E \; . \tag{6.3}$$

Second, a weak magnetic field is assumed, *i.e.* the cyclotron frequency ω_c is:

$$\omega_\mathrm{c} = \frac{q}{m} B \ll \omega \; . \tag{6.4}$$

And lastly, $\mathbf{\dot{r}_0} \lesssim \mathbf{\dot{r}_1}$.

In the paper, the authors regard the scenario where the UV probe pulse excites an electron which travels a certain distance x before the IR pump pulse arrives and generates the transient grating. Thus, the IR pulse defines the potential along the direction of travel and modulates the kinetic energy of the electrons. To calculate the resulting acceleration, they integrate over the optical cycles of the IR pulse and obtain a variation of kinetic energy given by:

$$\Delta E_{\text{kin}} = \epsilon \cdot e^{-A-B\Delta t^2} \sin(\Omega \Delta t + \Psi) \ , \tag{6.5}$$

where Φ represents the incident pump laser fluence and σ is related to the pump pulse duration at full width at half maximum $\tau = \sigma\sqrt{8\ln 2}$, R is the reflectivity, α the incidence angle and Ψ the phase shift. The amplitude[3] is $\epsilon = \frac{2\Phi e^2\sqrt{R}\cos\alpha}{\epsilon_0 m_e^2 \omega c^2} p_x$, the modulation frequency is $\Omega = \frac{2p_x\cos\alpha}{m_e c}\omega$ and the damping parameters are $A = \frac{2\sigma^2\omega^2 p_x^2\cos^2\alpha}{(m_e c)^2}$ and $B = \frac{p_x^2\cos^2\alpha}{2(m_e c\sigma)^2}$. The first damping term e^{-A} arises because the electron moves a finite distance within the IR pulse duration, which changes $\Delta\Phi$ reducing the energy modulation. The second term $e^{-B\Delta t^2}$ takes account of the decreasing IR field intensity with increasing distance from the surface, *i.e.* with increasing pump-probe delay. Knowing all parameters, Bovensiepen *et al.* could calculate an expected kinetic energy modulation and plot it with the data, see Fig. 6.2(a). Their calculated parameters agree quantitatively very well with the fitted parameters.

Despite the good agreement between the model and the data, there is the simplification of a clear temporal separation between pump and probe pulses. *A priori* it is not clear whether this simplification obscures some effect at small delays, both positive and negative, during overlap of the two pulses. Especially for dynamics like the increase of exchange splitting of the Gd(0001) d-bands discussed in Chapter 5, already a small contribution from the ponderomotive acceleration might significantly impact such fine and very fast effects. To better assess possible effects from the ponderomotive oscillations, Xinwei Zheng dropped the simplifying assumption and derived the kinetic energy modulation more generally, covering the temporal overlap of the pump and probe pulses, in her Master's thesis [170]. In the following Section 6.1.1, her derivation will be outlined and the consequences for electron dynamics around time zero discussed.

6.1.1 Model Extension and Phase Shift Influence on Electron Dynamics

We consider an electromagnetic wave at normal incidence onto a metal being reflected off the surface. The wave has a Gaussian pulse shape to represent the IR pump pulse in the experiment. The incoming wave interferes with the reflected wave producing a standing wave in front of the metal surface. The reflection happens at $x = 0$ and $t = 0$

---

[3] In the paper, Gaussian units are used. The ϵ given in this thesis is converted to SI units by multiplication with $\frac{1}{4\pi\epsilon_0}$.

where the reflected wave acquires a phase shift Ψ and loses some intensity due to the reflectivity R. The electric fields of the waves are described by:

$$\mathbf{E_1} = \mathbf{E_0} e^{-\frac{(x-ct)^2}{4\sigma^2 c^2}} e^{i(kx-\omega t)} \tag{6.6}$$

$$\mathbf{E_2} = \sqrt{R}\mathbf{E_0} e^{-\frac{(x+ct)^2}{4\sigma^2 c^2}} e^{i(-kx-\omega t-\Psi)} \ . \tag{6.7}$$

The resulting standing wave intensity is given by the product of the sum of the two fields:

$$\begin{aligned} I(x,t) &= (\mathbf{E_1}+\mathbf{E_2})(\mathbf{E_1}+\mathbf{E_2})^* \\ &= |\mathbf{E_1}|^2 + |\mathbf{E_2}|^2 + 2\sqrt{R}\mathbf{E_0}^2 \cdot e^{-\frac{x^2}{2\sigma^2 c^2}} \cdot e^{-\frac{t^2}{2\sigma^2}} \cdot \cos(2kx+\Psi) \ . \end{aligned} \tag{6.8}$$

If the wave packets travel under an incidence angle α with respect to the surface normal of the metal, x has to be substituted by $x\cos(\alpha)$ in Eq. (6.8). The third summand represents the standing wave, *i.e.* the transient optical grating which provides the potential for the photoemitted electrons in the experiment.

Once the electrons are excited, they travel a certain distance from the metal surface with momentum p_x before the pump pulse arrives and generates the transient grating. Using Eqs. (6.1) and (6.2), the equation of motion for an electron in the potential of the grating can be set up:

$$\begin{aligned} \frac{\partial p_x}{\partial t} &= -m_e \nabla \Phi_\mathrm{p} = -\frac{e^2}{4 m_e \omega^2} \nabla I(x,t) \\ &= \frac{e^2 \sqrt{R}}{m_e \omega c} \mathbf{E_0}^2 \cdot e^{-\frac{x^2}{2\sigma^2 c^2}} \cdot e^{-\frac{t^2}{2\sigma^2}} \cdot \sin\left(\frac{2\omega}{c} x + \Psi\right) \ . \end{aligned} \tag{6.9}$$

The wavevector k was substituted by ω/c and the second contribution from $\nabla I(x,t)$ was neglected, as the gradient of the Gaussian envelope is much smaller than the gradient of the sine function. As in [168], we additionally assume p_x to be constant. As we will see below, this is justified by our data, from which we obtain $\Delta E_\mathrm{kin}/E_\mathrm{kin} \approx 10^{-3}$ and thus $\Delta p_x/p_x \approx 10^{-3}$ as well. With these approximations the distance traveled by an electron is:

$$x = \int_\tau^t \frac{p_x}{m_e} \mathrm{d}t = \frac{p_x}{m_e}(t-\tau) \ , \tag{6.10}$$

with τ being the time when the electron was emitted by the UV probe pulse. The transient grating modifies the kinetic energy of the electron after it has been emitted at τ and while it is moving within the grating. Using Eqs. (6.9) and (6.10) the kinetic energy changes by:

$$\begin{aligned} \Delta E_\mathrm{kin}(\tau) &= \frac{p_x}{m_e} \Delta p_x(\tau) = \frac{p_x}{m_e} \int_\tau^\infty \frac{\partial p_x}{\partial t} \mathrm{d}t \\ &= \frac{e^2 \sqrt{R} p_x}{m_e^2 \omega c} \mathbf{E_0}^2 \, \mathrm{Im}\left\{ \int_\tau^\infty e^{-\frac{p_x^2}{m_e^2 c^2}\frac{(t-\tau)^2}{2\sigma^2} - \frac{t^2}{2\sigma^2} + i\frac{2\omega p_x}{m_e c}(t-\tau) - i\Psi} \mathrm{d}t \right\} \ . \end{aligned} \tag{6.11}$$

Here, the sine function was expressed as the imaginary part of an exponential. To further reduce complexity, we assume the electron to be much slower than the speed of light $p_x/m_e \ll c$. We introduce $y = p_x/m_e c$ and neglect y^2 in terms of the kind $1 \pm y^2$. By rearranging the expression in the integral and completing the square to obtain a Gaussian-like expression depending on t, the integral in Eq. (6.11) can be solved:

$$\begin{aligned}
&\int_\tau^\infty e^{-\frac{1}{2\sigma^2}\left((1+y^2)t^2-(2y^2\tau+i4\omega\sigma^2 y)t+y^2\tau^2\right)-i(2\omega y\tau-\Psi)}\mathrm{d}t \\
&=\int_\tau^\infty e^{-\frac{1}{2\sigma^2}\left((t-y^2\tau-i2\omega\sigma^2 y)^2+y^2\tau^2(1-y^2)+4\omega^2\sigma^4 y^2\right)-i(2\omega y\tau(1-y^2)-\Psi)}\mathrm{d}t \\
&= e^{-2\omega^2\sigma^2 y^2-\frac{y^2\tau^2}{2\sigma^2}} \cdot e^{-i(2\omega y\tau-\Psi)} \\
&\quad \cdot \frac{\sqrt{2\pi}\sigma}{2}\left(1-\operatorname{erf}\left(\frac{\tau}{\sqrt{2}\sigma}(1-y^2)-i\sqrt{2}\omega\sigma y\right)\right) \ .
\end{aligned} \tag{6.12}$$

The error function is the integral of the Gaussian in t. The crucial difference to the approach in [168] is, that the lower integration limit is the parameter τ instead of $-\infty$. Inserting Eq. (6.12) back into Eq. (6.11), we get:

$$\begin{aligned}
\Delta E_{\mathrm{kin}}(\tau) = \frac{1}{2}\frac{\sqrt{2\pi}\sigma e^2\sqrt{R}p_x}{\omega m_e^2 c}{\mathbf{E_0}}^2 \cdot e^{\frac{-2\omega^2\sigma^2 p_x^2}{(m_e c)^2}-\frac{p_x^2}{2(\sigma m_e c)^2}\tau^2} \\
\mathrm{Im}\left\{1-\operatorname{erf}\left(\frac{\tau}{\sqrt{2}\sigma}(1-y^2)-i\sqrt{2}\omega\sigma y\right)e^{-i(\frac{2\omega p_x}{m_e c}\tau-\Psi)}\right\} \ .
\end{aligned} \tag{6.13}$$

Using the definition of the incident pump laser fluence $\Phi = 1/2\epsilon_0 c{\mathbf{E_0}}^2\sqrt{2\pi}\sigma$ as in [168] (converted to SI units), we can rewrite Eq. (6.13) with the same definitions for $\epsilon, A, B, \Omega, \Psi$ and σ as in Eq. (6.5):

$$\Delta E_{\mathrm{kin}}(\tau) = \epsilon e^{-A-B\tau^2}\,\mathrm{Im}\left\{\frac{1}{2}\left(1-\operatorname{erf}\left(\frac{\tau}{\sqrt{2}\sigma}-i\frac{\sigma\Omega}{\sqrt{2}}\right)\right)e^{-i(\Omega\tau-\Psi)}\right\} \ . \tag{6.14}$$

We defined $t = 0$ as the time when the IR pump pulse is reflected off the metal surface. Thus, τ is the delay between the UV probe and IR pump pulses. With Eq. (6.14), the modulation of the kinetic energy of the photoelectrons can be described over the whole pump-probe delay range.

For consistency, to arrive at the simplified model of Eq. (6.5), one has to take the limit of $\tau \ll -\sigma$, which represents a clear separation of pump and probe pulses. Then, erf ≈ -1 and Eq. (6.14) becomes:

$$\begin{aligned}
\Delta E_{\mathrm{kin}}(\Delta t) &= -\epsilon e^{-A-B\Delta t^2}\sin(\Omega\Delta t-\Psi) \\
&= \epsilon e^{-A-B\Delta t^2}\sin(\Omega\Delta t-\Psi+\pi) \ .
\end{aligned} \tag{6.15}$$

Considering the inverted time axis in the paper, we change $\Delta t \rightarrow -\Delta t$ and end up with the same formula as presented in [168].

Coming back to Eq. (6.14), we can simulate the oscillating kinetic energy of the photoelectrons over the whole delay range and assess a possible influence of the oscillations on dynamics at positive delays. Figure 6.3 shows the oscillating kinetic energy over pump-probe delay for different phase shifts. The green curve was modeled using the parameters given in [168] ($\epsilon e^{-A}:\ 0.82\,\mathrm{meV}$, $B:\ 3.7\cdot10^{-3}\,\mathrm{ps}^{-2}$, $\Omega:\ 9.9\,\mathrm{rad\ ps}^{-1}$ and $\Psi:\ 170°$). For the other traces, the phase shift was changed as shown in the legend of the figure.

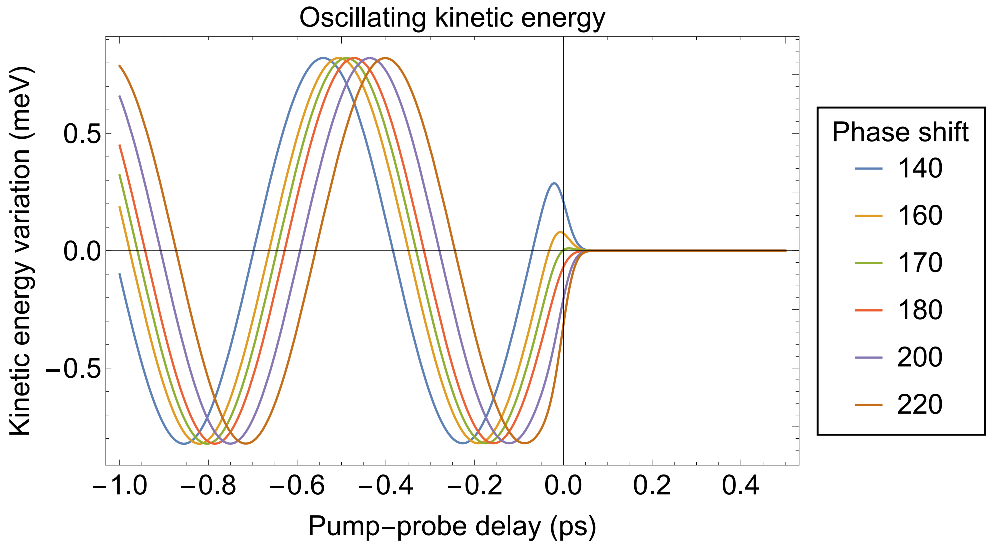

Figure 6.3: Modulation of kinetic energy over pump-probe delay calculated using Eq. (6.14) with parameters from [168], see text. The colored lines represent different phase shifts of the reflected light at the metal surface. At 170° there is no significant amplitude at time zero. At 140° or 200°, the kinetic energy is modified by about 30 % of the maximum amplitude. Image taken from [170].

We want to focus on the kinetic energy modulation around time zero. The original curve (green, $\Psi = 170°$) has no significant amplitude. As the phase shift deviates from $\Psi = 170°$, the influence of the oscillations becomes more prominent. At 30° deviation, the oscillations still contribute with about 30 % of the maximum amplitude at time zero. Thus, if the pump pulse experiences a strong phase shift when reflected off a metal surface, the contribution from ponderomotive oscillations can have a significant impact on dynamical effects which affect the band structure on a scale comparable to the oscillations. On the other hand, the oscillations can have a large amplitude, as we will see in the following sections. But can the phase shift at metal surfaces be of a magnitude that the oscillations become significant?

According to the Fresnel equations, the phase shift at the surface of a dielectric is either 0° or 180° depending on whether the light travels from the optically denser to the less dense medium ($n_1 > n_2$) or vice versa ($n_1 < n_2$), *cf. e.g.* [171]. For the treatment of metals, one can use the same formalism, but one has to introduce a term for absorption. Thus, the index of refraction becomes complex $n \to \tilde{n} = n + ik$ for the metal and consequently other quantities like the angle of reflection and the reflection and transmission coefficients become complex as well. The reflection coefficients can be described with a phase δ, which depends on the material parameters n and k and the angle of incidence. With Snell's law for an air-metal interface $n_1 \sin(\theta_\mathrm{i}) = \tilde{n}_2 \sin\left(\tilde{\theta}_\mathrm{t}\right)$ we have:

$$r_\perp = |r_\perp| e^{i\delta_\perp} = \frac{n_1 \cos(\theta_\mathrm{i}) - \tilde{n}_2 \cos\left(\tilde{\theta}_\mathrm{t}\right)}{n_1 \cos(\theta_\mathrm{i}) + \tilde{n}_2 \cos\left(\tilde{\theta}_\mathrm{t}\right)} \tag{6.16}$$

$$r_\parallel = \left|r_\parallel\right| e^{i\delta_\parallel} = \frac{\tilde{n}_2 \cos(\theta_\mathrm{i}) - n_1 \cos\left(\tilde{\theta}_\mathrm{t}\right)}{\tilde{n}_2 \cos(\theta_\mathrm{i}) + n_1 \cos\left(\tilde{\theta}_\mathrm{t}\right)} , \tag{6.17}$$

with the incidence and transmission angles $\theta_\mathrm{i,t}$. For metals in the optical and near-infrared wavelength range, the absorption coefficient shows a tendency towards $k \gg 1$ [172–174] (chapter 35, properties of metals in [172]), resulting in phase shifts of typically 150–180°. Thus, large phase shifts are not expected and the influence of the ponderomotive oscillations should in general be negligibly small in metals. In particular, we are justified to ignore the influence of the ponderomotive oscillations on the sub-100 fs dynamics in Gd as discussed in Chapter 5. For other materials it might be worthwhile to consider the phase shift and a possible influence of the ponderomotive oscillations on ultrafast electron dynamics in photoemission.

6.2 Oscillations on Gd(0001)

In the paper by Bovensiepen *et al.* [168] experimental data is presented for only one material with one set of parameters regarding the laser pulses. Their model, in contrast, provides several parameters which should affect the kinetic energy modulation of the photoelectrons. As they discuss, choosing the right conditions, like low pump photon energies, high pump fluences and high electron kinetic energies, the oscillations could be significantly enhanced. Meeting the above experimental conditions, we observed very strong oscillations at the Cental Laser Facility (CLF) at the STFC Rutherford Appleton Laboratory and used the opportunity to make a more systematic study with respect to the pump laser wavelengths and the material. In the following, we will look at the results on Gd(0001) pumped with 1300 nm laser pulses and discuss it with respect to the ponderomotive acceleration model. Thereafter, we regard the results of Gd pumped with 1600 nm and compare the results for the different pump wavelengths. We then switch to data measured on W(110) and study the wavelength dependence of the oscillations and discuss first ideas about the difference in peak shifts of mixed and bulk states due to the ponderomotive acceleration.

6.2.1 1300 nm Pump Laser Excitation

The data presented in this subsection was measured on a Gd/W(110) sample pumped under 65° with 1300 nm s-polarized IR pulses and probed under normal emission with 34.2 eV extreme ultraviolet (XUV) pulses. With pulse durations of 40 fs for the IR and 30 fs for the XUV laser, we obtain a cross-correlation of 50 fs. Unfortunately, we cannot use the experimentally determined pump laser fluence, as the values are clearly unreasonably high, see end of this section for a detailed discussion. We used the maximum pump fluence for which a shift of the spectrum due to space charge contributions was negligible.

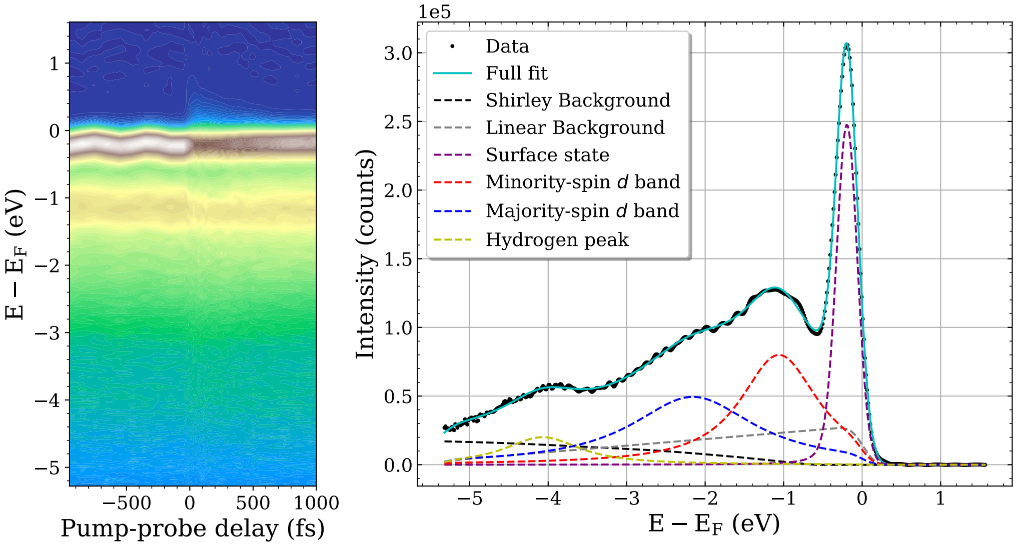

Figure 6.4: Left: Raw-data image plot of Gd/W(110) pumped with 1300 nm. Before time zero, the spectrum shows clear oscillations. Right: Static spectrum of Gd/W(110) with fit (solid line) and fit components (dashed lines). It corresponds to a vertical cross section of the raw data left.

A detail of the raw data set of Gd/W(110) is shown in Fig. 6.4. The oscillations of the photoelectron kinetic energy are clearly visible at negative pump-probe delays. The static spectrum in Fig. 6.4, right, corresponds to a vertical cross section of the raw-data image at negative delay. The components of the fits and the fit procedure are described in detail in Section 5.2.1. From the global fit we obtain the peak positions of the three Gd states: the surface state and the minority- and majority-spin bulk bands. Their dynamics are plotted in Fig. 6.5.

The peak positions of all states have similar oscillation amplitudes of about 26–31 meV. The black dashed lines are the fits of the oscillations using Eq. (6.5). Generally, the fits are satisfactory, but a higher point density would be desirable. For example, for the majority-spin *d* state the point at around −550 fs is a bit off and there is no spare data points to balance it.

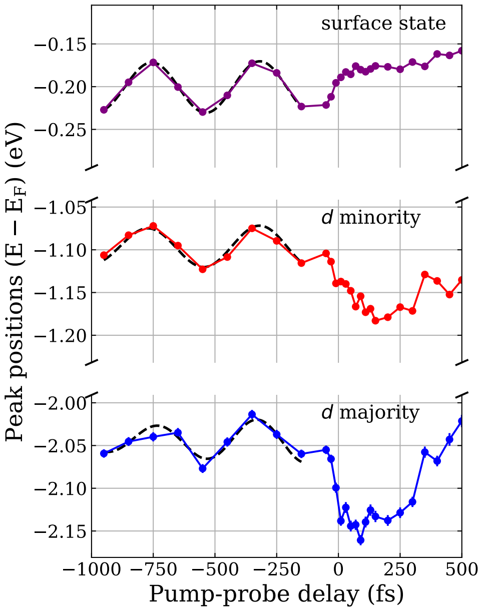

Figure 6.5: Dynamics of the three Gd states as obtained from a global fit of the raw data in Fig. 6.4. The dashed lines at negative delays are fits of the oscillations of the peak positions. The oscillation amplitude is similar for all states with about 26–31 meV.

Table 6.1 shows the values obtained from fitting the experimental data and values calculated from the ponderomotive acceleration model ($\epsilon = \frac{2\Phi e^2 \sqrt{R}\cos\alpha}{\epsilon_0 m_e^2 \omega c^2} p_x$ from Eq. (6.5)) using our experimental parameters. Due to unavailable pump fluences, we assume an absorbed fluence of $1\,\mathrm{mJ/cm^2}$ within the whole sample for the calculation, as this is a typical fluence used in such experiments [22, 128, 129, 168]. The other parameters are the reflectivity $R = 0.83$, the incidence angle $\alpha = 65°$, $\omega = 2\pi c/\lambda$ for $\lambda = 1300\,\mathrm{nm}$ and $p_x = \sqrt{2m_e E_{\mathrm{kin}}}$ with $E_{\mathrm{kin}} = E_{\mathrm{HHG}} - \Phi_{\mathrm{Gd}} - E_{\mathrm{B}}$, where $E_{\mathrm{HHG}} = 34.2\,\mathrm{eV}$, $\Phi_{\mathrm{Gd}} = 3.7\,\mathrm{eV}$ is the work function of Gd and E_{B} is the binding energy of the Gd states with respect to the Fermi level. We see, that the model yields comparable results to the data under the assumption of the pump fluence above.

In fact, we can reverse engineer our pump laser fluence assuming the model to be true. Of course, this is by no means a rigorous way to determine the pump laser fluence, yet we can make a rough assessment. To obtain the experimental amplitudes from the model, we deduce an absorbed fluence of about $1.3\,\mathrm{mJ/cm^2}$ or an incident fluence of $7.6\,\mathrm{mJ/cm^2}$ which at least seems plausible.

By and large, we can conclude that the ponderomotive acceleration model predicts reasonable amplitudes for our experimental conditions and we can enhance the kinetic

	ϵ [meV]		$2\pi/\Omega$ [fs]		$\Psi[^\circ]$
state	fit	model	fit	model	fit
surface	31 ± 1	22.2	438 ± 2	471	172 ± 2
d minority	26 ± 7	22.0	453 ± 25	478	164 ± 22
d majority	27 ± 12	21.6	406 ± 43	486	204 ± 50

Table 6.1: Oscillation amplitudes, periods and phase shifts of the three Gd states when pumped with 1300 nm. Amplitudes were calculated using our experimental parameters assuming an absorbed fluence of $1\,\mathrm{mJ/cm^2}$ within the whole sample. Amplitudes and periods from fitting of the data and expectations from the ponderomotive acceleration model are comparable. The phase shifts show some variation, but are in the expected range below 180° except for the highly uncertain phase of the majority-spin bulk state.

energy modulation by using high probe and low pump photon energies as well as high pump laser fluences.

According to the transient grating model, the period of the kinetic energy modulation should be determined by the pump laser wavelength, the photoelectron kinetic energy and the incidence angle of the pump laser beam ($\Omega = \frac{2p_x \cos\alpha}{m_e c}\omega$ from Eq. (6.5)). Given the experimental parameters, we can compare the experimentally determined period of the oscillations with the model expectations.

Table 6.1 lists the oscillation periods obtained from the fits of the data and calculated using the experimental parameters as stated above. Again, the experimental and theoretical results are comparable, although the model systematically overestimates the period. The small overestimation could originate from the setup geometry. Already small inaccuracies of few degrees around the incidence angle of $\alpha = 65^\circ$ can cause deviations in the period of about 10 %.

The statistical uncertainties from the fits increase from the surface state to the minority- and majority-spin states reflecting the worse data quality, see Fig. 6.5. This is rooted in the increasingly broadened and overlapping peak shapes of the more strongly bound states. They constitute a falling flank of intensity between $-3.5\,\mathrm{eV}$ and $-1\,\mathrm{eV}$ instead of a clear peak shape like the surface state, see Fig. 6.4, which makes the determination of the peak position in the fit harder.

The pump pulses undergo a phase shift when being reflected off the metal surface, which is imparted onto the kinetic energy modulation of the photoelectrons. As discussed at the end of Section 6.1.1, we expect phase shifts to be below 180°. From Table 6.1 we see, that there is a certain dispersion among the three states. The values for the surface and minority-spin d state lie in the expected range of phase shifts. The last value does not fit the picture, but it has a large uncertainty and possibly is an outlier. As we are only using the simplified function to fit the data, the fitting range is set to below 100 fs before time zero. Thus there is some uncertainty about the onset of the oscillations, which might introduce the variation we see in the phase shifts of the three states.

All in all, the transient grating model seems to adequately describe the kinetic energy modulation we see in this example data set. During a second beamtime at the Artemis lab, we performed the measurements using a pump wavelength of 1600 nm, which we will discuss in the following section. We ask ourselves, if the disparities, like the overestimated periods calculated from the model, are of a systematic nature or just scattering due to experimental uncertainties.

Pump Laser Fluence Determination

As mentioned above, the pump laser fluence determined experimentally yields unreasonably high values. The high fluence comes about due to the very small spot sizes measured with a charge-coupled device (CCD) camera. Evaluating the images, we obtain a size of about 72 µm × 133 µm (full width at $1/e$ height). At 1 kHz and with 260 mW power measured, we arrive at about $34\,\mathrm{mJ/cm^2}$ incidence fluence. At such pump fluences we would expect to see massive space charge or to even damage or destroy the sample, which is not the case.

Using a camera to take images of the laser spot reflected off the sample has major drawbacks. The camera used has a CCD chip, which is made of silicon. Silicon has a band gap of >1.1 eV [175], which requires 2 photon absorption at 1300 nm. Thus, after subtracting the background, one needs to take the square root of the intensity to measure the spot size or multiply the Gaussian standard deviation with $\sqrt{2}$ per dimension. Despite using both ways, we arrive at the spot size given above which is unrealistic. Unfortunately, we have no other data about the laser spots. Thus, we have to discard the direct measurement and resort to estimating the fluence from the observed dynamics.

Another way to assess our actual pump laser fluence is by comparison of our measured electronic temperature, via the Fermi edge broadening, with literature. From the large variation of electron temperatures and pump fluences in photoemission experiments [31, 129, 176] there seems to be no unique relation between the two quantities. Thus, we cannot unambiguously determine the pump laser fluence in our experiment from the electron temperature.

6.2.2 1600 nm Pump Laser Excitation

The data presented in this subsection was taken at a second beamtime in Artemis with an altered setup, thus the experimental parameters vary slightly compared to the previous section. The sample was pumped under 45° with 1600 nm s-polarized IR pulses and probed under normal emission with 35.7 eV XUV pulses. The local staff specifies the pulse durations with 40 fs for the IR and 30 fs for the XUV laser, thus we obtain a cross-correlation of 50 fs. The spot size evaluated from CCD images is about 70 µm × 95 µm (full width at $1/e$ height) which is smaller than expected or initially aimed for. At 1 kHz and with 75 mW power measured, we arrive at about 14 mJ/cm^2 incidence fluence. This value is more realistic compared to the measured pump fluence in Section 6.2.1. Nevertheless, we need to take the fluence with a grain of salt as the methodology is the same in both cases and yields unrealistically high values in the above section.

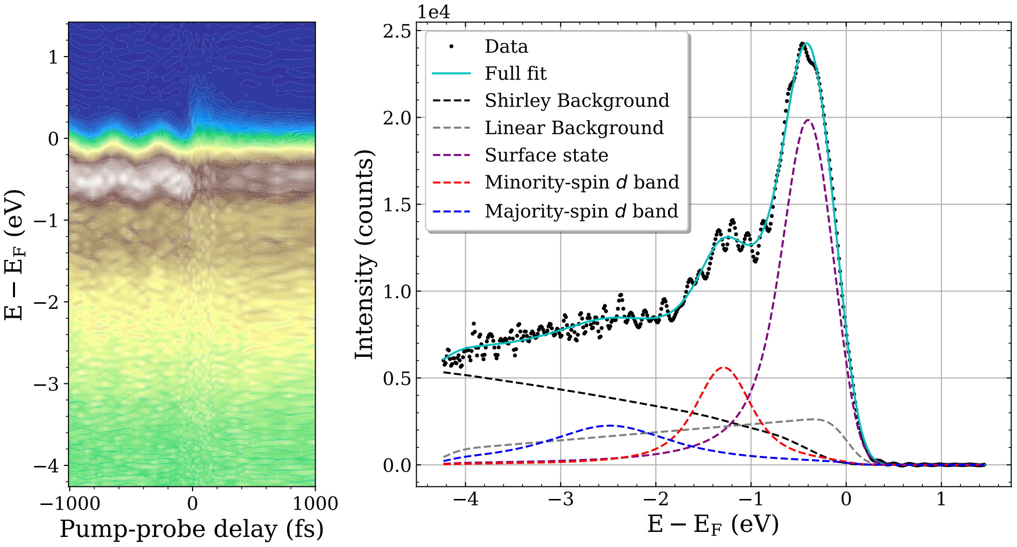

Figure 6.6: Left: Raw-data image plot of Gd/W(110) pumped with 1600 nm. Before time zero, the spectrum shows clear oscillations. Right: Static spectrum of Gd/W(110) with fit (solid line) and fit components (dashed lines). It corresponds to a vertical cross section of the raw data left.

A detail of the raw data set of Gd/W(110) is shown in Fig. 6.6, left. The oscillations of the photoelectron kinetic energy at negative pump-probe delays are expectedly even larger than when pumped with 1300 nm. The static spectrum in Fig. 6.6, right, corresponds to a vertical cut in the raw-data image on the left. Compared to Fig. 6.4, the data here has worse statistics. The majority-spin d state in the spectrum is hardly visible by eye and the surface state is significantly broader, to name two examples. Using the same fit procedure as before (the Hydrogen peak is omitted) we obtain the peak positions of the three Gd states whose dynamics are plotted in Fig. 6.7.

The peak positions of all states have similar oscillation amplitudes of about 60 meV. The black dashed lines are the fits of the oscillations using Eq. (6.5). As above, the fits are fairly satisfactory, but again, the majority-spin d state data deviates from a pure sinusoidal shape.

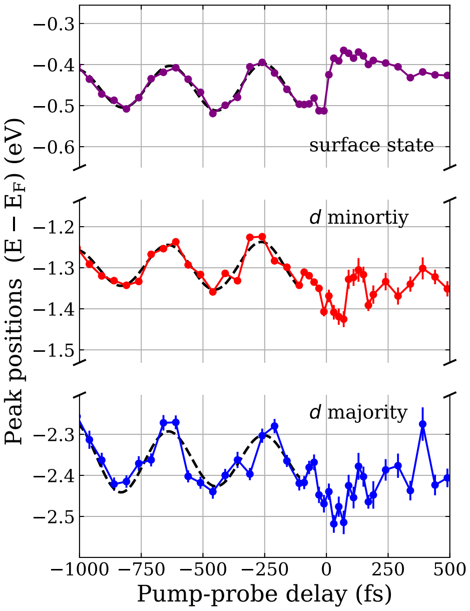

Figure 6.7: Dynamics of the three Gd states as obtained from a global fit of the raw data in Fig. 6.6. The dashed lines at negative delays are fits of the oscillations of the peak positions. The oscillation amplitude is similar for all states with about 60 meV.

Table 6.2 lists the values obtained from fitting the experimental data and values calculated with the ponderomotive acceleration model using our experimental parameters. Again, we assume an absorbed fluence of 1 mJ/cm^2 within the whole sample for the model calculation. In this section, we use the following parameters in the formula $\epsilon = \frac{2\Phi e^2 \sqrt{R}\cos\alpha}{\epsilon_0 m_e^2 \omega c^2} p_x$: The reflectivity $R = 0.79$, the incidence angle $\alpha = 45°$, $\omega = 2\pi c/\lambda$ for $\lambda = 1600\,\text{nm}$ and $p_x = \sqrt{2 m_e E_\text{kin}}$ with $E_\text{kin} = E_\text{HHG} - \Phi_\text{Gd} - E_\text{B}$, where $E_\text{HHG} = 35.7\,\text{eV}$, $\Phi_\text{Gd} = 3.7\,\text{eV}$ and E_B is the binding energy of the Gd states. The model calculation yields values of the same order as the data under the assumption of the pump fluence above.

Reverse engineering in the same manner as in Section 6.2.1, we deduce an absorbed fluence of about 1.65 mJ/cm^2 or an incident fluence of 7.9 mJ/cm^2 which seems plausible as well. However, comparing the demagnetization or shift of band positions after time zero between pumping with 1300 nm and 1600 nm, we see that in the former case the pump effect looks more pronounced. This contradicts the similar pump fluences that we assess from the ponderomotive acceleration model and points out the limitations of this approach.

	ϵ [meV]		$2\pi/\Omega$ [fs]		$\Psi[°]$
state	fit	model	fit	model	fit
surface	59 ± 6	36.9	380 ± 6	340	152 ± 8
d minority	61 ± 11	36.4	380 ± 11	344	161 ± 14
d majority	59 ± 18	35.7	384 ± 14	351	148 ± 21

Table 6.2: Oscillation amplitudes, periods and phase shifts of the three Gd states when pumped with 1600 nm. Amplitudes were calculated using our experimental parameters assuming an absorbed fluence of $1\,\mathrm{mJ/cm^2}$ within the whole sample. Amplitudes and periods from fitting of the data and expectations from the ponderomotive acceleration model are comparable. The phase shifts show some variation, but are all in the expected range below 180°.

In analogy to Section 6.2.1, we find that the calculated oscillation periods are similar to the experimental results. In contrast to the above section, the model this time underestimates the period instead of overestimating it. In both cases, the deviations are of the order of 10 %, which is reasonable within the uncertainties of the experimental parameters[4]. The phase shifts meet the expectations and are again below 180°.

Summing up, we find a good agreement between model calculations and experimental data. At least for the oscillation periods we can state, that the model's deviations are of no simple systematic nature, but scatter around the experimental data.

Up to now, all data we have investigated regarding kinetic energy modulations were measured on Gd/W(110) samples. We wondered, if this might be related to a characteristic of Gd thin films, as such oscillations in photoemission spectra have not been reported elsewhere to our knowledge. But according to the transient grating model, these oscillations should occur at any metal surface. Thus, we decided to perform an investigation on our substrate W(110). In addition, by measuring on W(110) we simplify the system under investigation as we avoid some potential influences from the Gd top layer. First, we avoid complications simply because of the fact that there is a thin film on the metal substrate and second, Gd is ferromagnetic which possibly could play a role as well. On this simpler system, we varied the pump photon energies to make a more systematic study of the ponderomotive model with respect to this parameter.

6.3 Oscillations on W(110)

The pump and probe laser parameters used to measure the data presented in this section are largely the same as in the previous section, except for the pump photon energies and spot sizes. We used five different wavelengths to pump the tungsten sample: 1148 nm, 1300 nm, 1384 nm, 1450 nm and 1610 nm. The experimental pump fluences are again unreliable. The spot sizes determined from the CCD images range from $46 \times 90\,\mu\mathrm{m}^2$ to $77 \times 177\,\mu\mathrm{m}^2$ (full width at $1/e$ height). Considering the incidence angle of 45°, the repetition rate of the laser system of 1 kHz and 150 mW power measured, we would arrive at incident pump fluences in the range of 14–46 mJ/cm^2, the latter being unrealistically high.

---

[4] The uncertainties in Table 6.2 are the statistical uncertainties arising from the fit. Uncertainties from other sources like the setup geometry are not included.

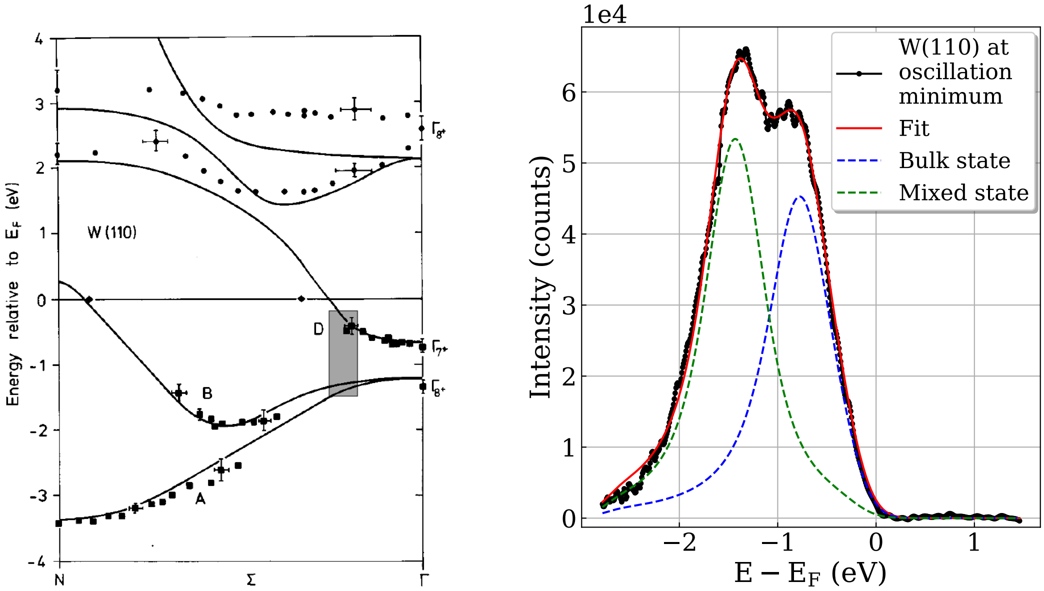

(a) W(110) band structure

(b) W(110) spectrum at oscillation minimum

Figure 6.8: States of the W(110) sample. (a) Band structure calculation and experimental data along $\Gamma - \Sigma - N$. The shaded area indicates the estimated $k_\perp$-vector probed in our experiment. Image taken from [177]. (b) Spectrum of W(110) with fit (solid line) and fit components (dashed lines). This spectrum is taken at an oscillation minimum of the raw-data image pumped with 1610 nm in Fig. 6.9.

W(110) is a well-studied material that has been investigated with a variety of methods, both experimentally and theoretically [177–183]. In [177], a band structure calculation by Christensen *et al.* [179] complemented with experimental data from [177, 182] show the band dispersion of W(110) along $\Gamma - \Sigma - N$, *cf.* Fig. 6.8a. In our measured spectra (Fig. 6.8b), we can identify two peaks at about (-0.69 ± 0.04) eV and (-1.33 ± 0.03) eV with the bands labeled Γ_{7+} and Γ_{8+} in Fig. 6.8a. In addition to those two bulk bands, there is a surface resonance at about -1.2 eV [177, 181], which is not separable from the Γ_{8+} state in our spectra. Thus, henceforth we will use the labels "bulk state" for the peak at -0.69 eV and "mixed state" for the one at -1.33 eV binding energy.
Willis *et al.* [184] calculated the W band structure up to 48 eV above E_F. Taking their work as a basis we can assess the $k_\perp$-vector of our transition from our photon energy of 35.7 eV and the peaks we observe. The so estimated $k_\perp$-vector is marked as the shaded area in Fig. 6.8a. From the energetic position of the peaks, a $k_\perp$-vector closer to Γ would seem more likely.

The spectrum in Fig. 6.8b was fitted with two Lorentzian functions cut off by the Fermi edge and convolved with a Gaussian distribution for the experimental resolution. The integrated signal intensity was used as a Shirley-like background.
Note, the Fermi level E_F in all graphs is the unperturbed Fermi level which is the average of the oscillating Fermi levels before time zero. Per time step, the individual Fermi levels in the fit oscillate in energy similar to the two W states. The unperturbed Fermi level, necessary to have a fixed reference point, is obtained in the same way as for Gd, *cf.* end of Section 5.2.1, by fitting the oscillating Fermi levels and using the offset of the sinusoidal fit as the Fermi level position.

Pumping W(110) with IR laser pulses leads to large oscillations in the kinetic energy of the measured photoelectrons. Fig. 6.9 shows the electron dynamics in a series of raw-data images for the five different pump wavelengths. The two most obvious features are, first, the strong increase in oscillation amplitude and, second, the increase of the modulation period with increasing pump wavelength.

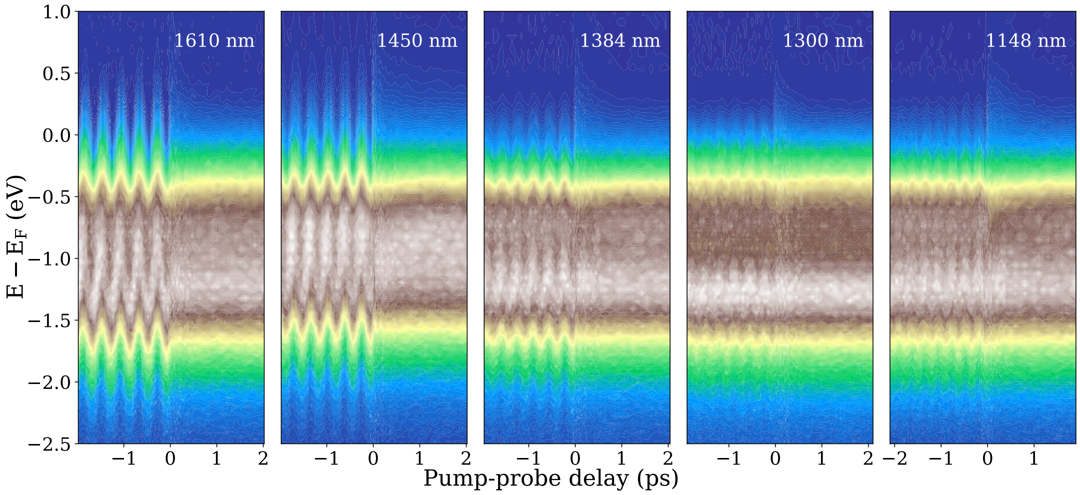

Figure 6.9: Dynamics of W(110) for different pump wavelengths. The oscillation amplitude and modulation period increase with increasing pump wavelength.

Apart from these main features, there are some variations in the peak intensities between the different data sets. The most prominent difference to the other spectra is seen for a pump wavelength of 1300 nm, where the peak intensity of the bulk state is clearly lower than for the other pump wavelengths. These differences in peak intensities occur in static measurements as well. Thus, we suspect an influence of the sample surface quality, as the sample was flashed every time after changing the pump wavelength. Other experimental influences, like the sample temperature, base pressure and time between flash and measurement, are similar for all data sets and among the slight variations of these factors there are no clear trends between peak intensity and experimental factor. Otherwise, it is not clear, why the peak intensities should change between different data sets. Fortunately, for the following results, the peak intensities are not crucial.

Coming back to the main features, we realize, that the two trends, for the oscillation amplitude and for the modulation period, qualitatively agree with the expectations from the transient grating model, as $\Omega \propto \omega$ and $\epsilon \propto 1/\omega$. To obtain a more quantitative result, all spectra for all pump-probe delays were evaluated and the oscillations of the two peaks fitted using Eq. (6.5). Two examples of those fits are shown in Fig. 6.11 and the trends of the resulting fit parameters are plotted in Fig. 6.10. The parameters for the Fermi level are shown as well, although its determination is difficult because there is no high intensity in our spectra around the Fermi level except for the tail of the bulk state.

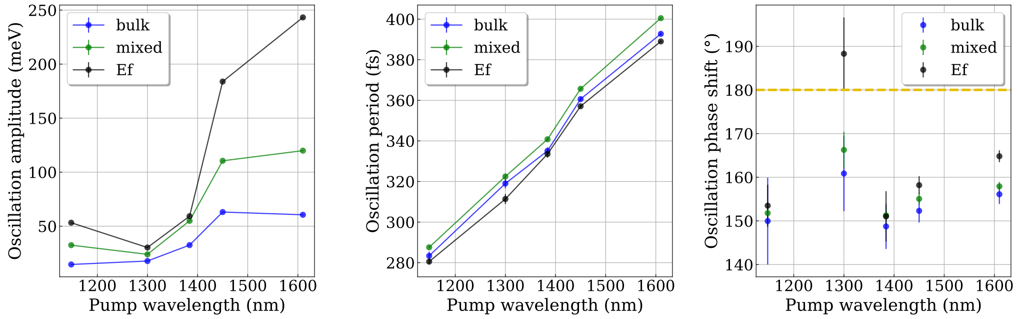

(a) amplitudes **(b)** periods **(c)** phase shifts

Figure 6.10: Oscillation fit parameters versus pump wavelength. (a) The fitted amplitudes increase step-like with increasing pump wavelength. (b) The oscillation periods depend linearly on the pump wavelength. (c) The phase shifts are in a range 150–165° for all pump wavelengths.

Additionally, we can cross-check our pump laser pulse duration, as the damping $B = \frac{p_x^2 \cos^2 \alpha}{2(m_e c \sigma)^2}$ depends on the pulse duration σ. From the fits of the two states and the Fermi level of the data set pumped with 1610 nm, we obtain a pulse duration of (35 ± 3) fs. This value is close to the expected pulse duration of 40 fs. Though this data set yields very good results, deviations are larger for other data sets. For instance, the pulse duration obtained from the data set pumped with 1148 nm is 12 fs and thus clearly too small.

Let us shortly discuss the three parameters beginning with the phase shift. The phase shifts of the standing waves are in a range of 150–165° for all pump wavelengths, see Fig. 6.10c, which agrees with our expectations from the transient grating model and the discussion thereof, see end of Section 6.1.1. The one outlier for the Fermi level pumped with 1300 nm might result from the difficulty to fit the Fermi level in that scan. As the intensity of the bulk state is low in this data set, the intensity at the Fermi level is so as well resulting in very large uncertainties for the fitted Fermi level.

The oscillation period shows a clear linear dependence on the pump wavelength, see Fig. 6.10b, which agrees with the transient grating model. Moreover, we obtain a reasonable quantitative agreement between our data and the prefactor in the model.

On average, the slope in our data is $(0.243 \pm 0.007)\,\mathrm{fs\,nm^{-1}}$ which is about 10 % larger than the model would predict ($0.219\,\mathrm{fs\,nm^{-1}}$).

For the oscillation amplitudes, the pump wavelength dependence is less obvious, see Fig. 6.10a. The trend is more step-like and does not correspond to the model, which would predict a linear dependence on λ. Unfortunately, the oscillation amplitude scales with the pump laser fluence, which is not reliable in our case. In addition, should the surface quality vary, this could influence the amplitudes as well, as the IR reflection R could change. However, the last point should only play a minor part compared to the uncertainty in the pump fluence. In any case, we have to be careful with the significance of the exact amplitude trends. Qualitatively, the increase of the oscillation amplitude with increasing pump wavelength does match in experiment and transient grating model.

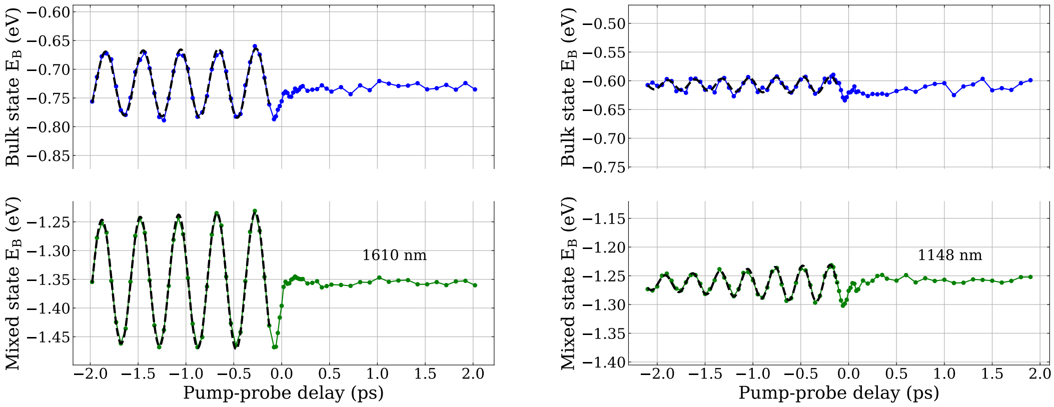

(a) 1610 nm pump

(b) 1148 nm pump

Figure 6.11: Electron dynamics of the bulk and mixed states for (a) 1610 nm and (b) 1148 nm pump wavelength. The dashed lines are fits using Eq. (6.5). The oscillation amplitudes are clearly larger when the sample is pumped with longer wavelengths, but in both cases the oscillation amplitudes are larger in the mixed state than in the bulk state.

Nevertheless, there is one unexpected aspect which is not affected by the above uncertainties. Already present in Fig. 6.10a, but more obvious in Figs. 6.11 and 6.12, the two states oscillate with different amplitudes. This is especially apparent for the large pump wavelengths, *c.f.* Fig. 6.11a, but also visible for short pump wavelengths, *c.f.* Fig. 6.11b. This result is unexpected, as it objects the predictions from the transient grating model.

To recapitulate, in the transient grating model, electrons are photoemitted and while on the way to the detector, they experience an acceleration due to the transient grating formed by the IR pump pulse. In this picture, the electrons are free and should accelerate in the potential in equal measure, only depending on their kinetic energy. But, in our case, the kinetic energies are very similar (29.4 eV and 30.1 eV) and cannot account for

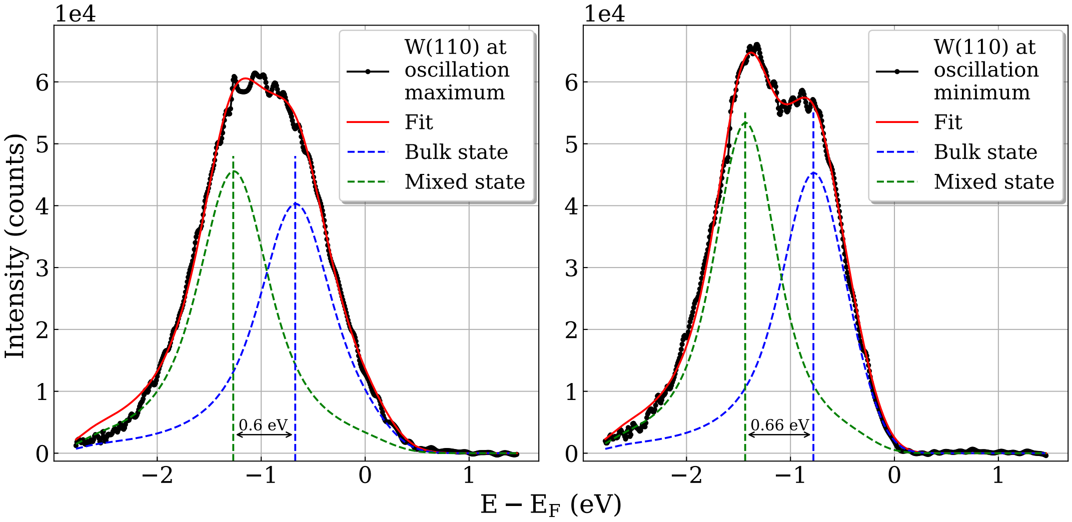

Figure 6.12: Spectra of W(110) with fit (solid line) and fit components (dashed lines) for two different pump-probe delays when pumped with 1610 nm. Left: Spectrum at oscillation minimum. Right: Spectrum at oscillation maximum. The two peaks oscillate with different amplitudes, thus changing the general shape of the spectrum and the energetic separation of the two states from 0.6 eV to 0.66 eV.

the large difference in oscillation amplitudes, *e.g.* 61 meV and 120 meV for the bulk and mixed state, respectively, when pumped with 1610 nm. Interestingly, such a behavior was not observed in Gd/W(110), *c.f.* Section 6.2. The surface state of Gd does show a slightly larger oscillation amplitude, but within error bars the amplitudes of the bulk states are comparable.

Accompanying the oscillations in the amplitude, we find similar oscillations in the half width at half maximum (HWHM) in the bulk and mixed states, see Fig. 6.13. The phase and period of the oscillations in the HWHM follows the oscillations in the amplitudes when pumped with 1610 nm. At a pump wavelength of 1148 nm, when the oscillations get weaker, the HWHM show strong noise and the assessment of the oscillations is hardly feasible.
We performed global fits setting the HWHM constant but found no qualitative impact on the oscillations of the peak positions. In particular, the different amplitudes for the two states persisted.

One approach is to explain the above observation in a classical picture by, for example, more carefully analyzing the spatial distribution of the photoemitted electrons. The different spatial distribution could come about by the different orbital character or symmetry of the states. Then the idea is, that electrons from different initial states take different paths to the detector and are affected differently by the transient grating. An electron emitted under an angle α to the normal direction will see a potential that

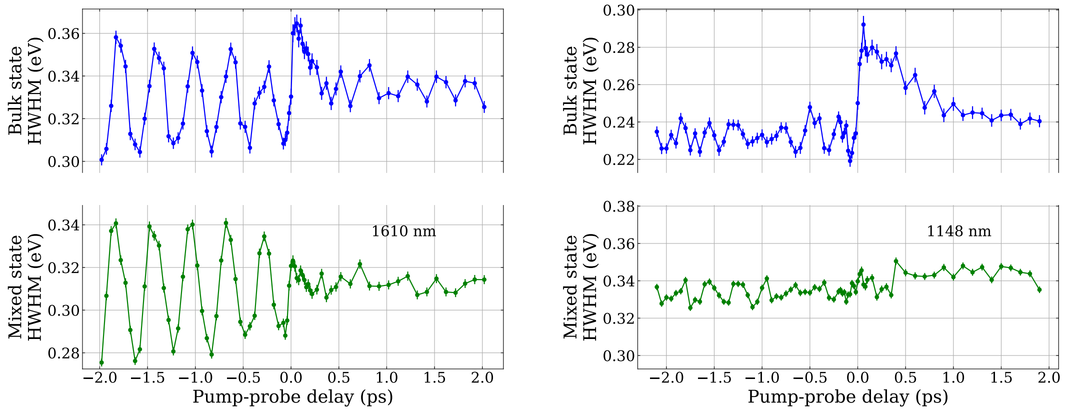

(a) 1610 nm pump

(b) 1148 nm pump

Figure 6.13: Dynamics of the HWHM of the W(110) bulk and mixed states for (a) 1610 nm and (b) 1148 nm pump wavelength. For 1610 nm pump wavelength, the oscillations of the HWHM before time zero resemble the oscillations of the peak positions shown in Fig. 6.11 with respect to the phase and period. At 1148 nm pump wavelength, the noise makes an assessment difficult.

is stretched by $1/\cos(\alpha)$, stretching the oscillation period accordingly. However, the oscillation amplitude should not be affected. The electron might change its momentum direction, as the acceleration is directed along the normal direction, bending the path towards the normal direction. But again, the impact is of the order $1/\cos(\alpha)$. With a detection angle of about 5°, $1/\cos(\alpha) \approx 1.004$ and thus any contribution from the angular distribution will be much smaller than the effect of the different amplitudes. Under these considerations, a fully classical explanation is not evident.

Another idea to explain the different amplitudes is to drop the assumption that the electron is free when subjected to the ponderomotive potential. Thereby, we would assume the electron to still have some information of its initial or final state when accelerated in the transient grating, so that electrons excited out of different states could be accelerated by different amounts. This idea is rather vague and highly controversial, as the general understanding in photoemission, both in the one-step and the three-step description of photoemission [109, 185], is that the electron is free within very short time and length scales of atomic distances and at most a few femtoseconds, respectively. In our data, we see the difference in oscillation amplitudes up to 2 ps or about 5 µm distance from the surface, which contradicts the well-established theoretical descriptions of PES. To follow the idea of non-free electrons, it is necessary to find a physical reason why the plane wave description of the photoemitted electrons should break down in the case of W(110) for our experimental setup.

In a collaboration with J. Braun we discussed how the effect of ponderomotive acceleration could be represented in the fully relativistic one-step model of photoemission [117, 186]. He proposed to extend the classical approach by introducing a complex phase in the plane wave of the final state as the effect of the disturbance by the ponderomotive potential. The plane wave phase $\exp(ikx)$ is determined by the parameters k and x which are taken from the experiment, where k is the electron momentum at the distance x from the sample surface which corresponds to the measured energy at a certain pump-probe delay in the experiment. One set of those parameters is used to calculate the whole photoemission spectrum.

In addition, the calculation is performed in two steps. First, the classical photoemission process is used to obtain an initial state of the unperturbed system. Then, the matrix elements are calculated for the disturbed final state with the undisturbed initial state.

	$E_{\mathrm{max}} - E_{\mathrm{min}}$ [meV]		
state	model 1	model 2	experiment
bulk	165	153	121 ± 4
mixed	94	82	240 ± 4

Table 6.3: Difference of the W(110) bulk and mixed state peak positions between the maximum and minimum of the ponderomotive oscillations. We compare experimental results (pumped with 1610 nm) with theoretical calculations by J. Braun using an extended fully relativistic one-step photoemission model. For the model, two sets of parameters were used: Model 1 uses experimental parameters for k and x obtained from the mixed state, model 2 uses parameters for k and x obtained from the bulk state. Despite disagreement with the experimental values, both parameter sets yield qualitatively different amplitudes in the two W(110) states.

Preliminary results using this new approach for the photoemission of W(110) show that indeed a different amplitude can be obtained for the mixed and bulk states, *cf.* Fig. 6.14 and Table 6.3. The table shows the difference in the W(110) peak positions between the maximum and minimum of an oscillation. For the theoretical calculations two different sets of parameters were used. One (k, x) value pair is extracted from the mixed state, the other from the bulk state. Per state, the binding energies were extracted for the oscillation minimum at about -1.6 ps and the oscillation maximum at about -1.8 ps. The experimental data set for a pump wave length of 1610 nm was used, *cf.* Fig. 6.11a.

The difference of the peak positions in the theoretical calculations are 94 meV (mixed state parameters) and 82 meV (bulk state parameters) for the mixed state and 165 meV and 153 meV for the bulk state. This difference is also evident from the calculated spectra in Fig. 6.14. The black curve is the spectrum of the undisturbed photoemission. The blue curves are the spectra for a parameter set extracted at the maximum of an oscillation in the experimental data, the orange curves for a minimum of an oscillation. Dark coloring indicates that the parameter set was taken for the bulk state, light coloring for the mixed state.

The spectra calculated from the oscillation maxima for both states are very similar (blue curves), the according spectra for the oscillation minima (orange curves) show slightly different shifts to lower energies. The crucial point is, however, that for both models (dark and light coloring) the shift of the bulk and mixed state peaks are different, the bulk state shift being larger than the mixed state shift (comparing the high- and

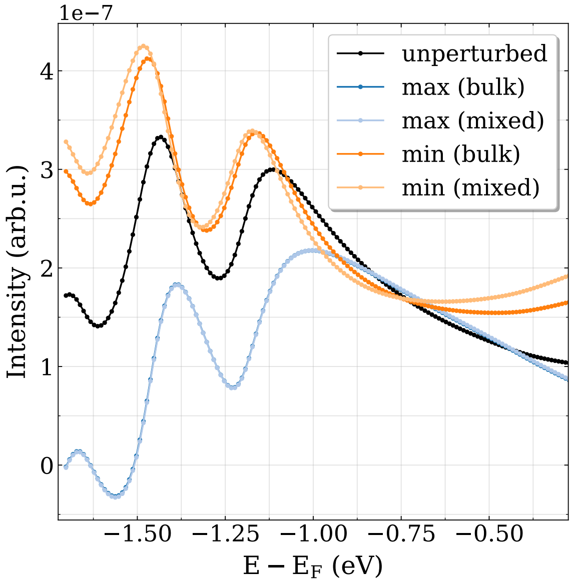

Figure 6.14: Spectra of W(110) calculated by J. Braun with the extended fully relativistic one-step model of photoemission. The black curve is the unperturbed photoemission spectrum of W(110). The other four curves correspond to different parameter sets used to model the effect of the ponderomotive oscillations. For the model, two parameters were extracted from the experiment: The energy shift of the photoelectrons and the corresponding pump-probe delay. The labels 'bulk' and 'mixed' refer to whether the parameters were extracted from the bulk or mixed state and 'min' and 'max' indicate whether the oscillation is in an energetic minimum or maximum. Despite variations in peak shape and intensity the major feature of different peak position shifts for the two states is reproduced in the calculations, *cf.* blue and orange curves.

low-energy peak positions between the blue and orange curves). Unfortunately, the magnitude of the oscillations is reversed between the experimental observations and the calculations.

So, despite deviating values, both model calculations yield the qualitatively different peak shifts of the two states as seen in the experimental data. This would indicate that a disturbance of the plane wave in vacuum far from the sample system does affect the transitions in the sample.

However, the preliminary results are as yet very sensitive to the chosen parameters. With the values from experiment, these two parameters produce a factor of the order 10^5 in the exponent resulting in a highly oscillating phase. In the theoretical calculation, small variations in k and x produce very different results. Hence, the new approach needs to be refined to model the experiment more satisfactorily, especially, as it makes a highly controversial assumption about the free state of photoemitted electrons, which is a well-established concept in photoemission spectroscopy (PES).

6.4 Summary

In conclusion, we have studied how pump laser pulses can influence photoemitted electrons long after their excitation and after they have left the sample surface. We found oscillations in the kinetic energy of such photoemitted electrons which can be reasonably well described by a model developed by Bovensiepen *et al.* [168]. The model assumes a ponderomotive acceleration of the free photoemitted electrons by a transient grating formed by the interference of the incoming and reflected IR pump laser pulse.

We extended the model to describe the time span of overlapping pump and probe pulses and found a potential influence of the ponderomotive acceleration on other pump laser-induced dynamics on time scales of the pump-probe cross-correlation. In our case, this influence is negligible.

Measurements on Gd/W(110) thin films with 1300 nm and 1600 nm pump pulse wavelength show strongly enhanced oscillation amplitudes compared to observations by Bovensiepen *et al.* [168]. Our data is compatible with the model within the uncertainties due to a highly uncertain experimental pump laser fluences.

A pump photon energy-dependent series of measurements on W(110) shows a good agreement with predictions from the ponderomotive acceleration, but also reveals some surprising results. Clearly, oscillation amplitudes and modulation periods increase with increasing pump wavelength. Fits to the data yield parameters like the oscillation amplitude, period and phase which generally follow the trends expected from the theoretical model.
However, the mixed and bulk states in W(110) exhibit prominently different oscillation amplitudes, with the difference being significantly larger than predicted by the ponderomotive acceleration model. This behavior is especially unexpected as the electrons are generally assumed to be free once they leave the sample surface and should react in a similar fashion to a given potential. A first preliminary calculation by J. Braun using a modified fully relativistic one-step model of photoemission yields different shifts of the bulk and mixed states, although the magnitudes of the oscillations for the two states are inverse compared to the experimental results. Moreover, the model so far is very sensitive to the experimental parameters which suggests some deficiency in the current version. Still, the principle result of different amplitudes for the two states in W(110) encourages further exploration.

Chapter 7

Summary and Conclusion

High-technology industry continuously advances the development of magnetic storage devices with ever higher storage density and faster reading and writing of bits, but new approaches are sought for as current technologies run into a limit for the switching speed of magnetic bits. Ultrafast switching using short laser pulses promises technological merits, however, the physics of laser-induced magnetization dynamics also comprise a wealth of fundamental physical phenomena which are not yet comprehensively understood. By more thoroughly understanding the fundamental physics science can provide a good base of knowledge for more directed research and development of new technologies.

We investigated the ultrafast magnetization dynamics in Gd trying to understand in detail the mechanisms causing the demagnetization and to reconcile the partially conflicting results found in literature. Using different experimental techniques we obtain complementing information of the dynamics achieving a more complete picture of the physics. First, using X-ray magnetic circular dichroism (XMCD) in reflection we studied the laser-induced dynamics in Gd over a wide range of time scales for a series of pump laser fluences and modeled these dynamics with an extension of the microscopic three-temperature model (M3TM). Second, using angle-resolved photoemission spectroscopy (ARPES) with high temporal resolution, we delved into the sub-100 fs dynamics where the magnetic signal shows an unexpected short-lived increase before demagnetization sets in. Third, in our ARPES study, we observed oscillations in the measured kinetic energy of photoemitted electrons and investigated this effect for a variety of pump photon energies.

In Chapter 4, we focused on improving the understanding of the dominant driving mechanisms behind ultrafast magnetization dynamics in Gd. Though a full picture still eludes, we can shed light onto several aspects of the dynamics. Using XMCD in reflection, we varied the pump laser fluence and recorded the magnetization dynamics in Gd/W(110) thin films. Generally, our data shows a two-step demagnetization with time scales of below 1 ps and tens of ps, similar to previous magneto-optical Kerr effect (MOKE) [128] and XMCD [23] studies but contradicting ARPES data [22, 129], which shows only one time scale for each magnetic subsystem, the $4f$ and $5d6s$ moments. However, the observed time scales for the $5d6s$ and $4f$ moments in the ARPES studies are similar to the two steps observed for the $4f$ moments in our XMCD data. We discuss the possibility that a hybridization between the $4f$ and $5d6s$ states, caused by the core-hole in the probing process in XMCD, imprints the fast $5d6s$ dynamics onto the $4f$ dynamics. We observe a shift of the unoccupied $4f$ state towards the Fermi level enabling a hybridization with the valence bands which could alter the availability of states for the $3d \rightarrow 4f$ transition.

Our pump laser fluence-dependent data set of the magnetization dynamics of Gd, a type II ferromagnet (showing a two-step demagnetization), complements similar data sets for type I materials, which show a single-step demagnetization. Successfully modeling the data using an extended M3TM, we can show that Elliott-Yafet-type scattering plays a dominant role in the laser-induced magnetization dynamics in Gd. However, with vanishing orbital momentum, Gd is a special case and the applicability of the model to systems with non-vanishing orbital momentum remains uncertain.

On the sub-ps time scale, we find an exponential dependence of the demagnetization amplitude on the pump laser fluence implying that a complete demagnetization of single-crystalline Gd is not practically possible on this time scale. However, researchers have observed even a reversal of magnetic orientation of alloys containing Gd hinting at more complex processes in multi-atomic structures. On the slow time scale, the demagnetization follows a linear trend with increasing pump laser fluence. Notably, at high pump laser fluences, the demagnetization shows a reduced efficiency which might be related to the already high disorder in the system. The physical cause behind the reduced efficiency is not known so far.

A comparison of dynamics measured at the Gd M_4 and M_5 absorption edges suggests no significant changes in the contributions of the angular orbital momentum L and the spin momentum S to the total spin moment, but the result is preliminary since the sums rules for absorption measurements cannot be applied directly for reflection measurements.

Pumping with lower pump photon energies reduces and slows down the demagnetization in Gd on the fast, sub-ps time scale implying an influence of the initial hot electron distribution onto the early dynamics. Hot electrons of higher energies could amplify spin transport and increase spin-flip scattering probabilities.

In Chapter 5, we shed light onto the first 100 fs of ultrafast magnetization dynamics trying to discover physical processes while the electron subsystem is itself out of equilibrium. Using ARPES, we find similar overall dynamics in the exchange splitting of Gd/W(110) thin films to literature. However, in our measurements, the majority- and minority-spin bulk bands react instantaneously to the laser excitation and we see no delay in the majority-spin bulk band response as reported in literature. Also in contrast to literature, both bands show more similar time scales of the dynamics with time constants of (34 ± 13) fs and (430 ± 90) fs for the majority-spin bulk state and (83 ± 45) fs and (290 ± 160) fs for the minority-spin bulk state.

Most surprising, though, is an increase of the exchange splitting in the first 100 fs after laser excitation denoting an increase in magnetization in the bulk bands. Intriguingly, the majority-spin surface and bulk states exhibit a shift in binding energy in opposing directions, despite the same orientation of the spins. Thereby, the majority-spin bulk band moves away from the Fermi level to higher binding energies, contrary to what one would expect if the laser pulse just caused a demagnetization.

An effect proposed by Dewhurst *et al.* [148] might explain our observations. In this picture, optically induced spin transfer (OISTR) between different parts of a material give rise to different magnetization dynamics at different sites. Applying this concept to Gd and the dynamics we observe, the laser pulse excites electrons from the majority-spin surface state to the majority-spin bulk state, thus moving spin momentum from the surface to the bulk and causing the opposing shift in the peak positions. In the minority-spin states, the dynamics are more involved and harder to observe, particularly since we cannot measure the unoccupied minority-spin surface state. Still, traces of this effect seem to show in our data.

The OISTR effect should depend on the sample temperature as at lower temperatures the spin polarization in the individual states is comparatively higher and a rearrangement of electrons with this higher spin-polarization should induce a larger exchange of spin momentum between the involved regions. The effect might have been hidden in previous experiments at higher temperatures, with longer pump pulses and less temporal resolution, but be reflected in the delayed response of the majority-spin bulk band to the laser excitation [129].

In Chapter 6, using ARPES, we investigated the influence of the pump laser onto photoemitted electrons which appear as oscillations in the measured kinetic energy at negative pump-probe delays, *i.e.* when the photoemitting ultraviolet (UV) pulse arrives at the sample before the infrared (IR) pulse.

Oscillations of that kind have been described in literature [168]. The authors propose a model in which the electrons experience a ponderomotive acceleration by the transient grating formed by the interference of the incoming and reflected parts of the IR pump laser. We extended this model to include the time range where the probe and pump pulses overlap and could infer that, in principle, the ponderomotive acceleration can affect pump-laser induced dynamics on the time scale of the pump-probe cross-correlation. Fortunately, this influence is negligible in our measurements.

On Gd/W(110) thin films, we find strongly enhanced oscillations up to 30 meV, compared to 1 meV in literature [168], which are compatible with model predictions. Unfortunately, we have to consider large uncertainties in the pump laser fluence in evaluating our data.

In a similar study on W(110) for varying pump laser wavelengths we find that the oscillation amplitudes and modulation periods increase with increasing pump wavelengths. The oscillation amplitudes, periods and phases extracted from the experimental data show a dependency on the wavelength that one would expect from the ponderomotive acceleration model. However, the oscillation amplitudes of the two measured W(110) states differ by about a factor 2 which is much larger than what should result from the ponderomotive acceleration model. Particularly puzzling is the fact, that electrons are generally assumed to be free within few fs after excitation and should experience a similar force if subjected to the same potential.

Preliminary calculations using a modified one-step model of photoemission can obtain the difference in the oscillation amplitudes, but the high sensitivity of the model on experimental parameters hints at an shortcoming in this approach and motivates further research.

Concluding, we could contribute to the understanding of and illuminate some new fundamental aspects of the complexities in the physical phenomena of ultrafast magnetization dynamics. Although a comprehensive picture of the intricate interplay of physical processes underlying laser-induced magnetization dynamics in ferromagnets still eludes, each finding helps advancing fundamental physical understanding and thus the progress to a knowledge-driven development and optimization of technological devices.

Appendix A

Laser Fluence Dependence of Magnetization Dynamics in Gd

A.1 Thermocouple Calibration

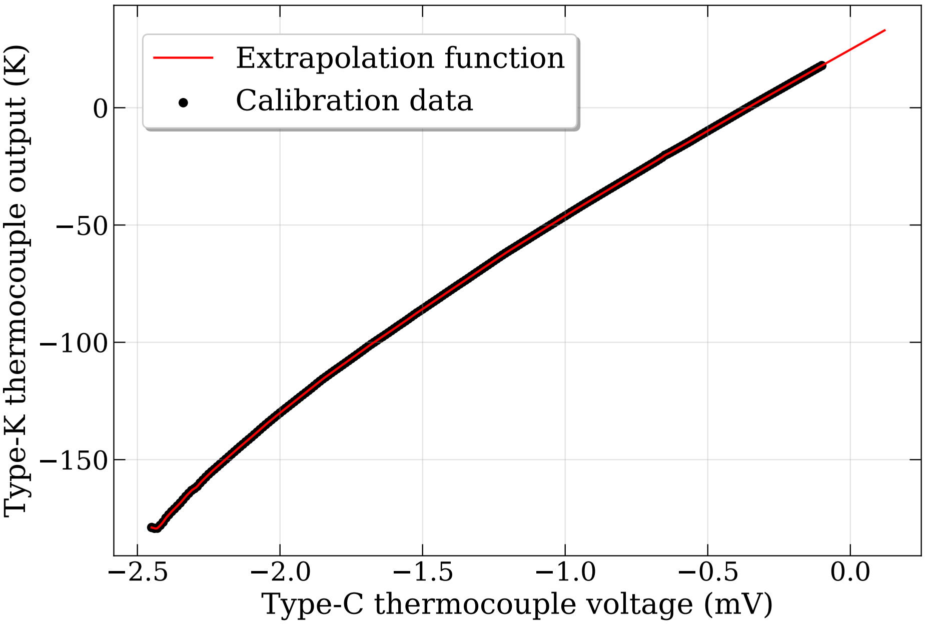

Figure A.1: Calibration of the type-C thermocouple for low temperatures using an additionally installed type-K thermocouple for reference.

Due to experimental circumstances we are using a type-C thermocouple to measure low temperatures outside its specified operation range. This necessitates to calibrate the type-C thermocouple. Therefore, a type-K thermocouple was installed at the sample in addition to the type-C thermocouple and the manipulator was warmed-up and cooled down several times recording the output of the two thermocouples. Figure A.1 shows the output of the type-K thermocouple versus the type-C thermocouple voltage. The calibration data is the mean of the warm-up data which was extrapolated using Python's

interpolate.interp1d() function with an added linear extrapolation part.
The cooling down data shows large variations between different cycles whereas the warming-up data is consistent. We presume that the additionally installed type-K thermocouple connection might be susceptible to changes in temperature. Since the cooling down takes only about one hour while the warming-up takes more than 10 h, it is more probable that the cooling down data is affected by the imperfect type-K thermocouple connection. On these grounds we decided to use only the warming-up data for the thermocouple calibration.

A.2 Saturation Correction of Absorption Data

As explained by Nakajima *et al.* [95], total electron yield measurements are not directly proportional to the absorption coefficient as is the case in transmission experiments. In transmission, the absorption coefficient directly determines how strongly the X-ray intensity is reduced. For total electron yield, one has to consider that the excited electrons need to escape from the sample surface to be detected either by a channeltron or as a sample current. Thus, the interplay of the penetration length of the X-rays λ_x and the escape depth of the excited electrons λ_e influences the relation between the electron yield Y_e and the absorption coefficient μ. According to [95], the relation for a sample of semi-infinite thickness is given by:

$$Y_e = C \left(\frac{1}{1 + \lambda_e / \lambda_x \cos(\theta)} \right) \mu \ , \tag{A.1}$$

where θ is the incidence angle with respect to the sample normal. The proportionality constant is given by $C = I_0 G \lambda_e / \cos(\theta)$ where I_0 is the number of incident photons and G is the electron gain function which describes the average number of electrons produced by an initial Auger-electron, which is proportional to the photon energy.

Considering extreme cases, we can see how saturation affects the absorption signal. If $\lambda_e \gg \lambda_x \cos(\theta)$, where $\lambda_x \cos(\theta)$ is the penetration depth along the surface normal, then $1/(1 + \lambda_e/\lambda_x \cos(\theta)) \approx \lambda_x \cos(\theta)/\lambda_e$ and (with $\lambda_x = 1/\mu$) $Y_e \approx C \cos(\theta)/\lambda_e$ is constant and we have complete saturation. If $\lambda_e \ll \lambda_x \cos(\theta)$ then $Y_e \approx C\mu$ and there is no saturation effect.

To correct for saturation effects in our absorption measurements we need values for λ_e and λ_x. We use the approach for semi-infinite samples since our large angle $\theta = 85.5°$ makes the penetration depth small versus the sample thickness d_{sample}, $\lambda_x \cos(\theta) \ll d_{\text{sample}}$. Furthermore, we assume $C = 1$ as was done in [95] for Fe, Co and Ni. This is justified if C does not depend strongly on energy. With $C = 1$, our results will only be proportional and not equal to μ, but since we regard only ratios in the sum rules, this should not affect the results.

We use the universal curve of the inelastic mean free path for the electron escape depth and obtain $\lambda_e \approx 2\,\text{nm}$ for 1 keV electrons. For the penetration length of the

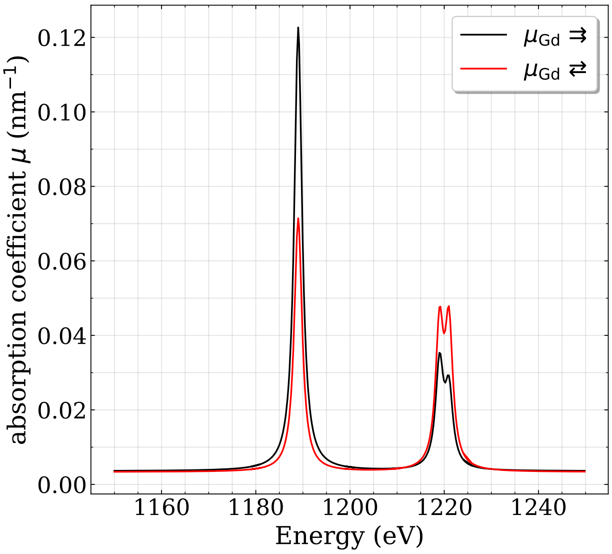

Figure A.2: Approximation of the absorption coefficient for Gd as determined by Prieto *et al.* [96]. The function consists of three Lorentz peaks of 1 eV HWHM whose peak heights are set equal to the absorption coefficients given in [96].

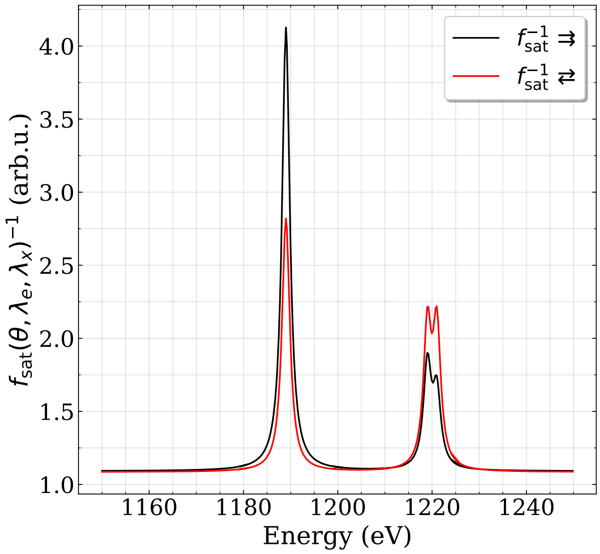

Figure A.3: Correction function for our absorption measurements of Gd to account for saturation effects. The function, as described in [95], is given in Eq. (A.1). We assume $C = 1$, have $\lambda_e = 2\,\mathrm{nm}$ and $\theta = 85.5°$, and use $\lambda_x = 1/\mu$ from Fig. A.2.

X-rays $\lambda_x = 1/\mu$ we use data published by Prieto *et al.* [96]. From the tabulated values (Table II in [96]) for the Gd M absorption edges we construct an approximate energy- and polarization-dependent function for μ, see Fig. A.2. For the function we assume a combination of a constant background and one Lorentz peak for the M_5 and two Lorentz peaks for the M_4 absorption edges. The background is given by the value of the absorption coefficient between the maxima and the maxima of the Lorentz peaks are set equal to the respective values for the absorption edges. The Lorentz peaks have a half width at half maximum (HWHM) of 1 eV. The value for the second Lorentz peak for anti-parallel polarization was read off the graph in Figure 3 in [96].

Using this rough approximation for the absorption coefficient, we calculate the correction function (equation (6) in [95]):

$$f_{\mathrm{sat}}(\theta, \lambda_e, \lambda_x) = \frac{1}{1 + \lambda_e/\lambda_x \cos(\theta)} \ , \tag{A.2}$$

which is depicted in Fig. A.3 and pertains the general shape of μ in Fig. A.2.

Applying this correction function to our raw absorption data (Fig. A.4a) we obtain the saturation-corrected data shown in Fig. A.4b and used in Sections 3.2.2 and 4.1.

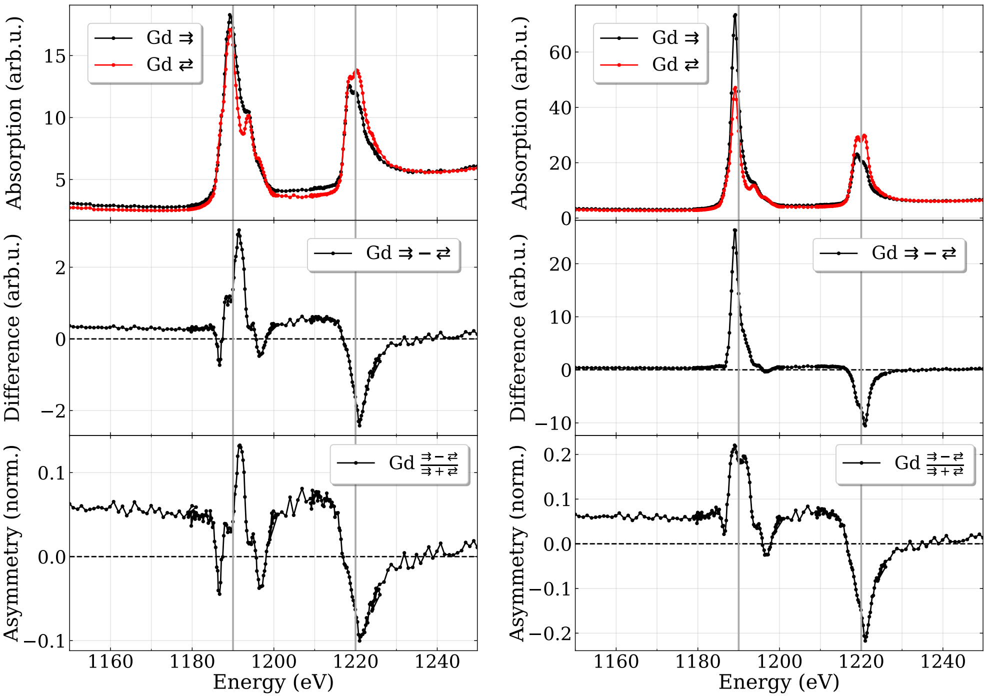

(a) Raw data

(b) Corrected data

Figure A.4: Absorption spectra of the Gd M$_5$ and M$_4$ absorption edges for a 10 nm single-crystalline sample. (a) shows the raw absorption data and (b) displays the same data after correcting for saturation effects as described above. At the top, the normalized signals for parallel ($\rightrightarrows$) and antiparallel ($\rightleftarrows$) magnetization of the sample with respect to the probing light polarization are plotted. Below, the difference of these signals, the XMCD, is depicted. At the bottom, the asymmetry is shown. The absorption signal was obtained from the sample current induced by the absorbed light. The incidence angle between the X-ray beam and the sample surface normal is $\theta = 85.5^\circ$ (*cf.* Fig. 3.7). The vertical lines indicate the central energies of the absorption edges at which the data in Figs. 4.2 and 4.3 was measured.

A.3 Laser Fluence Dependence of Magnetization Dynamics in Gd for Pump Photon Energies of 0.95 eV and 3.1 eV

Supplementing the data presented in Section 4.2.2, the results on demagnetization in Gd probed via X-ray magnetic circular dichroism (XMCD) in reflection for pump laser energies of 0.95 eV and 3.1 eV are presented in Figs. A.5 and A.6. The results are mostly similar to the results for a pump energy of 1.55 eV: We observe two steps in the demagnetization on time scales of about 1 ps and some tens of ps, the point of minimal magnetization shifts towards later delays with increasing pump fluence and the sample remagnetizes on a time scale of 357 ps and 491 ps, respectively for 0.95 eV and 3.1 eV pump photon energy.

The pump laser fluences in the 0.95 eV data set are uncertain in a similar way to the data set presented in Section 4.2.2. However, in the 3.1 eV data set, the uncertainties are especially large and hard to assess. An outstanding, obviously unrealistic value for the pump laser fluence is marked with a star, see Fig. A.6. The addition of non-linear optical elements in the pump laser beamline seem to have caused unexpected fluctuations in the beam, especially regarding the spot size. This was particularly drastic for the 3.1 eV pump laser beam. We are lacking necessary spot size measurements and unfortunately cannot, in retrospect, determine the pump laser fluence reliably for these data sets.

abs. fluence* [mJ/cm^2]	A_1 [arb. units]	τ_1 [ps]	A_2 [arb. units]	τ_2 [ps]	τ_{rec} [ps]
4.4	0.19 ± 0.02	0.61 ± 0.22	0.06 ± 0.02	30 ± 26	357 ± 15
6.5	0.22 ± 0.03	0.44 ± 0.18	0.12 ± 0.03	7 ± 4	357 ± 15
8.0	0.27 ± 0.01	0.46 ± 0.12	0.46 ± 0.03	33 ± 4	357 ± 15
10.9	0.40 ± 0.02	0.90 ± 0.15	0.47 ± 0.03	35 ± 6	357 ± 15
12.2	0.48 ± 0.02	1.19 ± 0.13	1.79 ± 0.20	131 ± 10	357 ± 15

Table A.1: Fit parameters for the fit curves displayed in Fig. A.5 using the fit function Eq. (4.10). The recovery time τ_{rec} is fitted globally for all fluences. The first demagnetization step occurs on a sub-ps time scale, the second step lies between a few to a hundred ps depending on the pump laser fluence. For the lowest fluence, the demagnetization is very weak and the uncertainties in the parameters become large. The uncertainties are one standard deviation of the fit parameters. The "*" indicates that there might be a large systematic offset for all pump laser fluences.

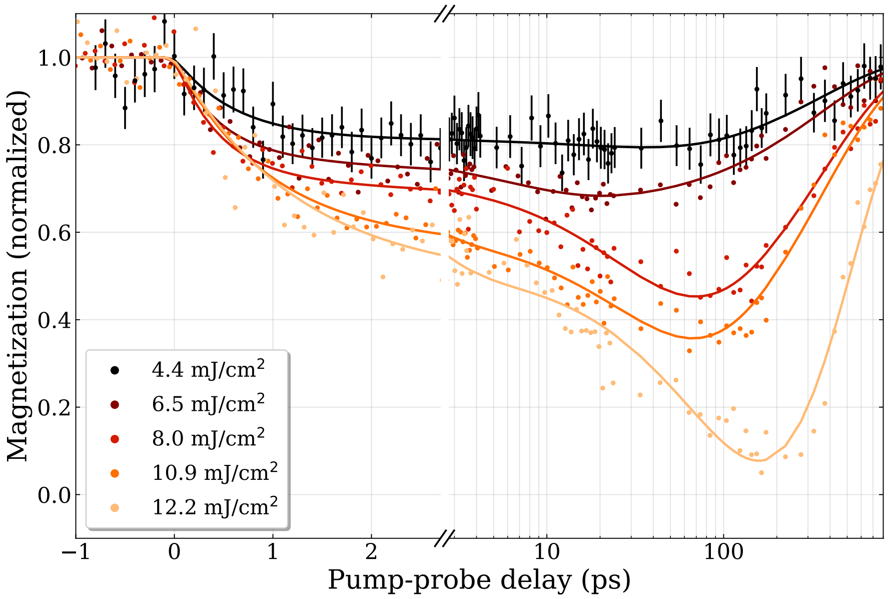

Figure A.5: Pump laser-induced demagnetization in Gd measured via XMCD in reflection at the Gd M_5 absorption edge (markers) including the fit function from Eq. (4.10) (lines) for a variety of absorbed pump laser fluences. The error bars in the top data set are derived from statistical uncertainty of the count rates and representative for all data sets. The sample temperature is (125 ± 10) K. The pump photon energy is 0.95 eV.

abs. fluence [mJ/cm^2]	A_1 [arb. units]	τ_1 [ps]	A_2 [arb. units]	τ_2 [ps]	τ_{rec} [ps]
2.0	0.24 ± 0.08	0.97 ± 0.69	0.09 ± 0.08	10 ± 14	491 ± 41
2.9	0.36 ± 0.03	0.64 ± 0.24	0.48 ± 0.05	31 ± 8	491 ± 41
11.1	0.57 ± 0.02	0.93 ± 0.18	0.86 ± 0.16	99 ± 22	491 ± 41

Table A.2: Fit parameters for the fit curves displayed in Fig. A.6 using the fit function Eq. (4.10). The recovery time τ_{rec} is fitted globally for all fluences. The first demagnetization step occurs on a sub-ps time scale, the second step lies between a few to a hundred ps depending on the pump laser fluence. For the lowest fluence, the demagnetization is very weak and the uncertainties in the parameters become large. The uncertainties are one standard deviation of the fit parameters. The pump laser fluences are highly uncertain in this data set.

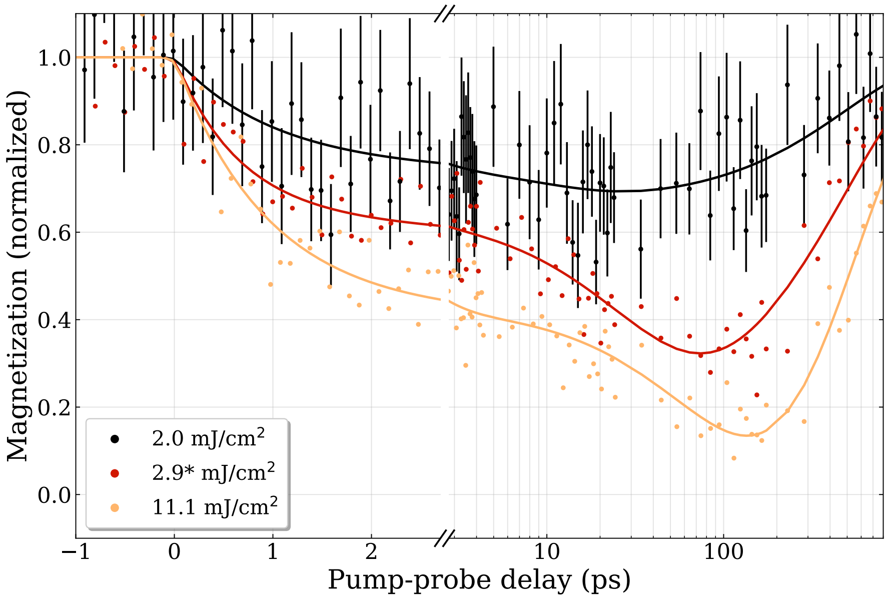

Figure A.6: Pump laser-induced demagnetization in Gd measured via XMCD in reflection at the Gd M_5 absorption edge (markers) including the fit function from Eq. (4.10) (lines) for a variety of absorbed pump laser fluences. The error bars in the top data set are derived from statistical uncertainty of the count rates and representative for all data sets. The sample temperature is $(125 \pm 10)\,\mathrm{K}$. The pump photon energy is 3.1 eV. The "*" indicates that this pump laser fluence is particularly uncertain and probably an outlier.

A.4 Fit Parameter Dependence on Pump Laser Fluence

In Section 4.2.2, we have fitted data of magnetization dynamics in Gd when pumped with 1.55 eV laser pulses, see Fig. 4.7 and Table 4.1. Figure A.7 shows the dependence of those fit parameters on the pump laser fluence. The red lines are exponential fits.

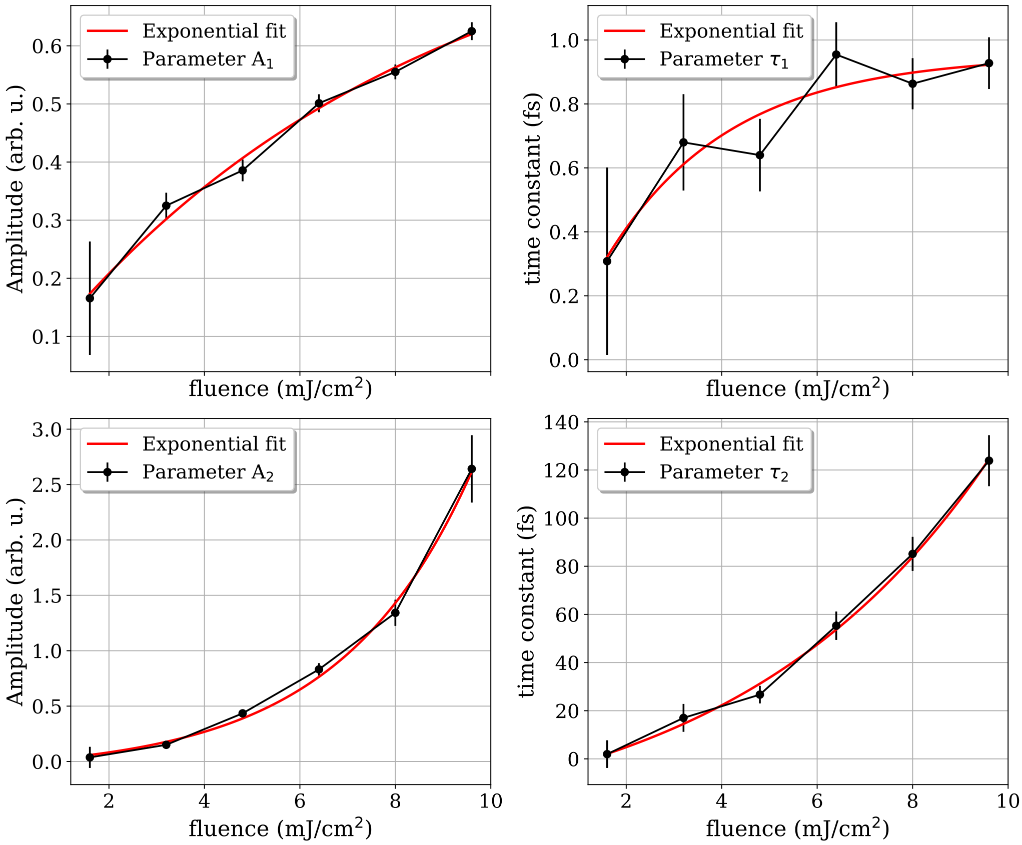

Figure A.7: Fit parameters versus pump laser fluence. The fit parameters were obtained by fitting the data shown in Fig. 4.7, their values can be found in Table 4.1. The red lines are exponential fits.

Appendix B

Optically Induced Spin Transfer in Gd

B.1 Global Fit Results for All Pump-Probe Delays

On the following pages, for the sake of completeness, we show all individual fit results of the global fit of the photoemission data for the Gd/W(110) sample pumped with 1300 nm presented in Chapters 5 and 6. The fit components are the same as for Fig. 5.2 in Section 5.2.1. In the top right corner of each figure is the pump-probe delay. For this data set, the probe energy is 34.2 eV, the incidence angle is 65° and the sample temperature is about 50 K. The pump laser fluence is discussed in Section 6.2.1.

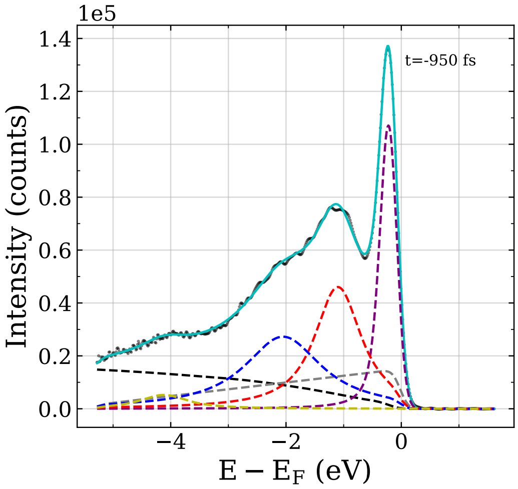
1e5
1.4
1.2
1.0
0.8
0.6
0.4
0.2
0.0
Intensity (counts)
t=-950 fs
−4
−2
0
$\mathrm{E}-\mathrm{E_F}$ (eV)

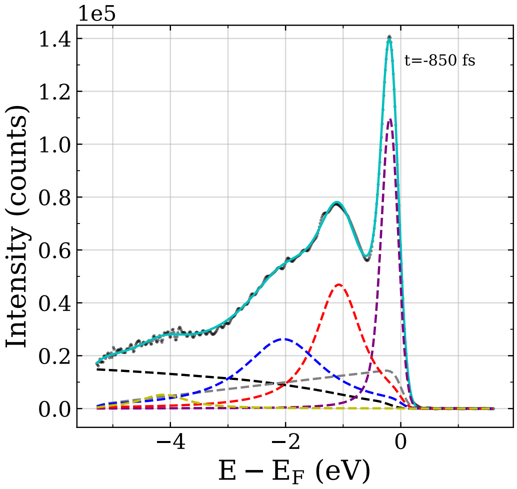
1e5
1.4
1.2
1.0
0.8
0.6
0.4
0.2
0.0
Intensity (counts)
t=-850 fs
−4
−2
0
$\mathrm{E}-\mathrm{E_F}$ (eV)

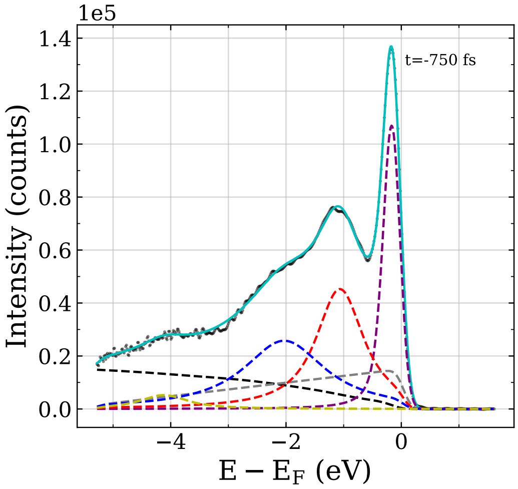
1e5
1.4
1.2
1.0
0.8
0.6
0.4
0.2
0.0
Intensity (counts)
t=-750 fs
−4
−2
0
$\mathrm{E}-\mathrm{E_F}$ (eV)

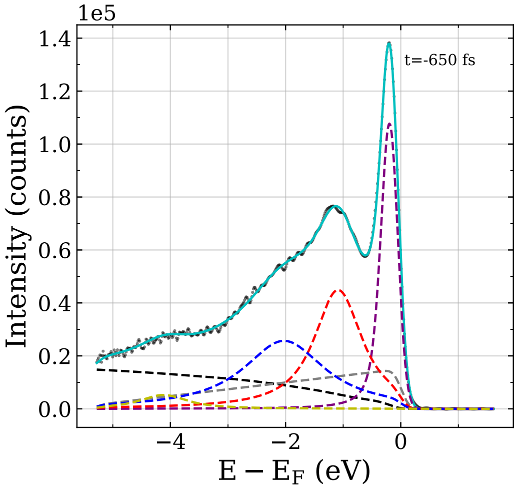
1e5
1.4
1.2
1.0
0.8
0.6
0.4
0.2
0.0
Intensity (counts)
t=-650 fs
−4
−2
0
$\mathrm{E}-\mathrm{E_F}$ (eV)

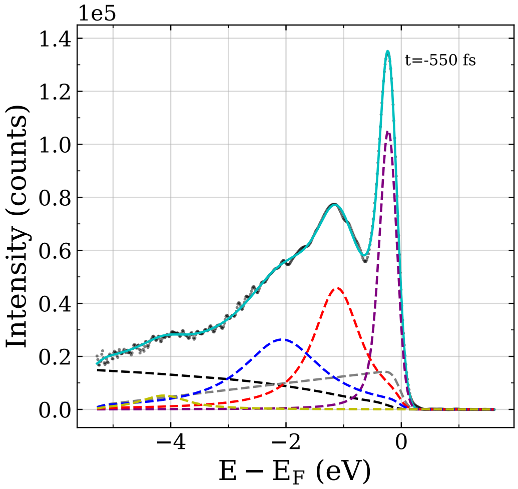
1e5
1.4
1.2
1.0
0.8
0.6
0.4
0.2
0.0
Intensity (counts)
t=-550 fs
−4
−2
0
$\mathrm{E}-\mathrm{E_F}$ (eV)

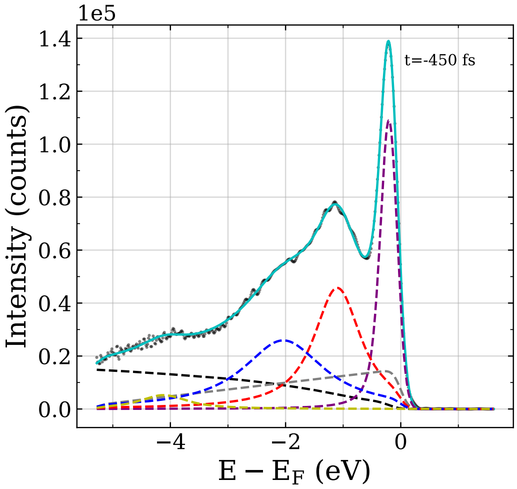
1e5
1.4
1.2
1.0
0.8
0.6
0.4
0.2
0.0
Intensity (counts)
t=-450 fs
−4
−2
0
$\mathrm{E}-\mathrm{E_F}$ (eV)

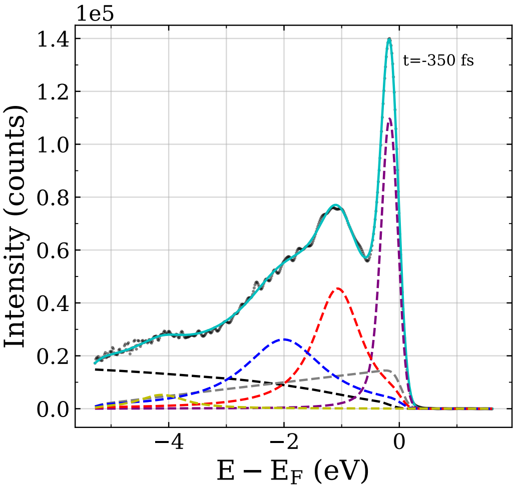
1e5
1.4
1.2
1.0
0.8
0.6
0.4
0.2
0.0
Intensity (counts)
t=-350 fs
−4
−2
0
E − E_F (eV)

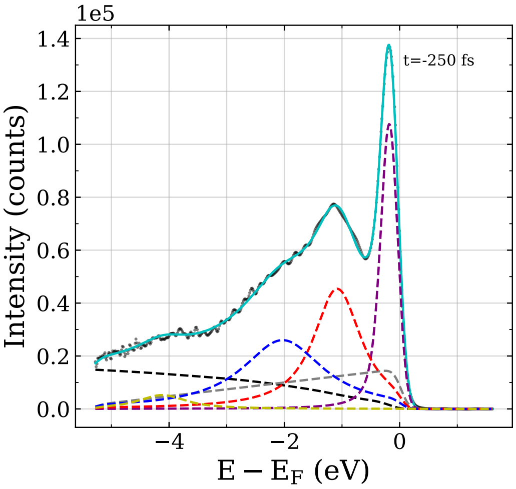
1e5
1.4
1.2
1.0
0.8
0.6
0.4
0.2
0.0
Intensity (counts)
t=-250 fs
−4
−2
0
E − E_F (eV)

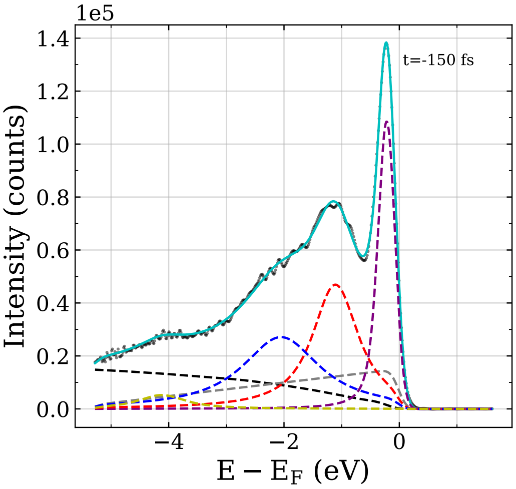
1e5
1.4
1.2
1.0
0.8
0.6
0.4
0.2
0.0
Intensity (counts)
t=-150 fs
−4
−2
0
E − E_F (eV)

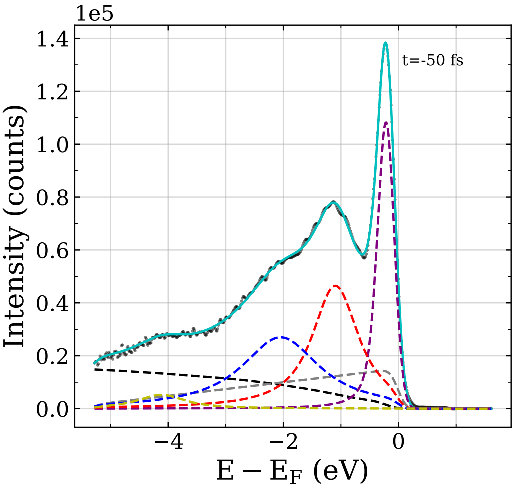
1e5
1.4
1.2
1.0
0.8
0.6
0.4
0.2
0.0
Intensity (counts)
t=-50 fs
−4
−2
0
E − E_F (eV)

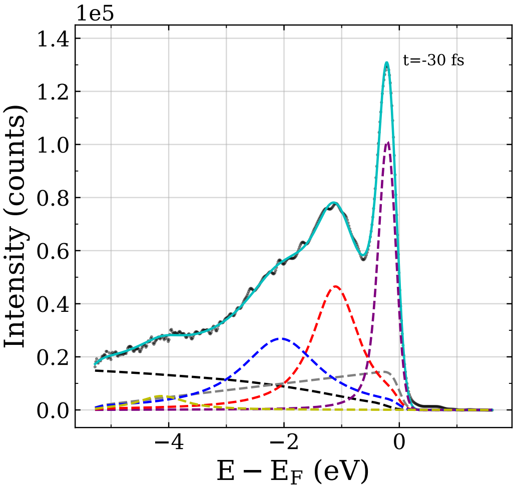
1e5
1.4
1.2
1.0
0.8
0.6
0.4
0.2
0.0
Intensity (counts)
t=-30 fs
−4
−2
0
E − E_F (eV)

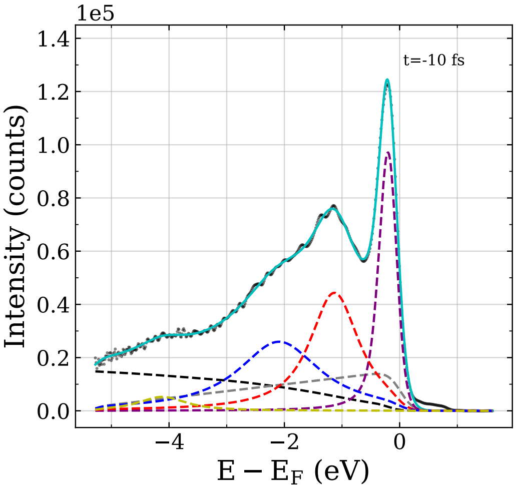
1e5
1.4
1.2
1.0
0.8
0.6
0.4
0.2
0.0
Intensity (counts)
t=-10 fs
−4
−2
0
E − E_F (eV)

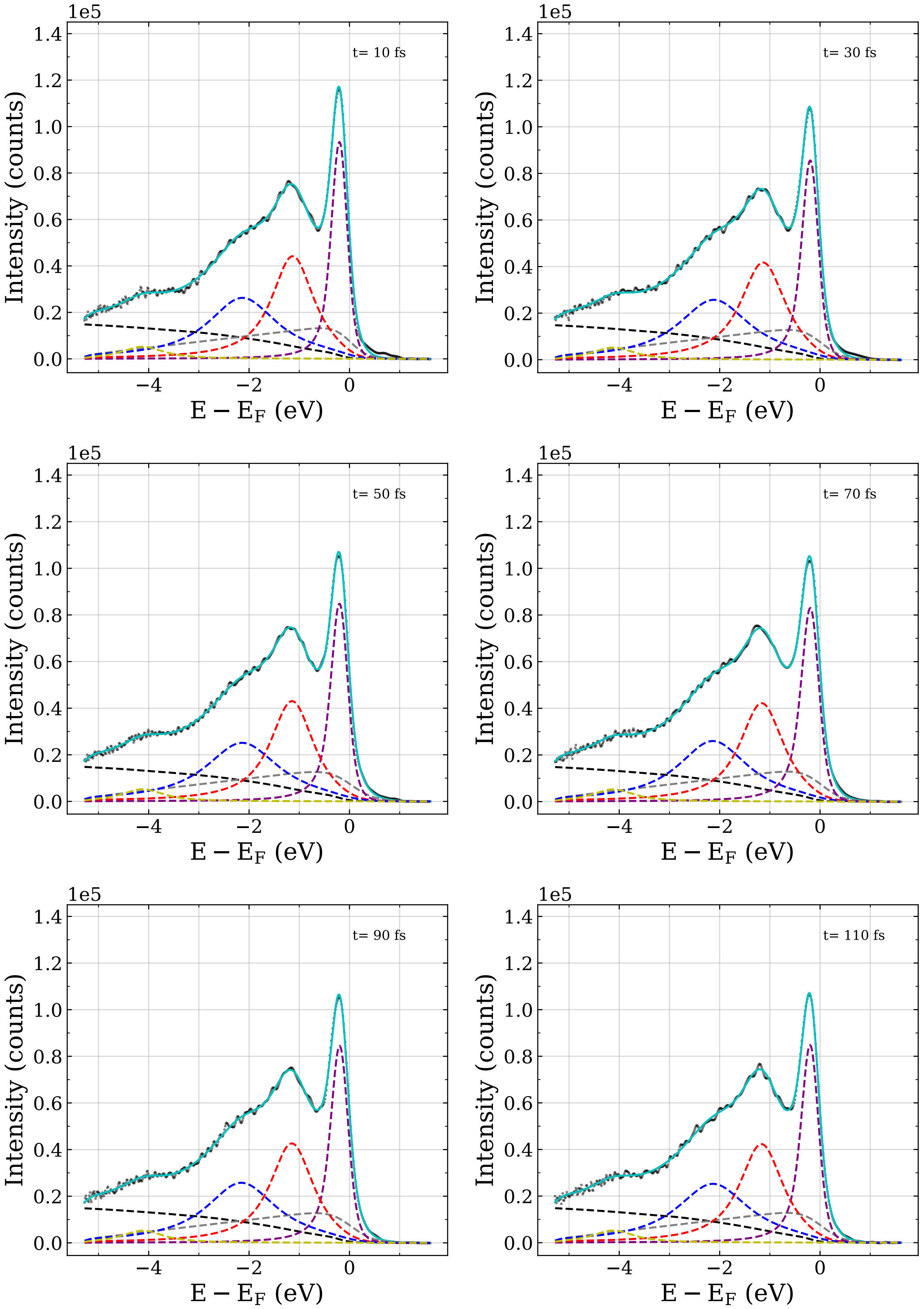
1e5
t= 10 fs
t= 30 fs
t= 50 fs
t= 70 fs
t= 90 fs
t= 110 fs
Intensity (counts)
0.0
0.2
0.4
0.6
0.8
1.0
1.2
1.4
−4
−2
0
$\mathrm{E - E_F}$ (eV)

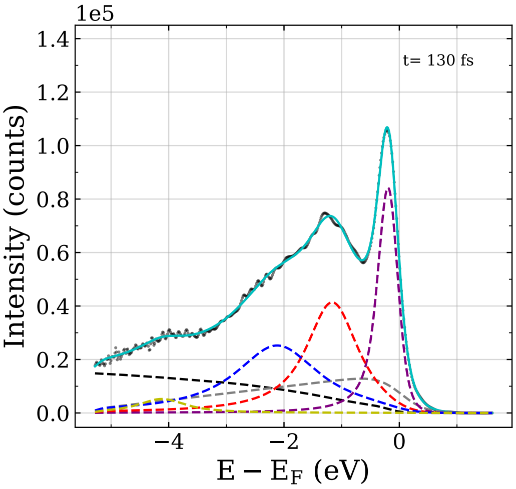
1e5
t= 130 fs
1.4
1.2
1.0
0.8
0.6
0.4
0.2
0.0
Intensity (counts)
−4
−2
0
$\mathrm{E-E_F}$ (eV)

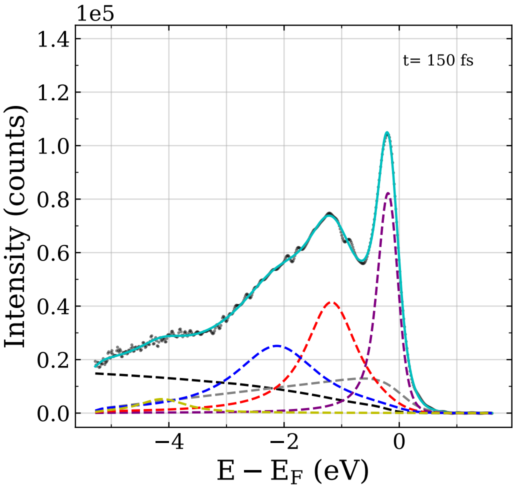
1e5
t= 150 fs
1.4
1.2
1.0
0.8
0.6
0.4
0.2
0.0
Intensity (counts)
−4
−2
0
$\mathrm{E-E_F}$ (eV)

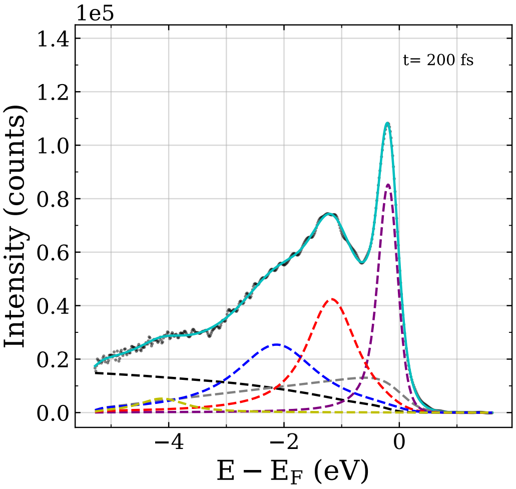
1e5
t= 200 fs
1.4
1.2
1.0
0.8
0.6
0.4
0.2
0.0
Intensity (counts)
−4
−2
0
$\mathrm{E-E_F}$ (eV)

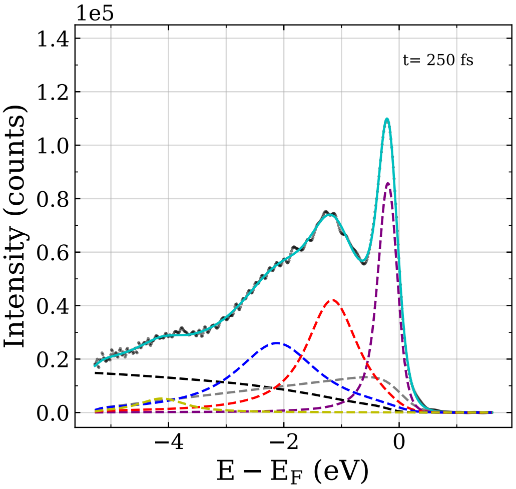
1e5
t= 250 fs
1.4
1.2
1.0
0.8
0.6
0.4
0.2
0.0
Intensity (counts)
−4
−2
0
$\mathrm{E-E_F}$ (eV)

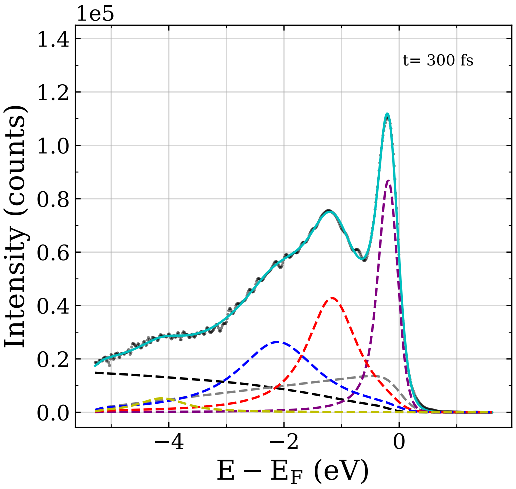
1e5
t= 300 fs
1.4
1.2
1.0
0.8
0.6
0.4
0.2
0.0
Intensity (counts)
−4
−2
0
$\mathrm{E-E_F}$ (eV)

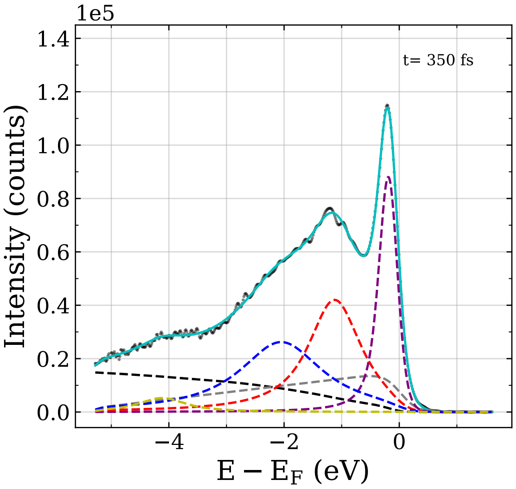
1e5
t= 350 fs
1.4
1.2
1.0
0.8
0.6
0.4
0.2
0.0
Intensity (counts)
−4
−2
0
$\mathrm{E-E_F}$ (eV)

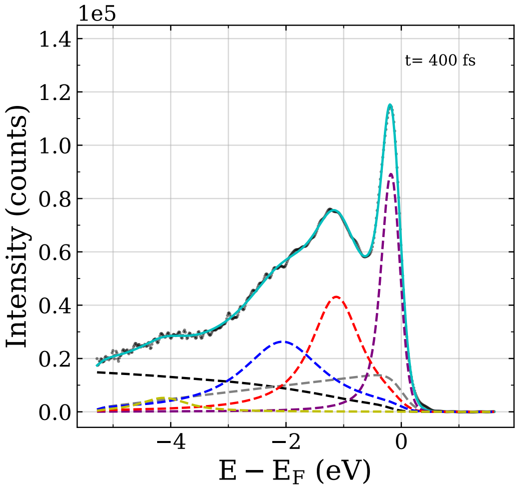
1e5
1.4
1.2
1.0
0.8
0.6
0.4
0.2
0.0
Intensity (counts)
t= 400 fs
−4
−2
0
$\mathrm{E-E_F}$ (eV)

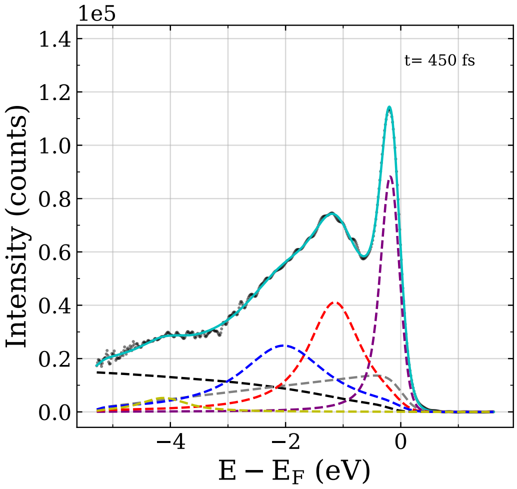
1e5
1.4
1.2
1.0
0.8
0.6
0.4
0.2
0.0
Intensity (counts)
t= 450 fs
−4
−2
0
$\mathrm{E-E_F}$ (eV)

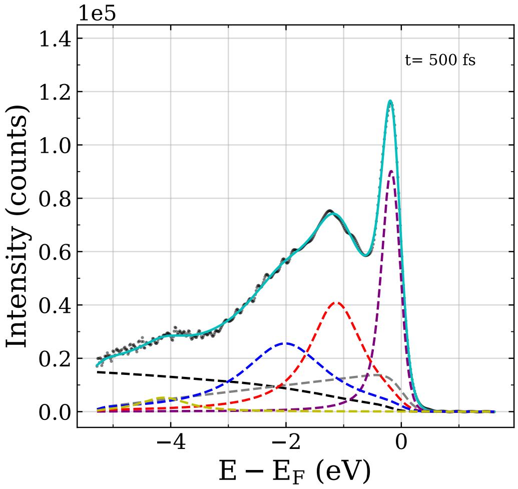
1e5
1.4
1.2
1.0
0.8
0.6
0.4
0.2
0.0
Intensity (counts)
t= 500 fs
−4
−2
0
$\mathrm{E-E_F}$ (eV)

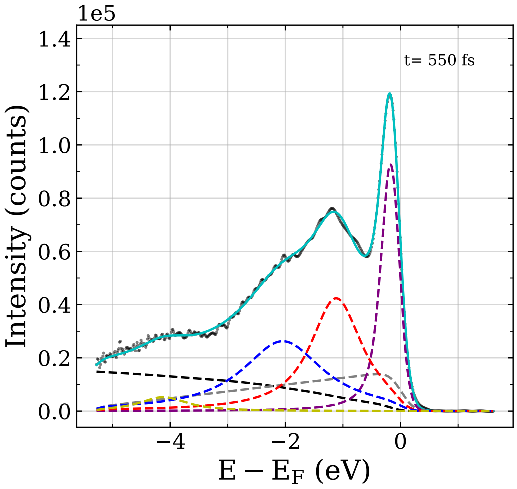
1e5
1.4
1.2
1.0
0.8
0.6
0.4
0.2
0.0
Intensity (counts)
t= 550 fs
−4
−2
0
$\mathrm{E-E_F}$ (eV)

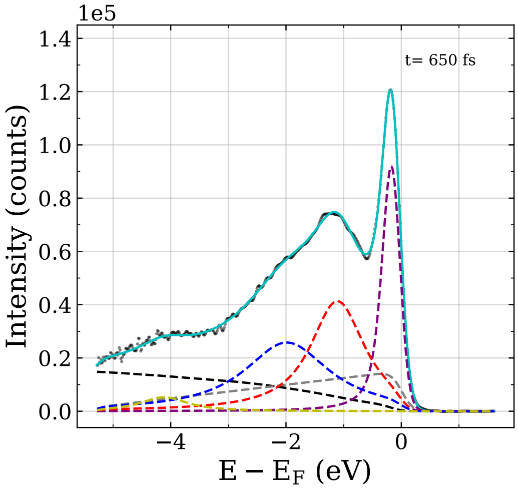
1e5
1.4
1.2
1.0
0.8
0.6
0.4
0.2
0.0
Intensity (counts)
t= 650 fs
−4
−2
0
$\mathrm{E-E_F}$ (eV)

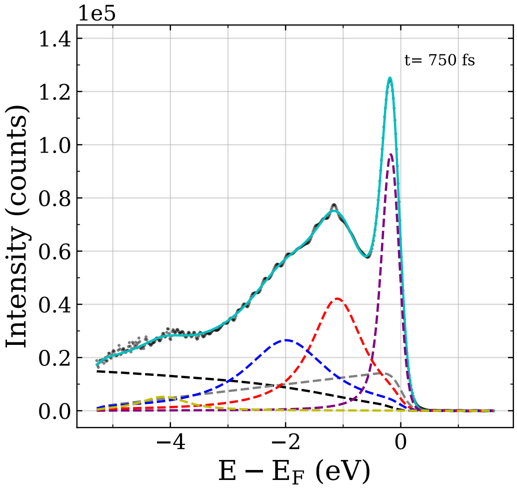
1e5
1.4
1.2
1.0
0.8
0.6
0.4
0.2
0.0
Intensity (counts)
t= 750 fs
−4
−2
0
$\mathrm{E-E_F}$ (eV)

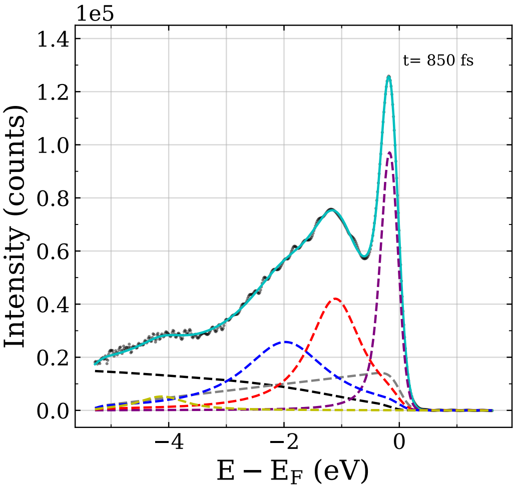
1e5
t= 850 fs
Intensity (counts)
0.0
0.2
0.4
0.6
0.8
1.0
1.2
1.4
−4
−2
0
$E - E_F$ (eV)

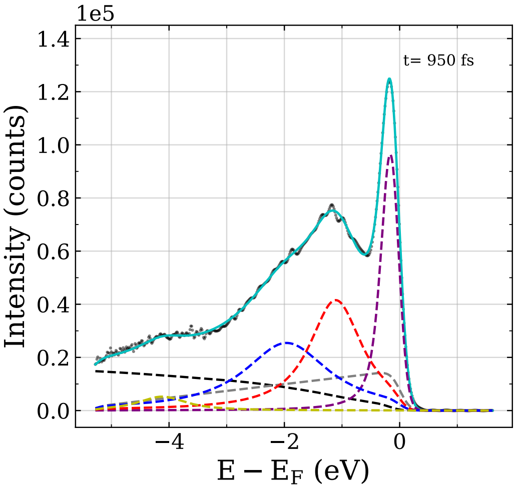
1e5
t= 950 fs
Intensity (counts)
0.0
0.2
0.4
0.6
0.8
1.0
1.2
1.4
−4
−2
0
$E - E_F$ (eV)

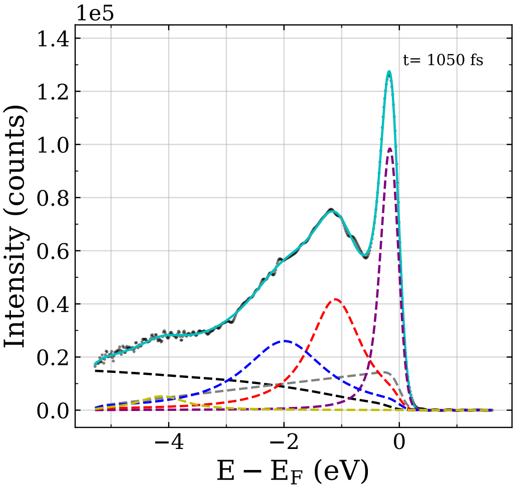
1e5
t= 1050 fs
Intensity (counts)
0.0
0.2
0.4
0.6
0.8
1.0
1.2
1.4
−4
−2
0
$E - E_F$ (eV)

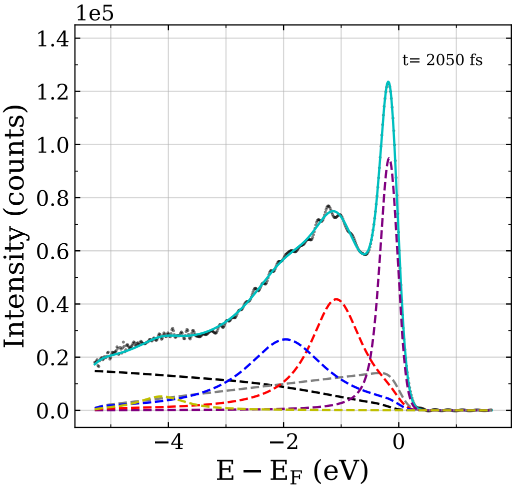
1e5
t= 2050 fs
Intensity (counts)
0.0
0.2
0.4
0.6
0.8
1.0
1.2
1.4
−4
−2
0
$E - E_F$ (eV)

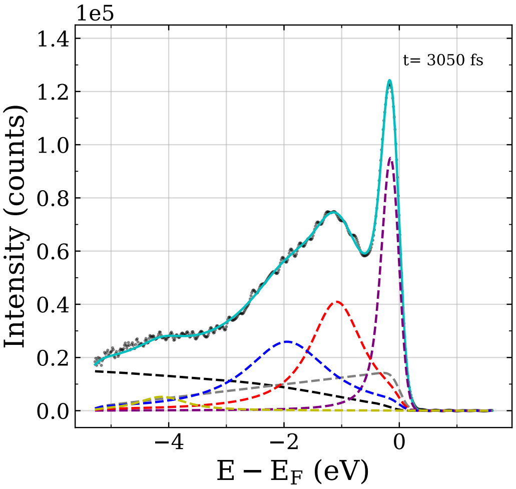
1e5
t= 3050 fs
Intensity (counts)
0.0
0.2
0.4
0.6
0.8
1.0
1.2
1.4
−4
−2
0
$E - E_F$ (eV)

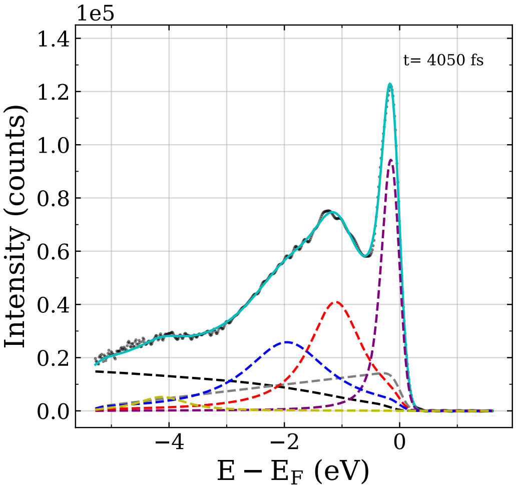
1e5
t= 4050 fs
Intensity (counts)
0.0
0.2
0.4
0.6
0.8
1.0
1.2
1.4
−4
−2
0
$E - E_F$ (eV)

Bibliography

[1] K. Vahaplar, A. M. Kalashnikova, A. V. Kimel, D. Hinzke, U. Nowak, R. Chantrell, A. Tsukamoto, A. Itoh, A. Kirilyuk, and T. Rasing. „Ultrafast Path for Optical Magnetization Reversal via a Strongly Nonequilibrium State“. In: *Physical Review Letters* 103.11 (2009), p. 117201. DOI: `10.1103/physrevlett.103.117201` (cit. on p. 1).

[2] J. Stöhr and H. C. Siegmann. *Magnetism*. Springer-Verlag GmbH, 2006 (cit. on pp. 1, 5, 6, 23, 24, 26, 27).

[3] C. H. Back, R. Allenspach, W. Weber, S. S. P. Parkin, D. Weller, E. L. Garwin, and H. C. Siegmann. „Minimum Field Strength in Precessional Magnetization Reversal“. In: *Science* 285.5429 (1999), pp. 864–867. DOI: `10.1126/science.285.5429.864` (cit. on p. 1).

[4] I. Tudosa, C. Stamm, A. B. Kashuba, F. King, H. C. Siegmann, J. Stöhr, G. Ju, B. Lu, and D. Weller. „The ultimate speed of magnetic switching in granular recording media“. In: *Nature* 428.6985 (2004), pp. 831–833. DOI: `10.1038/nature02438` (cit. on p. 1).

[5] E. Beaurepaire, J.-C. Merle, A. Daunois, and J.-Y. Bigot. „Ultrafast Spin Dynamics in Ferromagnetic Nickel“. In: *Physical Review Letters* 76.22 (1996), pp. 4250–4253. DOI: `10.1103/physrevlett.76.4250` (cit. on pp. 1, 5–7, 43).

[6] C. D. Stanciu, F. Hansteen, A. V. Kimel, A. Kirilyuk, A. Tsukamoto, A. Itoh, and T. Rasing. „All-Optical Magnetic Recording with Circularly Polarized Light“. In: *Physical Review Letters* 99.4 (2007), p. 047601. DOI: `10.1103/physrevlett.99.047601` (cit. on pp. 1, 62, 70).

[7] J.-Y. Bigot, M. Vomir, and E. Beaurepaire. „Coherent ultrafast magnetism induced by femtosecond laser pulses“. In: *Nature Physics* 5.7 (2009), pp. 515–520. DOI: `10.1038/nphys1285` (cit. on pp. 2, 43).

[8] G.-M. Choi, A. Schleife, and D. G. Cahill. „Optical-helicity-driven magnetization dynamics in metallic ferromagnets“. In: *Nature Communications* 8.1 (2017), p. 15085. DOI: `10.1038/ncomms15085` (cit. on pp. 2, 43).

[9] M. Battiato, K. Carva, and P. M. Oppeneer. „Superdiffusive Spin Transport as a Mechanism of Ultrafast Demagnetization“. In: *Physical Review Letters* 105.2 (2010), p. 027203. DOI: `10.1103/physrevlett.105.027203` (cit. on pp. 2, 18, 19, 43, 67, 79, 83).

[10] M. Krauß, T. Roth, S. Alebrand, D. Steil, M. Cinchetti, M. Aeschlimann, and H. C. Schneider. „Ultrafast demagnetization of ferromagnetic transition metals: The role of the Coulomb interaction“. In: *Physical Review B* 80.18 (2009), p. 180407. DOI: `10.1103/physrevb.80.180407` (cit. on pp. 2, 43).

[11] D. Steil, S. Alebrand, T. Roth, M. Krauß, T. Kubota, M. Oogane, Y. Ando, H. C. Schneider, M. Aeschlimann, and M. Cinchetti. „Band-Structure-Dependent Demagnetization in the Heusler Alloy Co_2Mn_{1-x} Fe_xSi". In: *Physical Review Letters* 105.21 (2010), p. 217202. DOI: `10.1103/physrevlett.105.217202` (cit. on pp. 2, 43).

[12] B. Y. Mueller, T. Roth, M. Cinchetti, M. Aeschlimann, and B. Rethfeld. „Driving force of ultrafast magnetization dynamics". In: *New Journal of Physics* 13.12 (2011), p. 123010. DOI: `10.1088/1367-2630/13/12/123010` (cit. on pp. 2, 43).

[13] B. Koopmans, H. Kicken, M. van Kampen, and W. de Jonge. „Microscopic model for femtosecond magnetization dynamics". In: *Journal of Magnetism and Magnetic Materials* 286 (2005), pp. 271–275. DOI: `10.1016/j.jmmm.2004.09.079` (cit. on pp. 2, 43).

[14] E. Carpene, E. Mancini, C. Dallera, M. Brenna, E. Puppin, and S. D. Silvestri. „Dynamics of electron-magnon interaction and ultrafast demagnetization in thin iron films". In: *Physical Review B* 78.17 (2008), p. 174422. DOI: `10.1103/physrevb.78.174422` (cit. on pp. 2, 43).

[15] B. Koopmans, G. Malinowski, F. D. Longa, D. Steiauf, M. Fähnle, T. Roth, M. Cinchetti, and M. Aeschlimann. „Explaining the paradoxical diversity of ultrafast laser-induced demagnetization". In: *Nature Materials* 9.3 (2009), pp. 259–265. DOI: `10.1038/nmat2593` (cit. on pp. 2, 15–18, 43, 44, 50, 51, 61, 67, 86).

[16] D. Steiauf and M. Fähnle. „Elliott-Yafet mechanism and the discussion of femtosecond magnetization dynamics". In: *Physical Review B* 79.14 (2009), p. 140401. DOI: `10.1103/physrevb.79.140401` (cit. on pp. 2, 43).

[17] D. Steiauf, C. Illg, and M. Fähnle. „Demagnetization on the fs time-scale by the Elliott-Yafet mechanism". In: *Journal of Physics: Conference Series* 200.4 (2010), p. 042024. DOI: `10.1088/1742-6596/200/4/042024` (cit. on pp. 2, 43).

[18] M. Plihal and D. L. Mills. „Spin-flip exchange scattering of low-energy electrons in ferromagnetic iron". In: *Physical Review B* 58.21 (1998), pp. 14407–14415. DOI: `10.1103/physrevb.58.14407` (cit. on pp. 2, 43).

[19] A. B. Schmidt, M. Pickel, M. Wiemhöfer, M. Donath, and M. Weinelt. „Spin-Dependent Electron Dynamics in Front of a Ferromagnetic Surface". In: *Physical Review Letters* 95.10 (2005). DOI: `10.1103/physrevlett.95.107402` (cit. on pp. 2, 43).

[20] P. Tengdin, W. You, C. Chen, X. Shi, D. Zusin, Y. Zhang, C. Gentry, A. Blonsky, M. Keller, P. M. Oppeneer, H. C. Kapteyn, Z. Tao, and M. M. Murnane. „Critical behavior within 20 fs drives the out-of-equilibrium laser-induced magnetic phase transition in nickel". In: *Science Advances* 4.3 (2018), eaap9744. DOI: `10.1126/sciadv.aap9744` (cit. on pp. 2, 43).

[21] M. Sultan, A. Melnikov, and U. Bovensiepen. „Ultrafast magnetization dynamics of Gd(0001): Bulk versus surface". In: *physica status solidi (b)* 248.10 (2011), pp. 2323–2329. DOI: `10.1002/pssb.201147105` (cit. on p. 2).

[22] B. Frietsch, J. Bowlan, R. Carley, M. Teichmann, S. Wienholdt, D. Hinzke, U. Nowak, K. Carva, P. M. Oppeneer, and M. Weinelt. „Disparate ultrafast dynamics of itinerant and localized magnetic moments in gadolinium metal“. In: *Nature Communications* 6.1 (2015), p. 8262. DOI: `10.1038/ncomms9262` (cit. on pp. 2, 5, 21, 23, 54, 55, 57, 58, 69, 79, 80, 83–86, 107, 123).

[23] M. Wietstruk, A. Melnikov, C. Stamm, T. Kachel, N. Pontius, M. Sultan, C. Gahl, M. Weinelt, H. A. Dürr, and U. Bovensiepen. „Hot-Electron-Driven Enhancement of Spin-Lattice Coupling in Gd and Tb $4f$ Ferromagnets Observed by Femtosecond X-Ray Magnetic Circular Dichroism“. In: *Physical Review Letters* 106.12 (2011), p. 127401. DOI: `10.1103/physrevlett.106.127401` (cit. on pp. 2, 54, 60, 63, 69, 72, 123).

[24] K. Bobowski, M. Gleich, N. Pontius, C. Schüßler-Langeheine, C. Trabant, M. Wietstruk, B. Frietsch, and M. Weinelt. „Influence of the pump pulse wavelength on the ultrafast demagnetization of Gd(0 0 0 1) thin films“. In: *Journal of Physics: Condensed Matter* 29.23 (2017), p. 234003. DOI: `10.1088/1361-648x/aa6c92` (cit. on pp. 2, 43, 67, 68).

[25] M. Sultan, U. Atxitia, A. Melnikov, O. Chubykalo-Fesenko, and U. Bovensiepen. „Electron- and phonon-mediated ultrafast magnetization dynamics of Gd(0001)“. In: *Physical Review B* 85.18 (2012), p. 184407. DOI: `10.1103/physrevb.85.184407` (cit. on pp. 3, 6, 55, 85, 87, 88, 91, 95).

[26] A. Kirilyuk, A. V. Kimel, and T. Rasing. „Ultrafast optical manipulation of magnetic order“. In: *Reviews of Modern Physics* 82.3 (2010), pp. 2731–2784. DOI: `10.1103/revmodphys.82.2731` (cit. on pp. 5, 7, 9, 15).

[27] S. Wienholdt, D. Hinzke, K. Carva, P. M. Oppeneer, and U. Nowak. „Orbital-resolved spin model for thermal magnetization switching in rare-earth-based ferrimagnets“. In: *Physical Review B* 88.2 (2013), p. 020406. DOI: `10.1103/physrevb.88.020406` (cit. on p. 5).

[28] S. V. Halilov, A. Y. Perlov, P. M. Oppeneer, A. N. Yaresko, and V. N. Antonov. „Magnetocrystalline anisotropy energy in cubic Fe, Co, and Ni: Applicability of local-spin-density theory reexamined“. In: *Physical Review B* 57.16 (1998), pp. 9557–9560. DOI: `10.1103/physrevb.57.9557` (cit. on p. 5).

[29] S. I. Anisimov, B. L. Kapeliovich, and T. L. Perel’man. „Electron emission from metal surfaces exposed to ultrashort laser pulses“. In: *J. Exp. Theor. Phys.* 39.2 (1974), p. 375 (cit. on pp. 6, 15).

[30] H. E. Elsayed-Ali, T. Juhasz, G. O. Smith, and W. E. Bron. „Femtosecond thermoreflectivity and thermotransmissivity of polycrystalline and single-crystalline gold films“. In: *Physical Review B* 43.5 (1991), pp. 4488–4491. DOI: `10.1103/physrevb.43.4488` (cit. on pp. 6, 7, 15).

[31] A. Melnikov, H. Prima-Garcia, M. Lisowski, T. Gießel, R. Weber, R. Schmidt, C. Gahl, N. M. Bulgakova, U. Bovensiepen, and M. Weinelt. „Nonequilibrium Magnetization Dynamics of Gadolinium Studied by Magnetic Linear Dichroism in Time-Resolved $4f$ Core-Level Photoemission“. In: *Physical Review Letters* 100.10 (2008), p. 107202. DOI: `10.1103/physrevlett.100.107202` (cit. on pp. 6, 109).

[32] M. Lisowski, P. A. Loukakos, U. Bovensiepen, J. Stähler, C. Gahl, and M. Wolf. „Ultra-fast dynamics of electron thermalization, cooling and transport effects in Ru(001)“. In: *Applied Physics A: Materials Science & Processing* 78.2 (2004), pp. 165–176. DOI: `10.1007/s00339-003-2301-7` (cit. on p. 6).

[33] S.-S. Wellershoff, J. Hohlfeld, J. Güdde, and E. Matthias. „The role of electron–phonon coupling in femtosecond laser damage of metals“. In: *Applied Physics A Materials Science & Processing* 69.S1 (1999), S99–S107. DOI: `10.1007/s003399900305` (cit. on p. 6).

[34] U. Bovensiepen. „Coherent and incoherent excitations of the Gd(0001) surface on ultrafast timescales“. In: *Journal of Physics: Condensed Matter* 19.8 (2007), p. 083201. DOI: `10.1088/0953-8984/19/8/083201` (cit. on pp. 6, 7, 57, 62, 67, 71).

[35] P. A. Loukakos, M. Lisowski, G. Bihlmayer, S. Blügel, M. Wolf, and U. Bovensiepen. „Dynamics of the Self-Energy of the Gd(0001) Surface State Probed by Femtosecond Photoemission Spectroscopy“. In: *Physical Review Letters* 98.9 (2007), p. 097401. DOI: `10.1103/physrevlett.98.097401` (cit. on pp. 6, 76, 81).

[36] F. D. Longa, J. T. Kohlhepp, W. J. M. de Jonge, and B. Koopmans. „Influence of photon angular momentum on ultrafast demagnetization in nickel“. In: *Physical Review B* 75.22 (2007), p. 224431. DOI: `10.1103/physrevb.75.224431` (cit. on p. 7).

[37] J. Walowski, G. Müller, M. Djordjevic, M. Münzenberg, M. Kläui, C. A. F. Vaz, and J. A. C. Bland. „Energy Equilibration Processes of Electrons, Magnons, and Phonons at the Femtosecond Time Scale“. In: *Physical Review Letters* 101.23 (2008), p. 237401. DOI: `10.1103/physrevlett.101.237401` (cit. on p. 7).

[38] L. D. Landau and E. Lifshitz. „On the theory of the dispersion of magnetic permeability in ferromagnetic bodies“. In: *Phys. Z. Sowjet.* 8 (1935), pp. 153–169 (cit. on p. 7).

[39] S. Mankovsky, D. Ködderitzsch, G. Woltersdorf, and H. Ebert. „First-principles calculation of the Gilbert damping parameter via the linear response formalism with application to magnetic transition metals and alloys“. In: *Physical Review B* 87.1 (2013), p. 014430. DOI: `10.1103/physrevb.87.014430` (cit. on p. 8).

[40] Y. Liu, Z. Yuan, R. Wesselink, A. A. Starikov, and P. J. Kelly. „Interface Enhancement of Gilbert Damping from First Principles“. In: *Physical Review Letters* 113.20 (2014), p. 207202. DOI: `10.1103/physrevlett.113.207202` (cit. on p. 8).

[41] C. P. Bean and J. D. Livingston. „Superparamagnetism“. In: *Journal of Applied Physics* 30.4 (1959), S120–S129. DOI: `10.1063/1.2185850` (cit. on p. 9).

[42] S. Mørup and E. Tronc. „Superparamagnetic relaxation of weakly interacting particles“. In: *Physical Review Letters* 72.20 (1994), pp. 3278–3281. DOI: `10.1103/physrevlett.72.3278` (cit. on p. 9).

[43] M. F. Hansen and S. Mørup. „Models for the dynamics of interacting magnetic nanoparticles“. In: *Journal of Magnetism and Magnetic Materials* 184.3 (1998), pp. 262–274. DOI: `10.1016/s0304-8853(97)01165-7` (cit. on p. 9).

[44] U. Atxitia, O. Chubykalo-Fesenko, R. W. Chantrell, U. Nowak, and A. Rebei. „Ultrafast Spin Dynamics: The Effect of Colored Noise“. In: *Physical Review Letters* 102.5 (2009), p. 057203. DOI: `10.1103/physrevlett.102.057203` (cit. on p. 9).

[45] W. F. Brown. *Micromagnetics*. New York: Interscience Publishers, John Wiley & Sons, 1963 (cit. on p. 9).

[46] P. N. Cordones. „Micromagnetic models for high-temperature magnetization dynamics“. PhD thesis. Universidad Autonoma de Madrid, 2015 (cit. on pp. 10–15).

[47] G. Eilers, M. Lüttich, and M. Münzenberg. „Giant nonlocal damping by spin-wave emission: Micromagnetic simulations“. In: *Physical Review B* 74.5 (2006), p. 054411. DOI: `10.1103/physrevb.74.054411` (cit. on p. 9).

[48] H. A. Mook and R. M. Nicklow. „Neutron Scattering Investigation of the Magnetic Excitations in Iron“. In: *Physical Review B* 7.1 (1973), pp. 336–342. DOI: `10.1103/physrevb.7.336` (cit. on p. 10).

[49] U. Atxitia, O. Chubykalo-Fesenko, N. Kazantseva, D. Hinzke, U. Nowak, and R. W. Chantrell. „Micromagnetic modeling of laser-induced magnetization dynamics using the Landau-Lifshitz-Bloch equation“. In: *Applied Physics Letters* 91.23 (2007), p. 232507. DOI: `10.1063/1.2822807` (cit. on pp. 11, 14).

[50] A. Donges. „Computer Simulations of Ultrafast Magnetic Phenomena“. PhD thesis. University of Konstanz, 2018 (cit. on p. 12).

[51] V. G. Bar’yakhtar. „Phenomenological description of relaxation processes in magnetic materials“. In: *Zhurnal Eksperimental’noi i Teoreticheskoi Fiziki* 60.4 (1984), p. 863 (cit. on p. 12).

[52] V. G. Baryakhtar and A. G. Danilevich. „The phenomenological theory of magnetization relaxation (Review Article)“. In: *Low Temperature Physics* 39.12 (2013), pp. 993–1007. DOI: `10.1063/1.4843275` (cit. on p. 12).

[53] U. Atxitia, D. Hinzke, and U. Nowak. „Fundamentals and applications of the Landau–Lifshitz–Bloch equation“. In: *Journal of Physics D: Applied Physics* 50.3 (2016), p. 033003. DOI: `10.1088/1361-6463/50/3/033003` (cit. on pp. 13–15).

[54] D. A. Garanin, V. V. Ishchenko, and L. V. Panina. „Dynamics of an ensemble of single-domain magnetic particles“. In: *Theoretical and Mathematical Physics* 82.2 (1990), pp. 169–179. DOI: `10.1007/bf01079045` (cit. on p. 13).

[55] D. A. Garanin. „Fokker-Planck and Landau-Lifshitz-Bloch equations for classical ferromagnets“. In: *Physical Review B* 55.5 (1997), pp. 3050–3057. DOI: `10.1103/physrevb.55.3050` (cit. on pp. 13, 16).

[56] D. A. Garanin and O. Chubykalo-Fesenko. „Thermal fluctuations and longitudinal relaxation of single-domain magnetic particles at elevated temperatures“. In: *Physical Review B* 70.21 (2004), p. 212409. DOI: `10.1103/physrevb.70.212409` (cit. on p. 14).

[57] R. F. L. Evans, D. Hinzke, U. Atxitia, U. Nowak, R. W. Chantrell, and O. Chubykalo-Fesenko. „Stochastic form of the Landau-Lifshitz-Bloch equation“. In: *Physical Review B* 85.1 (2012), p. 014433. DOI: `10.1103/physrevb.85.014433` (cit. on p. 14).

[58] O. Chubykalo-Fesenko, U. Nowak, R. W. Chantrell, and D. Garanin. „Dynamic approach for micromagnetics close to the Curie temperature“. In: *Physical Review B* 74.9 (2006). DOI: `10.1103/physrevb.74.094436` (cit. on p. 14).

[59] D. A. Garanin. „Generalized equation of motion for a ferromagnet“. In: *Physica A: Statistical Mechanics and its Applications* 172.3 (1991), pp. 470–491. DOI: `10.1016/0378-4371(91)90395-s` (cit. on p. 14).

[60] R. F. L. Evans, U. Atxitia, and R. W. Chantrell. „Quantitative simulation of temperature-dependent magnetization dynamics and equilibrium properties of elemental ferromagnets“. In: *Physical Review B* 91.14 (2015), p. 144425. DOI: `10.1103/physrevb.91.144425` (cit. on p. 14).

[61] B. Koopmans, J. J. M. Ruigrok, F. D. Longa, and W. J. M. de Jonge. „Unifying Ultrafast Magnetization Dynamics“. In: *Physical Review Letters* 95.26 (2005). DOI: `10.1103/physrevlett.95.267207` (cit. on p. 15).

[62] R. J. Elliott. „Theory of the Effect of Spin-Orbit Coupling on Magnetic Resonance in Some Semiconductors“. In: *Physical Review* 96.2 (1954), pp. 266–279. DOI: `10.1103/physrev.96.266` (cit. on p. 16).

[63] Y. Yafet. „g Factors and Spin-Lattice Relaxation of Conduction Electrons“. In: *Solid State Physics*. Ed. by F. Seitz and D. Turnbull. Vol. 14. Solid State Physics. Academic Press, 1963, pp. 1–98. DOI: `10.1016/s0081-1947(08)60259-3` (cit. on p. 16).

[64] U. Atxitia and O. Chubykalo-Fesenko. „Ultrafast magnetization dynamics rates within the Landau-Lifshitz-Bloch model“. In: *Physical Review B* 84.14 (2011), p. 144414. DOI: `10.1103/physrevb.84.144414` (cit. on p. 16).

[65] T. Roth, A. J. Schellekens, S. Alebrand, O. Schmitt, D. Steil, B. Koopmans, M. Cinchetti, and M. Aeschlimann. „Temperature Dependence of Laser-Induced Demagnetization in Ni: A Key for Identifying the Underlying Mechanism“. In: *Physical Review X* 2.2 (2012), p. 021006. DOI: `10.1103/physrevx.2.021006` (cit. on pp. 18, 43, 51).

[66] S. Essert and H. C. Schneider. „Electron-phonon scattering dynamics in ferromagnetic metals and their influence on ultrafast demagnetization processes“. In: *Physical Review B* 84.22 (2011), p. 224405. DOI: `10.1103/physrevb.84.224405` (cit. on p. 18).

[67] K. Carva, M. Battiato, and P. M. Oppeneer. „Ab Initio Investigation of the Elliott-Yafet Electron-Phonon Mechanism in Laser-Induced Ultrafast Demagnetization“. In: *Physical Review Letters* 107.20 (2011), p. 207201. DOI: `10.1103/physrevlett.107.207201` (cit. on p. 18).

[68] C. Stamm, T. Kachel, N. Pontius, R. Mitzner, T. Quast, K. Holldack, S. Khan, C. Lupulescu, E. F. Aziz, M. Wietstruk, H. A. Dürr, and W. Eberhardt. „Femtosecond modification of electron localization and transfer of angular momentum in nickel“. In: *Nature Materials* 6.10 (2007), pp. 740–743. DOI: `10.1038/nmat1985` (cit. on pp. 18, 19).

[69] V. P. Zhukov, E. V. Chulkov, and P. M. Echenique. „Lifetimes and inelastic mean free path of low-energy excited electrons in Fe, Ni, Pt, and Au: *Ab initio* GW+T calculations“. In: *Physical Review B* 73.12 (2006), p. 125105. DOI: `10.1103/physrevb.73.125105` (cit. on p. 19).

[70] S. Abdelouahed and M. Alouani. „Magnetic anisotropy in Gd, GdN, and $GdFe_2$ tuned by the energy of gadolinium $4f$ states“. In: *Physical Review B* 79.5 (2009), p. 054406. DOI: `10.1103/physrevb.79.054406` (cit. on p. 21).

[71] M. Farle, K. Baberschke, U. Stetter, A. Aspelmeier, and F. Gerhardter. „Thickness-dependent Curie temperature of Gd(0001)/W(110) and its dependence on the growth conditions“. In: *Physical Review B* 47.17 (1993), pp. 11571–11574. DOI: `10.1103/physrevb.47.11571` (cit. on pp. 22, 23).

[72] P. Kurz, G. Bihlmayer, and S. Blügel. „Magnetism and electronic structure of hcp Gd and the Gd(0001) surface“. In: *Journal of Physics: Condensed Matter* 14.25 (2002), pp. 6353–6371. DOI: `10.1088/0953-8984/14/25/305` (cit. on pp. 22, 78, 88, 90).

[73] D. Li, P. A. Dowben, J. E. Ortega, and F. J. Himpsel. „Unoccupied surface electronic structure of Gd(0001)“. In: *Physical Review B* 49.11 (1994), pp. 7734–7738. DOI: `10.1103/physrevb.49.7734` (cit. on pp. 22, 56).

[74] J. K. Lang, Y. Baer, and P. A. Cox. „Study of the 4f and valence band density of states in rare-earth metals. II. Experiment and results“. In: *Journal of Physics F: Metal Physics* 11.1 (1981), pp. 121–138. DOI: `10.1088/0305-4608/11/1/015` (cit. on pp. 22, 56).

[75] S. Abdelouahed, N. Baadji, and M. Alouani. „Electronic structure and x-ray magnetic circular dichroism of gadolinium beyond the local spin density approximation“. In: *Physical Review B* 75.9 (2007), p. 094428. DOI: `10.1103/physrevb.75.094428` (cit. on pp. 22, 28, 56).

[76] K. M. Döbrich. „Bandstrukturen und Fermiflächen schwerer Lanthanidmetalle bei magnetischen Phasenübergängen“. PhD thesis. FU Berlin, 2007 (cit. on pp. 22, 23).

[77] B. Frietsch. „Magnetization Dynamics of Itinerant and Localized Electrons in Lanthanide Metals“. PhD thesis. FU Berlin, 2015 (cit. on pp. 22, 34, 35, 37, 38, 69, 76, 79, 80, 85–88, 91, 94, 95).

[78] M. Gleich. „Ultrafast demagnetization of gadolinium - studied by XMCD in reflection“. MA thesis. FU Berlin, 2015 (cit. on pp. 22, 33, 54, 68).

[79] K. Zakeri, T. R. F. Peixoto, Y. Zhang, J. Prokop, and J. Kirschner. „On the preparation of clean tungsten single crystals“. In: *Surface Science* 604.2 (2010), pp. L1–L3. DOI: `10.1016/j.susc.2009.10.020` (cit. on p. 22).

[80] B. Andres, P. Weiss, M. Wietstruk, and M. Weinelt. „Spin-dependent lifetime and exchange splitting of surface states on Ni(1 1 1)“. In: *Journal of Physics: Condensed Matter* 27.1 (2014), p. 015503. DOI: `10.1088/0953-8984/27/1/015503` (cit. on p. 22).

[81] S. A. Nepijko, M. Getzlaff, R. Pascal, C. Zarnitz, M. Bode, and R. Wiesendanger. „Lattice relaxation of Gd on W(110)“. In: *Surface Science* 466.1-3 (2000), pp. 89–96. DOI: `10.1016/s0039-6028(00)00724-x` (cit. on p. 23).

[82] F. J. Darnell. „Temperature Dependence of Lattice Parameters for Gd, Dy, and Ho“. In: *Physical Review* 130.5 (1963), pp. 1825–1828. DOI: `10.1103/physrev.130.1825` (cit. on p. 23).

[83] A. Aspelmeier, F. Gerhardter, and K. Baberschke. „Magnetism and structure of ultrathin Gd films“. In: *Journal of Magnetism and Magnetic Materials* 132.1-3 (1994), pp. 22–30. DOI: `10.1016/0304-8853(94)90296-8` (cit. on p. 23).

[84] E. D. Tober, R. X. Ynzunza, C. Westphal, and C. S. Fadley. „Relationship between morphology and magnetic behavior for Gd thin films on W(110)“. In: *Physical Review B* 53.9 (1996), pp. 5444–5448. DOI: `10.1103/physrevb.53.5444` (cit. on p. 23).

[85] D. Li, J. Zhang, P. A. Dowben, and M. Onellion. „Altering the Gd(0001) surface electronic structure with hydrogen adsorption“. In: *Physical Review B* 48.8 (1993), pp. 5612–5620. DOI: `10.1103/physrevb.48.5612` (cit. on pp. 23, 80).

[86] D. N. McIlroy, C. Waldfried, D. Li, J. Pearson, S. D. Bader, D.-J. Huang, P. D. Johnson, R. F. Sabiryanov, S. S. Jaswal, and P. A. Dowben. „Oxygen Induced Suppression of the Surface Magnetization of Gd(0001)“. In: *Physical Review Letters* 76.15 (1996), pp. 2802–2805. DOI: `10.1103/physrevlett.76.2802` (cit. on p. 23).

[87] B. T. Thole, G. van der Laan, and G. A. Sawatzky. „Strong Magnetic Dichroism Predicted in the $M_{4,5}$ X-Ray Absorption Spectra of Magnetic Rare-Earth Materials“. In: *Physical Review Letters* 55.19 (1985), pp. 2086–2088. DOI: `10.1103/physrevlett.55.2086` (cit. on p. 23).

[88] G. van der Laan, B. T. Thole, G. A. Sawatzky, J. B. Goedkoop, J. C. Fuggle, J.-M. Esteva, R. Karnatak, J. P. Remeika, and H. A. Dabkowska. „Experimental proof of magnetic x-ray dichroism“. In: *Physical Review B* 34.9 (1986), pp. 6529–6531. DOI: `10.1103/physrevb.34.6529` (cit. on p. 23).

[89] G. van der Laan and A. I. Figueroa. „X-ray magnetic circular dichroism—A versatile tool to study magnetism“. In: *Coordination Chemistry Reviews* 277-278 (2014), pp. 95–129. DOI: `10.1016/j.ccr.2014.03.018` (cit. on p. 23).

[90] B. T. Thole, P. Carra, F. Sette, and G. van der Laan. „X-ray circular dichroism as a probe of orbital magnetization“. In: *Physical Review Letters* 68.12 (1992), pp. 1943–1946. DOI: `10.1103/physrevlett.68.1943` (cit. on pp. 26, 65).

[91] P. Carra, B. T. Thole, M. Altarelli, and X. Wang. „X-ray circular dichroism and local magnetic fields“. In: *Physical Review Letters* 70.5 (1993), pp. 694–697. DOI: `10.1103/physrevlett.70.694` (cit. on pp. 26, 28, 65).

[92] M. Wietstruk. „Ultraschnelle Magnetisierungsdynamik in itineranten und Heisenberg-Ferromagneten“. PhD thesis. FU Berlin, 2010 (cit. on pp. 28, 72).

[93] A. Eschenlohr. „Element-resolved Ultrafast Magnetization Dynamics in Ferromagnetic Alloys and Multilayers“. PhD thesis. Universität Potsdam, 2012 (cit. on pp. 28, 30, 32, 51).

[94] S. Mangin, C. Bellouard, S. Andrieu, F. Montaigne, P. Ohresser, N. B. Brookes, and B. Barbara. „Magnetization reversal in exchange-coupled GdFe/TbFe studied by x-ray magnetic circular dichroism“. In: *Physical Review B* 70.1 (2004), p. 014401. DOI: `10.1103/physrevb.70.014401` (cit. on p. 28).

[95] R. Nakajima, J. Stöhr, and Y. U. Idzerda. „Electron-yield saturation effects in $\boldsymbol{L}$-edge x-ray magnetic circular dichroism spectra of Fe, Co, and Ni“. In: *Physical Review B* 59.9 (1999), pp. 6421–6429. DOI: `10.1103/physrevb.59.6421` (cit. on pp. 28, 29, 47, 128–130).

[96] J. E. Prieto, F. Heigl, O. Krupin, G. Kaindl, and K. Starke. „Magneto-optics of Gd and Tb in the soft x-ray resonance regions“. In: *Physical Review B* 68.13 (2003), p. 134453. DOI: `10.1103/physrevb.68.134453` (cit. on pp. 29, 47, 56, 66, 129, 130).

[97] A. Ankudinov and J. J. Rehr. „Sum rules for polarization-dependent x-ray absorption“. In: *Physical Review B* 51.2 (1995), pp. 1282–1285. DOI: `10.1103/physrevb.51.1282` (cit. on p. 29).

[98] R. Wu and A. J. Freeman. „Limitation of the Magnetic-Circular-Dichroism Spin Sum Rule for Transition Metals and Importance of the Magnetic Dipole Term“. In: *Physical Review Letters* 73.14 (1994), pp. 1994–1997. DOI: `10.1103/physrevlett.73.1994` (cit. on pp. 29, 65).

[99] G. van der Laan. „Angular momentum sum rules for x-ray absorption“. In: *Physical Review B* 57.1 (1998), pp. 112–115. DOI: `10.1103/physrevb.57.112` (cit. on p. 29).

[100] J. Grabis. „Soft X-Ray Resonant Scattering from Magnetic Heterostructures“. PhD thesis. Ruhr-Universität Bochum, 2005 (cit. on pp. 29, 58, 65).

[101] K. Carva, D. Legut, and P. M. Oppeneer. „Influence of laser-excited electron distributions on the X-ray magnetic circular dichroism spectra: Implications for femtosecond demagnetization in Ni“. In: *EPL (Europhysics Letters)* 86.5 (2009), p. 57002. DOI: `10.1209/0295-5075/86/57002` (cit. on p. 29).

[102] K. Holldack, T. Kachel, S. Khan, R. Mitzner, and T. Quast. „Characterization of laser-electron interaction at the BESSY II femtoslicing source“. In: *Physical Review Special Topics - Accelerators and Beams* 8.4 (2005), p. 040704. DOI: `10.1103/physrevstab.8.040704` (cit. on pp. 30, 51).

[103] K. Holldack, S. Khan, R. Mitzner, and T. Quast. „Femtosecond Terahertz Radiation from Femtoslicing at BESSY“. In: *Physical Review Letters* 96.5 (2006), p. 054801. DOI: `10.1103/physrevlett.96.054801` (cit. on pp. 30, 32, 51).

[104] S. Khan, K. Holldack, T. Kachel, R. Mitzner, and T. Quast. „Femtosecond Undulator Radiation from Sliced Electron Bunches“. In: *Physical Review Letters* 97.7 (2006), p. 074801. DOI: `10.1103/physrevlett.97.074801` (cit. on pp. 30, 51, 52).

[105] K. Holldack, J. Bahrdt, A. Balzer, U. Bovensiepen, M. Brzhezinskaya, A. Erko, A. Eschenlohr, R. Follath, A. Firsov, W. Frentrup, L. L. Guyader, T. Kachel, P. Kuske, R. Mitzner, R. Müller, N. Pontius, T. Quast, I. Radu, J.-S. Schmidt, C. Schüßler-Langeheine, M. Sperling, C. Stamm, C. Trabant, and A. Föhlisch. „FemtoSpeX: a versatile optical pump–soft X-ray probe facility with 100 fs X-ray pulses of variable polarization“. In: *Journal of Synchrotron Radiation* 21.5 (2014), pp. 1090–1104. DOI: `10.1107/s1600577514012247` (cit. on pp. 30–32, 51, 52).

[106] N. Pontius, K. Holldack, C. Schüßler-Langeheine, T. Kachel, and R. Mitzner. „The FemtoSpeX facility at BESSY II“. In: *Journal of large-scale research facilities JLSRF* 2 (2016), A46. DOI: `10.17815/jlsrf-2-71` (cit. on pp. 30, 32, 33).

[107] A. A. Zholents and M. S. Zolotorev. „Femtosecond X-Ray Pulses of Synchrotron Radiation“. In: *Physical Review Letters* 76.6 (1996), pp. 912–915. DOI: `10.1103/physrevlett.76.912` (cit. on p. 30).

[108] R. W. Schoenlein, S. Chattopadhyay, H. H. W. Chong, T. E. Glover, P. A. Heimann, C. V. Shank, A. A. Zholents, and M. S. Zolotorev. „Generation of Femtosecond Pulses of Synchrotron Radiation“. In: *Science* 287.5461 (2000), pp. 2237–2240. DOI: `10.1126/science.287.5461.2237` (cit. on p. 30).

[109] F. Reinert and S. Hüfner. „Photoemission spectroscopy—from early days to recent applications“. In: *New Journal of Physics* 7 (2005), pp. 97–97. DOI: `10.1088/1367-2630/7/1/097` (cit. on pp. 34, 35, 118).

[110] P. M. Echenique, R. Berndt, E. V. Chulkov, T. Fauster, A. Goldmann, and U. Höfer. „Decay of electronic excitations at metal surfaces“. In: *Surface Science Reports* 52.7-8 (2004), pp. 219–317. DOI: `10.1016/j.surfrep.2004.02.002` (cit. on p. 34).

[111] S. Hüfner. *Photoelectron Spectroscopy.* 3rd ed. Springer Berlin Heidelberg, 2003. DOI: `10.1007/978-3-662-09280-4` (cit. on pp. 34, 36–38).

[112] H. Hertz. „Ueber einen Einfluss des ultravioletten Lichtes auf die electrische Entladung“. In: *Annalen der Physik und Chemie* 267.8 (1887), pp. 983–1000. DOI: `10.1002/andp.18872670827` (cit. on p. 34).

[113] W. Hallwachs. „Ueber den Einfluss des Lichtes auf electrostatisch geladene Körper“. In: *Annalen der Physik und Chemie* 269.2 (1888), pp. 301–312. DOI: `10.1002/andp.18882690206` (cit. on p. 34).

[114] A. Einstein. „Über einen die Erzeugung und Verwandlung des Lichtes betreffenden heuristischen Gesichtspunkt“. In: *Annalen der Physik* 322.6 (1905), pp. 132–148. DOI: `10.1002/andp.19053220607` (cit. on p. 34).

[115] M. P. Seah and W. A. Dench. „Quantitative electron spectroscopy of surfaces: A standard data base for electron inelastic mean free paths in solids“. In: *Surface and Interface Analysis* 1.1 (1979), pp. 2–11. DOI: `10.1002/sia.740010103` (cit. on p. 36).

[116] J. Szajman, J. Liesegang, J. G. Jenkin, and R. C. G. Leckey. „Is there a universal mean-free-path curve for electron inelastic scattering in solids?“ In: *Journal of Electron Spectroscopy and Related Phenomena* 23.1 (1981), pp. 97–102. DOI: `10.1016/0368-2048(81)85039-6` (cit. on p. 36).

[117] J. Braun, J. Minár, and H. Ebert. „Correlation, temperature and disorder: Recent developments in the one-step description of angle-resolved photoemission“. In: *Physics Reports* 740 (2018), pp. 1–34. DOI: `10.1016/j.physrep.2018.02.007` (cit. on pp. 38, 118).

[118] I. C. E. Turcu, E. Springate, C. A. Froud, C. M. Cacho, J. L. Collier, W. A. Bryan, G. R. A. J. Nemeth, J. P. Marangos, J. W. G. Tisch, R. Torres, T. Siegel, L. Brugnera, J. G. Underwood, I. Procino, W. R. Newell, C. Altucci, R. Velotta, R. B. King, J. D. Alexander, C. R. Calvert, O. Kelly, J. B. Greenwood, I. D. Williams, A. Cavalleri, J. C. Petersen, N. Dean, S. S. Dhesi, L. Poletto, P. Villoresi, F. Frassetto, S. Bonora, and M. D. Roper. „Ultrafast science and development at the Artemis facility“. In: *ROMOPTO 2009: Ninth Conference on Optics: Micro- to Nanophotonics II.* Ed. by V. I. Vlad. SPIE, 2009. DOI: `10.1117/12.867540` (cit. on pp. 38–40).

[119] P. B. Corkum. „Plasma perspective on strong field multiphoton ionization“. In: *Physical Review Letters* 71.13 (1993), pp. 1994–1997. DOI: `10.1103/physrevlett.71.1994` (cit. on p. 38).

[120] M. Lewenstein, P. Balcou, M. Y. Ivanov, A. L'Huillier, and P. B. Corkum. „Theory of high-harmonic generation by low-frequency laser fields“. In: *Physical Review A* 49.3 (1994), pp. 2117–2132. DOI: `10.1103/physreva.49.2117` (cit. on p. 38).

[121] C. M. Cacho, V. R. Dhanak, L. B. Jones, C. J. Baily, K. L. Ronayne, M. Towrie, C. Binns, and E. A. Seddon. „Spin-resolved two-photon photoemission on $Fe_{77}B_{16}Si_5$ alloy“. In: *Journal of Electron Spectroscopy and Related Phenomena* 169.2-3 (2009), pp. 62–66. DOI: `10.1016/j.elspec.2008.11.002` (cit. on p. 40).

[122] H.-C. Mertins, D. Abramsohn, A. Gaupp, F. Schäfers, W. Gudat, O. Zaharko, H. Grimmer, and P. M. Oppeneer. „Resonant magnetic reflection coefficients at the Fe $2p$ edge obtained with linearly and circularly polarized soft x rays“. In: *Physical Review B* 66.18 (2002), p. 184404. DOI: `10.1103/physrevb.66.184404` (cit. on p. 45).

[123] B. L. Henke, E. M. Gullikson, and J. C. Davis. „X-Ray Interactions: Photoabsorption, Scattering, Transmission, and Reflection at E = 50-30,000 eV, Z = 1-92“. In: *Atomic Data and Nuclear Data Tables* 54.2 (1993), pp. 181–342. DOI: `10.1006/adnd.1993.1013` (cit. on p. 45).

[124] E. Gullikson. *X-Ray Interactions With Matter*. Center for X-Ray Optics, Lawrence Berkeley National Laboratory. 2020. URL: `http://henke.lbl.gov/optical_constants/` (visited on 2020-03-24) (cit. on p. 45).

[125] Omega Engineering Inc. *Type C Reference Tables ANSI/ASTM E-230*. 2019. URL: `https://assets.omega.com/resources/thermocouple-ref-tables-c-c.pdf` (visited on 2019-10-01) (cit. on p. 49).

[126] M. R. Fuchs, K. Holldack, M. Bullough, S. Walsh, C. Wilburn, A. Erko, F. Schäfers, and U. Mueller. „Transmissive x-ray beam position monitors with submicron position- and submillisecond time resolution“. In: *Review of Scientific Instruments* 79.6 (2008), p. 063103. DOI: `10.1063/1.2938400` (cit. on p. 50).

[127] A. Eschenlohr, M. Battiato, P. Maldonado, N. Pontius, T. Kachel, K. Holldack, R. Mitzner, A. Föhlisch, P. M. Oppeneer, and C. Stamm. „Ultrafast spin transport as key to femtosecond demagnetization“. In: *Nature Materials* 12.4 (2013), pp. 332–336. DOI: `10.1038/nmat3546` (cit. on p. 52).

[128] A. Eschenlohr, M. Sultan, A. Melnikov, N. Bergeard, J. Wieczorek, T. Kachel, C. Stamm, and U. Bovensiepen. „Role of spin-lattice coupling in the ultrafast demagnetization of Gd_{1-x} Tb_x alloys“. In: *Physical Review B* 89.21 (2014), p. 214423. DOI: `10.1103/physrevb.89.214423` (cit. on pp. 54, 69, 107, 123).

[129] R. Carley, K. Döbrich, B. Frietsch, C. Gahl, M. Teichmann, O. Schwarzkopf, P. Wernet, and M. Weinelt. „Femtosecond Laser Excitation Drives Ferromagnetic Gadolinium out of Magnetic Equilibrium“. In: *Physical Review Letters* 109.5 (2012), p. 057401. DOI: `10.1103/physrevlett.109.057401` (cit. on pp. 54, 58, 69, 80, 83, 85–87, 91, 94, 95, 97, 107, 109, 123, 125).

[130] M. Teichmann, B. Frietsch, K. Döbrich, R. Carley, and M. Weinelt. „Transient band structures in the ultrafast demagnetization of ferromagnetic gadolinium and terbium“. In: *Physical Review B* 91.1 (2015), p. 014425. DOI: `10.1103/physrevb.91.014425` (cit. on pp. 54, 69, 79, 80, 86, 94, 95).

[131] B. Andres, M. Christ, C. Gahl, M. Wietstruk, M. Weinelt, and J. Kirschner. „Separating Exchange Splitting from Spin Mixing in Gadolinium by Femtosecond Laser Excitation“. In: *Physical Review Letters* 115.20 (2015), p. 207404. DOI: `10.1103/physrevlett.115.207404` (cit. on pp. 55, 71, 74, 77–79, 81–83, 87).

[132] W. J. Lademan, A. K. See, L. E. Klebanoff, and G. van der Laan. „Multiplet structure in high-resolution and spin-resolved x-ray photoemission from gadolinium“. In: *Physical Review B* 54.23 (1996), pp. 17191–17198. DOI: `10.1103/physrevb.54.17191` (cit. on p. 56).

[133] A. C. Thompson, D. T. Attwood, E. M. Gullikson, M. R. Howells, K.-J. Kim, J. Kirz, J. B. Kortright, I. Lindau, Y. Liu, P. Pianetta, A. L. Robinson, J. H. Scofield, J. H. Underwood, G. P. Williams, and H. Winick. *X-ray data booklet.* Ed. by A. C. Thompson. 3rd edition. 2009 (cit. on p. 56).

[134] G. Champion, N. Lalioti, V. Tangoulis, M.-A. Arrio, P. Sainctavit, F. Villain, A. Caneschi, D. Gatteschi, C. Giorgetti, F. Baudelet, M. Verdaguer, and C. C. dit Moulin. „XMCD for Monitoring Exchange Interactions. The Role of the Gd 4f and 5d Orbitals in Metal-Nitronyl Nitroxide Magnetic Chains“. In: *Journal of the American Chemical Society* 125.27 (2003), pp. 8371–8376. DOI: `10.1021/ja034608u` (cit. on p. 56).

[135] F. Leuenberger, A. Parge, W. Felsch, K. Fauth, and M. Hessler. „GdN thin films: Bulk and local electronic and magnetic properties“. In: *Physical Review B* 72.1 (2005), p. 014427. DOI: `10.1103/physrevb.72.014427` (cit. on p. 56).

[136] M. Alouani. „Final-state rule and the absorption spectra of 3*d* ferromagnets“. In: *Physical Review B* 49.22 (1994), pp. 16038–16041. DOI: `10.1103/physrevb.49.16038` (cit. on p. 56).

[137] I. N. Levine. *Quantum Chemistry.* 5th ed. Upper Saddle River, New Jersey 07458: Prentice Hall, 2000 (cit. on p. 56).

[138] O. Berg. „Elektrischer Transport durch Nanokontakte von Selten-Erd-Metallen“. PhD thesis. Karlsruher Institut für Technologie, 2014 (cit. on p. 56).

[139] K. Ramasesha, S. R. Leone, and D. M. Neumark. „Real-Time Probing of Electron Dynamics Using Attosecond Time-Resolved Spectroscopy“. In: *Annual Review of Physical Chemistry* 67.1 (2016), pp. 41–63. DOI: `10.1146/annurev-physchem-040215-112025` (cit. on p. 57).

[140] C. Keller, M. Stichler, G. Comelli, F. Esch, S. Lizzit, W. Wurth, and D. Menzel. „Ultrafast Charge Transfer Times of Chemisorbed Species from Auger Resonant Raman Studies“. In: *Physical Review Letters* 80.8 (1998), pp. 1774–1777. DOI: `10.1103/physrevlett.80.1774` (cit. on p. 57).

[141] I. Radu, K. Vahaplar, C. Stamm, T. Kachel, N. Pontius, H. A. Dürr, T. A. Ostler, J. Barker, R. F. L. Evans, R. W. Chantrell, A. Tsukamoto, A. Itoh, A. Kirilyuk, T. Rasing, and A. V. Kimel. „Transient ferromagnetic-like state mediating ultrafast reversal of antiferromagnetically coupled spins“. In: *Nature* 472.7342 (2011), pp. 205–208. DOI: `10.1038/nature09901` (cit. on pp. 63, 70).

[142] M. Griffel, R. E. Skochdopole, and F. H. Spedding. „The Heat Capacity of Gadolinium from 15 to 355°K“. In: *Physical Review* 93.4 (1954), pp. 657–661. DOI: `10.1103/physrev.93.657` (cit. on p. 64).

[143] S. Y. Dan'kov, A. M. Tishin, V. K. Pecharsky, and K. A. Gschneidner. „Magnetic phase transitions and the magnetothermal properties of gadolinium“. In: *Physical Review B* 57.6 (1998), pp. 3478–3490. DOI: `10.1103/physrevb.57.3478` (cit. on p. 64).

[144] Y. Teramura, A. Tanaka, B. T. Thole, and T. Jo. „Effect of Coulomb Interaction on the X-Ray Magnetic Circular Dichroism Spin Sum Rule in Rare Earths“. In: *Journal of the Physical Society of Japan* 65.9 (1996), pp. 3056–3059. DOI: `10.1143/jpsj.65.3056` (cit. on p. 65).

[145] J. P. Petrakian, N. A. Mokhtar, and R. Fraisse. „Optical constants of gadolinium at various temperatures from polarimetric measurements. (Magnetic ordering effects)“. In: *Journal of Physics F: Metal Physics* 7.11 (1977), pp. 2431–2440. DOI: `10.1088/0305-4608/7/11/025` (cit. on pp. 66, 67).

[146] L. Waldecker, R. Bertoni, R. Ernstorfer, and J. Vorberger. „Electron-Phonon Coupling and Energy Flow in a Simple Metal beyond the Two-Temperature Approximation“. In: *Physical Review X* 6.2 (2016), p. 021003. DOI: `10.1103/physrevx.6.021003` (cit. on p. 68).

[147] T. Henighan, M. Trigo, S. Bonetti, P. Granitzka, D. Higley, Z. Chen, M. P. Jiang, R. Kukreja, A. Gray, A. H. Reid, E. Jal, M. C. Hoffmann, M. Kozina, S. Song, M. Chollet, D. Zhu, P. F. Xu, J. Jeong, K. Carva, P. Maldonado, P. M. Oppeneer, M. G. Samant, S. S. P. Parkin, D. A. Reis, and H. A. Dürr. „Generation mechanism of terahertz coherent acoustic phonons in Fe“. In: *Physical Review B* 93.22 (2016), p. 220301. DOI: `10.1103/physrevb.93.220301` (cit. on p. 68).

[148] J. K. Dewhurst, P. Elliott, S. Shallcross, E. K. U. Gross, and S. Sharma. „Laser-Induced Intersite Spin Transfer“. In: *Nano Letters* 18.3 (2018), pp. 1842–1848. DOI: `10.1021/acs.nanolett.7b05118` (cit. on pp. 71, 87–89, 92–94, 124).

[149] C. Schüßler-Langeheine. „Magnetic Properties of Thin Films of Heavy Lanthanide Metals Studied by Magnetic X-Ray Diffraction and High-Resolution Photoemission“. PhD thesis. FU Berlin, 1999 (cit. on p. 76).

[150] A. V. Fedorov, T. Valla, F. Liu, P. D. Johnson, M. Weinert, and P. B. Allen. „Spin-resolved photoemission study of photohole lifetimes in ferromagnetic gadolinium". In: *Physical Review B* 65.21 (2002), p. 212409. DOI: `10.1103/physrevb.65.212409` (cit. on p. 76).

[151] A. Rehbein, D. Wegner, G. Kaindl, and A. Bauer. „Temperature dependence of lifetimes of Gd(0001) surface states". In: *Physical Review B* 67.3 (2003), p. 033403. DOI: `10.1103/physrevb.67.033403` (cit. on pp. 76, 78).

[152] E. Weschke, C. Schüssler-Langeheine, R. Meier, A. V. Fedorov, K. Starke, F. Hübinger, and G. Kaindl. „Temperature Dependence of the Exchange Splitting of the Surface State on Gd(0001): Evidence against Spin-Mixing Behavior". In: *Physical Review Letters* 77.16 (1996), pp. 3415–3418. DOI: `10.1103/physrevlett.77.3415` (cit. on pp. 77, 78).

[153] B. Kim, A. B. Andrews, J. L. Erskine, K. J. Kim, and B. N. Harmon. „Temperature-dependent conduction-band exchange splitting in ferromagnetic hcp gadolinium: Theoretical predictions and photoemission experiments". In: *Physical Review Letters* 68.12 (1992), pp. 1931–1934. DOI: `10.1103/physrevlett.68.1931` (cit. on pp. 77–79).

[154] R. Wu, C. Li, A. J. Freeman, and C. L. Fu. „Structural, electronic, and magnetic properties of rare-earth metal surfaces: hcp Gd(0001)". In: *Physical Review B* 44.17 (1991), pp. 9400–9409. DOI: `10.1103/physrevb.44.9400` (cit. on pp. 78, 88).

[155] L. M. Sandratskii. „Exchange splitting of surface and bulk electronic states in excited magnetic states of Gd: First-principles study". In: *Physical Review B* 90.18 (2014), p. 184406. DOI: `10.1103/physrevb.90.184406` (cit. on pp. 78, 86).

[156] D. Wegner, A. Bauer, and G. Kaindl. „Magnon-broadening of exchange-split surface states on lanthanide metals". In: *Physical Review B* 73.16 (2006), p. 165415. DOI: `10.1103/physrevb.73.165415` (cit. on p. 78).

[157] M. Lisowski, P. A. Loukakos, A. Melnikov, I. Radu, L. Ungureanu, M. Wolf, and U. Bovensiepen. „Femtosecond Electron and Spin Dynamics in Gd(0001) Studied by Time-Resolved Photoemission and Magneto-optics". In: *Physical Review Letters* 95.13 (2005), p. 137402. DOI: `10.1103/physrevlett.95.137402` (cit. on pp. 78, 90).

[158] M. Getzlaff, M. Bode, S. Heinze, R. Pascal, and R. Wiesendanger. „Temperature-dependent exchange splitting of the magnetic Gd(0001) surface state". In: *Journal of Magnetism and Magnetic Materials* 184.2 (1998), pp. 155–165. DOI: `10.1016/s0304-8853(97)01140-2` (cit. on p. 78).

[159] K. Maiti, M. C. Malagoli, A. Dallmeyer, and C. Carbone. „Finite Temperature Magnetism in Gd: Evidence against a Stoner Behavior". In: *Physical Review Letters* 88.16 (2002), p. 167205. DOI: `10.1103/physrevlett.88.167205` (cit. on pp. 78, 79).

[160] D. Li, J. Pearson, S. D. Bader, D. N. McIlroy, C. Waldfried, and P. A. Dowben. „Spin-polarized photoemission studies of the exchange splitting of the Gd 5*d* electrons near the Curie temperature“. In: *Physical Review B* 51.19 (1995), pp. 13895–13898. DOI: `10.1103/physrevb.51.13895` (cit. on p. 78).

[161] M. Bode, M. Getzlaff, S. Heinze, R. Pascal, and R. Wiesendanger. „Magnetic exchange splitting of the Gd(0001) surface state studied by variable-temperature scanning tunneling spectroscopy“. In: *Applied Physics A: Materials Science & Processing* 66.7 (1998), S121–S124. DOI: `10.1007/s003390051113` (cit. on pp. 78, 79).

[162] B. Andres. „Spin and Magnetization Dynamics Studied by Spin-Resolved Photoemission“. PhD thesis. FU Berlin, 2016 (cit. on pp. 78, 83).

[163] E. Weschke and G. Kaindl. „Magnetic exchange splitting in lanthanide metals“. In: *Journal of Physics: Condensed Matter* 13.49 (2001), pp. 11133–11148. DOI: `10.1088/0953-8984/13/49/303` (cit. on p. 79).

[164] S. G. Han, Z. V. Vardeny, K. S. Wong, O. G. Symko, and G. Koren. „Femtosecond optical detection of quasiparticle dynamics in high-$T_C YBa_2Cu_3O_{7-\delta}$ superconducting thin films“. In: *Physical Review Letters* 65.21 (1990), pp. 2708–2711. DOI: `10.1103/physrevlett.65.2708` (cit. on p. 97).

[165] W. S. Fann, R. Storz, H. W. K. Tom, and J. Bokor. „Direct measurement of nonequilibrium electron-energy distributions in subpicosecond laser-heated gold films“. In: *Physical Review Letters* 68.18 (1992), pp. 2834–2837. DOI: `10.1103/physrevlett.68.2834` (cit. on p. 97).

[166] M. Bonn, D. N. Denzler, S. Funk, M. Wolf, S.-S. Wellershoff, and J. Hohlfeld. „Ultrafast electron dynamics at metal surfaces: Competition between electron-phonon coupling and hot-electron transport“. In: *Physical Review B* 61.2 (2000), pp. 1101–1105. DOI: `10.1103/physrevb.61.1101` (cit. on p. 97).

[167] A. L. Cavalieri, N. Müller, T. Uphues, V. S. Yakovlev, A. Baltuška, B. Horvath, B. Schmidt, L. Blümel, R. Holzwarth, S. Hendel, M. Drescher, U. Kleineberg, P. M. Echenique, R. Kienberger, F. Krausz, and U. Heinzmann. „Attosecond spectroscopy in condensed matter“. In: *Nature* 449.7165 (2007), pp. 1029–1032. DOI: `10.1038/nature06229` (cit. on p. 97).

[168] U. Bovensiepen, S. Declair, M. Lisowski, P. A. Loukakos, A. Hotzel, M. Richter, A. Knorr, and M. Wolf. „Ultrafast electron dynamics in metals: Real-time analysis of a reflected light field using photoelectrons“. In: *Physical Review B* 79.4 (2009), p. 045415. DOI: `10.1103/physrevb.79.045415` (cit. on pp. 97–100, 102–105, 107, 121, 125).

[169] G. Schmidt. *Physics of High Temperature Plasmas.* 2nd ed. 111 Fifth Avenue, New York, New York 10003: Academic Press, Inc., 1979 (cit. on pp. 99, 100).

[170] X. Zheng. „Time-resolved photoemission and ultrafast magnetization dynamics in Gd“. MA thesis. FU Berlin, 2018 (cit. on pp. 101, 104).

[171] M. Born and E. Wolf. *Principles of Optics*. 4th ed. Headington Hill Hall, Oxford: Pergamon Press, 1970 (cit. on p. 104).

[172] Optical Society Of America. *Handbook of Optics, Vol. 2: Devices, Measurements, and Properties*. 2nd ed. 2 Pennsylvania Plaza, New York City: McGraw-Hill Professional, 1994 (cit. on p. 105).

[173] P. B. Johnson and R. W. Christy. „Optical Constants of the Noble Metals“. In: *Physical Review B* 6.12 (1972), pp. 4370–4379. DOI: `10.1103/physrevb.6.4370` (cit. on p. 105).

[174] P. Johnson and R. Christy. „Optical constants of transition metals: Ti, V, Cr, Mn, Fe, Co, Ni, and Pd“. In: *Physical Review B* 9.12 (1974), pp. 5056–5070. DOI: `10.1103/physrevb.9.5056` (cit. on p. 105).

[175] W. Bludau, A. Onton, and W. Heinke. „Temperature dependence of the band gap of silicon“. In: *Journal of Applied Physics* 45.4 (1974), pp. 1846–1848. DOI: `10.1063/1.1663501` (cit. on p. 109).

[176] B. Frietsch, R. Carley, M. Gleich, M. Teichmann, J. Bowlan, and M. Weinelt. „Fluence-dependent dynamics of the 5d6s exchange splitting in Gd metal after femtosecond laser excitation“. In: *Japanese Journal of Applied Physics* 55.7S3 (2016), p. 07MD02. DOI: `10.7567/jjap.55.07md02` (cit. on p. 109).

[177] J. Feydt, A. Elbe, H. Engelhard, G. Meister, C. Jung, and A. Goldmann. „Photoemission from bulk bands along the surface normal of W(110)“. In: *Physical Review B* 58.20 (1998), pp. 14007–14012. DOI: `10.1103/physrevb.58.14007` (cit. on p. 113).

[178] B. Feuerbacher and B. Fitton. „Electronic Energy Levels of Hydrogen Adsorbed on Tungsten“. In: *Physical Review B* 8.10 (1973), pp. 4890–4892. DOI: `10.1103/physrevb.8.4890` (cit. on p. 113).

[179] N. E. Christensen and B. Feuerbacher. „Volume and surface photoemission from tungsten. I. Calculation of band structure and emission spectra“. In: *Physical Review B* 10.6 (1974), pp. 2349–2372. DOI: `10.1103/physrevb.10.2349` (cit. on p. 113).

[180] R. J. Smith, J. Anderson, J. Hermanson, and G. J. Lapeyre. „Study of W bulk bands with normal (001) photoemission using synchrotron radiation“. In: *Solid State Communications* 19.10 (1976), pp. 975–978. DOI: `10.1016/0038-1098(76)90633-5` (cit. on p. 113).

[181] R. H. Gaylord and S. D. Kevan. „Spin-orbit-interaction-induced surface resonance on W(011)“. In: *Physical Review B* 36.17 (1987), pp. 9337–9340. DOI: `10.1103/physrevb.36.9337` (cit. on p. 113).

[182] D. Li, P. A. Dowben, J. E. Ortega, and F. J. Himpsel. „Experimental determination of the unoccupied bands of W(110)“. In: *Physical Review B* 47.19 (1993), pp. 12895–12899. DOI: `10.1103/physrevb.47.12895` (cit. on p. 113).

[183] L. Plucinski, J. Minár, B. C. Sell, J. Braun, H. Ebert, C. M. Schneider, and C. S. Fadley. „Band mapping in higher-energy x-ray photoemission: Phonon effects and comparison to one-step theory“. In: *Physical Review B* 78.3 (2008), p. 035108. DOI: `10.1103/physrevb.78.035108` (cit. on p. 113).

[184] R. F. Willis and N. E. Christensen. „Secondary-electron-emission spectroscopy of tungsten: Angular dependence and phenomenology“. In: *Physical Review B* 18.10 (1978), pp. 5140–5161. DOI: `10.1103/physrevb.18.5140` (cit. on p. 113).

[185] P. J. Feibelman and D. E. Eastman. „Photoemission spectroscopy— Correspondence between quantum theory and experimental phenomenology“. In: *Physical Review B* 10.12 (1974), pp. 4932–4947. DOI: `10.1103/physrevb.10.4932` (cit. on p. 118).

[186] J. Braun, K. Miyamoto, A. Kimura, T. Okuda, M. Donath, H. Ebert, and J. Minár. „Exceptional behavior of d-like surface resonances on W(110): the one-step model in its density matrix formulation“. In: *New Journal of Physics* 16.1 (2014), p. 015005. DOI: `10.1088/1367-2630/16/1/015005` (cit. on p. 118).

Publications

[I] K. Bobowski, M. Gleich, N. Pontius, C. Schüßler-Langeheine, C. Trabant, M. Wietstruk, B. Frietsch, and M. Weinelt
Influence of the pump pulse wavelength on the ultrafast demagnetization of Gd(0001) thin films, Journal of Physics: Condensed Matter **29** (2017), 234003
DOI: 10.1088/1361-648x/aa6c92

[II] K. Bobowski, M. Gleich, B. Frietsch, C. Trabant, M. Wietstruk, U. Atxitia, and M. Weinelt
Unifying the concept of ultrafast magnetization dynamics in type I and type II materials (in preparation)

[III] K. Bobowski, B. Frietsch, X. Zheng, D. Lawrenz, W. Bronsch, J. Bowlan, C. Gahl, B. Andres, R. Carley, M. Teichmann, A. Scherz, C. Cacho, R. Chapman, S. Molodtsov, E. Springate, and M. Weinelt
Optically induced interface spin transfer and its impact on ultrafast magnetization dynamics (in preparation)

Supervised Theses

[I] Janos Pauer
Magnetization Dynamics of Gadolinium
Bachelor Thesis, FU Berlin, 2015

[II] Xinwei Zheng
Time-resolved photoemission and ultrafast magnetization dynamics in Gd
Master Thesis, FU Berlin, 2018

Acknowledgments

Stars and stones, it seems like it is finally done. But, of course, this dissertation would not have been possible without the substantial support of many actors. Thus, I would like to thank everyone who in some way or another supported me in my endeavor to make my PhD!

First of all, I would like to thank Prof. Martin Weinelt for the opportunity to work in his group and make my PhD as well as his scientific guidance and input in making sense out of confusing data and combining it into a more integral picture. In my time in the group I learned a lot and developed personally.

I want to thank Prof. Ralph Ernstorfer for his role as my second supervisor.

A big thank you goes to the Weinelt group for their help with all things, be it lab work, scientific discussions, administrative aspects or simply enjoyable moments in between all the work. I thank Cornelius Gahl for sharing his knowledge in laser- and optics-related matters, Ralph Püttner for instructive discussions about various fundamental physics aspects and help with the physics of the Compton experiment for Master students, Unai Atxitia for discussing about the theoretical fundamentals of laser-induced magnetization dynamics and his modeling of our data, the HHG and BESSY teams for their helping hands in lab work and data evaluation, Thea Postler for taking care of administrative affairs, and Kristof Zielke and Daniel Przyrembel for sharing their extensive knowledge and helping in technical issues.

Not only within my group I enjoyed support, but also from people without. Thus, I want to thank the experimental teams at the FemtoSpeX and Artemis beamlines for their support and extraordinary commitment to lead our beamtimes to success, but also for enjoyable coffee breaks. In particular, I am grateful to Christian Schüßler-Langeheine, Niko Pontius and Cephise Cacho for their leading roles in our cooperation projects.

For helpful discussions and theoretical background regarding the oscillations, I want to thank Jürgen Braun.

I am particularly glad to have worked together with Robert Carley. His positive and easy nature made any mutual activity much more fun and worthwhile still being highly instructive. Thanks for your invaluable help in taming the dragon! Weitermachen!

I want to thank the IMPRS people, students and heads alike, for the wonderful time spent together and for their support and understanding. This network is really enriching and I am happy to have been part of it.

I want to thank Markus Gleich for being a friend and colleague and struggling together with me through hard and easy times, night and day in the lab and office. The good atmosphere was an essential part in keeping me going. You saved me much time acting as my backup memory for all possible things I tended to forget. Cheers!

A cordial thanks to Jörg Behrmann for his support in helping me, a Python-toddler, to make my first steps and his further support in technical and programming questions

(besides being a dear friend).
Special thanks to Björn Frietsch, Marko Wietstruk, Christoph Trabant, Nele Thielemann-Kühn and Wibke Bronsch for taking part in supervising me as more or less direct project leaders.
Furthermore, I want to thank all the people directly involved in writing the thesis: Unai Atxitia for his invaluable support regarding the understanding of the theory behind magnetization dynamics and the writing of the theory chapter; Wibke Bronsch for proofreading most of the thesis; and all the other people proofreading parts of the thesis: Beatrice Andres, Markus Gleich, Sophia Ketterl, Dominic Lawrenz and Nele Thielemann-Kühn.

I am very grateful to my family for always being there and giving me the security that, no matter what, I would always have a place to go. Thanks for trusting in me and giving me all the room to focus on my work!

I was (and am) lucky to have many friends, too many to list everyone here. I am really grateful for having you all and being able to share my hobbies and have fun with you, but also for you being there for me if I needed help or support and listening to my complaints or cheering me up. Thanks for keeping my sanity at an acceptable level!
One person needs to be highlighted, though. Sophia Ketterl fills out many roles to support me. A loving thank you for giving me scientific input when needed, being patient with me being difficult when stressed and under pressure, keeping up my self-esteem if it was starting to break down, for the time spent together outside of work and on holidays making them much more worthwhile, for passing time together sharing the same hobbies but also giving me room to engage in my own hobbies, and anything else I might have forgotten to mention!

What else remains to say? Well, to put it in the words of Douglas Adams: “So long and thanks for all the fish!”.

Lebenslauf

Kamil Bobowski

Der Lebenslauf ist in der Online-Version aus Gründen des Datenschutzes nicht enthalten.

Selbstständigkeitserklärung

Hiermit erkläre ich, Kamil Bobowski, geboren am 12.11.1988 in Berlin, diese Dissertation selbstständig und nur unter Verwendung der angegebenen Hilfen und Hilfsmittel angefertigt zu haben. Die Arbeit wurde weder in einem früheren Promotionsverfahren angenommen noch als ungenügend beurteilt. Ich erkläre die Kenntnisnahme der dem Verfahren zugrunde liegenden Promotionsordnung des Fachbereichs Physik der Freien Universität Berlin veröffentlicht in den FU-Mitteilungen 34/2013 vom 02.09.2013.

Berlin, den 2. September 2020

Kamil Bobowski